The effect of MXene on the developmental pathways leading to posterior capsule opacification for use within an accommodative intraocular lens

Grace Carmen Cooksley

A Thesis submitted in partial fulfilment of the requirements of

the University of Brighton for the degree of Doctor of Philosophy

Abstract

Posterior capsule opacification (PCO) is the most common complication arising from the corrective surgery used to treat cataract patients. $Ti_3C_2T_x$ (MXene) has been applied as a transparent conductive electrode (TCE) in an adjustable focus lens model to provide changes in dioptric range for an accommodative IOL (AIOL) design. However, its impact on the wound-healing response of lens epithelial cells (LEC) contributing to PCO development is not yet known. This thesis investigates the effects of $Ti_3C_2T_x$ on the initial wound healing response and epithelial-mesenchymal transition (EMT) pathway of residual LEC, which occurs post cataract surgery (PCS) and contributes to PCO development.

$Ti_3C_2T_x$ was synthesised using the MILD method and processed to achieve uniform flake size and dispersed solutions across batches as confirmed by dynamic light scattering and scanning electron microscopy. Contact angle measurements confirmed the hydrophilic nature of $Ti_3C_2T_x$ by increasing the wettability of hydrophobic IOLs coated with $Ti_3C_2T_x$. ELISA analysis showed that LECs grown on $Ti_3C_2T_x$ coatings showed no significant upregulation of the pro-inflammatory cytokines IL-1β and IL-6. Cells treated with $Ti_3C_2T_x$ and IL-1β showed a significant suppression of both the gene and protein expression of IL-1β and markedly reduced the expression of IL-6 gene and protein and the *CXCL1* gene relative to cells treated with IL-1β alone, as quantified by q-PCR. RNA sequencing showed that $Ti_3C_2T_x$ coatings did not upregulate any hallmark inflammatory gene sets. Whilst no significant broad downregulation of pro-inflammatory gene sets was observed at the concentration of $Ti_3C_2T_x$ used, a marked reduction in the cytokine-cytokine receptor interaction pathways and secretion of pro-inflammatory cytokines occurred. Moreover, immunocytochemistry, scratch assay and western blot analysis showed that $Ti_3C_2T_x$ did not promote EMT pathways and repressed overexpression of migratory markers whilst increasing wound closure rate thereby promoting a positive resolution of LEC wound healing response. A potential mechanism was suggested that $Ti_3C_2T_x$ interacts with the cytokine-cytokine

receptor interaction pathway, promoting anti-inflammatory mechanisms to resolve the inflammation and EMT response in LECs. $Ti_3C_2T_x$ did not upregulate key senescence markers in FHL124 cells as shown by 5-ethynyl-2′-deoxyuridine (EdU) and p21 and p16 expression quantified by q-PCR. This work has shown for the first time that a silicone-based capsule bag model can be used to mimic in part the properties of the capsule bag for initial assessment of IOL materials in a 3-dimensional (3D) model prior to the use of invasive animal or human tissue derived capsule bag models. In conclusion, this body of work has demonstrated the ability of $Ti_3C_2T_x$ to promote positive resolution of the LEC wound healing response by suppressing hyperinflammation and EMT pathways contributing to PCO development.

Contents

Acknowledgements

I would like to first thank my supervisory team, Dr. Susan Sandeman, Dr Marcus Dymond, Dr Joseph Lacey and Prof. Yury Gogotsi for their support and encouragement in promoting my confidence throughout my PhD. I would like to thank Prof. Richard Faragher, Dr. Jon Salvage, Dr. Marcus Allen and the remaining staff and technical support at the University of Brighton for all the help throughout this work. To our colleagues at Rayner Intraocular Lenses, thank you for all your encouragement, it has been a wonderful experience to have met you all and worked alongside you. I would like to also thank the University of Brighton, the Doctoral Training Alliance and Rayner Intraocular Lenses for the funding that has allowed me the privilege of working on this body of work.

To my nan, thank you for everything, your belief and support. To my sibling, Jaspar, you inspire me with your bravery and strength, love you. To my step mum, Narn, thank you for always being there for me and uplifting me all these years. To Ginger, Bobo and Ozzy, the three best guineas in the whole world, thanks for all the free animal therapy. To Charlie, Richard, Agnes and Tomwise, thank you for all your understanding and support throughout this time, you have been the best. To Graco and the many teachers who inspired and encouraged me to reach this point. To my fellow PhD students, past and present, you have been the greatest companions throughout this journey. My special thanks go to Emma, Nic, Neda, Media, Natalia, Blair, Andra, Rico, Fernando, Ryan, Nadia, Soulef, Meriem, Charis, and Ana for all the laughs, encouragement, rants, and true friendship over the past few years. Each of you have inspired me to become a better researcher and person. To my darling Alex, you have brought so much light and love through your never-ending support and understanding. Thank you always and good luck with your own PhD journey.

This PhD has taught me to trust in your own path and never give up.

"Not all those who wander are lost;"
- J.R.R. Tolkien

Declaration

I declare that the research contained within this thesis, unless otherwise stated within text, is the original work of the author. The thesis has not been previously submitted in any form to any other university in fulfilment of any degree or qualification, nor has any of its material contained within.

Grace Cooksley   31/3/2023

List of Figures

Figure S27: Light microscope images of an implanted hydrophilic IOL (n=3).

Figure S28: Light microscope images of an implanted $Ti_3C_2T_x$-coated hydrophobic IOL (n=2).

Figure S29: Light microscope images of an implanted $Ti_3C_2T_x$-coated hydrophobic IOL (n=3).

List of Tables

Table 1.1: Evaluation of intraocular lenses available in the current market.

Table 1.2: Mean amplitude of accommodation by age.

Table 1.3: Properties of the accommodative intraocular lenses sold in the current lens market.

Table 2.1: Characterisation methods used to determine MXenes' structure, chemical composition and flake size.

Table 2.2: Characterisation of $Ti_3C_2T_x$ colloidal solutions between batches.

Table 2.3: Chemical composition of $Ti_3C_2T_x$ coatings.

Table 2.4: Contact angle analysis of intraocular lens types.

Table 3.1: Primers for genes of interest.

Table 3.2: Chapter 3 experiments with experimental conditions and summary of data.

Table 4.1: Samples in experiment with index number, sample condition and the replicate number with its sequence run number.

Table 5.1: GC/MS analysis of silicone extractables in the first ethanol wash.

Table 6.1: Primers for senescence marker genes of interest.

Table S1: Optimisation requirements for synthesised $Ti_3C_2T_x$ (MXene) batches.

Table S2: $Ti_3C_2T_x$ (MXene) batches with characterisation techniques and application in experiments.

Abbreviations

AH	Aqueous humour
AIOL	Accommodative intraocular lenses
Ct	Cycle threshold
DDR	DNA damage response
DEG	Differentially expressed genes
DLS	Dynamic light scattering
ELISA	Enzyme-linked immunosorbent assay
EMT	Epithelial mesenchymal transition
FBS	Foetal bovine serum
GC/MS	Gas chromatography/mass spectroscopy
LEC	Lens epithelial cells
LPS	Lipopolysaccharide
IL	Interleukin
IOL	Intraocular lenses
IOP	Intraocular pressure
MEM	Minimum essential medium
Nd: YAG	Neodymium-doped yttrium aluminium garnet
PBS	Phosphate buffer saline
PCO	Posterior capsule opacification
PCS	Post-cataract surgery
PMMA	Polymethyl methacrylate
q-PCR	Quantitative polymerase chain reaction
TGF-β	Transforming growth factor beta
TNF	Tumour necrosis factor

Chapter 1: Introduction

1.1   Background and overview

Cataracts, an ocular disease where the crystalline lens of the eye becomes opaque due to the aggregation of proteins, are the greatest contributor to avoidable blindness worldwide (1). Corrective surgery replaces the cloudy lens with an artificial intraocular lens (IOL) (2). However, this corrective surgery can lead to long-term complications. The most common post-operative complication is posterior capsule opacification (PCO) (3–5). Lens epithelial cells (LEC) remaining within the capsule bag, the body which holds the lens, undergo a wound-healing response which may trigger an epithelial-mesenchymal transition (EMT) of the LEC (5–7). The myofibroblasts migrate over the posterior capsule and form a 'secondary cataract' (8). PCO develops between the first two to five years post-surgery, at an occurrence of 5 – 50% depending on the patient's risk factors (9). PCO can be treated with neodymium yttrium aluminium garnet (Nd: YAG) laser ablation however this procedure can cause additional damage to the eye. There is a requirement for novel therapeutic interventions which prevents activation of pathways leading to PCO. Experimental models are paramount to assess novel treatments and IOL technology to prevent PCO (8). *In vitro* human capsule bag models provide a clinical insight into the pathophysiology of PCO and the putative impact of IOL on PCO development (10,11). However human tissue is expensive, time-dependent and limited in supply (12). The development of a replicate artificial capsule bag model has yet to be established to overcome the challenges of accessing donor tissue and the differences in response between animal and human models.

Another disadvantage of current IOLs is that they do not have the accommodative function of the natural lens, which mean patients require spectacles for near vision (2). Accommodative IOLs (AIOL) are designed to utilise the functional ciliary muscles to provide dynamic changes in focus. Currently, no commercially available AIOL provides patients with true accommodative function (13). A new development in optoelectronic materials with potential applications in AIOLs is the use of two-dimensional (2D) MXene nanomaterials as hydrophilic, flexible, transparent, conductive electrodes (TCE) which are capable of a sensitive and rapid response to

electrical stimulus for induction of a dynamic change in lens dioptic power (14). The novel family of MXenes, discovered in 2011, consists of transition metal carbides and/or nitrides. They can be processed as transparent films and have shown conductance of σ = 15 000 S cm^{-1}, exceeding graphene and other nanomaterials (15–20). Ward et al., (14) used $Ti_3C_2T_x$ as a TCE in an adjustable focus lens to induce changes in dioptic power providing proof of concept data for use of $Ti_3C_2T_x$ within an AIOL prototype using liquid crystal components. Nevertheless, there is uncertainty about the impact of $Ti_3C_2T_x$ on ocular inflammatory and fibrotic pathways within the capsule bag. Furthermore, the impact of $Ti_3C_2T_x$ on the developmental pathways leading to PCO is unknown. A new AIOL should provide accommodative function with no detriment to visual acuity or increase the risk of long-term complications such as PCO. Therefore, this thesis will assess the immune response and propensity of LECs to undergo EMT on interaction with $Ti_3C_2T_x$ coatings in order to understand the impact of $Ti_3C_2T_x$ on the developmental pathways leading to PCO.

In this chapter, the clinical treatment for cataracts will be discussed and the current IOL technology to restore visual acuity and accommodation will be evaluated. The use of $Ti_3C_2T_x$ in biomedical applications and more specifically, as a TCE in optoelectronic devices will be discussed. The current understanding of the biocompatibility of $Ti_3C_2T_x$ will be explored to demonstrate the current gap in knowledge with regard to its impact on the ocular environment and wound healing response. The established pathways contributing to PCO development will be discussed, in addition to experimental models used in PCO research to further elicit the key molecular mechanisms underpinning the condition and their use in assessing device interventions which could repress mechanisms leading to PCO.

1.2 Cataracts: a global clinical challenge

Cataracts are responsible for more cases of blindness globally than all other primary causes of blindness combined **(Fig. 1.1)** (1). In 2018, the World Health Organisation estimated 90 million people worldwide still live with cataract-associated blindness (21). Each year, an

additional 1 – 2 million people become blind due to their untreated cataracts, although 75% of these cases are treatable (22). The number of cases is expected to rise due to an expanding and ageing population (22). In 2018, the Royal National Institute of Blind People (RNIB) found cataracts to be the leading cause for 16% of the 350,000 people registered blind or partially sighted in the United Kingdom. This number is expected to increase by 30% between 2020 and 2030.
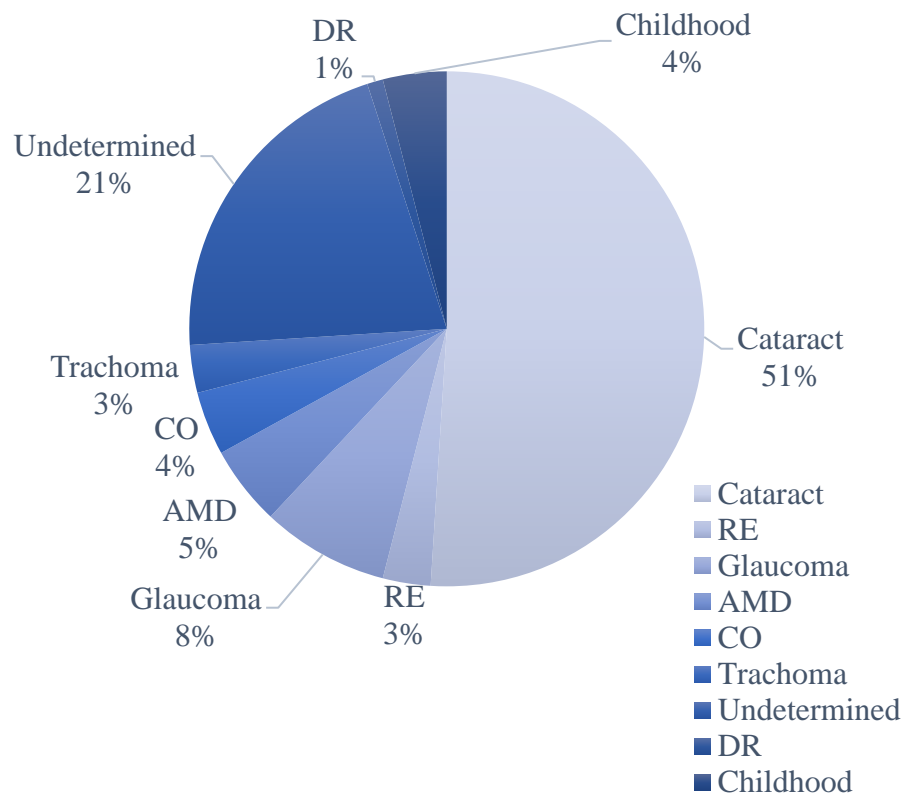
Figure 1.1: Global causes of blindness in 2010, estimated from 39 countries. AMD, age-related macular degeneration; CO, corneal opacities; DR, diabetic retinopathy; RE, uncorrected refractive errors (23).

A cataract occurs when the crystalline transparent lens becomes cloudy and opaque, resulting in reduced visual acuity. The lens consists of LECs and differentiated lens fibres. LECs are focussed at the anterior (A cells) and equatorial (E cells) of the capsule bag. On migrating laterally to the centre of the lens, the LECs withdraw from the cell cycle, elongate and differentiate into lens fibres which constitute the majority of the lens body (4,24,25).

Differentiated fibre cells are characterised by their lack of blood vessels and light-scattering organelles (26). To compensate for the loss of protein synthesis and to repair organelles, fibre cells immediately express high levels of crystallin proteins upon differentiation (27). Fibre cells contain three functional families of protein chaperones, α-, β- and γ-crystallin (26,27). α-crystallin chaperone proteins, also known as small heat shock proteins (sHSP), maintain transparency by binding to damaged, unfolding proteins to prevent aggregation which increases light scatter (26,27). These proteins are long-lived and are susceptible to age-related changes (26,27). Cataracts develop due to the build-up of damaged proteins which accumulate over a person's life and the ageing lens fibres. The ageing eye will have a depletion of α-crystallin in synergy with increased faulty protein synthesis contributing to disorganised fibre cell alignment and protein aggregation (22,26,27). This results in poor transparency and increased light scatter, characteristic of cataract development.

A patient with cataracts will have to undergo surgery to remove the diseased lens, which will then be replaced with an IOL. In England alone, 330,000 cataract surgeries are performed per year (23). IOL design and material can greatly impact the outcome of the surgical intervention. The next generation of IOL technology aims to provide an IOL for patients that restores all of the natural function of the human lens without increasing the risk of post-operative complications.

1.2.1 Cataract surgery and an introduction to intraocular lenses technology

Cataract surgery is one of the oldest and safest surgical procedures (28). The first recorded surgical cataract extraction was as early as 5 BC (**Fig. 1.2**). It was not until the later 1960s, that the currently applied phacoemulsification procedure to extract a cataractous lens was developed (28,29). This was shortly followed in 1972 by the addition of gel-like ophthalmic viscosurgical devices (OVDs) to the surgical procedure, which prevented the collapse of the capsule bag structure after lens extraction, prior to IOL implantation (28,29). Since the first implanted IOL in 1949 by Sir Harold Ridley, IOL technology has undergone significant development. The current

challenge for IOL technology is to provide patients with multi-focal lengths for near and distance vision, independent of spectacles (28,29).

5TH Century BC
Couching is the earliest known method for cataract removal. The cataract was not removed but dislodged.

16TH Century
First documented case of extracapsular extraction and intracapsular extraction.

20TH Century
Kelman invents phacoemulsification. Sir Harold Ridley implants the first IOL made from PMMA.

21ST Century
Current use of monofocal, multifocal and toric IOL. The development of accommodative lenses.

Figure 1.2: A brief timeline of the evolution of cataract surgery. IOL: intraocular lenses; PMMA: polymethyl methacrylate (28,29).

Modern day cataract surgery begins with small incisions around the cornea. An opening in the capsule bag is made through which the phacoemulsification probe is inserted. The probe breaks down the cataract and removes the segments from the capsule bag. OVD is inserted into the capsule bag to maintain its structure and protect the surrounding tissue then a pre-loaded injectable IOL is implanted within the capsule bag, where it unfolds and situates itself in a central position (29). Although 95% of cataract surgeries are successful in achieving visual acuity, there are still a number of cases that have long-term post-operative complications (30). The risk of developing complications is impacted by the surgeon's skill; the patient's own risk factors, IOL material and design (31). The composite material of an IOL affects the biocompatibility of the lenses when implanted. Polymethyl methacrylate (PMMA) was the first material used to produce IOLs due to its relative inertness and good longevity within the eye. Nevertheless, PMMA IOLs have large diameters, requiring large opening incisions which can be permeated by aqueous humour (AH) leading to surgical complications like glistenings and optic opacification (32).

Silicone IOLs are foldable and have lower PCO incidence. However, silicone has a low refractive index and allows for bacterial adhesion, increasing the risk of infection (32,33). Acrylic IOLs are commonly divided into hydrophobic and hydrophilic types. Hydrophobic acrylic IOLs have good elasticity and a lower risk of PCO development but these IOLs are easy to mark or scratch during implantation and require more attention to centre when implanted (34). Hydrophilic acrylic IOLs have excellent biocompatibility and require a relatively smaller opening incision. Nevertheless, there is some evidence to suggest that these IOLs increase the risk of developing PCO and can opacify due to calcium deposition (33).

The type of IOL determines the post-operative outcome in visual acuity, range of vision and likelihood of developing long-term complications. Monofocal IOLs improve visual acuity for patients. However, patients remain with one focal point and will still require spectacles for near vision (2). Multifocal IOLs utilise bifocal or trifocal points, allowing near, intermediate and distance vision but patients are more likely to experience dysphotopsias, artefacts of light often presenting as glares or halos across the visual axis, and post-surgical complications (2,32). Toric IOLs are given to cataract patients with astigmatism. However, if the IOLs become mis-aligned, the patient may experience blurred vision and require glasses (2). AIOLs are under development to return visual acuity to patients whilst retaining the accommodative function of the natural lenses (13). **Table 1.1** summarises the different types and the composite materials of the current market IOLs, excluding AIOLs.

Table 1.1: Properties of marketed intraocular lenses (2,32).

Type	*Advantages*	*Disadvantages*
Monofocal	Visual acuity	Spectacle-dependence
Multifocal	Spectacle independence Contrast sensitivity	Halos and glares Ineffectual
Toric	Corrects corneal astigmatism Spectacle independence	Lower rotational stability Misalignment causes blurred vision
Material		
PMMA	Longevity	Rigid Large diameter Glistenings and optic opacification
Silicone	Tendency to low PCO incidence Good resistance to Nd: YAG Foldable, easy to implant	Glistenings Low refractive index Thick optics Favour bacterial adhesion
Hydrophobic Acrylic	Foldable, easy to implant Tendency to low PCO incidence Good resistance to Nd: YAG	Can be marked or scratched Low tendency to self-centre Glistenings

Hydrophilic Acrylic
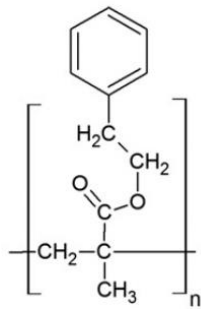
Foldable, easy to implant

Sub-2-mm incision size

Higher PCO incidence

Capsule bag contraction

Calcification

1.2.2 Accommodative intraocular lenses

Accommodation occurs when the lens becomes compressed, increasing its curvature resulting in an increase in optical power for near vision (35), stimulated by the relaxation and contraction of the ciliary muscles. The contraction of the ciliary muscles relaxes the zonules and causes the capsule to curve the lens, making it more convex (13). As a person ages, the capsule's ability to curve the lens decreases, resulting in a reduced amplitude of accommodation (**Table 1.2**) but not a complete loss of ciliary muscle function (36–38). AIOLs were first developed to utilise the functional ciliary muscles with flexible haptics that would move with the muscles and change the dioptric power of the lens accordingly (39). However, this mechanism did not produce the required increase in refractive power when implanted. More recent AIOL designs aim to encompass the entire capsule bag to utilise the contraction of the anterior and posterior capsule to provide dynamic changes in focus (40).

Table 1.2: Mean amplitude of lens accommodation by age (41).

Age group (years)	Mean amplitude (dioptres)
>10	14.5
10 – 29	8.4
30 – 50	3.0
51+	1.1

A summary of the current AIOLs on the market is shown in **Table 1.3.** In practice, many AIOLs cannot provide the dynamic change in dioptric power seen in the natural lens. 40 – 70% of patients fitted with AIOLs remain spectacle-dependent and over 50% experience dysphotopsias (2). Single-optic AIOLs rely on ciliary muscle contraction to displace the anterior of the lens optic and increase the dioptric (D) power (39). The basic optical principle states that as the distance between the AIOL and the cornea decreases, due to the ciliary muscle contraction, the power of the lens, if it is positive, will increase linearly with the amount of displacement i.e. as the lens displaces in a forward direction towards the cornea, the dioptric power of the lens increases, allowing the accommodation of the AIOL. The disadvantage of single-optic AIOLs are their limited accommodation; a 1 mm movement is equivalent to a 2 D power change (2,39). Furthermore, this mechanism is reliant on the flexibility of the capsule bag (2). Studies have shown that single-optic AIOLs such as Crystalens AT-45 did not improve near vision when compared to monofocal lens (13,39). Dual-optic AIOLs encompass the entire capsule bag so that the capsule tension can change the distance between the anterior and posterior optic. The contraction of ciliary muscles and subsequent relaxation of the capsule bag, shifts the anterior lens forward and increases dioptric power (39). Synchrony, a dual-optic AIOL was found to fail following long term use due to its dependence on the flexibility of the capsule bag, which will inevitably contract (2,13). To overcome this, the AIOL can be implanted in the ciliary sulcus, which has shown improved IOL support in primate models and is used for patients with posterior capsule rupture (PCR) (42). However, the ciliary sulcus is supplied by the circulatory system and trauma can cause inflammation and elevated intraocular pressure (IOP) (43).

Table 1.3: Properties of accommodative intraocular lenses sold in the current lens market (2). Adapted from Liang et al., (39), under the Creative Commons Attribution (CC BY) license. Copyright 2018 by International Journal of Ophthalmology Press. HEMA: (Hydroxyethyl)methacrylate.

	Crystalens	*ICU Lens*	*Tetraflex*	*Synchrony*	*Lumina*
Material	Silicone	Hydrophilic acrylic material	HEMA	Silicone	Acrylic
IOL Design	Biconvex hinged plate haptic	4 flexible haptics	Closed loop haptics	2 optics with 4 spring haptics	Elastic loop with a spring function
Mechanism of Action	Single optic forward motion	Single optic forward motion	Single optic forward motion	Dual optic IOL	Alvarez principle
Location	Capsule bag	Capsule bag	Capsule bag	Capsule bag	Ciliary sulcus
Measured Accommodation (D)	> 0.4	1.36 – 2.25	2	1	2 – 3
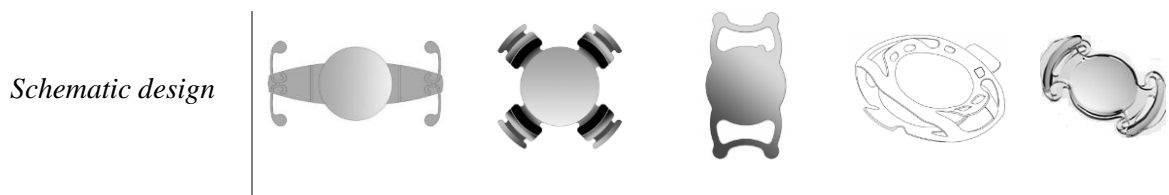
1.2.3 Two-dimensional nanomaterial for experimental accommodative intraocular lens technology

The focus for the next generation of AIOLs is to provide true accommodative function to patients and to reduce post-operative complications caused by the mechanism of action used by the AIOLs. Recent advances in applying two dimensional nanomaterials as TCE in optoelectronics devices could provide potential avenues for AIOL development. For example, graphene electrodes have been used in smart contact lenses due to their ability to retain transparency and conductivity; requirements of a lens-based system to ensure visual acuity and be functional as part of electronic circuits for sensor function (44–47). Smart biosensor systems combine an electronic-based sensor with a soft contact lens to detect the concentration of a biomarker and transmit these dynamic changes as fluctuations in current (46–48). Graphene smart contact lenses have been used in dehydration protection, electromagnetic interference shielding and biosensing (46–48). Graphene TCEs have transparency, transmittance of up to 90%, high chemical stability and good flexibility (49). Choi et al., (50) produced a soft optoelectronic device consisting of ultrathin MoS_2-graphene films applied to a hemispherically curved image sensor (CurvIS) which would mimic the retina's function. However, graphene has a high sheet resistance, ranging between $>30 – 900$ Ω. sq^{-1} depending on the synthesis method of the graphene film (44). Spray-coated MXene films produced lower sheet resistance than graphene films ($500 – 8000$ Ω sq^{-1}) at 40-90% transmittances (51). MXene has also been exploited as an TCE in wearable devices in photodetection, human motion monitoring and voice detection for an artificial ear application (52–54). MXene has also been applied as a TCE within a proof of concept adaptive focus design using liquid crystal components (**Fig. 1.3**). A test cell was constructed, sandwiching a layer of liquid crystal (5CB) between spin-coated $Ti_3C_2T_x$ glass

slides. $Ti_3C_2T_x$ was used as a TCE to allow the conductance of an electric field across the liquid crystal, changing its molecular orientation bringing the image into focus. An external power source would be required to induce the electric field across the liquid crystal/ $Ti_3C_2T_x$ sandwiched layers.
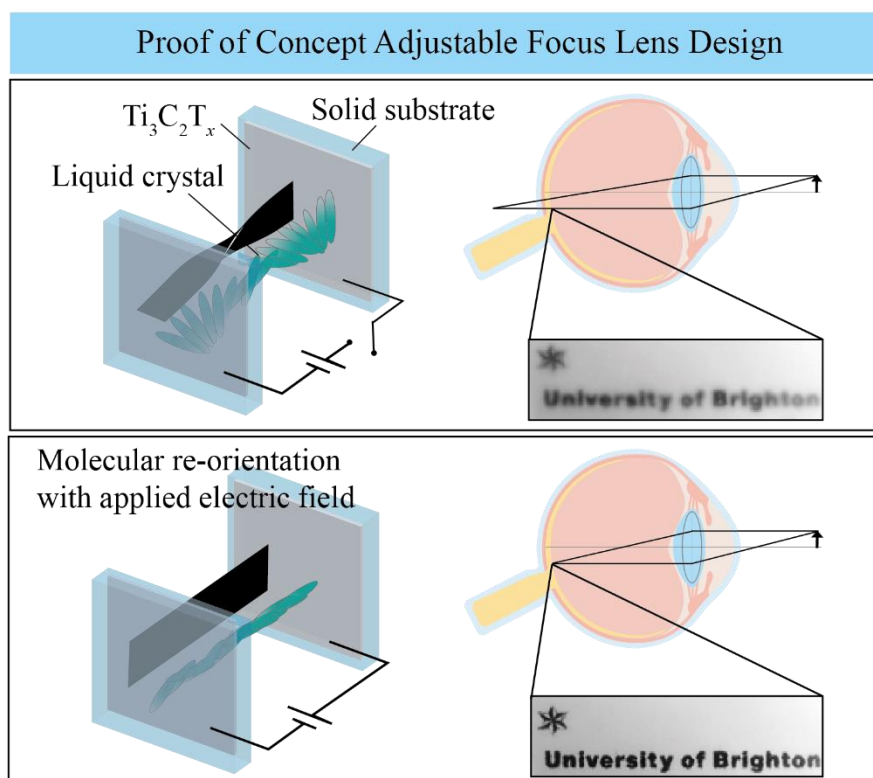
Figure 1.3: Schematic of adjustable focus lens proof of concept design. Adapted from Ward et al., (14), under the Creative Commons Attribution (CC BY) license. Copyright 2020 by authors. WILEY-VCH Verlag GmbH & Co. KGaA, Weinheim.

1.3   MXenes and their use for biomedical applications

MXenes, a family of 2D transition metal carbides and/or nitrides, offer unique and favourable properties for use in optoelectronic medical devices including high electrical conductance, transparency, elasticity, hydrophilicity and versatile solution processing (17,51,55,56). MXenes have a general formula of $M_{n+1}X_nT_x$ where M stands for a transition metal, X for carbon and/or nitrogen and T_x for the surface functional terminations such as O, OH,

F (19). MXenes are synthesised by etching its precursor MAX phase, with a general formula of $M_{n+1}AX_n$ where A represents an element from the 13th or 14th group of the periodic table. The metallic bonding between the M layers and A layers are stronger than the van der Waals interactions found in graphene. To remove the A layers to produce MXene, the layers are etched by hydrofluoric acid (HF) (57). Unetched MAX phase is removed by cycles of washing and centrifuging until a neutral pH is achieved (19). There are more than 30 experimentally synthesised members of the MXene family derived from various transition metals and carbon or nitride groups **(Fig. 1.4)** (55).

n = 1		n = 2		n = 3		n = 4
Ti_2N	Mo_2N	$Ti_3(C,N)_2$	Hf_3C_2	Ti_4N_3	V_4C_3	$(Mo_4V)C_4$
Ti_2C	Mo_2C	Ti_3C_2	Zr_3C_2	Nb_4C_3	Ta_4C_3	
V_2C	Nb_2C	$(Cr_2Ti)C_2$	$(Cr_2V)C_2$	$(Nb,V)_4C_3$	$(Ti,Nb)_4C_3$	
$(Ti,V)_2C$	$(Ti, Nb)_2C$	$(Mo_2Sc)C_2$	$(Mo_2Ti)C_2$	$(Nb,Zr)_4C_3$	$(Mo_2Ti_2)C_3$	
$W_{1.3}C$	$Mo_{1.3}C$		$(Ti,V)_3(C_2$			
$Nb_{1.3}C$	$Mo_{1.3}Y_{0.6}C$					

Figure 1.4: Synthesised MXene types reported to date. Adapted from Gogotsi et al., (58)**.**

The current biomedical applications of MXenes under investigation include photothermal therapy (PTT), antibacterial and within wound-healing strategies (15). PTT is a non-invasive electromagnetic radiation anti-cancer treatment causing heat-induced tumour death by exposure with a near-infrared (NIR) light. Photothermal agents are applied to localise the laser irradiation. MXenes have been applied as photothermal agents due to their efficient light-to-heat conversion. Lin et al., (59) showed that MXenes had an effective photothermal ablation at a depth of ~4 mm in 4T1-tumour bearing mice.

The antibacterial properties of MXenes have been explored by Rasool et al., (60) against *Escherichia coli* (*E.coli*) and *Bacillus subtilis* (*B.subtilis*). Delaminated (DL) $Ti_3C_2T_x$ presented

the greatest impact against bacterial cell viability with a loss of 97.70 ± 2.87% and 97.04 ± 2.91% for *E. coli* and *B.subtilis* respectively. Magnesium dioxide (MnO_2) and molybdenum disulfide (MoS_2) have been exploited for their reported antibacterial activity and increased membrane penetration leading to bacterial death when aligned vertically. This vertical orientation was proposed to produce 'nanoknives' that pierce the bacterial membrane leading to the lysis of cytosolic materials. The authors found that the vertical alignment of MnO_2 sheets improved antibacterial performance in comparison to the randomly aligned [61].

Advanced wound healing strategies have been developed to provide additional support to physiological healing response processes and patient pain management. Zhou et al., [62] developed a multifunctional antibacterial haemostatic scaffold, incorporating MXene due to its promising antibacterial properties, *in vivo* biodegradability and the potential to stimulate cell regeneration as a conductive element for electrical transmission. The scaffold increased wound closure rates, promoted healthy tissue healing and promoted the early formation of scar tissue and deposition of collagen and granulation tissue, exceeding the wound-healing response of any other group.

MXenes can be processed into transparent and conductive films for application as TCEs which could be utilised within optoelectronic medical devices [14,20]. Zhang et al., [20] produced spin-casted $Ti_3C_2T_x$ films with transmittance of 93 % at ~ 4 nm, with DC conductivity of ~ 5736 S cm^{-1}. The high transmittance of thinner $Ti_3C_2T_x$ films coupled with their low sheet resistance of 201 Ω sq^{-1} was found to be lower than graphene's sheet resistance of 10 492 Ω sq^{-1}. Ward et al., [14] showed $Ti_3C_2T_x$ coatings could be optimised to achieve high conductivity whilst maintaining optic transparency. The study demonstrated that the presence of $Ti_3C_2T_x$ coatings alone on IOLs did not significantly change the optic power or lens system's contrast and resolution relative to the uncoated IOLs. This work continued by assessing the potential of $Ti_3C_2T_x$ as a TCE for an adjustable focus lens system, constructing a test cell utilising $Ti_3C_2T_x$ as a conductive material to provide an electric current to change the alignment of liquid crystals, achieving a dynamic change in focus. This study showed that as voltage was applied to the test

cell, an image was brought into more into focus, which increased in focus as the voltage was increased. This proof-of-concept adaptive focus design showed how MXene can be applied in ophthalmic devices and should be explored further as a biomedical application for the nanomaterial.

1.3.1 Biocompatibility assessment of MXenes

The first synthesised and most studied of all of the MXene types, $Ti_3C_2T_x$ has also been evaluated in biocompatibility studies to assess fundamental issues of toxicity, inflammatory pathway activation and oxidative stress prior to its use in medical devices. Dai et al., (63) injected $Ti_3C_2T_x$ composite nanosheets at different concentrations into healthy mice and found no obvious toxicology damage to the main organs or elevated white blood cell response in comparison to the control mice. The cell line HaCaT keratinocytes reached 80% cell viability when incubated with $Ti_3C_2T_x$ and using an *in vivo* zebrafish model, injections of up to 100 μm mL^{-1} $Ti_3C_2T_x$ was found to remain non-toxic with no significant effect to embryos. Zhou et al., (62) found in porcine models there was high cell viability and minimal LDH release, with no toxicity to major organs and complete removal from the system by day 7 on exposure to MXenes in a wound dressing prototype. Moreover, Ozulumba et al., (64) investigated $Ti_3C_2T_x$ MXene as a component for extracorporeal systems for blood-toxin removal due to its high surface area and hydrophilic nature. Fresh frozen human plasma was spiked with 1000 pg mL^{-1} IL-8, -6 and TNF-α then incubated with ML and DL $Ti_3C_2T_x$ for 4 hours. ML $Ti_3C_2T_x$ showed significant removal of IL-8 at 5 mg whereas DL $Ti_3C_2T_x$ demonstrated significant removal of IL-8 at 5 mg, IL-6 at 10 mg and TNF-α at 50 mg. The study continued by treating THP-1 monocytes with lipopolysaccharide (LPS), a component of the bacterial cell membrane that activates the immune system and found that both DL and ML MXene significantly repressed cytokine expression through a mechanism not solely linked to adsorption of LPS or inflammatory cytokines directly. Ward et al., (14) showed no significant difference in human lens epithelial (HLE)-B3 cell viability when incubated with $Ti_3C_2T_x$-coated IOLs in comparison to the cell only control and uncoated IOLs controls. The study also showed that $Ti_3C_2T_x$ coatings did not incite ROS production nor increase the release

16

of inflammatory cytokines IL-6, -8 and TNF by THP-1 monocytes suggesting biocompatibility using these *in vitro* models. However, the impact of MXene on the specific developmental pathways of PCO by residual LEC remains unknown.

1.4   Posterior capsule opacification

PCO is the most common complication arising from cataract surgery, causing a secondary loss in visual acuity and increased light scatter. Patients have a 5 – 50% incidence rate of developing the condition, typically two to five years post-surgery (3,9,65). During cataract surgery the opaque fibrotic lens is aspirated from the anterior and posterior capsule, which together makes up the capsule bag. PCO develops when the residual LECs within the capsule bag undergo a wound-healing process in response to the stress caused by the corrective surgery. Histology studies have elucidated some of the cellular processes that occur during PCO development (**Fig. 1.5**). PCO is diagnosed by slit lamp evaluation with built-in image analysis (33). PCO is managed with Nd: YAG laser ablation to remove any fibrotic LEC from the posterior capsule and IOL optic (**Fig. 1.7 E**). In a long-term, retrospective study conducted by Ursell et al., (66) 20,763 eyes implanted with monofocal, single focus, acrylic lenses found PCO incidence rate of between 4.7 – 18.6 % at 3 years and 7.1 – 22.6 % at 5 years. During the procedure, the laser pulse is applied at a few millijoules for 2-3 nanoseconds (67). The age of the patient and severity of PCO determines the power of the laser used to create an opening in the fibrotic capsule (68). The procedure can lead to complications such as retinal detachment, cystoid macular oedema, IOL displacement, mild anterior uveitis and transient intraocular pressure (66,69). Currently, there is no alternative therapeutics interventions for patients (70).
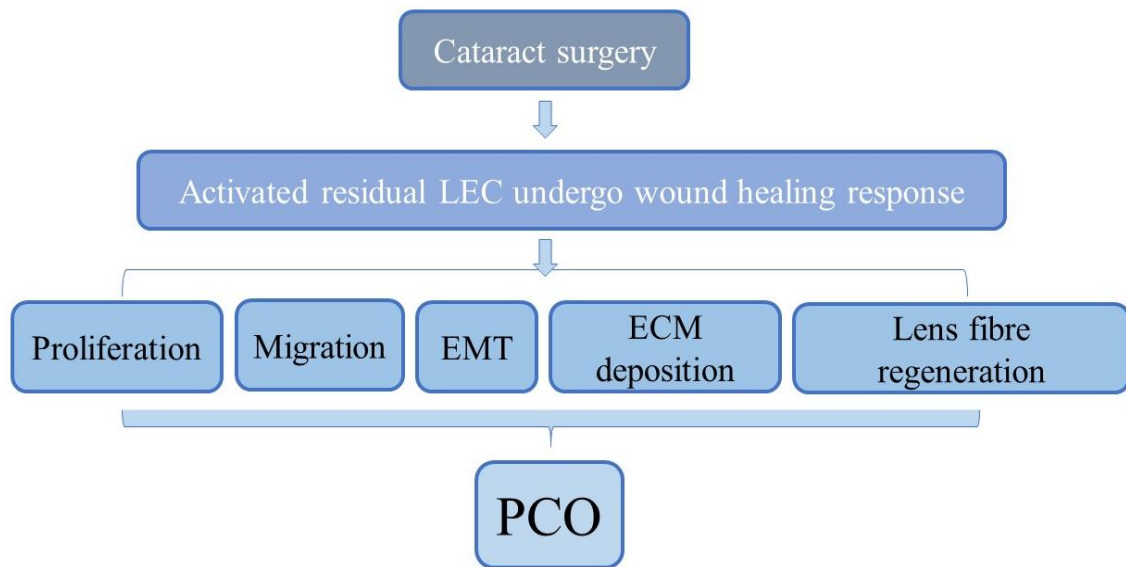
Figure 1.5: Overview of the histological developmental pathways of posterior capsule opacification. Adapted from Awasthi et al., (71). LEC: lens epithelial cells; EMT: epithelial-mesenchymal transition; ECM: extracellular matrix; PCO: posterior capsule opacification.

1.4.1 Factors contributing to posterior capsule opacification

The key factors affecting onset and severity of PCO are surgical technique, patients' own risk factors and IOL material and design. It can be difficult to separate cause and effect for each risk factor in patients due to their similarities in the propensity towards PCO development. This presents a significant challenge in developing effective preventative IOL designs and optimising surgical procedures for patients. Nevertheless, the use of foldable materials, square edge optic design and the use of the cortical clean-up technique to remove residual LEC in the capsule bag has significantly improved incidence of PCO in patients (72,73).

1.4.1.1 Surgical interventions to prevent posterior capsule opacification

Whilst cataract surgery is one of the most successful outpatient procedures, the surgical technique and experience of the surgeon greatly influences the outcome of the surgery and the development of long-term complications such as PCO. The surgical procedure begins with performing a capsulorhexis in the anterior capsule to access the diseased lens. A circular

capsulorhexis of 4.5 – 5 mm has been shown to reduce PCO rates (9,74,75). Performing a continuous curvilinear capsulorhexis (CCC) in aphakic eyes fuses the posterior capsule to the anterior capsule, forming a Soemmerring's ring. This provides a closed environment over the visual axis of the posterior capsule, delaying the migration of LECs (9). During phacoemulsification of the cataractous lens, the surgeon can perform cortical cleaving hydrodissection. This cleaves the capsule bag from the outer cortex of the lens with hydraulic force which subsequently removes the LEC (9,75). This technique also reduces time to aspirate the lens nucleus and remaining cortex, producing a more efficient removal of the lens.

Once the lens is removed, cortical clean-up and capsule polishing can enhance removal of residual LECs and lens fibres (9,75). Paik et al., (76) showed reduced PCO rate when capsule polishing was used however, overall Nd:YAG laser ablation rates were not reduced. Menapace et al., (77) found polishing of the anterior capsule reduced fibrotic PCO but did not affect regenerative PCO. Implantation of the IOL and endocapsular devices are an important step in preventing PCO development. In-the-bag fixation of the optic and haptics is required to create an IOL optic-barrier effect to migrating LECs (9). Endocapsular devices encompass capsule rings, open capsule devices and protective membranes (78,79). Capsule rings and devices prevent PCO by radially stretching the capsule bag, separating the anterior and posterior capsule completely which allows for unobstructed circulation of AH (**Figure 1.6**) (78). Many ring designs also have a squared edge which acts a barrier to LEC migration. Protective membranes, manufactured by Sharklet Technologies, can be implanted to act as artificial capsule bags. A square-edge haptic ridge provides a height of 1.2 mm to secure the IOLs in place. The outer surface is covered in a surface topography specifically engineered to prevent cell bio-adhesion. Visual acuity is maintained by a 5 mm diameter hole within the patterned posterior surface. Implanted membranes in New Zealand rabbits showed reduced PCO development however, the rapid opening of the membrane following injection caused difficulty in positioning when within the capsule (80). The application of such capsule devices is decided on a patient-specific basis (9,78).
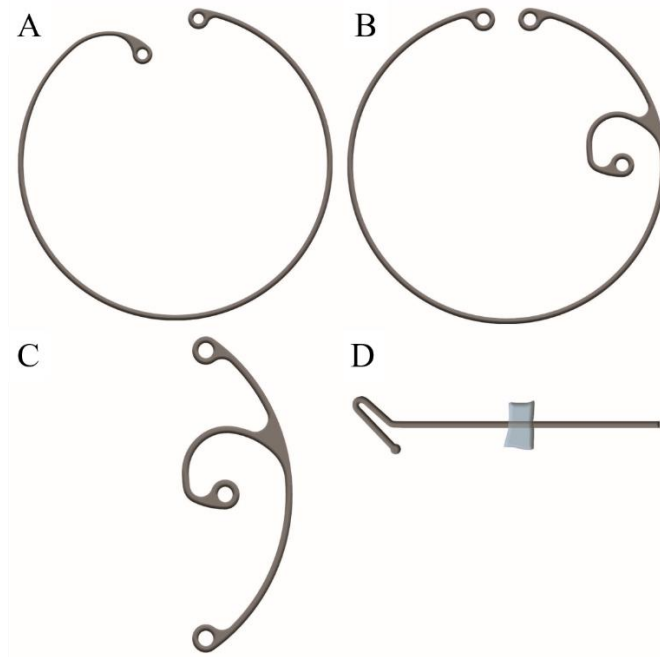
Figure 1.6: Capsule ring design. Capsule tension ring (**Fig. 1.6 A**). Modified capsule tension ring (**Fig. 1.6 B**). Capsule tension segment (**Fig. 1.6 C**). Capsule retention hook (**Fig. 1.6 D**). Copyright Morcher GmbH, Stuttgart, Germany.

1.4.1.2 Patient risk factors in developing posterior capsule opacification

Susceptibility in developing PCO is heavily influenced by age of the patient and the presence of any pre-existing conditions although gender does not seem to influence PCO formation (9). Younger patients are more likely to develop PCO due to the greater proliferative activity of the residual LEC relative to older patients (81–84). Wei et al., (85) found that aged FHL124 cells had reduced cell proliferation, dysregulation in the cell stress response and reduced propensity to undergo EMT, contributing to the lower rates in PCO development. Diabetic patients have shown increased risk of developing cataracts, aligning with a higher cataract surgery rate relative to other populations (86). One mechanism behind this correlation is due to increased activation of the polyol pathway which uses aldose reductase to catalyse glucose to sorbitol. The increased sorbitol then increases osmotic and oxidative stress leading to LEC apoptosis and damage to lens fibres (86). Aldose reductase inhibition has been shown to reduce EMT pathways in LEC (87). Higher osmotic pressure in diabetic patients has also been correlated

with a quicker onset of PCO although the severity of PCO development long-term has not been shown to be significantly worsened relative to non-diabatic cataract patients (9,88).

Patients presenting with pre-existing ocular diseases prior to their cataract surgery have an increased risk of PCO development (89). Dry eye disease (DED) is one of the most common ocular conditions, characterised by decreased tear production or increased tear evaporation (90). This can cause inflammation to the local corneal cells. Inflammation is a key initiator for the onset of PCO. Therefore, any disorders such as DED and uveitis that cause elevated levels of inflammatory components within the eye, significantly increase the likelihood of PCO formation post-cataract surgery (PCS) (9,89). For patients with such conditions, the selection of base material and optic design can hinder some of the effects of these complications.

1.4.1.3 IOL design and construction material impact on posterior capsule opacification

IOLs can be designed as a single-piece or three-piece. A single-piece IOL can provide better in-the-bag stability however, incidence of PCO have been found to be higher in comparison to three-piece IOLs (91,92). IOLs with a squared optic edge design have shown a reduction in PCO development, regardless of material (**Fig. 1.7 A)** (8,93–98). This is due to a barrier effect that is created by the sharp edge against the posterior capsule, providing maximum contact with the capsule bag. This prevents the migration of LECs along the visual axis of the posterior capsule (**Fig. 1.8 F**). In a rounded optic edge design, this barrier is not in place and cells can migrate along the capsule wall (**Fig. 1.7 B**). Nevertheless, the square-edge design relies on contraction of the posterior capsule to meet the optic edge of the IOL which may not occur in some patients (34).
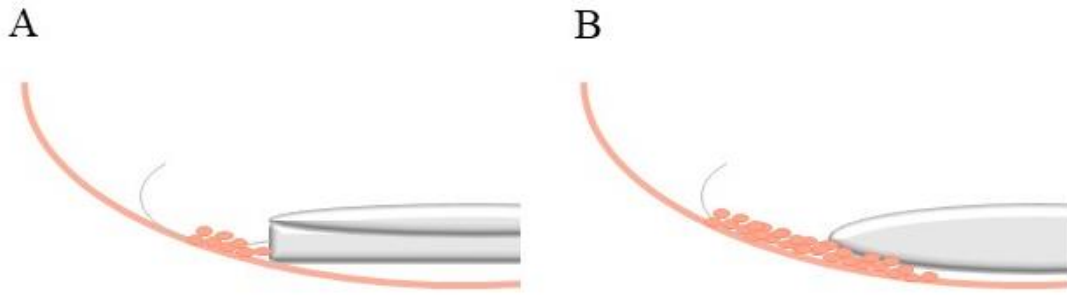
Figure 1.7: Schematic diagram of IOL design impeding cell migration. A square-edge design acts a barrier to migrating lens cells, preventing obstruction of the central posterior region (**Fig. 1.7 A**). Without this barrier effect, cells are free to migrate along the posterior surface, forming a fibrotic mass across the visual axis (**Fig. 1.7 B**) (32,99).

IOL construction material influences the cell interface with the IOL and therefore, the development of long-term complications such as PCO. The importance of selecting the appropriate base material for each patient is exemplified by Apple et al., (2020) (73). A comparative autopsy tissue analysis in 5416 globes obtained between the years of 1988 and 2000 showed a reduced PCO and Nd: YAG laser capsulotomy incidence rate in globes implanted with IOLs manufactured from silicone and acrylic compared to the relatively older PMMA IOLs (**Fig. 1.8 D**). Moreover, the greater flexibility in acrylic and silicone based IOLs allows for smaller opening incisions which is correlated with a better outcome post-surgery (34,100,101). Nevertheless, there is controversy on the degree in which the individual IOL base materials impact the development of post-operative complications. Silicone derived IOLs show a lower PCO rate relative to PMMA based IOLs as the silicone deters cell adhesion (101). However, silicone can also incite a fibrotic response in LEC, contributing to PCO and anterior capsule opacification (ACO) (**Fig. 1.8 A**). There is a consensus that hydrophobic acrylic IOLs show lower rates of PCO development in comparison to hydrophilic IOLs (**Fig. 1.8 B, C**). This is thought to be due to the wettability of the hydrophilic material providing a good bio-adhesive surface for cells to adhere and grow over (101). There have been several studies which suggest there is no significant difference between the acrylic lens types. Bai et al., (2015) (95) found no statistically

22

significant difference in PCO grade after 24 months in a paired-eye design of 60 patients implanted with a 360-degree square edge hydrophilic acrylic IOL (Rayner C-flex 570C) or a square edge hydrophobic acrylic IOL (Sensar AR40E). Additional clinical studies using larger cohort studies should be conducted to provide more evidence on the impact of IOL base material on long term complications such as PCO (5,66).
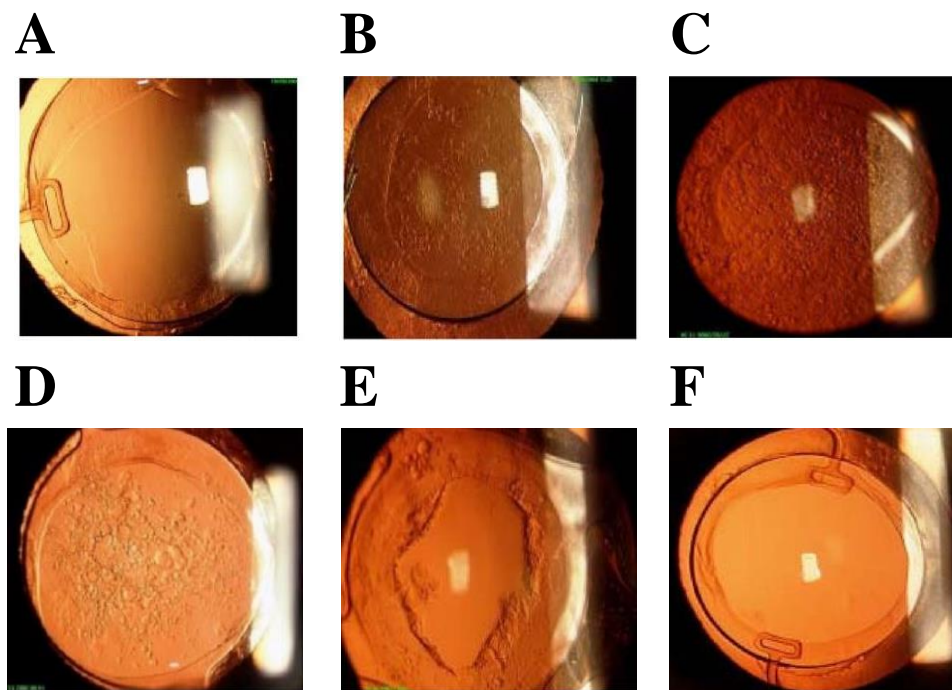
Figure 1.8: Posterior capsule opacification development across intraocular lens types. Silicone 8 months post-surgery, absent of PCO **(Fig. 1.8 A)**. Hydrophobic acrylic IOL with significant PCO development post-5 years **(Fig. 1.8 B)**. Hydrophilic acrylic IOL with significant PCO, 2 years post-surgery **(Fig. 1.8 C)**. PMMA IOL at 18 months post-surgery with significant PCO **(Fig. 1.8 D)**. Nd:YAG treated lens **(Fig. 1.8 E)**. Tecnis foldable IOL with a square edge optic, showing a clear visual axis 1-year post-surgery **(Fig. 1.8 F)**. Adapted from Ram et al., (4). Permission for reprint from authors, with acknowledgement. Copyright 2019 Delhi Ophthalmological Society.

1.4.2 Modelling of posterior capsule opacification

Experimental models of PCO provide insight into the underlying molecular mechanisms of the pathology and provide the opportunity to test new IOL technology and preventative measures against PCO. *In vitro* PCO models include primary and three immortalized LEC lines, HLE-B3, SRA01/04 and FHL124. HLE-B3 cells are the most commonly used due to their high availability and predominance in PCO literature (3,25,102,103). It is an immortalised cell line derived from female infant human LEC less than 1 year of age. The cells are transformed by a hybrid of adenovirus 12 and simian virus 40 "AD12-SV40" and are stable for 30 passages (104). FHL124 cells are a non-transformed cell line cultured from capsule-epithelial explants on microporous membrane. Cells continue to express an epithelial morphology over 20 passages and undergo senescence-induced pathways at passage 42 (85).

In vitro models provide a dynamic and cost-effective route, mostly used to identify key markers involved in the developmental pathways of PCO. Joseph et al., (25) used mouse LEC-derived induced pluripotent stem cells (iPSCs) to determine key markers in the EMT pathway. Extracted LECs from one-month mice lenses were left to differentiate into a mesenchymal cell type then reprogrammed into iPSCs by delivering transcription factors using a virus vector. iPSCs were then transformed into LECs. Primary LECs showed higher expression of E-cadherin, Connexin-43, vimentin and lower expression of α-SMA relative to the mesenchymal cell line. Awasthi et al., (105) explored the role of growth factors in LEC proliferation by treating LECs with TGF-β which suppressed cell proliferation. The addition of fibroblast growth factor (FGF) reversed this, promoting LEC proliferation.

In vivo and *ex vivo* models can be used to test new IOL technology and investigate matrix contraction and capsule bag wrinkling. Eldred et al., (106) used human donor capsule bags to monitor cell progression over the posterior capsule and wrinkling. Treatment with TGF-β2 significantly increased capsule wrinkling whereas matrix metalloproteinases (MMP)-2-neutralizing antibody reduced cell coverage from 92.92 % ± 7.08 % to 21.76 % ± 13.66 %. Access

to human and animal tissue is restricted for many laboratories therefore, there is a requirement for artificial capsule bag model that can be used to mimic a human model. Huidong et al., (107) created a silicone-based capsule bag model with similar dimensions and mechanical properties of human donor capsule bags to develop new AIOL designs, which could be exploited for biological modelling. Thus far, PCO experimental models have provided an insight into the EMT of LEC, higher deposition of ECM and capsule wrinkling which develops during PCO development (12). Current understanding of the developmental pathways leading to PCO indicate an initial wound-healing response by LECs triggered by the cataract surgery.

1.4.3 Pathophysiology of posterior capsule opacification

The wound healing response of LEC PCS is believed to be the first key developmental stage of PCO. Ocular inflammation is initiated PCS as a result of the opening incision and subsequent lens cell removal (108). The disruption of the blood aqueous barrier allows plasma protein and immune cell infiltration. Within the first 24 hours of the inflammatory response, the LEC transcriptome upregulates genes involved in the augmentation of the innate immune response and pro-inflammatory proteins **(Fig. 1.9 A)** (109). At 48 hours PCS, the residual LECs start to express elevated levels of inflammatory mediators' IL-6, IL-1β, and IL-8, initiating chronic inflammation pathways **(Fig. 1.9 B)** (110–114). After 48 hours, migrating neutrophils and macrophages attracted by secreted chemokines cleave the inactive precursor of latent TGF-β in the AH **(Fig. 1.9 C)** (115). TGF-β, amongst other growth factors, stimulates the proliferation, transdifferentiation and migration of LECs (116). The activated TGF-β binds to LECs via type I and type II receptor serine-threonine kinases on the cell surface (8). This begins a cascade of SMAD proteins signalling, the messengers activated via TGFβ signalling (117,118). These signalling pathways lead to *TGF-β* gene transcription, activation of Rho GTPases, and stimulation of the phosphatidylinositol-3-kinase (PI3)/Akt and mitogen-activated protein kinase (MAPK) pathways. These events are associated with myofibroblast formation, EMT-related matrix contraction, cell differentiation, and inhibition of normal LEC pathways (8). Patients

present with opacification of the posterior capsule caused by the migrated fibrotic cells and partial vision loss **(Fig. 1.9 D)**.

Current literature suggests IL-1β, IL-6, IL-8 and TGF-β are key mediators involved in PCO development. IL-1β can be expressed by LECs, corneal epithelial cells and to some extent, corneal stromal cells (111,119,120). IL-1β is a pro-inflammatory cytokine that stimulates the release of additional cytokines to promote chronic inflammation (111,112,121). Ferrick et al., (111) injected IL-1β in *in vivo* rat eyes and found ocular inflammation was initiated within 10 - 24 hours post-injection. IL-8-activated neutrophils were seen 20 hours post-injection, with IL-8-induced ocular inflammation subsiding after 48 hours. The authors concluded the impact of IL-1β produces a greater inflammatory response due to the long-lasting effects of the pathway cascade it initiates relative to IL-8, which acts a specific chemoattractant for neutrophils. IL-6 is hypothesised to upregulate ECM production involved in the contraction of the capsule bag and EMT pathway. Nishi et al., (114) found IL-6 release was significantly higher in the AH of LECs obtained during cataract surgery in comparison to medium controls. This is further supported by Ma et al., (110) who treated HLE-B3 cells with IL-6 and showed within 24 hours of stimulation, IL-6 promoted ECM synthesis leading to capsule bag wrinkling.
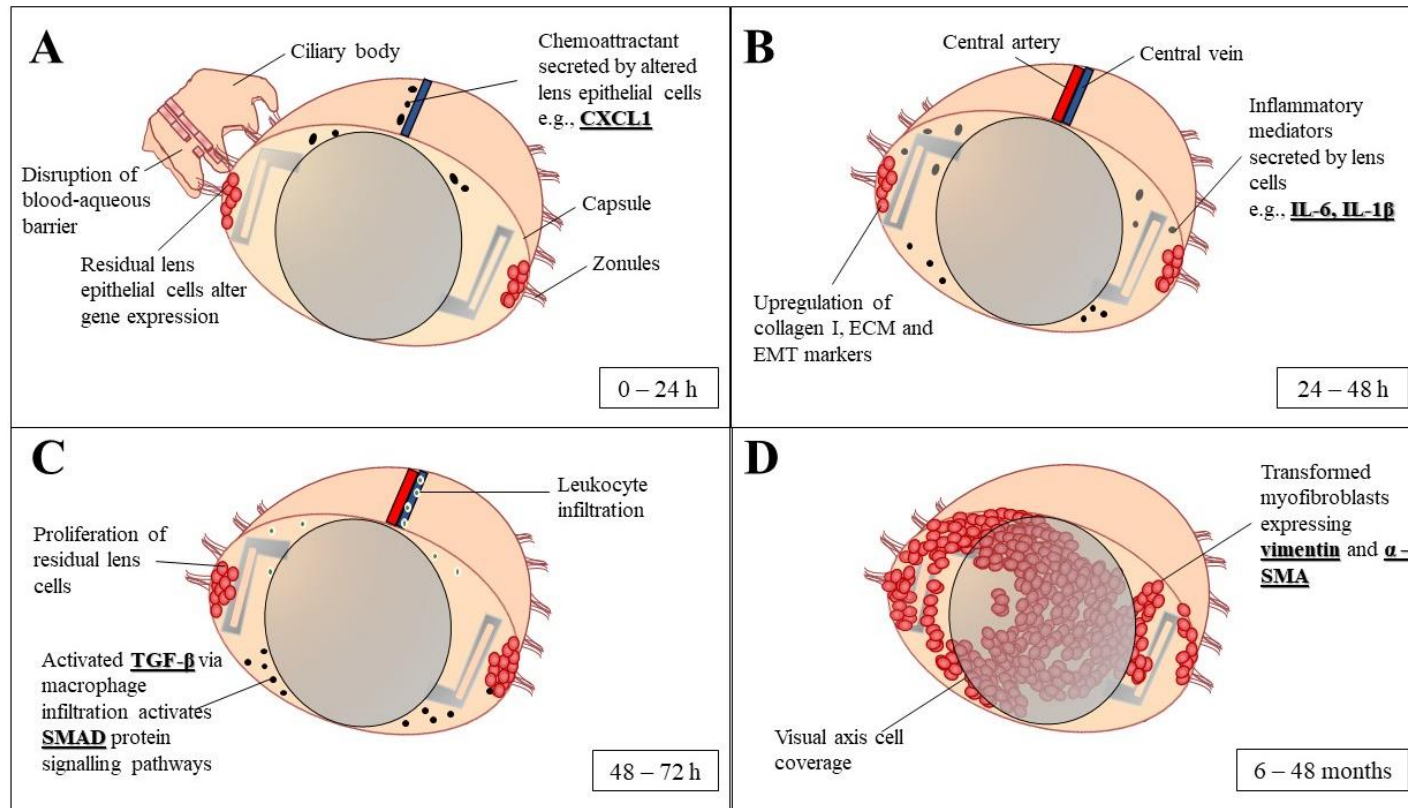
Figure 1.9: Schematic overview of the capsule bag post cataract surgery and key pathways involved in the development of posterior capsule opacification. Residual lens epithelial cells undergo the wound healing response (**Fig. 1.9 A**). Upregulation of inflammatory mediators (**Fig. 1.9 B**). Leukocyte infiltration and inflammatory mediators activates dormant TGF-β residing in the aqueous humour (**Fig. 1.9 C**). The transdifferentiated lens cells migrate over the posterior capsule (**Fig. 1.9 D**). IL: interleukin; TGF-β: transforming growth factor beta. Adapted from Cooksley et al., (5), under the Creative Commons Attribution (CC BY) license. Copyright 2021 by authors. Licensee MDPI, Basel, Switzerland.

TGF-β is a well-established key mediator within PCO development (3,6,12,109,116,117,122). The isoforms TGF-β1 and -β2 are found in AH, ciliary processes and within the limbal epithelium, where they are hypothesised to be involved in the transdifferentiation of conjunctival to corneal epithelium (6,123). Moreover, Nishi et al., (124) found that LECs express TGF-β2 under physiological conditions. The TGF-β receptor kinase is involved in both normal and pathological ocular conditions (115,125). TGF-β is important in maintaining corneal integrity, in tissue repair, and in the regulation of cell proliferation and death (115,125). Hyper-activation of the growth factor can lead to an exaggerated wound-healing response and increased ECM deposition by cells, which may cause fibrotic corneal disease, fibrosis of lens and retinal epithelium, and loss of vision (6,115,118,123).

Short-term exposure of TGF-β within the capsule bag leads to the induction of chronic ECM production and capsule wrinkling. Possible mechanisms behind this are the upregulation of *TGF-β* gene expression following exposure to TGF-β or the ability of TGF-β to bind to collagen IV, a predominant component of the capsule bag (3). In PCO development, TGF-β is also involved in the activation of the EMT pathway in LEC promoting the differentiation of the epithelial cells to migratory spindle-like myofibroblasts (117,126–129). The activation of TGF-β inhibits the proliferation of LECs induced by FGF in favour of initiating transdifferentiation by upregulating the expression of α-SMA genes (6,118,130). Furthermore, TGF-β has been shown to increase the secretion of ECM components by LECs. In this process, ECM turnover is disturbed; there is a greater production of fibronectin, collagen I and IV, and inhibitors of MMPs partnered with reduced ECM degradation. The increased ECM leads to capsule wrinkling and thickening of the posterior capsule (6,7,130).

More recently, cellular senescence has been suggested to be involved in PCO development. Senescence is the phenomenon when a cell will exit the cell cycle and no longer undergo division but remain metabolically active (131). Senescent cells release cytokines and other pro-inflammatory mediators to encourage their removal by immune cells (132). This is a necessary step to avoid the build-up of senescent cells in tissue (132). If this removal does not occur, it can

28

lead to inflammatory diseases such as cataracts, corneal disorders and potentially, PCO (132). Resveratrol, a polyphenol which has been shown to reverse senescence in liver epithelial cells (133), was shown to revert TGF-β2-induced EMT and impede LEC migration (70). Nevertheless, the role of senescence in the induction of hyperinflammation and EMT pathways contributing to PCO development and how $Ti_3C_2T_x$ may affect this phenomenon has yet to be explored.

The recent use of $Ti_3C_2T_x$ as a TCE within a prototype AIOL (14), highlights a requirement for an investigation of the potential effects of $Ti_3C_2T_x$ on the developmental pathways of PCO. The benefit of providing accommodative function could increase the risk of developing PCO, resulting in further postoperative treatment for patients. Whilst it is known that $Ti_3C_2T_x$ does not induce pro-inflammatory cytokines and ROS production in THP-1 monocytes, it is still not known the impact of $Ti_3C_2T_x$ on the wound-healing response of LEC PCS, the upregulation of pro-inflammatory cytokines IL-6 and IL-1β and the EMT pathway contributing to LEC migration across the posterior capsule and IOL optic. Therefore, this thesis will aim to understand the impact of $Ti_3C_2T_x$ on the initial wound-healing response and EMT pathway of residual LECs PCS, contributing to PCO development.

1.5 Research aims and objectives

AIOLs are a key next step in the development of IOL technology to provide cataract patients with visual acuity and adjustable focus. Whilst a number of approaches for AIOL have been developed, none provide true accommodation for patients. MXenes are a family of 2D nanomaterials that possess the suitable properties to act as TCEs within an accommodative mechanism to trigger a change in dioptric power. However, the impact of MXene on the most common complication of cataract surgery, PCO, has yet to be investigated. A newly developed AIOL should provide visual acuity, with controlled, dynamic change in focal point at no increased risk of poor wound healing and the development of long-term complications for the patient.

Whilst it has been shown that $Ti_3C_2T_x$ can perform as a TCE in a proof-of-concept adaptive focus design, the impact of $Ti_3C_2T_x$ within the capsule bag and the wound-healing response of LEC PCS is unknown. $Ti_3C_2T_x$ did not induce release of pro-inflammatory cytokines, ROS production or cause any cell toxicity in several cell lines. However, the impact of $Ti_3C_2T_x$ on the wound-healing response and hyperinflammation of LEC PCS, leading to the induction of EMT and myofibroblast formation is not yet known. Additionally, whilst there are established human and animal capsule bag models to investigate PCO, there has yet to be an artificial capsule bag model allowing early triage of materials and devices for use within the capsule bag environment prior to more costly and invasive models and an approach to reduced reliance on animal sources.

This thesis will investigate the hypothesis that $Ti_3C_2T_x$ can be optimised as a coating for AIOL implantation in a design capable of reducing hyperinflammation and EMT associated pathways associated with the development of PCO. Its aim is to investigate the impact of $Ti_3C_2T_x$ on LEC hyperinflammation, specifically focussed on pro-inflammatory cytokines IL-1β, IL-6 and the CXC chemokine subfamilies and the propensity of LEC to undergo senescence and EMT upon exposure to $Ti_3C_2T_x$ coatings. This project will also develop a proof-of-concept silicone-

based capsule bag model to assess the impact of $Ti_3C_2T_x$-coated IOLs on cell migration relative to commercially available IOL types.

1.5.1 Objectives

- Synthesise $Ti_3C_2T_x$, optimising the uniformity of different batches of the colloidal solutions for biological assessment

- Optimise the spray-coating deposition technique for uniform, conductive coatings upon tissue culture well plates

- Establish a positive control to mimic the inflammation and EMT responses in LECs, contributing to PCO development

- Evaluate the propensity of $Ti_3C_2T_x$ (MXene) coatings to induce or suppress the pro-inflammatory profile within LECs

- Investigate how $Ti_3C_2T_x$ (MXene) coatings alters the expression of EMT cytoskeletal and cell nuclei markers

- Establish key hallmark inflammation gene sets upregulated in IL-1β-treated cells and how $Ti_3C_2T_x$ (MXene) coatings affects their expression

- Investigate how $Ti_3C_2T_x$ (MXene) coatings changes lipid composition of LEC

- Evaluate the genomic and lipidomic profile of IL-1β and $Ti_3C_2T_x$ (MXene) treated LECs to elicit the mechanisms by which changes in cytokine expression occur following exposure to by $Ti_3C_2T_x$ (MXene) coatings

- Preliminarily assess the impact of $Ti_3C_2T_x$ (MXene) coatings on the induction of senescence associated pathways in exposed LECs and the potential role of senescence in PCO development

- Develop an *in vitro* silicone-based capsule bag model to mimic the developmental pathways of PCO and investigate $Ti_3C_2T_x$ (MXene)-coated IOL types

Chapter 2: Synthesis and characterisation of $Ti_3C_2T_x$ (MXene)

2.1 Introduction

2.1.1 Synthesis and characterisation methods for $Ti_3C_2T_x$ (MXene)

MXene is etched from its 3D precursor MAX phase with a general formula of $M_{n+1}AX_n$ where A represents elements from group 13 and 14 of the periodic table (134,135). MXene synthesis can be achieved by two strategies, top-down or bottom-up. Bottom-up strategies constructs single or few-layered MXenes by atom-by-atom fabrication using chemical vapor deposition (136). The top-down approach selectively breaks the A and M metallic bonds in the MAX phase to form single MXene flakes by acid, molten salt and electrochemical etching followed by delamination (**Fig. 2.1**) (57). In acid etching, HF or *in situ* HF is used (134,135). The higher wt.% HF, the greater the defects and lower stability of synthesised MXene flakes (134). The top-down approach has milder conditions as during this synthesis method there is a lower temperature applied and no requirement for a gas flow. The etchant used determines the surface functional groups on the synthesised MXene, allowing surface properties to be tuned (134,137). The minimally intensive layer delamination (MILD) method results in surface terminations including hydroxyl (-OH) and oxygen (-O) which increases the hydrophilicity of the synthesised MXene, a favourable property in this body of work (55).

In 2016, the MILD method was developed to achieve large single flakes with fewer defects (134,138). *In situ* HF is produced as an etching agent by the addition of lithium fluoride (LiF) and hydrochloric acid (HCl). The ratio of LiF to HCl can influence the quality of the synthesised MXene colloidal solution (134). Increasing the molar ratio of LiF to MAX phase from 5:1 to 7.5:1, intercalates Li^+ ions into the multilayer MXenes, allowing delamination by manual shaking (138). MXene is commonly used as a polydisperse solution which typically contains single, multi-layered, small, and large flakes (18,134,139). Washing is required to safely remove the residual acid and achieve a pH of ≥ 6. Processing or liquid phase exfoliation (LPE) impacts the final product's flake size for example, extended periods of shaking increase the delamination process of the flakes (137). Intercalation via the addition of chemicals and

sonication achieves single delaminated flakes (**Fig. 2.1**) (18,139). Sonication applies direct mechanical force to produce a uniform MXene solution with a good poly dispersant solution (18,134,140). However, the use of sonication breaks the larger flakes into smaller flakes (18). Larger flakes have greater conductivity (14). Thus, as sonication time and power increases, conductivity of the solution decreases. To prevent oxidation during sonication, a low temperature should be maintained.
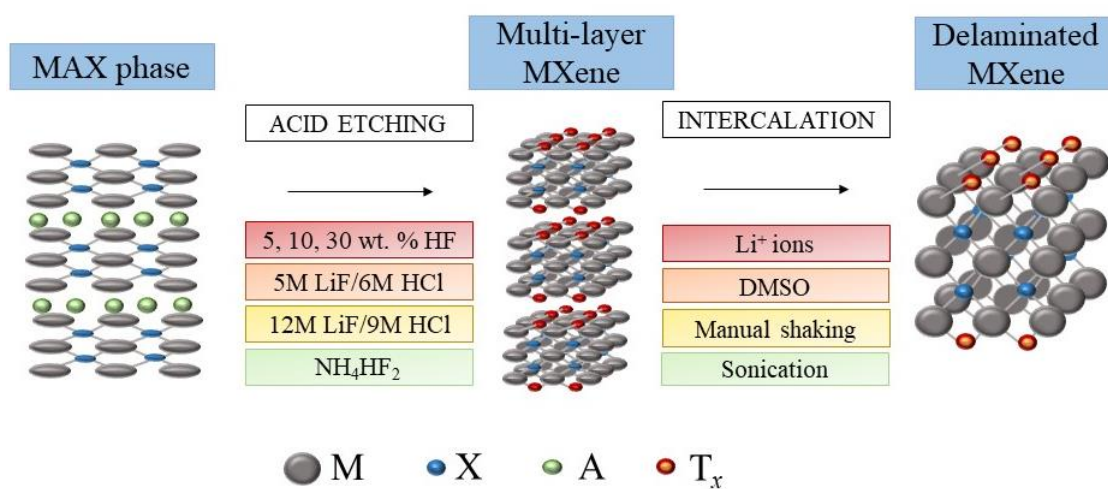
Figure 2.1: Top-down synthesis route of the precursor MAX phase etched into multi-layer MXene. Intercalation is required to achieve single or few-layered MXene flakes (55,134,136,141).

2.1.2 Solution processing of $Ti_3C_2T_x$ (MXene)

Appropriate storage of MXene is vital to maintain its stability and to prevent oxidation (137). Oxidation of MXene leads to a loss in its functionalisation, for example, exposure of $Ti_3C_2T_x$ to air reduces its conductivity (141). Stability can be achieved by keeping MXene stored under 5 °C or -20°C for long-term storage, with low light exposure. MXene solutions can also be stored under argon or in solvent such as DMSO (134,141). MXene in the form of films or coatings have greater stability relative to their colloidal solution (138,141).

Liquid-phase fabrication techniques include deposition by spin, spray or dip coating or printing (134). Inkjet, screen and extrusion printing are digital deposition techniques, allowing for automation for research and industry purposes (138). Direct deposition techniques are more suitable for obtaining thin, continuous, conductive films. Dip-coating is a simple process for MXene film deposition on a substrate (**Fig. 2.2 A**). The high negative zeta potential of the MXene nanosheets forms a stable, homogenous solution ideal for dip-coating (138). Spin-coating of MXene colloidal solution yields high-quality transparent films with well-aligned MXene flakes due to the centrifugal forces (**Fig. 2.2 C**) (55). Due to the reduced sheet roughness and resistance, there is a greater flow of electric charge across spin-coated substrates (138). Spray-coating provides a simple, fast and controlled deposition of $Ti_3C_2T_x$ thin films on large surface areas (**Fig. 2.2 B**) (55). This technique utilises delaminated MXene dispersions with a concentration range of 0.1 mg/mL to 10 mg/mL. Upon optimising the substrates' surface, MXene coatings are strongly attached even after deformation (138). Spray coating also provides greater control over film resolution and thickness than spin- and dip-coating (138).
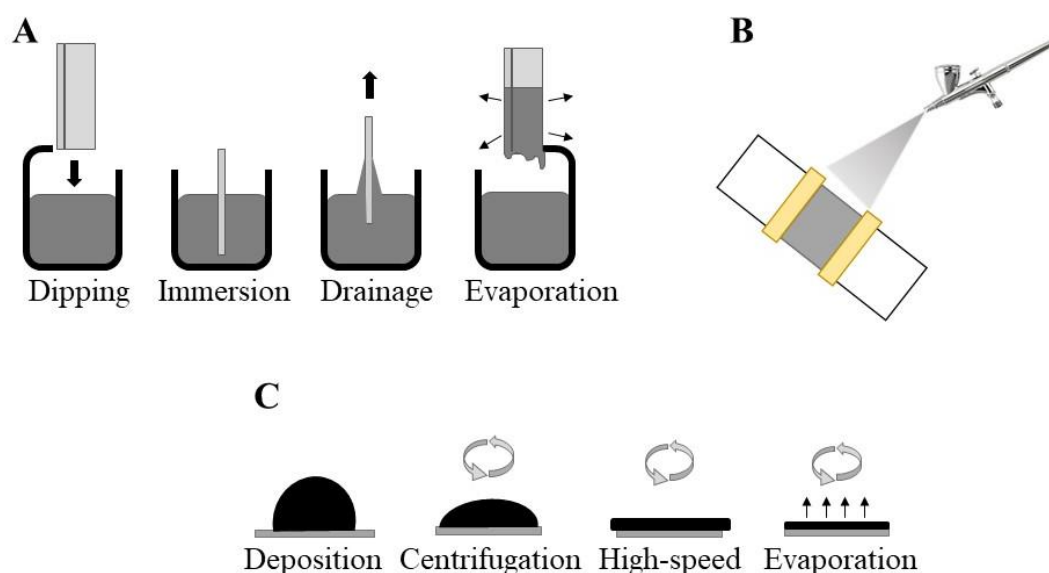
Figure 2.2: Liquid-phase processing of MXenes. Transparent, conductive films can be produced by dip-coating (**Fig. 2.2 A**), spray-coating (**Fig. 2.2 B**) and spin-coating (**Fig. 2.2 C**) (55,138).

2.1.3 Characterisation of $Ti_3C_2T_x$ (MXene)

MXene requires multiple methods to characterise its physical and chemical properties (**Table 2.1**) (134,135,137). Characterisation of synthesised MXene is key in optimising the synthesis and processing methods which will achieve the best quality of MXene (137). Yield and concentration of MXene is determined by vacuum filtration to produce a film, which after drying, is weighed to calculate initial solution concentration (137). Ultraviolet visible (UV-vis) spectroscopy analysis can be used to calculate concentration by producing serial dilutions of the synthesised MXene solution and creating a calibration curve using the Beer-Lambert law (134,135,137). UV-vis can also be used to identify the different MXene types due to their characteristic absorbance peak caused by their transition metal composition and structure (142). Average flake size is quantified using microscopy techniques such as SEM imaging and indirect methods such as dynamic light scattering (DLS). DLS quantification should always be supported by microscopy imaging (134). DLS analysis also shows the polydispersity index (pdi) of the MXene colloidal solution, to determine uniformity between the synthesised flakes. The morphology of MXene, either multi-layer, delaminated, single or few-layer flakes can be found through SEM and TEM. Raman spectroscopy, energy dispersive X-Ray (EDX) spectroscopy and X-ray photoelectron spectroscopy (XPS) shows the chemical composition of the synthesised MXenes and can identify if there has been efficient etching of the precursor MAX phase (134). The MXene type, surface terminations and composition greatly affect its properties and subsequently, its application. Therefore, full characterisation before application of MXenes is fundamental.

Table 2.1: Characterisation methods used to determine MXene structure, chemical composition and flake size. XRD: X-ray diffraction; SEM: scanning electron microscopy; TEM: transmission electron microscopy; EDX: energy dispersive X-ray; DLS: dynamic light scattering (134,142).

Technique	Method	Characterisation
XRD	Interaction of X-rays with crystalline structure	Structure and morphology
SEM	Electron microscopy of surface	
TEM	Electron microscopy over a cross-section	
Raman	Interaction of light with chemical bonds	
EDX	Interaction of X-rays on elemental composition	Elemental composition
XPS		
UV/vis	Absorption spectra	MXene type identification
DLS	Scattering of laser light source by particles in a suspension	Flake size and poly dispersant index

2.1.4 Chapter aims

The aim of this chapter was to synthesise and characterise $Ti_3C_2T_x$ MXene for use in an appropriate and consistent form to investigate the impact of $Ti_3C_2T_x$ on the developmental pathways linked to PCO. The MILD method synthesis route, using *in situ* HF acid as etchant, was used to produce $Ti_3C_2T_x$ colloidal solutions with uniform flake size and dispersity across the batches for biological evaluation.

2.2 Materials and methods

2.2.1 Synthesis of $Ti_3C_2T_x$ (MXene)

$Ti_3C_2T_x$ MXene was etched from the MAX phase Ti_3AlC_2 using the MILD method (**Fig. 2.3**). Ti_3AlC_2 (MAX phase) powder was obtained from Drexel University, Philadelphia, USA and was synthesised as described in literature (143). From Batch 1 to 4, the synthesis method was optimised to achieve the best yield and uniform flake size and pdi. The reaction time was left for 24 hours and 48 hours. Colloidal solutions were sonicated for 20, 30 and 60 minutes to determine the optimum time required to achieve uniform flake size within the solution. Finally, an additional centrifugation wash stage was added post-sonication. The method and processing of Batch 5 achieved stable, high yield and uniform solutions and is described here. In brief, 10 mL 9 M of HCl (Sigma Aldrich, UK), 0.8 g LiF (Sigma Aldrich, UK) and 0.5 g of Ti_3AlC_2 (MAX phase) powder was continuously stirred at $35 - 40$ ºC for 24 hours. The ratio of 9 M HCl: 7.5 M LiF was optimised to achieve MXene with the best quality (132). The synthesised colloidal sediment was washed by resuspending in 50 mL deionised water (dH_2O) and centrifuging for 5 minutes at 3500 rpm until a pH of $5 - 6$ was achieved (ALC PK 120R Centrifuge, DJB Labcare Ltd., UK). The sediment was separated into four tubes, resuspended in 15 mL and shaken for 15 minutes (Flask Shaker, Gallenhamp, Germany), then centrifuged for 1 hour at 3500 rpm. The sediment was then resuspended in 15 mL dH_2O, and ice-bath sonicated for 20 minutes (Elma Ultrasonic Cleaner S30H, 320W, Germany). The colloidal solution was topped up to 50 mL and centrifuged for 1 hour at 3500 rpm. The MXene supernatant was collected for physical characterisation and further experiments.
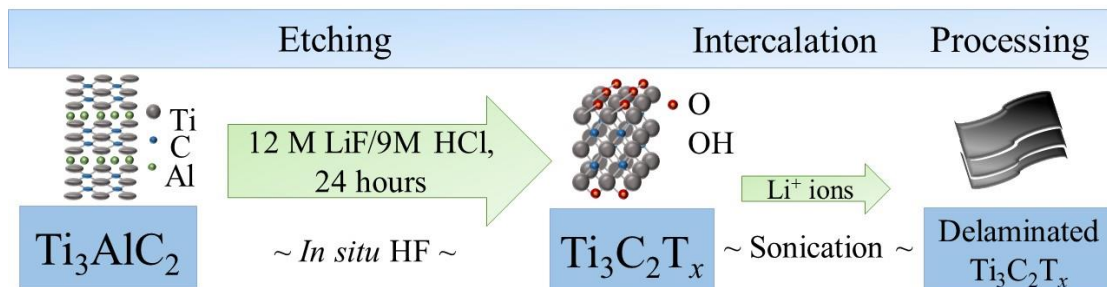
Figure 2.3: Overview of MILD method and solution processing stages of the synthesised MXene used.

2.2.2 Preparation of free-standing $Ti_3C_2T_x$ (MXene) films to determine concentration

A 4 mL volume of the synthesised $Ti_3C_2T_x$ solution was vacuum pump-filtered using an EMD Millipore™ 47 mm Glass Vacuum Filter membrane (Fisher Scientific, UK) for 1 hour. The filtered MXene was left to dry at 80 °C for an additional hour. The free-standing film was then weighed, and the concentration of the colloidal solution (mg mL^{-1}) was determined using the known filtrated volume.

2.2.3 Spin-coating of $Ti_3C_2T_x$ (MXene) on intraocular lens types

RayONE hydrophobic IOLs (RAY800C; Rayner Intraocular Lenses, UK) were plasma etched using atmospheric air for 3 minutes at 11 sccm, 10 cm^{3}min^{-1} (HPT 200, Henniker Plasma, UK). Lenses were placed on a glass slide attached to the centre of the spin coater (Ossila, UK) and 20 µL of $Ti_3C_2T_x$ solution was left to settle on the optic for 60 seconds. The lenses were first spun for 30 seconds at 6000 rpm, then 30 seconds at 5000 rpm. This cycle was repeated three times. IOLs were sterilised under ultraviolet light for 1 hour and pre-conditioned in culture media for 24 hours before use.

2.2.4 Spray-coating of $Ti_3C_2T_x$ (MXene)

The required volume of $Ti_3C_2T_x$ to achieve uniform and conductive spray coated films was investigated. Hydrophilic polymer discs were washed in 100% ethanol and dH$_2$O then dried. Two

discs were spray coated for each concentration; 1, 2, 3, 4 and 5 mg/mL. The nozzle was kept at 15 cm from the discs and applied in one direction. A battery circuit was used to test the conductivity of the $Ti_3C_2T_x$-coated discs. To spray coat tissue grade 12-well cell culture plates (Sarstedt, Germany), the plates were covered in parafilm, exposing the designated wells. A volume of $Ti_3C_2T_x$ supernatant was added to the nozzle. The nozzle was kept at 15 cm from the tissue grade culture wells and half of the required volume was applied, in a left to right motion across the well surface. The plate was rotated and sprayed left to right until the final volume was coated evenly.

2.2.5 Dynamic light scattering analysis

Analysis of particle size dispersity was conducted by DLS at a 90° scattering angle. 1 µL of the synthesised $Ti_3C_2T_x$ colloidal solutions were diluted in 1 mL of deionised water within a polystyrene cuvette (Zetasizer Nano Series (Malvern) Series No. MAL105782, USA). Particle size was calculated from five measurements of each sample.

2.2.6 Scanning electron microscopy of $Ti_3C_2T_x$ (MXene) films

Free-standing MXene films were prepared as described in **2.2.2**. The film was cut using tweezers and mounted to the side of a hexagonal nut, perpendicular to the electron beam. High-resolution images were produced through SEM (Field Emission Scanning Electron Microscope, Zeiss Sigma, Germany), with a 1.5 kV accelerating voltage. Thickness measurements of single delaminated flakes were estimated using the stored vector profile. This profile provides a histogram of the grey scale contrast within a cross section. The difference in contrast between the background and the $Ti_3C_2T_x$ flake was related back to the scale factor for an estimation of the flake's thickness. Fourteen measurements were taken across the entire sample.

2.2.7 Scanning electron microscopy of $Ti_3C_2T_x$ (MXene) coatings

Thickness measurements of $Ti_3C_2T_x$ coatings, prepared as described in **2.2.4**, on 12-well cell culture plates (Sarstedt, Germany) were quantified SEM (Field Emission Scanning Electron Microscope, Zeiss Sigma, Germany), with a 1.5 kV accelerating voltage. Thickness of the coating was determined by measuring the $Ti_3C_2T_x$ layer, where the tissue culture plate was used as the baseline. These samples were also analysed for chemical composition using energy-dispersive X-ray detector (EDS) with a 20 kV accelerating voltage.

2.2.8 UV-vis characterisation of $Ti_3C_2T_x$ (MXene) colloidal solution

UV-vis spectroscopy was used to confirm the presence of MXene in the synthesised colloidal solution. The neat supernatant was diluted 1:1 in dH_2O then serial dilutions were analysed using an UV-vis spectrophotometer against a blank (UV-VIS Recording Spectrophotometer, UV-2401(PC), Shimadzu Corporation, Kyoto Japan). Transmittance was recorded from 200 to 1000 nm. A calibration curve was calculated using Excel (Microsoft, Redmond, WA).

2.2.9 UV-vis characterisation of $Ti_3C_2T_x$ (MXene) coatings

UV-vis spectroscopy was used to assess the stability of $Ti_3C_2T_x$ coatings after 24-hour incubation, as per experimental conditions, and 7 days post-incubation with culture media. 2 mL of minimum essential medium (MEM) was incubated with 5 mg/mL $Ti_3C_2T_x$ coatings, prepared as described in **2.2.4**. The MEM samples were analysed before and after incubation with the $Ti_3C_2T_x$ coatings using an UV spectrophotometer against a blank (UV-VIS Recording Spectrophotometer, UV-2401(PC), Shimadzu Corporation, Kyoto Japan). Transmittance was recorded from 200 to 1000 nm.

2.2.10 Contact angle analysis

Hydrophobic and hydrophilic lenses were supplied (RAY800C; RAY600C; Rayner Intraocular Lenses Limited, UK). The hydrophobic composite includes cross-linked polyurethane acrylates and methacrylates, and the hydrophilic composite includes 2-hydroxyethyl methacrylate/methyl methacrylate polymers. RayONE hydrophobic lenses were coated as described in **2.2.3**. Contact angle was measured using the SCA 20 software, (OCA 15EC, DataPhysics Instruments GmbH, Germany). The sessile drop method was used. Dosage was set at 5 µL. Contact angle measurements were set manually, using the baseline and ecliptic outline tools **(Fig. 2.4)**. The average contact angle for the lens type per experimental repeat was calculated from three measurements.
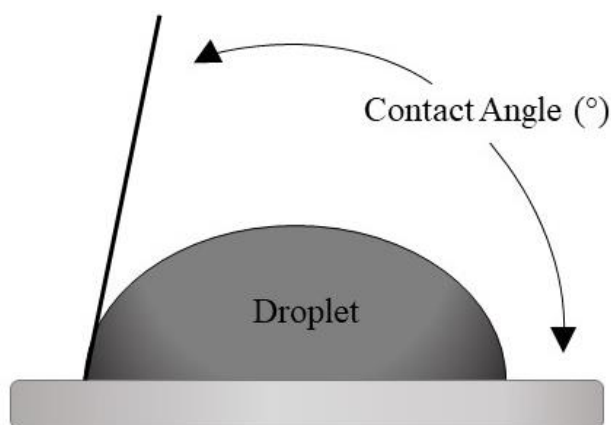
Figure 2.4: Schematic diagram of the manual mode measurement tool to calculate contact angle. Upon contact with the lens' surface, an image was captured for a static contact angle. Measurements were calculated from a manual positioning of the baseline and ecliptic outline of the droplet. Three contact angle measurements at different positions of the lens were taken for each lens type.

2.3 Results

2.3.1 Synthesis of $Ti_3C_2T_x$ (MXene)

$Ti_3C_2T_x$ (MXene) was synthesised using the MILD method, creating *in situ* HF to etch the aluminium layers of its composite MAX phase. Synthesis method was optimised from Batch 1 to 5 (**Table S1**). There was no difference in yield or uniformity of flake size when the synthesis incubation time was increased. The pdi value did not improve upon decreasing the sonication time to 20 minutes from 60 minutes. The additional centrifugation wash stage post-sonication improved the uniformity and stability of the colloidal solution. The synthesis method and use of bath sonication that was used for Batch 5 was used henceforth due to the sufficient pdi value, average flake size and concentration produced. Ice-bath sonication was used to achieve a monodispersed solution with a consistent average flake size across batches (18). Individual batches used in this thesis are reported in **Table 2.2.**

Table 2.2: Characterisation of $Ti_3C_2T_x$ colloidal solutions between batches. Mean ± SD.

Batch No.	Z-average (d. nm)	Polydispersity index	Concentration (mg mL^{-1})
1	381.02 ± 15.23	0.61 ± 0.04	5.00
2	332.48 ± 3.68	0.25 ± 0.01	3.60
3	344.42 ± 5.85	0.28 ± 0.04	2.30
4	373.46 ± 11.97	0.32 ± 0.07	4.70
5	471.90 ± 10.97	0.24 ± 0.01	3.10
6	524.98 ± 7.22	0.20 ± 0.02	4.10
7	294.86 ± 1.82	0.22 ± 0.01	2.40
8	205.18 ± 1.16	0.26 ± 0.02	3.70
9	294.20 ± 1.98	0.27 ± 0.03	3.80
10	353.40 ± 6.34	0.28 ± 0.02	4.50
11	577.00 ± 13.02	0.34 ± 0.02	2.00

12	259.70 ± 4.45	0.26 ± 0.03	3.40
13	294.30 ± 2.19	0.21 ± 0.01	5.00
14	438.90 ± 7.01	0.27 ± 0.03	2.70
15	281.30 ± 6.00	0.24 ± 0.04	2.10
16	374.90 ± 20.47	0.41 ± 0.01	2.20

2.3.2 Dynamic light scattering analysis

Batch 5 produced an average flake diameter of 471.90 ± 10.97 and its pdi was 0.24 ± 0.01 (**Fig. 2.5**). DLS graphs for all of the batches are reported in **Fig. S1**.
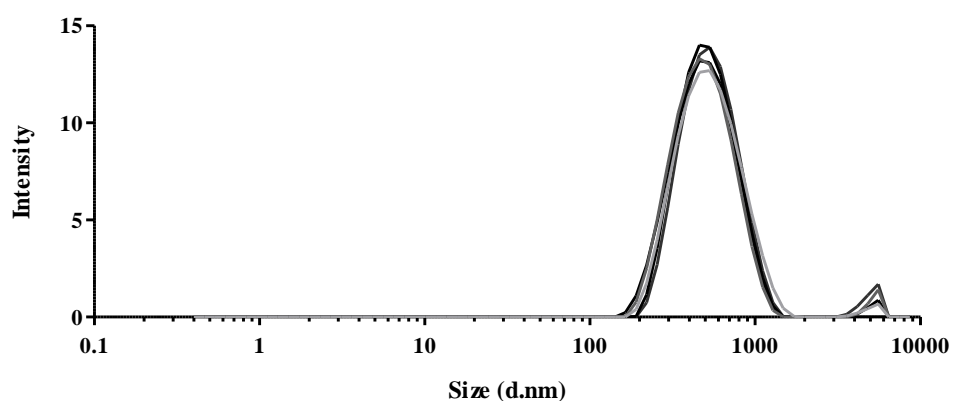
Figure 2.5: Size distribution of flakes by intensity of light scattering. Average z-average and poly dispersant index was calculated from five readings. (Zetasizer Nano Series (Malvern) Series No. MAL105782, USA)

2.3.3 Scanning electron microscopy of $Ti_3C_2T_x$ (MXene) films

Vacuum filtration of $Ti_3C_2T_x$ colloidal solution compressed the flakes, stacking them at various orientations on top of one another (**Fig. 2.6 A**). Single or few-layered flakes were observed throughout the sample, indicated by white arrows (**Fig. 2.6 B**). Average thickness of the few-layered delaminated flakes was 11.32 ± 2.38 nm (Mean $\pm$ SD).
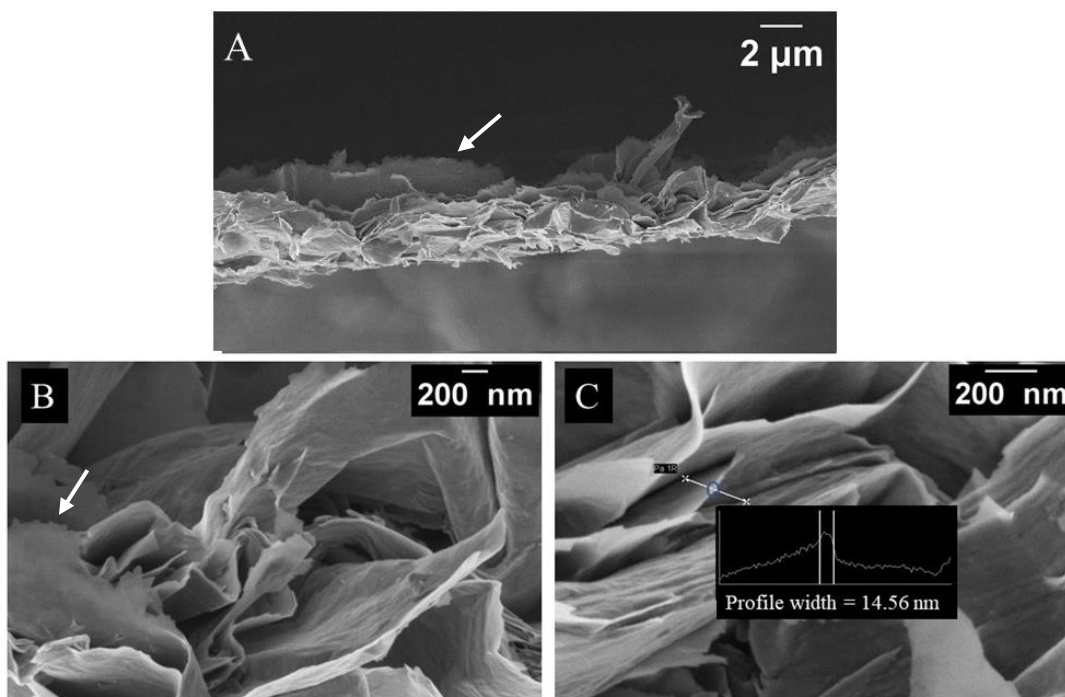
Figure 2.6: Scanning electron microscopy of $Ti_3C_2T_x$ free-standing film (Field Emission Scanning Electron Microscope, Zeiss Sigma, Germany). Cross section of $Ti_3C_2T_x$ free-standing film produced through vacuum filtration (**Fig. 2.6 A**). Magnified view of cross-section, showing single or few-layer $Ti_3C_2T_x$ flakes (**Fig. 2.6 B**). Stored vector profile to measure individual $Ti_3C_2T_x$ flakes (**Fig. 2.6 C**). White arrows indicate single, delaminated flakes.

2.3.4 Scanning electron microscopy of $Ti_3C_2T_x$ (MXene) coatings

Average thickness of $Ti_3C_2T_x$ coatings on cell culture plates was $1 - 2$ μm (**Fig. 2.7**). The chemical composition of the $Ti_3C_2T_x$ coatings is shown in **Table 2.3**.
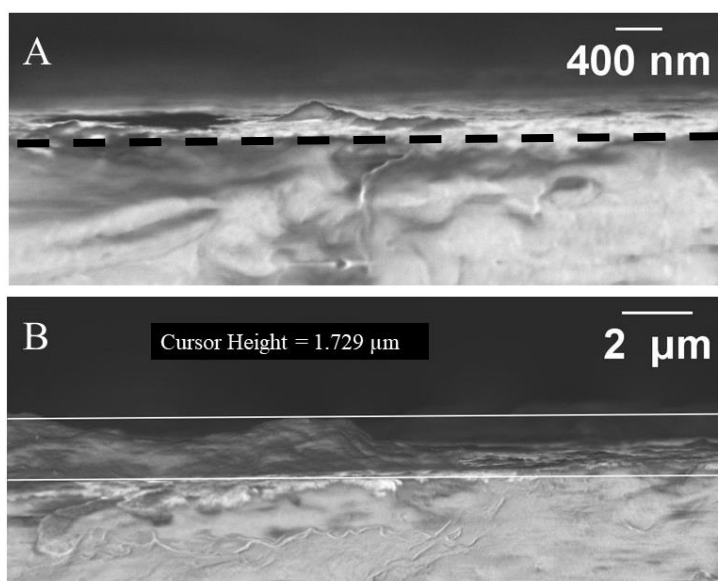
Figure 2.7: Scanning electron microscopy of $Ti_3C_2T_x$ coatings on cell culture well plates (Field Emission Scanning Electron Microscope, Zeiss Sigma, Germany). Cross section of $Ti_3C_2T_x$ coating on cell culture well. The coating edge is indicated by the dotted black line (**Fig. 2.7 A**). Measurement profile of $Ti_3C_2T_x$ coatings. (**Fig. 2.7 B**).

Table 2.3: Chemical composition of $Ti_3C_2T_x$ coatings (Field Emission Scanning Electron Microscope, Zeiss Sigma, Germany).

Elements	Wt (%)	σ
C	97.7	0.1
O	1.1	0.1
Ti	0.6	0.0
F	0.6	0.1

2.3.5 UV-vis characterisation of $Ti_3C_2T_x$ (MXene) colloidal solution

The synthesised $Ti_3C_2T_x$ colloidal solutions produced a broad absorbance peak between 700 – 800 nm, as found in literature (**Fig. 2.8 A**) (14,135,142). A calibration curve of serial dilutions of $Ti_3C_2T_x$ is shown in **Fig. 2.8 B**. UV-vis graphs for all the batches are reported in **Fig. S2**.
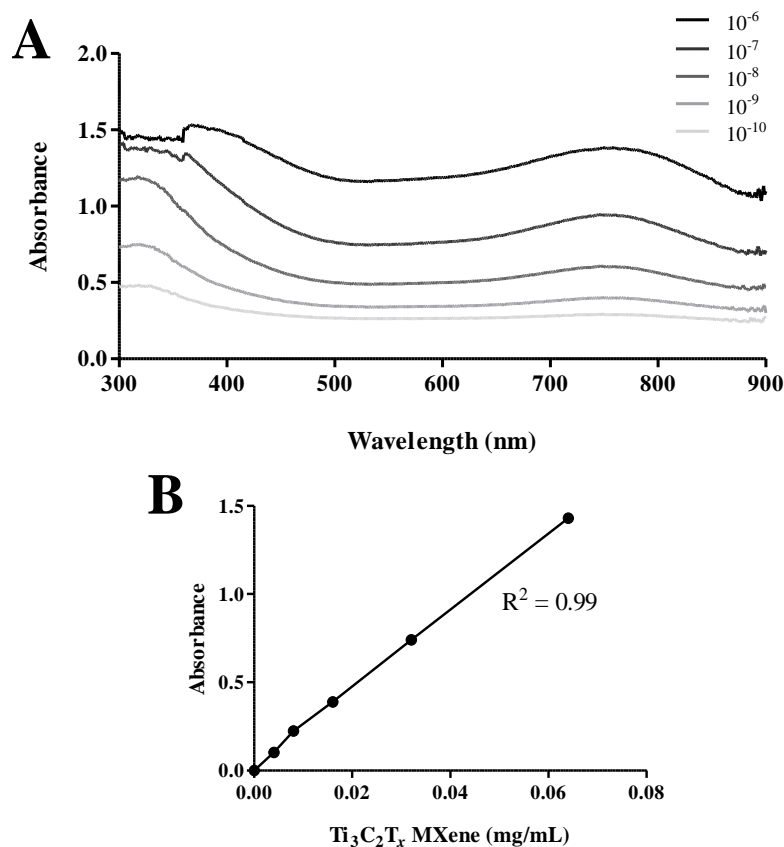
Figure 2.8: Ultraviolet spectroscopy analysis of serial diluted $Ti_3C_2T_x$ (MXene) colloidal solution. A broad absorbance peak of 700 – 800 nm was observed, confirming the synthesis of $Ti_3C_2T_x$ (**Fig. 2.8 A**). Calibration curve of $Ti_3C_2T_x$ MXene concentration against wavelength absorbance. Serial dilutions of the colloidal solutions were made up. Line of best fit was plotted. R^2 value of 0.9989 (**Fig. 2.8 B**).

2.3.6 UV-vis characterisation of $Ti_3C_2T_x$ (MXene) coatings

$Ti_3C_2T_x$ coatings show good stability in media under experimental conditions. The collected media showed no detection of the plasmonic peak of $Ti_3C_2T_x$ after 24-hour and 7-day incubation to show degradation of the coatings over the time period (**Fig. 2.9**).

47
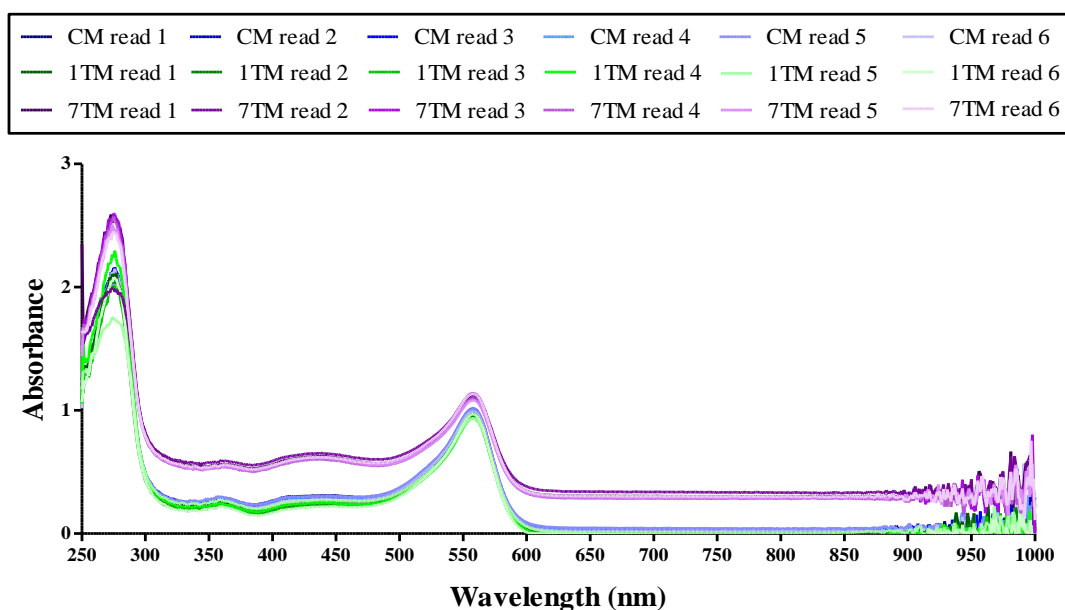
Figure 2.9: Ultraviolet spectroscopy analysis of culture media pre- and post-incubation with Ti$_3$C$_2$T$_x$ coatings. Pre-treatment culture media had a peak at 280 nm and 580 nm, indicative of the foetal calf serum and phenol red additions to the media (blue). Media after 24-hour (green) and 7-day (purple) incubation with Ti$_3$C$_2$T$_x$ coatings showed no change in absorbance across the wavelength spectrum. (CM: control media; 1TM: 1-day Ti$_3$C$_2$T$_x$ coating incubation; 7TM: 7-day Ti$_3$C$_2$T$_x$ coating incubation).

2.3.7 Contact angle analysis

Internal contact angle values of the IOLs and spin-coated Ti$_3$C$_2$T$_x$ IOLs are reported in **Table 2.4** (144). Hydrophobic materials are characterised by a contact angle of greater than 90° whereas hydrophilic materials have a contact angle of less than 90° (145). None of the IOLs reported a value above 90 °. The RayONE hydrophobic acrylic lenses showed the greatest contact angle (**Fig. 2.10 A**) whilst the hydrophilic acrylic lenses showed the lowest contact angle (**Fig. 2.10 B**). Ti$_3$C$_2$T$_x$ coatings decreased the contact angle of the deposited water droplet relative to the hydrophobic lens (**Fig. 2.10 C, D**).
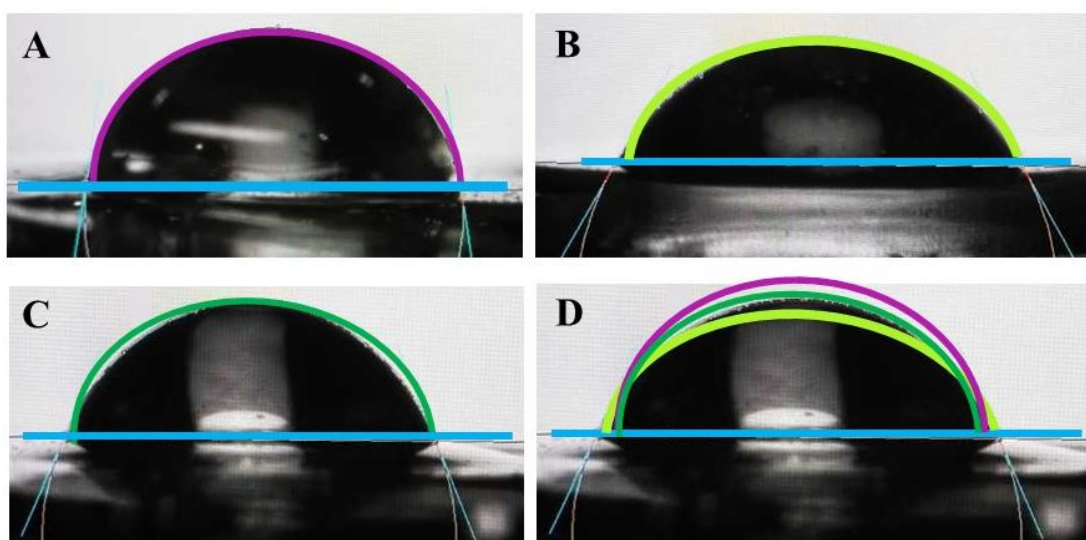
Figure 2.10: Captured images of the sessile drops on the intraocular lens types. Three measurements were taken for each hydrophobic (**Fig. 2.10 A**), hydrophilic (**Fig. 2.10 B**) and $Ti_3C_2T_x$-coated hydrophobic acrylate intraocular lens (**Fig. 2.10 C**). Manual measurements were computed from the baseline (blue) and ecliptic outline measurements (dark blue, yellow and green, respectively) as displayed. The ecliptic outlines for all IOL types were mapped on to the $Ti_3C_2T_x$-coated hydrophobic acrylate intraocular lens to compare the difference in wettability contact angle (**Fig. 2.10 D**).

Table 2.4: Contact angle analysis of intraocular lens types (Rayner Intraocular Lenses, UK). Mean ± SD (n=4)

IOL Type	Internal Contact Angle (°)
Hydrophobic	71.92 ± 9.99
Hydrophilic	40.90 ± 10.28
$Ti_3C_2T_x$-coated Hydrophobic	54.09 ± 9.94

2.4 Discussion

In this chapter, a consistent route for $Ti_3C_2T_x$ synthesis was successfully optimised at Batch 5 and this method was used to synthesise further batches. It was found that a synthesis reaction

time of 24 hours, sonication period of 20 minutes and centrifugation washes of ≥ 5 pre-sonication and one wash post-sonication were required to achieve a stable, high yield and uniform colloidal solutions across batches. It was shown that the average flake size between batches ranged between $300 - 500$ d. nm and that all pdi values were below 0.5. Spray-coated $Ti_3C_2T_x$ coatings were produced with a thickness of $1 - 2$ µm and showed good stability under experimental conditions. This chapter also showed that the addition of $Ti_3C_2T_x$ coatings to hydrophobic IOL optics increased the wettability of the optic surface closer to that of a hydrophilic lens, supporting previously reported literature on the hydrophilic nature of $Ti_3C_2T_x$ (19).

$Ti_3C_2T_x$ is synthesised by selectively etching the aluminium from its corresponding MAX phase, Ti_3AlC_2 by direct addition of HF acid or in situ formation (134). The MILD synthesis method, as described in **2.1.1**, is a milder etching process (≤ 5 wt % HF) which produces $Ti_3C_2T_x$ with a less open structure comparative to the direct HF etchant (10 or 50 wt % HF) (134). $Ti_3C_2T_x$ synthesised in this way produces larger flake sizes and as a result, solutions with greater conductivity. Maleski et al., (18) showed $Ti_3C_2T_x$ films made up of flakes ~1 µm had the best capacitance of 290 F/g at 2 mV/s. Sonication is a method to control flake size by applying mechanical force to a poly dispersed solution (18). Sonication can increase the likelihood of flake defects and reduces conductivity by reducing flake size (18). For the purpose of this project, uniformity across synthesised batches was a priority, justifying the use of sonication. When applied as coatings, a battery circuit confirmed the sonicated batches remained conductive.

The MXene batches were physically characterised by UV-vis spectroscopy, DLS and SEM. DLS analysis is an established method to determine the diffusion of macromolecules within a solution (146,147). The technique utilises Brownian motion of particles that states smaller particles move faster than larger particles in a solution (147). Light scattering is used to characterise the diffusion speed of the particles and subsequently size distribution of the macromolecules within the solution (146). Xia et al., (148) reported the MILD method synthesis of $Ti_3C_2T_x$ with a post-synthesis probe sonication stage of 20 minutes found an average flake length of 274.17 ± 79.53 nm and width of 163.19 ± 50.49 nm as quantified by SEM imaging. The

pdi of a nanoparticle material is classified acceptable if ≤ 0.5 (149). Quain et al., (150) presented a pdi of 0.472 for their delaminated supernatant whilst Driscoll et al., (151) showed a pdi of 0.390 for their delaminated supernatant synthesised using direct HF etching. Moreover, Ward et al., (14) found a pdi of 0.5 using the MILD method synthesis. Zhao et al., (152) presented a pdi of 0.255 using the MILD method synthesis and 1-hour ultrasonication. Therefore, the DLS analysis of the synthesised MXene batches in this project were found to be in the range of average flake size and pdi found in published literature (**Fig. 2.5**). The average thickness measurement of the synthesised few-layered flakes corresponded to those reported in literature (**Fig. 2.6**) (153). $Ti_3C_2T_x$ coatings on cell culture well plates showed good stability in culture media at 37 °C over 24-hour and 7-day incubation (**Fig. 2.9**). MXene composition determines the perceived colour of the colloidal solution and films (135,142). UV-vis spectroscopy analysis can be used to identify the MXene types using their unique wavelength absorbance range. UV-vis spectroscopy analysis showed a broad peak at 700 – 800 nm, attributed to the plasmonic peak of $Ti_3C_2T_x$ synthesis (**Fig. 2.8**) (14,18,134,142).

Contact angle analysis determines the wettability of a solid by the angle at which a liquid drop deposits on its surface. An internal contact angle of $0 - 90°$ shows high wettability of a solid whereas a contact angle ≥ 90° determines the solid has low wettability (154). The hydrophobic acrylate IOLs presented an average contact angle of 71.9° ± 10.0° which would be classified as good wettability and a hydrophilic solid. These IOLs are described as relatively hydrophobic lenses rather than true hydrophobic materials which would result in poor biocompatibility within a medical device. The hydrophobic acrylate IOLs used in this project are classified hydrophobic relative to the hydrophilic acrylate IOLs. Coatings of $Ti_3C_2T_x$ applied to the hydrophobic acrylate IOLs reduced the contact angle to 54.1 ± 9.9, increasing surface wettability and increasing the hydrophilicity of the surface (**Table 2.4**). The results support existing literature on the hydrophilic properties of $Ti_3C_2T_x$ (155).

In conclusion, $Ti_3C_2T_x$ synthesised using the MILD method and bath sonicated for 20 minutes achieved sufficient yield, concentration and stability. The use of sonication produced

uniform flake sizes and pdi across batches. Moreover, this chapter showed that stable $Ti_3C_2T_x$ coatings could be applied to tissue culture well plates using spray-coating to yield coatings of 1 – 2 µm (**Fig. 2.7**). Finally, this chapter confirmed the hydrophilic nature of $Ti_3C_2T_x$ coatings by contact angle analysis. $Ti_3C_2T_x$ was then investigated for its impact on inflammatory processes and EMT pathways leading to PCO development (**Chapter 3**). $Ti_3C_2T_x$ batches used in this project were synthesised as per the method for Batch 5. The batch number used in the following experiments are reported in **Table S2**.

Chapter 3: The impact of $Ti_3C_2T_x$ (MXene) on the wound healing response of lens epithelial cells contributing towards posterior capsule opacification development

3.1 Introduction

3.1.1 Developmental pathways of posterior capsule opacification

PCO presents as a fibrotic mass across the visual axis as the residual LECs remaining in the capsule bag undergo a wound-healing response initiated by surgical trauma. There are two types of PCO: regenerative and fibrotic. Regenerative PCO develops as a result of residual LECs attempting to construct a new lens (156). It includes the presence of lone differentiated lens fibres in the capsule bag referred to as Soemmerring's ring, and swollen globular cells known as Elschnig's pearls (3,75,157). Fibrotic PCO is characterised by the intracellular processes of the residual LEC promoting hyperproliferation, differentiation into myofibroblasts and migration (156). This body of work focussed on developing an *in vitro* model to examine cellular pathways leading to fibrotic PCO and therefore, will be discussed primarily.

The capsule bag, a membrane structure which contains the lens, is made of two sections, the anterior capsule with a single row of LEC and the acellular posterior capsule (74). Residual LECs PCS are commonly located in the edges of the capsule bag due to the iris creating a visual barrier for surgeons to access these areas with a phacoemulsification needle (**Fig. 3.1 A**). LECs undergo hyperproliferation, migration and increased ECM synthesis. Cells migrate from the edges across the capsule bag, invading the previously cell-free posterior capsule, laying down ECM as they colonise (12). This contributes to capsule wrinkling, increased light scatter alongside loss in visual acuity due to the migration of cells across the visual axis of the posterior capsule (**Fig. 3.1 B**) (3,12).
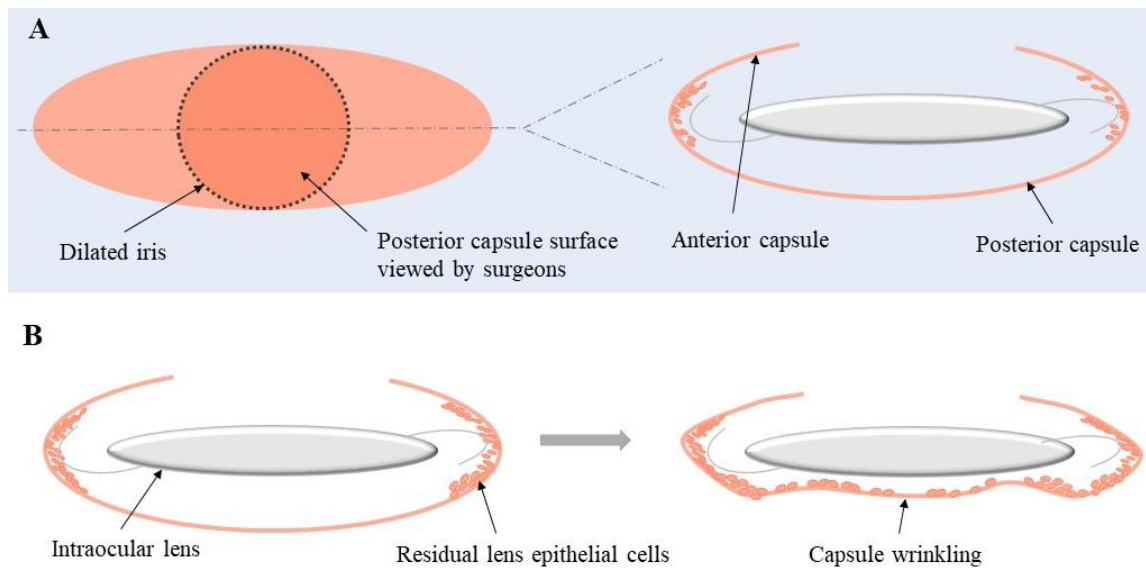
Figure 3.1: Schematic diagram of cell migration and capsule wrinkling post-cataract surgery. During surgery, surgeons are limited by the iris size to view the capsule bag and remove any residual lens epithelial cells (LEC) (**Fig. 3.1 A**). Residual LECs re-colonise the capsule bag, producing increased extracellular matrix leading to capsule wrinkling (**Fig. 3.1 B**).

3.1.2 Interleukin-1 inflammation pathways

The wound-healing response of LEC is believed to be the first key pathway in PCO development. During this response, upregulation of pro-inflammatory cytokines contributes to the initiation of inflammatory pathways including increased synthesis of ECM proteins, EMT of residual LECs and contraction of the capsule bag (110,111,113,114). Despite the isolation of key cytokines involved, the interaction of these cytokines is yet to be fully characterised. IL-1 is a pleiotropic cytokine that triggers a cascade of other pro-inflammatory mediators (111,158,159). Chronic exposure to IL-1 contributes to diseases such as autoinflammatory, metabolic syndromes, chronic inflammation, malignancy and potentially, PCO (159,160). In breast cancer tumours, high levels of IL-1 are linked to tumour proliferation and migration (159). IL-1 is found in two forms, IL-1α and IL-1β however, their structure and biological function are similar to one another and the two bind to the same receptor IL-1R (159,161). IL-1α is expressed by cells under

stress or triggered by cell death, processed by calcium-dependent proteases or other inflammasomes (159,162–164). Some endothelial and epithelial cells express IL-1α at a steady state (164). The regulation of IL-1α expression is dependent on specificity protein 1 (Sp1), AP1 and nuclear factor kappa beta (NF-κB) transcription factors in a cell-type specific manner (159,164). The presence of IL-1α, precursor or mature, induces the expression of IL-1R on resident macrophages, fibroblasts, epithelial and endothelial cells leading to their upregulation of IL-1β (159,163).

IL-1β release can also be induced by ROS production and pathogen or danger associated molecular patterns (PAMP/DAMPs) (**Fig. 3.2**). These molecular patterns are recognised by pattern recognition receptors (PRRs) such as toll-like receptors (TLRs) and nucleotide-binding and oligomerization domain (NOD)-like receptors (NLRs) (159,163). These receptors interact with apoptosis-associated speck-like protein containing a caspase-recruitment domain (ASC) and caspase-1, forming an inflammasome complex (159). The inflammasomes will cleave the precursor IL-1β protein into its mature biologically-active form (159,163). One such inflammasome is NLRP3 which is activated when NF-κB induces the transcription of the IL-1β gene leading to the synthesis of precursor IL-1β, which is then processed into its active form via the NLRP3 inflammasome (**Fig. 3.2**) (159). The efflux of potassium can also induce the formation of the NLRP3 inflammasome. LPS, an established instigator of inflammation via blood-borne infections can induce NLRP3 inflammasome formation via other caspases such as caspase-4, -5 and -11 (159). Alternative pathways leading to the synthesis of active IL-1β include serine and neutrophil proteases such as cathepsin G and proteinase-3. On activation by PAMP/DAMPs or ROS species, IL-1β initiates acute inflammatory pathways in the local microenvironment, recruiting leukocytes and other pro-inflammatory cytokines such as IL-6.
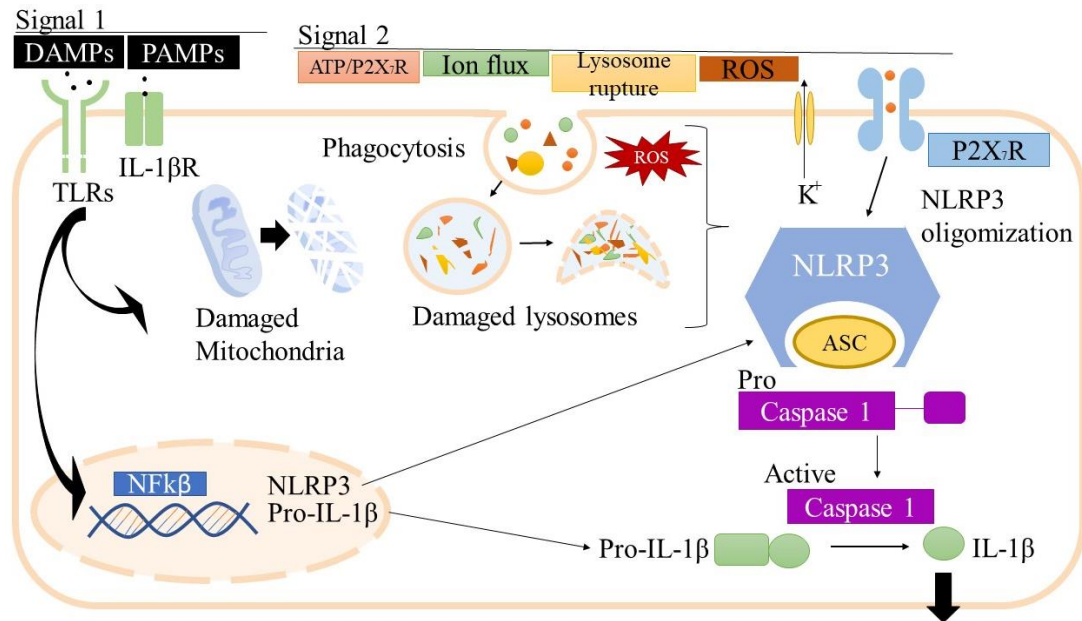
Figure 3.2: Activation of IL-1β release during inflammation. IL-1β is released by a two-step regulation. The transcription of the *IL-1β* gene is induced by the binding of PAMPs/DAMPs and other signals to TLRs and IL-1βR which activates transcription factors such as NF-κB to transcribe *IL-1β* and *NLRP3* genes. As synthesised pro-IL-1β is cleaved by caspase-1 inflammasomes into its mature bioactive form. The NLRP3 inflammasome can be activated by potassium efflux, ROS production and lysosome damage (165–167). (PAMPs/DAMPs: pathogen or danger associated molecular pattern; TLR: toll-like receptors; IL-1βR: interleukin 1 beta receptor; ASC: apoptosis-associated speck-like protein containing a caspase-recruitment domain)

IL-1β and IL-6 have been shown to work in synergy in conditions such as multiple myeloma, angiogenesis, rheumatoid arthritis and other autoinflammatory conditions (6,168). A potential pathway by which IL-1 signalling may contribute towards PCO development begins with the release of IL-1α by the surgically stressed cells **(Fig. 3.3 A)** (159). IL-1α binds to IL-1 receptors on the lens cells, initiating the release of IL-1β **(Fig. 3.3 B)** (159,163,168). Planck et al., (158) found that IL-1α leads to the upregulation in release of IL-1β and other immunological proteins in retinal pigment epithelial cells. IL-1β auto-binds to IL-1R amplifying its own signal promoting hyperinflammation (5,109). Moreover, the binding of IL-1α and IL-1β to LEC incites IL-6 and IL-8 release **(Fig. 3.3 C)**. Eskan et al., (169) found a reduction in IL-6 and IL-8 release

after treating human gingival epithelial cells with an IL-1βR blocker, supporting the hypothesis that stimulation of IL-1 activation pathways promotes IL-6 and IL-8 release.
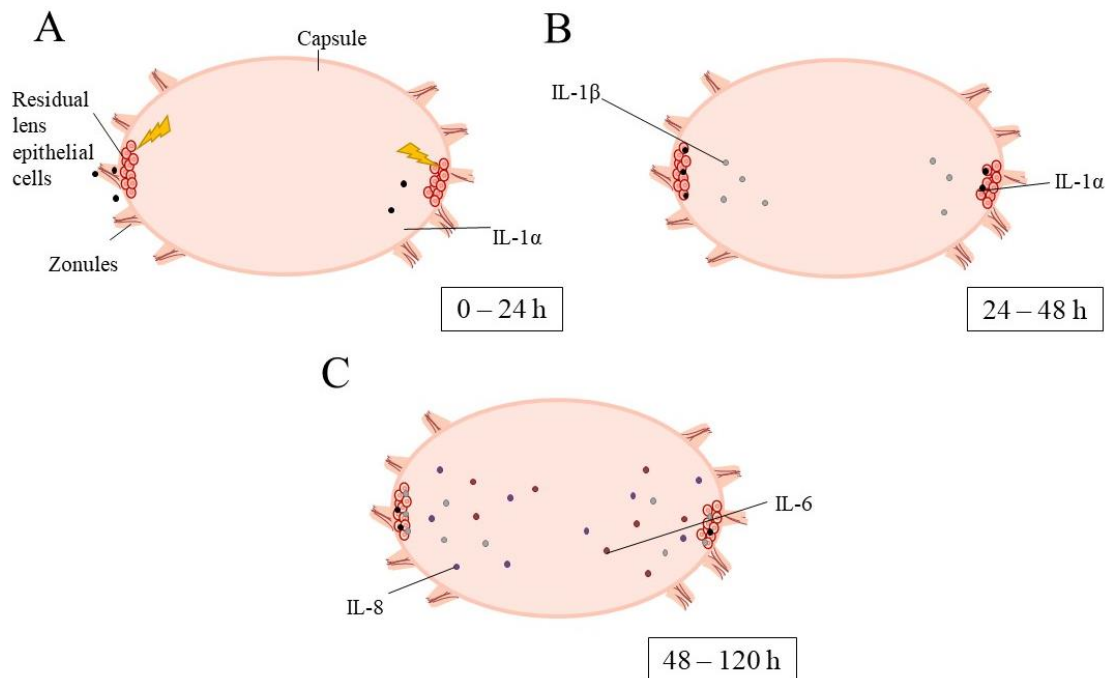
Figure 3.3: Schematic overview of the proposed cytokine-induced chronic inflammation leading to PCO development. Residual lens epithelial cells residing in the capsule bag post-cataract surgery begin to express IL-1α in response to surgical trauma. (**Fig. 3.3 A**). IL-1α binds to the residual lens cells initiating release of IL-1β (**Fig. 3.3 B**). Lens cells express IL-6 and -8 on IL-1α and -1β stimulation, promoting further developmental pathways of PCO (**Fig. 3.3 C**). (IL: interleukin) (110,111,113,161,168).

The increased levels of IL-6 and IL-8 can stimulate further LEC intracellular pathways contributing to PCO, including the EMT of residual LEC (110,111,113). Ma et al., (110) used HLE-B3 cells to establish the role of IL-6 within the promotion of ECM synthesis and growth factor signalling in PCO formation. Within 24 h of IL-6 stimulation, ECM production by the LECs had significantly increased. Lens cells treated with WP1066, an inhibitor of the JAK/STAT3 pathway showed a marked decrease in collagen, fibronectin and TGF-β2 ($p > 0.01$). The authors concluded that increased ECM production PCS could be linked to the activation of the JAK/STAT3 pathway by IL-6. Moreover, HLE-B3 cells treated with IL-6 and TGF-β2

showed significantly higher expression of collagen, fibronectin, and α-SMA, a marker of EMT, in comparison to cells treated only with IL-6 or TGF-β2 alone. Evidence to date suggests a role for IL-1β and IL-6 in upregulation of inflammatory pathways by activated LECs and propensity towards PCO.

3.1.3 Epithelial-mesenchymal transition

EMT has a major role in the wound healing response and tissue repair (170). EMT occurs in several processes within the body and is characterised into three types (25,171). Type 1 EMT is associated with embryo- and organogenesis; the transition from the primitive epithelial to mesenchymal cells (171,172). This occurs in gastric and neuroepithelial cells (172). In mesodermal and endodermal organs, a mesenchymal-epithelial transition (MET) can then occur. Type 2 EMT involves myofibroblast transdifferentiation of epithelial or endothelial cells, normally as a result of chronic inflammation and poor resolution of the wound healing response (171,172). Type 3 EMT includes cancer metastasis to form secondary tumour sites (173,174).

PCO is characterised within the Type 2 EMT category (**Fig. 3.4**). Residual LEC undergo EMT upon activation of latent TGF-β1 and 2 within the AH by migrating leukocytes (175). Fibronectin has also been shown to promote myofibroblast differentiation in LEC (176). These inducers upregulate a cascade of signalling pathways including the transcription factor family Snail and SMAD2/3 independent and dependent pathways. This promotes the suppression of epithelial markers E-cadherin and cytokeratins in synergy with an upregulation in N-cadherin, vimentin and α-SMA. Typically, LEC will form polarised sheets, held by the presence of cell adhesion molecules such as E-cadherin. The basement membrane locks the epithelial cells to the matrix surface, maintaining an apicobasal polarity by intracellular filaments (170). LEC undergoing EMT lose their apicobasal polarity, uniform shape, and tight junctions becoming irregular-shaped myofibroblasts which interact by focal points (**Fig. 3.4**) (25).
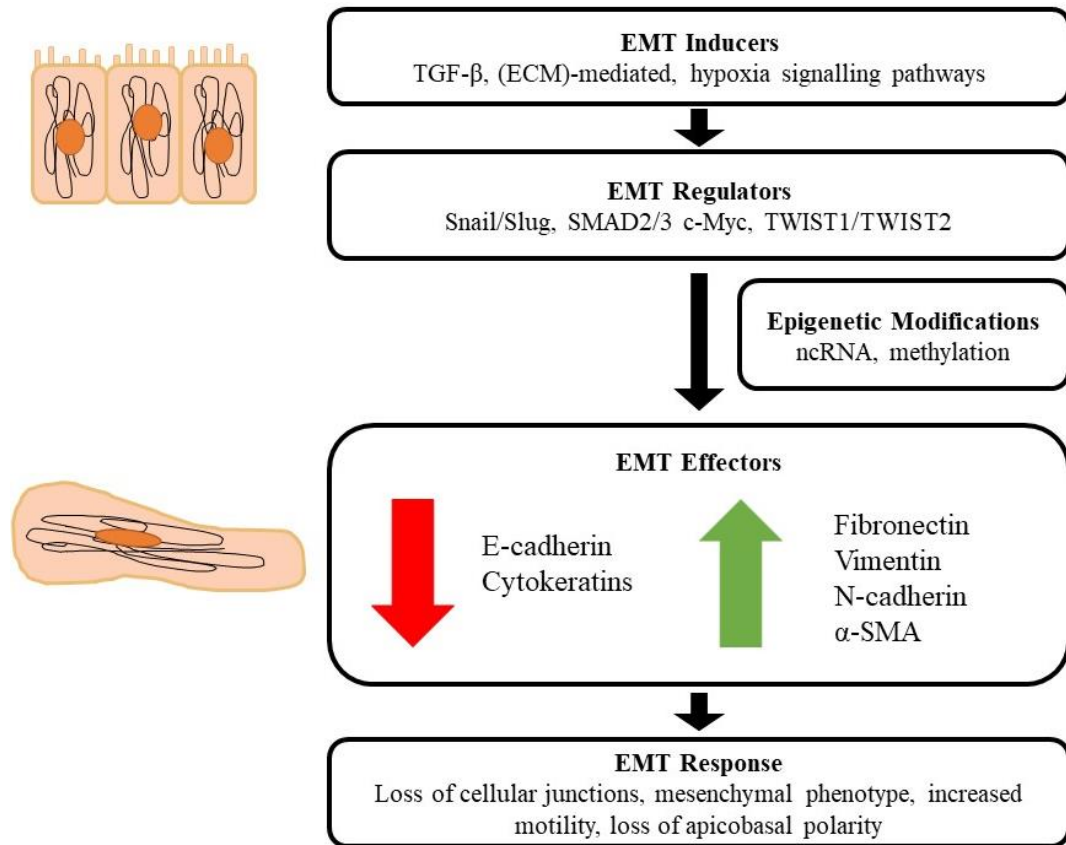
Figure 3.4: Sequential events leading to Type II EMT in PCO development. EMT inducers instigate a cascade of signalling pathways and transcription factors contributing to the downregulation of epithelial markers and an upregulation of mesenchymal markers in LECs. This subsequently leads to a loss of the epithelial phenotype and function. (EMT: epithelial mesenchymal transition; TGF-β: transforming growth factor beta; ECM: extracellular matrix; ncRNA: non-coding ribonucleic acid; α-SMA: alpha smooth muscle actin) (25,170–173).

3.1.3.1 Transforming growth factor beta 2 and SMAD signalling

TGF-β is present within the AH in a latent state until activated in a trauma response. TGF-β binds to type I and II receptor serine/threonine kinases, becoming a TGF-β receptor complex (**Fig. 3.5**) (8). Type II receptor phosphorylates type I receptor' kinase domain, initiating SMAD signalling (8). Therefore, SMAD2/3 expression is used as a marker for TGF-β signalling (117,118). SMAD proteins are divided into three groups. Receptor activated SMADs (R-SMAD) are expressed in response to TGF-β and regulate transcription of TGF-β target genes (8). SMAD2

60

and SMAD3 are examples of R-SMADs. Common mediator SMADs (co-SMAD) include SMAD4 and act to coactivate R-SMADs. Inhibitory SMADs bind to type I receptor, preventing the activation of SMAD signalling (170).

Activation of SMAD signalling begins with R-SMADs, SMAD2 and 3. Phosphorylation of type I receptor creates a docking site in the Gly/Ser (GS)-rich domain for SMAD2/3 to be phosphorylated at the Ser residues in their C-terminal domain. SMAD2/3 interacts with SMAD4, forming a SMAD complex which is transported into the LEC nucleus, activating TGF-β target gene transcription (**Fig. 3.5**) (8,170). The SMAD complex binds directly to the promoter for the transcription factor gene *SNAI1*, inducing transcription factor gene SNAI1, 2 and TWIST expression. Moreover, the SMAD complex can interact with Snail1 directly, suppressing the expression of E-cadherin (170,173). The SMAD complex can also induce E3 ubiquitin ligase HDM2 gene transcription which upregulates p53 degradation. This contributes to Snail1-mediated EMT by inhibiting EMT-regulatory miRNAs which in turn prevents the suppression of EMT transcription factor activity (170).

Alongside SMAD-dependent signalling pathways, TGF-β signalling includes other SMAD-independent pathways. The presence of active TGF-β initiates the expression of MMP-2 and MMP-9, leading to matrix contraction via the MAPK pathway (**Fig. 3.5**). In human cataracts, MAPK was found to upregulate Slug, part of the Snail transcription factor family, downregulating E-cadherin expression (170). The TGF-β receptor complex can directly interact with Rho GTPases and the PI3K/Akt pathway activating myofibroblast differentiation and stress fibre formation (8,170). ERK1/2 signalling is also activated in TGF-β2-induced EMT (177). These pathways induce cell remodelling and structural changes as the LEC undergo trans differentiation from an epithelial phenotype to a mesenchymal type. This leads to higher expression of vimentin and α-SMA filaments. Therefore, these protein filaments are established markers of EMT (178–182).
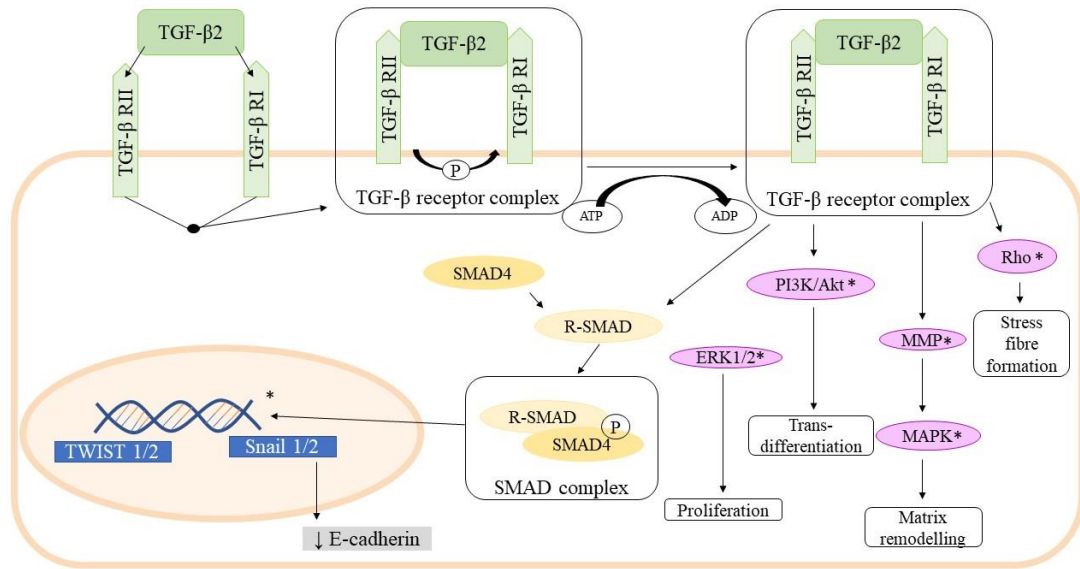
Figure 3.5: TGF-β-initiated signalling pathways involved in EMT of residual LECs. TGF-β binds to serine/threonine kinases, forming a TGF-β receptor complex. This receptor complex initiates SMAD-dependent (yellow) and SMAD-independent (purple) signalling pathways, including Rho GTPases, PPI3K/Akt, MMP and MAPK. *Expressed from TGF-β gene transcription. (TGF-β: transforming growth factor beta; PI3K: phosphatidylinositol 3-kinase; MMP: matrix metalloproteinase; MAPK: mitogen-activated protein kinase; ERK: extracellular signal-regulated kinase) (8,33,170).

3.1.3.2 Vimentin and alpha smooth muscle actin

Vimentin is a type III intermediate filament that forms a network around the nucleus of the cell and spans the cytoplasm to the cell membrane (173,178,183). It plays a crucial role in structural stability, cell adhesion, polarisation, and migration (184,185). Vimentin is also involved in several pathological conditions such as arthritis, cancer, and cataracts (173,183,186). Vimentin is highly expressed in mesenchymal cells and cells that have undergone EMT (173,178,183). The greater abundance of vimentin filaments in cells undergoing EMT is linked to the cells newly acquired elongated morphology, loss of apicobasal polarity and ability to migrate (173,183). Vimentin works with other intermediate filaments and microtubules to assist cell mobility. It also can be phosphorylated by the Akt pathway which further increases its expression and upregulates other important factors regulating EMT (183).

Alongside its role in EMT, vimentin may also be involved in the wound-healing response of the lens epithelium (179,180). In mock cataract surgery studies, vimentin has been shown to direct the migration of repair cells to the wound site area during wound healing. Epithelial tissue repairs itself by a collective migration of epithelial 'repair' cells (179,180). This migration is led by cells with a mesenchymal-like phenotype which possess a high expression of vimentin (179). Based on its multiple roles in key pathways contributing to PCO development, vimentin is an appropriate and established marker to quantify tendency of LEC to undergo EMT and wound-healing leading to PCO formation.

Additionally, α-SMA is an isoform of the actin filament, predominantly found in smooth muscle cells and myofibroblasts (187). α-SMA has been shown to be expressed in normal state LECs. Activated myofibroblasts supporting the wound healing response, correlate with higher levels of α-SMA (182,187). During PCO development, TGF-β inhibits the proliferation of LECs in favour of initiating transdifferentiation by upregulating the expression of α-SMA genes (6,118,130). This suggests the higher expression of α-SMA is an appropriate marker for myofibroblast formation, within an inflammation response contributing to PCO development.

3.1.4 Chapter aims

Whilst it is known that hyperinflammation of LEC PCS contributes to PCO development, the activation pathways linked to pro-inflammatory cytokine production and subsequent fibrosis remain poorly understood. $Ti_3C_2T_x$ has been shown to repress rather than upregulate IL-6 and IL-8 release in THP-1 monocytes. However, its impact on inducing IL-1β and IL-6 release in LEC is unknown. The impact of $Ti_3C_2T_x$-coated surfaces on LEC proliferation, migration and promotion of EMT pathways has also not been assessed. Therefore, this chapter aimed to understand the impact of $Ti_3C_2T_x$ on the wound healing response of residual LEC, specifically the hyperinflammation and EMT of LEC that contribute to PCO development. Firstly, it examined the impact of IOL material and $Ti_3C_2T_x$ coatings on cell viability and cytokine production to provide clarity on IOL materials' propensity towards PCO development and how

$Ti_3C_2T_x$ may alter this response. Secondly, it established a cell-based model to examine the cytokine-induced inflammatory pathway-initiated PCS using the immortalised cell line human lens epithelial cells (HLE-B3). Thirdly, this chapter investigated the impact of $Ti_3C_2T_x$ (MXene) on suppression of pro-inflammatory cytokine protein and gene upregulation in HLE-B3 cells. Finally, the chapter determined the effect of $Ti_3C_2T_x$ on the EMT pathway, a key pathway in the development of PCO using migration studies and expression of key EMT protein markers vimentin, α-SMA and SMAD2/3 in FHL124 cells.

3.2   Materials and methods

3.2.1 Passaging of human lens epithelial cells HLE-B3 and FHL124

Human lens epithelial cells (HLE-B3) (American Type Culture Collection ATCC CRL-11421™) were grown in minimum essential medium (MEM) (Gibco, UK) supplemented with 10% foetal bovine serum (FBS) (Gibco, UK) and 1% non-essential amino acids (NEAA) (Gibco, UK) in a T75 flask at 37 ⁰C, 5% CO_2. Foetal human lens epithelial cells (FHL124) cells were a kind gift from Professor Michael Wormstone (University of East Anglia), characterised in Wormstone et al., (82). The cells were grown in MEM supplemented with 5% FBS in a T75 flask at 37 ⁰C, 5% CO_2. Both cell types were passaged by standard trypsinisation. At 70 – 80 % confluence, the media was aspirated, and 2 mL of trypsin-EDTA (0.05%) (Gibco, UK) was added and incubated at 37 ⁰C for two minutes. The cells were gently dispersed, and 4 mL of media was added to neutralise the trypsin. The cell solution was centrifuged at 300 rpm for 5 minutes. The cell pellet was resuspended in 1 mL of fresh media and split into two T75 flasks with 10 mL of media. Media was replaced every 3 – 4 days.

3.2.2 Cell viability of human lens epithelial cells grown on intraocular lens types

3.2.2.1 Live/Dead™ stain

RayONE hydrophobic IOLs were spin-coated as described in **2.2.3**. Four of each hydrophobic (cross-linked polyurethane acrylates and methacrylates) (RAY800C; Rayner Intraocular Lenses, UK), hydrophilic (2 hydroxyethyl methacrylate/methyl methacrylate polymer) (RAY600C; Rayner Intraocular Lenses, UK)and $Ti_3C_2T_x$-coated hydrophobic IOLs were UV-sterilised for 1 hour in a 48-well tissue culture plate (Sarstedt, Germany) then preequilibrated in media supplemented with 1% penicillin streptomycin for 48 hours, with a media change at 24 hours.

HLE-B3 cells were seeded onto each IOL optic and the adjacent column of a 48-well tissue culture plate at a concentration of 2.5 x 10^3 cells 250 μL^{-1}. Experimental repeats were carried out in triplicate. The plate was kept at 37 °C, 5 % CO_2. Live/Dead™ cell imaging kit (Thermo Fisher Scientific, UK) was used to visualise the cells. Dead stain (1 μL) was added to 1 mL live stain and diluted 1:1 with PBS. The media was aspirated from the plate and 100 μL of the fluorescent stain was added to each well. The plate was incubated for 15 minutes, then the cells were visualised by LAS AF software (Leica Microsystems TCS SPH; Serial No. 5100000331. Germany). Images were analysed using Image J.

3.2.2.2 MTS quantification

IOL types were prepared as described in **3.2.2.1**. A standard curve of cell concentration was prepared by adding 100 μL of media to the first two columns of a 96-well tissue culture plate (Sarstedt, Germany) excluding the top row. HLE-B3 cells were seeded into the top two rows at a concentration of 5 x 10^5 cells 100 μL^{-1}. From the second row, the cell suspension was triturated down until the second-last row, leaving the last row as a media control.

HLE-B3 cells were seeded onto each IOL optic and the two adjacent columns of a 48-well tissue culture plate at a concentration of 2×10^5 cells 100 μL^{-1}. For the positive control for cell toxicity, 100 μL of 0.1 mic mL^{-1} tin maleate was added to one column. Experimental repeats were carried out in triplicate. The plates were kept at 37 °C, 5 % CO$_2$. At 24 hours, 20 μL of CellTiter 96® AQ$_{ueous}$ One Solution Reagent (Promega. Cat. No. G3580) was added per well. Plates were wrapped in foil and incubated for 2 hours at 37 °C, 5 % CO$_2$. Samples were transferred to a fresh 96-well tissue culture plate and absorbance measured at 490 nm (ELx800™ Absorbance Microplate Reader, BioTek). Cell viability percentage was calculated using Excel (Microsoft, Redmond, WA).

3.2.2.3 LDH quantification

IOL types were prepared as described in **3.2.2.1**. HLE-B3 cells were seeded onto the IOLs' optic and the adjacent two columns of a 48-well tissue culture plate at a concentration of 2×10^5 cells 250 μL^{-1}. The final column was left as a media control. Experimental repeats were carried out in triplicate. The plate was kept at 37 °C, 5 % CO$_2$ for 24 hours. 45 minutes prior to the addition of CytoTox 96® Reagent, 10 μL of 10X Lysis Solution was added to one column. CytoTox 96® Reagent was prepared by adding 12 mL Assay Buffer to a Substrate Mix bottle and inverting to dissolve. 50 μL aliquots of each well was transferred to a new 96-well tissue culture plate (Sarstedt, Germany) with 50 μL CytoTox 96® Reagent. The plate was covered and incubated for 30 minutes at room temperature. 50 μL of Stop solution was then added and the plate was read at 490 nm (ELx800™ Absorbance Microplate Reader, BioTek). Percentage of lysed cells was calculated using Excel (Microsoft, Redmond, WA).

3.2.3 Release of interleukin-6, and -8 by human lens epithelial cells grown on intraocular lens types

RayONE hydrophobic IOLs were spin-coated as described in **2.2.3**. IOL types were prepared as described in **3.2.2.1**. HLE-B3 cells were seeded onto each IOL optic and adjacent

two columns of a 48-well plate at a concentration of 2.5×10^4 cells $500\ \mu L^{-1}$. One column was spiked with 50 ng mL^{-1} of IL-1β (Abcam, UK) as a positive control to incite IL-6 and IL-8 production. The final column contained 500 µL of media. Technical and experimental repeats were carried out in triplicate. The plate was kept at 37 °C, 5% CO_2. At 24 hours, media samples were collected in Eppendorf tubes, centrifuged at 11600 rpm for 5 minutes and the media was stored in fresh Eppendorf tubes. Samples were kept at -20 °C until required. Detection of IL-6 and -8 release were undertaken following the BD Bioscience protocol.

In brief, a Nunc-Immuno™ polysterone Maxisorp ELISA flat bottom plate (Thermofisher Scientific, UK) was coated in the appropriate capture antibody diluted in 0.1 M sodium carbonate (1:250) for incubation overnight at 4 °C. The plates were washed three times in PBS with 0.05% Tween-20 (wash buffer) and incubated for 1 hour at room temperature (RT) with 200 µL/well of PBS with 10% FBS (assay diluent). After washing, 100 µL of the sample and standard were added in duplicates and incubated for 2 hours at RT. Samples were analysed neat. Following further washing, 100 µL/well of detection antibody, Sav-HRP and assay diluent (1:1:250) were added for 1 hour at RT. The plates were then washed with wash buffer seven times with 30 – 60 second soaks. 100 µL/well of tetramethylbenzidine and hydrogen peroxide (H_2O_2) (1:1) was added and incubated for 20 minutes in the dark. 50 µL/well of 2N H_2SO_4 was added, and absorbance was measured at 450 nm (ELx800™ Absorbance Microplate Reader, BioTek). The samples' absorbance was corrected to a blank control and converted to concentration using Excel (Microsoft, Redmond, WA).

3.2.4 Optimisation of interleukin-1 beta and -alpha treatment to stimulate interleukin 6, 8 and tumour necrosis factor release by lens epithelial cells

To optimise the incubation period with IL-1β and IL-1α for maximum cytokine production, HLE-B3 cells were seeded into the wells of a 12-well plate at a concentration of 1×10^5 cells mL^{-1} (Sarstedt, Germany). The second column was spiked with 100 ng mL^{-1} of IL-1β per well. A final column was prepared with 1 mL MEM spiked with 100 ng mL^{-1} IL-1β. The plate set-up was

repeated, substituting IL-1β with IL-1α (Abcam, UK). Technical and experimental repeats were carried out in triplicate. The plate was kept at 37 °C, 5 % CO_2. Media samples were collected in Eppendorf tubes at 2, 4 and 24 hours.

To optimise the IL-1β spiking concentration, HLE-B3 cells were seeded into the wells of a 12-well plate at a concentration of 1×10^5 cells mL^{-1} (Sarstedt, Germany). Treatment groups included cells spiked with 50, 100 and 150 ng mL^{-1} IL-1β. The adjacent columns were treated the same, minus cells. The plate was kept at 37 °C, 5% CO_2. Media samples were collected in Eppendorf tubes at 24 hours. All samples were centrifuged at 11600 rpm for 5 minutes and the media was removed into fresh Eppendorf tubes. Samples were kept at -20 °C until required. Detection of IL-6, 8 and tumour necrosis factor (TNF) release were undertaken following the BD Bioscience protocol as described in **3.2.3**. IL-1α-treated samples were analysed neat. IL-1β-treated samples were analysed using a dilution factor of 1 in 200, except for detection of TNF which was analysed neat.

3.2.5 Stimulation of interleukin-1 beta release by human lens epithelial cells

To detect IL-1β release following IL-1β treatment, HLE-B3 cells were seeded into the wells of a 12-well plate at a concentration of 1×10^5 cells mL^{-1} and primed with 50 ng mL^{-1} IL-1β (Sarstedt, Germany). Technical and experimental repeats were carried out in triplicate. The plate was incubated at 37 °C, 5 % CO_2. At 2 hours, the media was removed from one column, and the wells were washed three times in phosphate buffer saline (PBS) to remove any exogenous IL-1β. Fresh media was added to the wells. This was repeated in the adjacent column at 24 hours. Media samples were collected in Eppendorf tubes at 24 (for the 2 hour-treated samples) 72 and 120 hours for both 2- and 24-hour treated samples.

To detect IL-1β release by IL-1α treatment, HLE-B3 cells were seeded into the wells of a 12-well plate at a concentration of 1×10^5 cells mL^{-1} and primed with 50 ng mL^{-1} IL-1α (Sarstedt, Germany). Media samples were collected at 24 hours. The samples were centrifuged at 116 rpm for 5 minutes and the media was stored in fresh Eppendorf tubes. Samples were kept at -20 °C

until required. Detection of IL-1β release were undertaken following the BD Bioscience protocol as described in **3.2.3**. All samples were analysed neat.

3.2.6 Release of interleukin-6, and -8 by human lens epithelial cells spiked with $Ti_3C_2T_x$ (MXene)

HLE-B3 cells were seeded into the wells of a 12-well plate at a concentration of 1×10^5 cells mL^{-1} (Sarstedt, Germany). Treatment groups included IL-1α-treated cells (50 ng mL^{-1}), lipopolysaccharide (LPS)-treated cells (2 µg/mL) and $Ti_3C_2T_x$-treated cells (1 mg mL^{-1}). LPS-treated cells were used as a positive control for cells undergoing inflammation for use as a comparison to cells treated with IL-1α. The adjacent columns were treated the same, minus cells. Technical and experimental repeats were carried out in triplicate. The plate was kept at 37 °C, 5% CO_2. At 24 hours, media samples were collected in Eppendorf tubes, centrifuged at 11600 rpm for 5 minutes and the media was removed into fresh Eppendorf tubes. Samples were kept at -20 °C until required. Detection of IL-6 and -8 release were undertaken following the BD Bioscience protocol as described in **3.2.3**. Samples were analysed neat.

3.2.7 Release of interleukin-6, and -8 by interleukin-1 beta-primed human lens epithelial cells incubated with $Ti_3C_2T_x$ (MXene) colloidal solution

HLE-B3 cells were seeded into the wells of a 12-well plate at a concentration of 1×10^5 cells mL^{-1} and primed with 50 ng mL^{-1} IL-1β (Sarstedt, Germany). Technical and experimental repeats were carried out in triplicate. The plates were kept at 37 °C, 5% CO_2. At 24 hours, the media was collected in Eppendorf tubes and the wells were washed three times in PBS. Treatment groups included the addition of $Ti_3C_2T_x$ colloidal solution (0.5 or 1 mg mL^{-1}) and media only. At 0, 1 and 2 hours, media samples were collected in Eppendorf tubes, centrifuged at 11600 rpm for 5 minutes and the media was stored in fresh Eppendorf tubes. Samples were kept at -20 °C until required. Detection of IL-6 and -8 release were undertaken following the BD Bioscience protocol as described in **3.2.3**. Samples were analysed neat.

3.2.8 Release of interleukin-6 after incubation with $Ti_3C_2T_x$ (MXene) solution and coatings

PBS or MEM was spiked with IL-6 at a concentration of 1000 pg mL^{-1} (1 mL). Treatment groups included $Ti_3C_2T_x$ colloidal solution (5 mg mL^{-1}), $Ti_3C_2T_x$ coatings, prepared as described in **2.2.4** (5 mg mL^{-1}) and both $Ti_3C_2T_x$ treatment conditions spiked with 1000 pg mL^{-1} IL-6. PBS or MEM with $Ti_3C_2T_x$ treatment only and PBS or MEM only controls were also included. Samples were shaken at 120 rpm for 24 hours at 37 °C to mimic experimental conditions. All samples were collected, centrifuged at 11600 rpm for 5 minutes and the supernatant was stored in fresh Eppendorf tubes. Samples were kept at -20 °C until required. Detection of IL-6 was undertaken following the BD Bioscience protocol as described in **3.2.3**. Samples were analysed neat.

3.2.9 Release of interleukin-6, and -1 beta by interleukin-1 beta-primed human lens epithelial cells with $Ti_3C_2T_x$ (MXene) coatings

HLE-B3 cells were seeded into the wells of a 12-well tissue culture plate at a concentration of 1 x 10^5 cells mL^{-1} and primed with 100 ng mL^{-1} IL-1β for 24 hours at 37 °C, 5% CO$_2$. In the $Ti_3C_2T_x$ treated conditions, wells were spray-coated with 5 mg mL^{-1} coatings as described in **2.2.4**. Treatment groups included $Ti_3C_2T_x$-treated cells (5 mg mL^{-1} coatings), IL-1β-treated cells (100 ng mL^{-1}) and cells treated with $Ti_3C_2T_x$ and IL-1β. Cell only and media only controls were also included. Technical and experimental repeats were carried out in triplicate. Media samples were collected in Eppendorf tubes, centrifuged at 11600 rpm for 5 minutes then the media was stored in fresh Eppendorf tubes and stored at -20 °C. Technical and experimental repeats were carried out in triplicate. Detection of IL-1β and IL-6 were undertaken following the BD Biosciences protocol as described in **3.2.3**. Samples were analysed neat except the IL-1β-treated cell condition which was analysed using a dilution factor of 1 in 50.

3.2.10 Upregulation in gene fold change of interleukin-6, -1 beta and CXCL1 in interleukin-1 beta-primed human lens epithelial cells with $Ti_3C_2T_x$ (MXene) coatings

HLE-B3 cells were seeded into the wells of a 12 well tissue culture plate at a concentration of 6 x 10^5 cells mL^{-1}. Treatment and control groups were set up to include cells only, $Ti_3C_2T_x$-treated cells (5 mg mL^{-1} coatings), IL-1β-treated cells (100 ng mL^{-1}) and cells treated with $Ti_3C_2T_x$ and IL-1β. In the $Ti_3C_2T_x$ treated conditions, wells were spray-coated with 5 mg mL^{-1} coatings as described in **2.2.4**. Each treatment and control group were prepared in duplicate and incubated for 24 hours at 37 °C, 5% CO_2. Experimental repeats were carried out in quintuple. At 24 hours, cells were trypsinised, and centrifuged at 11600 rpm for 5 minutes to form a cell pellet. Total RNA was extracted using a RNeasy® Mini Kit (Qiagen, UK) and quantified using a Nanodrop Lite Spectrophotometer (Thermo Fisher Scientific, UK). gDNA elimination and cDNA generation was achieved using a QuantiTect® Reverse Transcription Kit (Qiagen, UK). Gene expression of primers (**Table 3.1**) was quantified using a Rotor-Gene® SYBR® Green PCR Kit (Qiagen, UK) against the housekeeping gene actin.

Table 3.1: Primers for genes of interest (Qiagen, UK).

Gene Name	Protein Encoded	Catalog Number
ACTB_2	Actin	QT01680476
CXCL1	C-X-C motif chemokine ligand 1	QT00199752
IL-6	Interleukin-6	QT00083720
IL-1β	Interleukin-1 beta	QT00021385

3.2.11 Migration of human lens epithelial cells grown on $Ti_3C_2T_x$ (MXene) coatings

Three wells of a 12 well tissue culture plate was spray coated with $Ti_3C_2T_x$ at a concentration of 2 mg mL^{-1} and sterilised according to the method described in **2.2.4**. The coated and cell only control wells were seeded with HLE-B3 cells at a concentration of 5 x 10^5 cells mL^-

[1] then incubated for 24 hours at 37 °C, 5 % CO_2. Each condition had duplicate technical repeats in the six experimental repeats. The media was aspirated, and a vertical scratch was made using a p200 tip through the centre of each well. The wells were gently washed thrice in warmed PBS and fresh media was added. Images were captured at 0, 24, 48, 72 and 120 hours using a Zeiss Primovert HDcam (Carl Zeiss Microscopy GmbH, Germany). Cells were fixed with 3.7% formaldehyde (Sigma Aldrich, UK) diluted in PBS and stained with 0.1% crystal violet in PBS (Sigma Aldrich, UK) at 0- and 120-hour time points. Wound area, scratch width and wound closure rate was quantified using Fiji: Image J analysis (188). Images were analysed using Fiji: Image J with the wound healing size tool plugin (**Fig. 3.6**) (188).
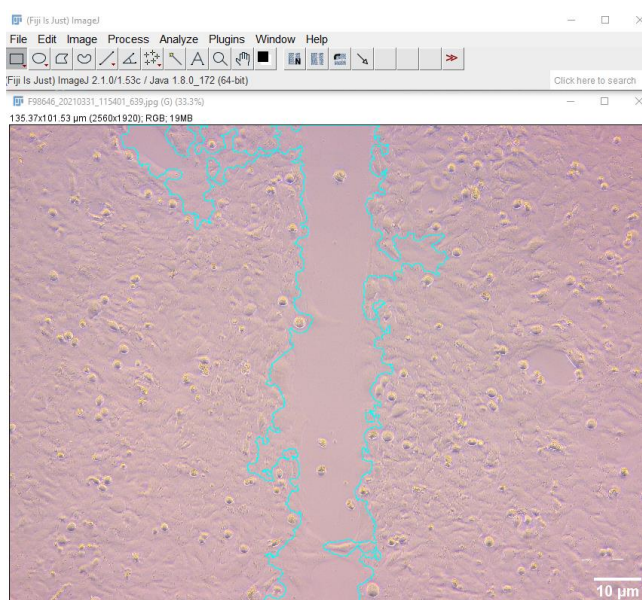
Figure 3.6: Wound healing size tool used to quantify wound closure. ImageJ/Fiji® Scale bar 10μM.

3.2.12 Expression of EMT markers in human lens epithelial cells grown on $Ti_3C_2T_x$ (MXene) coatings quantified by immunocytochemistry

FHL124 cells were seeded at a concentration of 1×10^5 cells mL^{-1} onto 16 mm coverslips (Fisherbrand™ UK). Treatment and control groups were set up to include cell only, $Ti_3C_2T_x$-treated cells (2 mg mL^{-1} coatings), TGF-β2-treated cells (20 ng mL^{-1}) and cells treated with

Ti$_3$C$_2$T$_x$ and TGF-β2 and included a no primary antibody control. Coverslips were spray coated with 2 mg mL^{-1} Ti$_3$C$_2$T$_x$ and sterilised according to the method described in **2.2.4**. Technical and experimental repeats were carried out in duplicate and triplicate, respectively. Coverslips were incubated for 24 hours at 37 °C, 5 % CO$_2$, rinsed in PBS then fixed in 3.7 % formaldehyde (Sigma Aldrich, UK) in PBS for 10 minutes. The coverslips were washed in 10% BSA in PBS (Sigma Aldrich, UK), then in 0.5% Triton-X (Tx) in PBS (Sigma Aldrich, UK) for 20 minutes and finally in 5% BSA, 0.5% Tx diluted in PBS. Alpha smooth muscle actin (α-SMA) (1μg mL^{-1}) (Thermofisher Scientific, UK), vimentin (2 μg mL^{-1}) (Thermofisher Scientific, UK), and SMAD2/3 (1:50 dilution) (Cell Signalling Technology, UK) antibodies were added and coverslips were incubated for 24 hours at 4 °C. The coverslips were washed in PBS thrice, followed by a 4-hour incubation with secondary antibody Goat anti-Mouse IgG (1 μg mL^{-1}) at 4 °C in the dark. Coverslips were washed and 10 μl DAPI (1 mg mL^{-1}) was added for 10 minutes. The coverslips were inverted onto microscope slides and visualised using a Zeiss LSM800 Confocal Microscope (Carl Zeiss Microscopy GmBh, Germany). Images were analysed using Fiji: Image J analysis. Fluorescence intensity over area was calculated for cytoskeletal markers vimentin and α-SMA. SMAD2/3 was quantified by cell counting of the stained nuclei (189). Total cell counts using DAPI nuclei staining was used to normalise SMAD2/3 stain for cell number across the conditions. Any detection of non-specific binding of the secondary antibody in the no primary antibody incubation control was subtracted from the cell only and treated cells conditions.

3.2.13 Expression of EMT markers in human lens epithelial cells grown on Ti$_3$C$_2$T$_x$ (MXene) coatings quantified by western blot analysis

FHL124 cells were treated as described in **3.2.12**. Cells were trypsinised, centrifuged at 11600 rpm for 5 minutes, placed in ice with addition of 50 μL RIPA buffer and proteinase inhibitor (ThermoFisher Scientific, UK). Samples were centrifuged for 40 minutes at 4 °C and the supernatant was collected for quantification of total protein using the Bradford assay

according to manufacturer's instructions. Samples were diluted with RIPA buffer and 6x laemmli buffer to 20 µg 25 µL^{-1} then heated at 95 °C for 5 minutes. The total volume of the samples was loaded into the wells of a 10 % SDS-TrisHCl gel (Bio-rad, UK) and proteins were separated at a constant voltage of 100 V for 1 hour. The proteins were transferred to a polyvinyl difluoride (PVDF) membrane using the Mini Trans-Blot® Cell (Bio-rad, UK) set at a constant voltage of 100 V for 1 hour. The membrane was blocked with 5% BSA in tris-buffered saline with 1% Tween® 20 (TBST) (Sigma Aldrich, UK), then incubated with anti-α-SMA (1:250 dilution) (ThermoFisher Scientific, UK), vimentin (1:500 dilution) (ThermoFisher Scientific, UK) and SMAD2/3 (1:250 dilution) (Cell Signalling Technology, UK) antibodies for 16 – 18 hours at 5 °C. Beta-actin (1:500 dilution) (ThermoFisher Scientific, UK) was included as a housekeeping control. After four 10-min wash cycles in TBST, the membrane was incubated in secondary antibody goat anti-mouse IgG1 (HRP) (1:1000 dilution) (ThermoFisher Scientific, UK) for 1 hour at room temperature. The membrane was washed again and developed using Image Studio™ software and a C-Digit Blot Scanner (LI-COR Model no. 3600, LI-COR Inc. Lincoln, NE, USA). Membranes were stripped three times, re-developed to show a clear stripped blot then re-probed. Raw densiotrometry data was analysed using Fiji: Image J analysis (190).

3.2.14 Statistical analysis

Statistical analysis was performed in Graph Pad Prism version 5 (GraphPad Software, US). For the standard curves, the known concentration standards and wavelength absorbance was compared using linear regression analysis. Parametric statistical significance was determined using a one-way ANOVA. $P \leq 0.05$ was considered statistically significant.

3.3   Results

3.3.1 Cell viability of human lens epithelial cells grown on intraocular lens types

Cell viability was quantified by Live/Dead™ stain and MTS whilst cell lysis was measured by the LDH assay to preliminary assess the biocompatibility of cells across the $Ti_3C_2T_x$-coated

IOLs and other IOL types. The presence of $Ti_3C_2T_x$-coating on the IOL' optic did not significantly lower cell viability relative to the cell only control (**Fig. 3.7 B**). $Ti_3C_2T_x$ did not induce cell lysis in cells growing over the optic coating (**Fig. 3.7 C**). There was no significant difference in cell viability or cell lysis of cells grown on IOL types relative to the cell only control. All IOL types showed significant differences from the positive control tin maleate and lysis solution for cell viability and lysis, respectively. Live/Dead™ stain showed high calcein expression ($\geq$ 80 %) across all IOL types with no significant difference in comparison to the tissue culture well (**Fig. 3.7 A**). The presence of $Ti_3C_2T_x$-coating on the IOL' optic showed no significant difference in cell viability or cell lysis relative to the other IOL types and the cell only control.
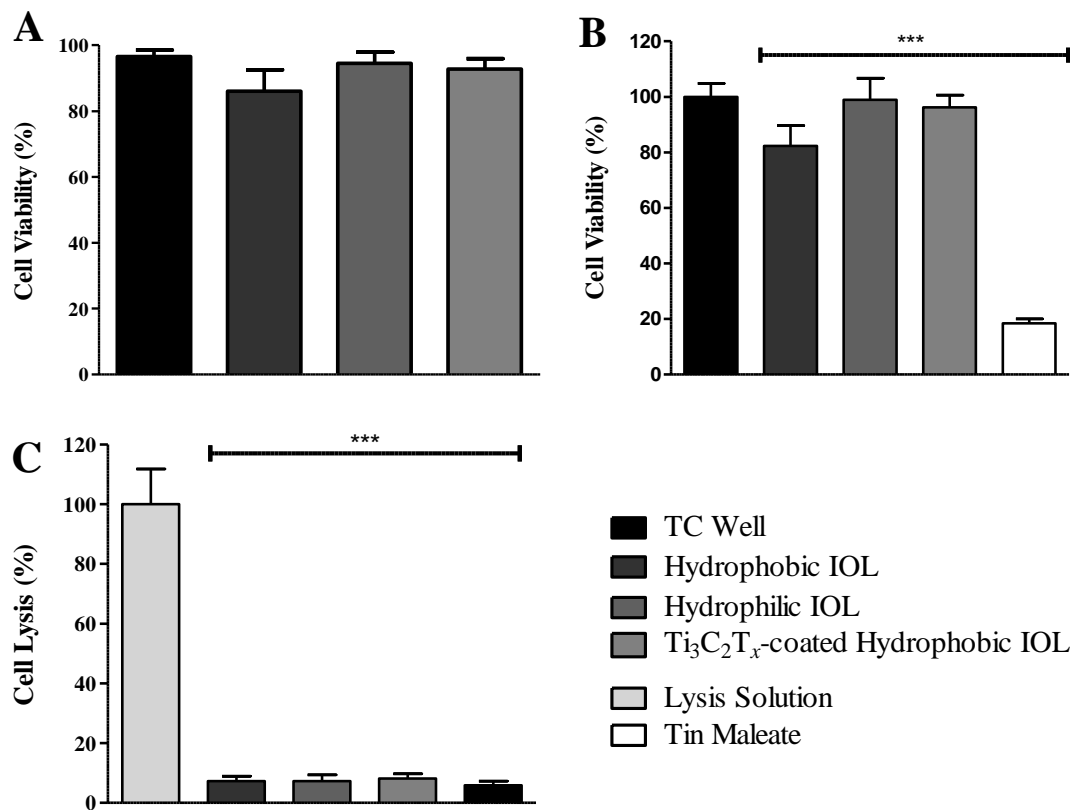
Figure 3.7: Cell compatibility of human lens epithelial (HLE-B3) cells grown on intraocular lens types (Rayner Intraocular Lenses Ltd, UK). Cell viability was quantified using Live/Dead™ (**Fig. 3.7 A**), and MTS (**Fig. 3.7 B**) and cell lysis was quantified using LDH (**Fig. 3.7 C**). Tin maleate and lysis solution were used as a positive control for cell toxicity and lysis. Media background values were subtracted from all conditions. Significance was determined using a one-way

ANOVA and post-hoc Bonferroni's multiple comparison test. ***p ≤ 0.001. (Cell only: cells alone; Lysis solution: cells treated with 10X Lysis Solution; Hydrophobic (RAY800C; Rayner Intraocular Lenses, UK): cells grown on hydrophobic optics; Hydrophilic (RAY600C; Rayner Intraocular Lenses, UK): cells grown on hydrophilic optics; $Ti_3C_2T_x$-coated Hydrophobic: cells grown on $Ti_3C_2T_x$-coated optics; Tin maleate: cells treated with tin maleate) (Mean ± SEM; n=3).

3.3.2 Release of interleukin-6, and -8 by human lens epithelial cells grown on intraocular lens types

$Ti_3C_2T_x$-coated IOLs did not significantly increase pro-inflammatory cytokines relative to the cell only control and other IOL types. (**Fig. 3.8**). There was a low detection of IL-6 and -8 by cells grown on the IOLs and no significant difference between the IOL types. Cells grown on hydrophilic IOLs showed a marked reduction in the release of IL-6 and IL-8. However, this was not statistically significant. The cell only control showed high IL-6 and IL-8 release and was subtracted from the other conditions. Raw data is shown in **Fig. S3**.
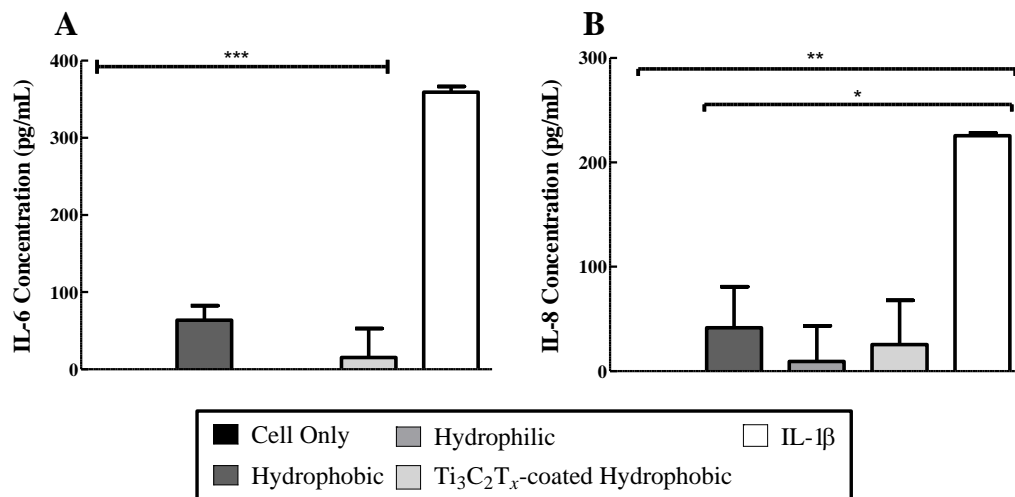
Figure 3.8: Release of pro-inflammatory cytokines by human lens epithelial (HLE-B3) cells grown on intraocular lens types (Rayner Intraocular Lenses Ltd, UK). Release of IL-6 (**Fig. 3.8 A**) and IL-8 (**Fig. 3.8 B**) as quantified by ELISA. Cells were spiked with IL-1β (50 ng mL^{-1}) as a positive control to express IL-6 and IL-8. Cytokine release by cells alone were subtracted from

the other conditions. Significance was determined using a one-way ANOVA and post-hoc Bonferroni's multiple comparison test. *p ≤ 0.05; **p ≤ 0.01; ***p ≤ 0.001. (Cell only: cells alone; Hydrophobic (RAY800C; Rayner Intraocular Lenses, UK): cells grown on hydrophobic optics; Hydrophilic (RAY600C; Rayner Intraocular Lenses, UK): cells grown on hydrophilic optics; $Ti_3C_2T_x$-coated Hydrophobic: cells grown on $Ti_3C_2T_x$-coated optics; IL-1β: cells treated with IL-1β) (Mean ± SEM; n=3).

3.3.3 Optimisation of interleukin-1 beta and -alpha treatment to stimulate interleukin-6, -8 and tumour necrosis factor release by lens epithelial cells

The optimum IL-1β and IL-1α incubation period to induce IL-6, IL-8 and TNF was investigated. HLE-B3 cells required 4-hour and 24-hour stimulation by the pro-inflammatory mediators IL-1β and IL-1α respectively, to express significant concentrations of IL-8 and IL-6 in comparison to the cell only control (**Fig. 3.9**). Cells treated with IL-1β showed a significant upregulation in IL-6 and IL-8 relative to cells treated with IL-1α (p ≤ 0.01, p ≤ 0.001 respectively). The HLE-B3 cells exhibited no release of TNF in response to either of the immunostimulants. In later experiments, HLE-B3 cells were treated for 24-hour prior to sample collection. Cell controls are shown in **Fig. S4**.
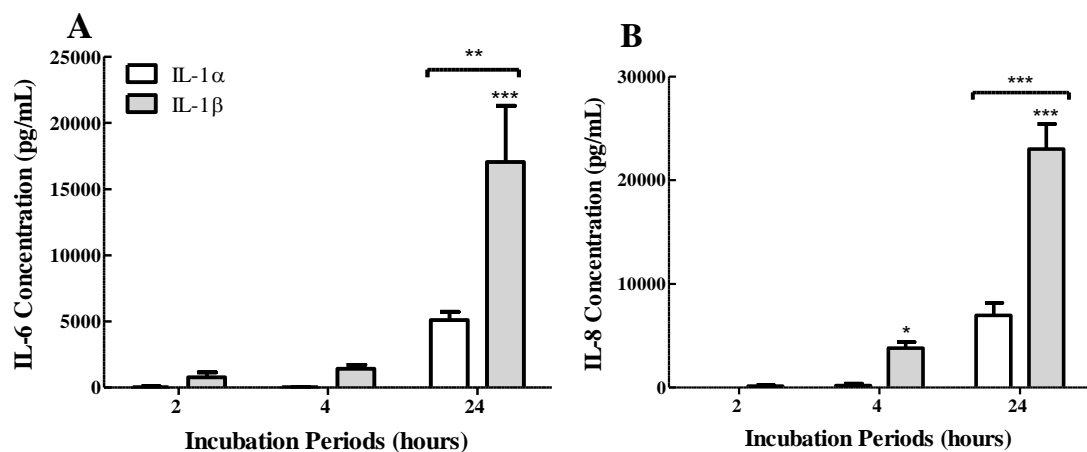
Figure 3.9: Release of pro-inflammatory cytokines by human lens epithelial (HLE-B3) cells after spiking with IL-1α (white) and IL-1β (grey). Release of IL-6 (**Fig. 3.9 A**) and IL-8 (**Fig. 3.9 B**)

as quantified by ELISA. Samples were taken at 2, 4 and 24 hour-periods. Cells treated with IL-1β (50 ng mL^{-1}) and IL-1α (50 ng mL^{-1}) showed significant upregulation in IL-6 and IL-8 after 4 h and 24 h respectively, relative to cells alone ($p \leq 0.001$). Significance was determined using a two-way ANOVA and post-hoc Bonferroni's multiple comparison test. Significance between the cell only (Cell only) and the other conditions are denoted by asterisks directly above the columns. Significance between the other conditions is denoted with a capped line and asterisks between the groups. *$p \leq 0.05$, **$p \leq 0.01$, ***$p \leq 0.001$. (Mean $\pm$ SEM; n=3).

The optimum IL-1β spiking concentration was also determined. Across the three different spiking concentrations, no significant difference in IL-6 production was found (**Fig. 3.10 A**). For IL-8 quantification, 100 ng mL^{-1} IL-1β showed a greater significance difference relative to the cell only ($p \leq 0.01$). Nevertheless, the three concentrations did not significantly differ in their ability to incite IL-8 release (**Fig. 3.10 B**). In future experiments, 50 ng mL^{-1} IL-1β was used to spike the cells for an immunological response.
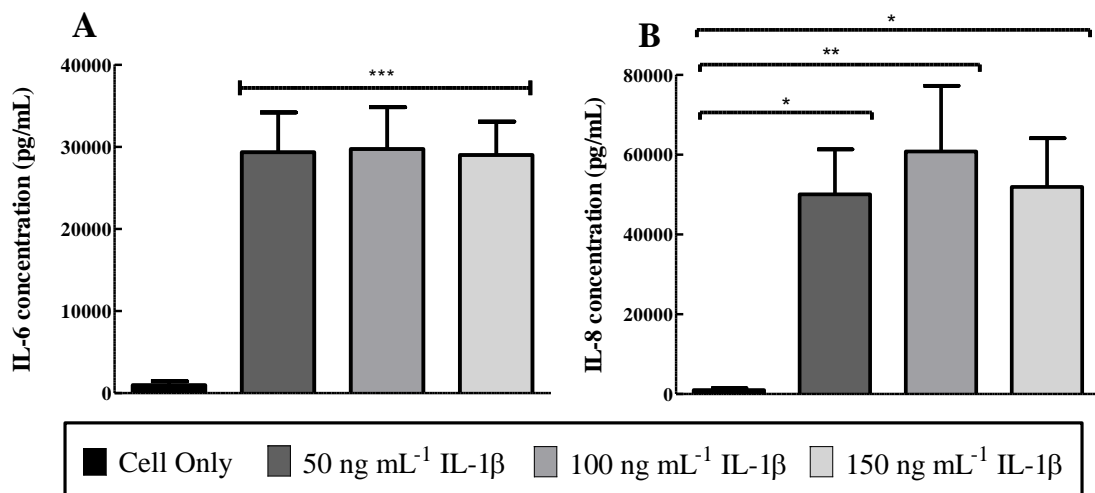
Figure 3.10: Release of pro-inflammatory cytokines by human lens epithelial (HLE-B3) cells after spiking with concentrations of IL-1β. Cells were treated with 50, 100, 150 ng mL^{-1} IL-1β and quantified for IL-6 (**Fig. 3.10 A**) and IL-8 (**Fig. 3.10 B**). Release of pro-inflammatory cytokines did not significantly differ between the different IL-1β spiking concentrations. Significance was determined using a one-way ANOVA and post-hoc Bonferroni's multiple

comparison test. *p ≤ 0.05; *p ≤ 0.01; ***p ≤ 0.001. (Cell only: cells alone; 50 ng mL⁻¹ IL-1β: cells treated with 50 ng mL⁻¹ IL-1β; 100 ng mL⁻¹ IL-1β: cells treated with 100 ng mL⁻¹ IL-1β; 150 ng mL⁻¹ IL-1β: cells treated with 150 ng mL⁻¹ IL-1β) (Mean ± SEM; n=3).

3.3.4 Stimulation of interleukin-1 beta release by human lens epithelial cells

HLE-B3 cells did not express IL-1β without stimulation (**Fig. 3.10**). The induction of IL-1β release was determined. 2-hour treatment of IL-1β was insufficient time to incite significant IL-1β release by the HLE-B3 cells. Cells that were treated for 24 hours with IL-1β showed significant release of IL-1β post-72 and -120 hours (**Fig. 3.11 A**). IL-1α induces release of IL-1β by the HLE-B3 cells after 24-hour stimulation (**Fig. 3.11 B**).
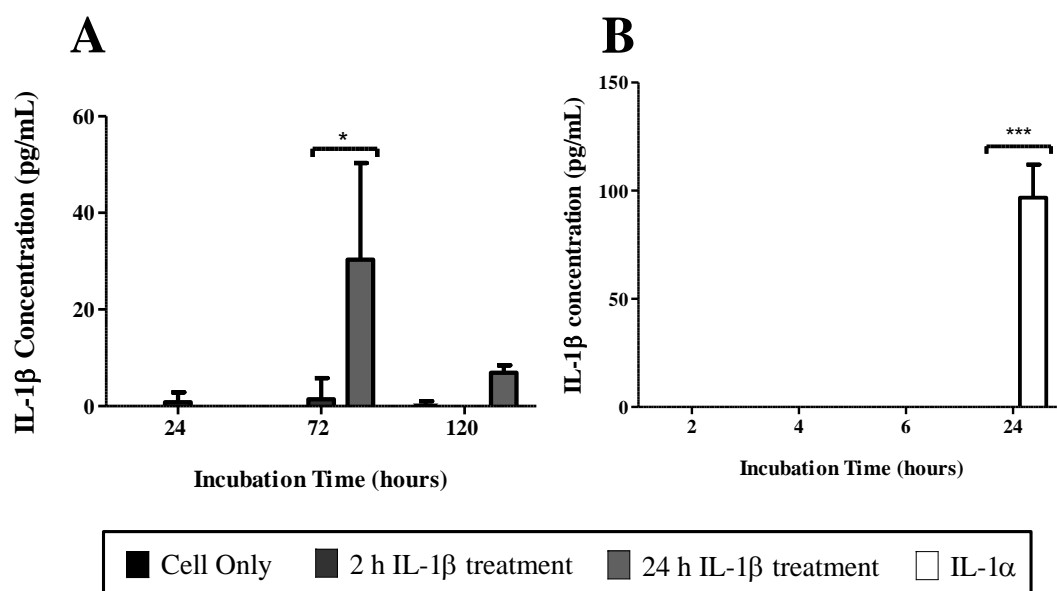
Figure 3.11: Induction of IL-1β release in human lens epithelial HLE-B3 cells by spiking with IL-1β and IL-1α. Cells were pre-treated with IL-1β (50 ng mL⁻¹), washed then quantified for IL-1β release after 24, 72 and 120 h (**Fig. 3.11 A**). Cells treated with IL-1α (50 ng mL⁻¹) showed significant upregulation in release of IL-1β after 24 h (p ≤ 0.001) (**Fig. 3.11 B**). Significance was determined using a two-way ANOVA (**Fig. 3.11 A**) or a one-way ANOVA (**Fig. 3.11 B**) and post-hoc Bonferroni's multiple comparison. *p ≤ 0.05, ***p ≤ 0.001. (Cell only: cells alone; 2 h

IL-1β treatment: cells incubated with IL-1β for 2 h; 24 h IL-1β treatment: cells incubated with IL-1β for 24 h; IL-1α: cells treated with IL-1α) (Mean ± SEM; n=3).

3.3.5 Release of interleukin-6, -8, and -1 beta by human lens epithelial cells spiked with Ti$_3$C$_2$T$_x$ (MXene)

The induction of IL-6, IL-8 and IL-1β by Ti$_3$C$_2$T$_x$ was compared against LPS and IL-1α, established progenitors of IL-6, IL-8 and IL-1β release. Release of IL-6 (**Fig. 3.12 A**) and IL-8 (**Fig. 3.12 B**) was incited by LPS, a bacterial cell membrane protein used to simulate blood-borne infection. Nevertheless, LPS did not induce IL-1β release (**Fig. 3.12 C**) in LECs. IL-1α treatment significantly increased all cytokine production, supporting **Fig. 3.9** and **Fig. 3.11**. IL-1α treatment significantly upregulated IL-6 production relative to cells treated with LPS ($p \leq 0.001$). Cells treated with Ti$_3$C$_2$T$_x$ colloidal solution showed significant reduction in IL-6 and IL-8 release relative to the cell only and positive controls IL-1α and LPS ($p \leq 0.001$). Ti$_3$C$_2$T$_x$ did not incite IL-1β release in HLE-B3 cells.
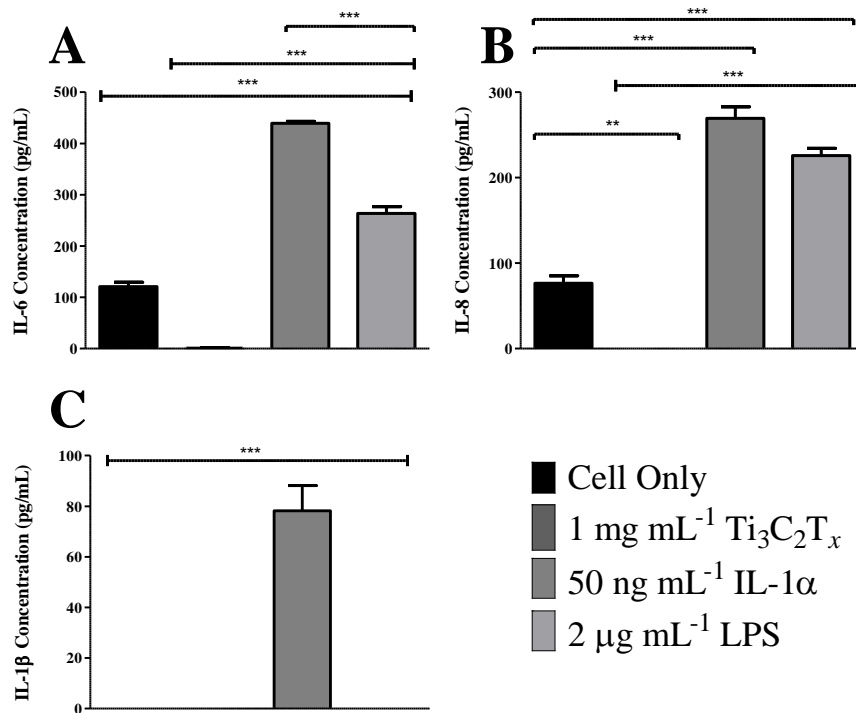
Figure 3.12: Release of pro-inflammatory cytokines by human lens epithelial (HLE-B3) cells after Ti$_3$C$_2$T$_x$ treatment. LPS and IL-1α was used as a positive control for IL-6 (**Fig. 3.12 A**), IL-

8 (**Fig. 3.12 B**), and IL-1β (**Fig. 3.12 C**) release. $Ti_3C_2T_x$ colloidal solution (1 mg mL^{-1}) significantly downregulated IL-6 and IL-8 ($p \leq 0.001$, $p \leq 0.01$ respectively). IL-1α (50 ng mL^{-1}) and LPS (2μg mL^{-1}) significantly upregulated all pro-inflammatory cytokines ($p \leq 0.001$). Significance was determined using a one-way ANOVA and post-hoc Bonferroni's multiple comparison test. **$p \leq 0.01$, ***$p \leq 0.001$. (Cell only: cells alone; $Ti_3C_2T_x$: cells grown on $Ti_3C_2T_x$ coatings; IL-1α: cells treated with IL-1α; LPS: cells incubated with LPS) (Mean ± SEM; n=3).

3.3.6 Release of interleukin-6, and -8 by interleukin-1 beta-primed human lens epithelial cells post-treatment incubated with $Ti_3C_2T_x$ (MXene) solution

Immediately upon adding fresh media or $Ti_3C_2T_x$ colloidal solution, there was low release of IL-6 and IL-8 detected (0 – post). IL-8 release was significantly higher in all cells treated with IL-1β than the cell only control ($p \leq 0.001$). At 1 h $Ti_3C_2T_x$ treatment, cells treated with IL-1β and $Ti_3C_2T_x$ at both concentrations, significantly suppressed IL-6 and -8 release in comparison to the cells primed with IL-1β replaced by fresh media alone ($p \leq 0.001$). This was also found at 2 h (**Fig. 3.13**).
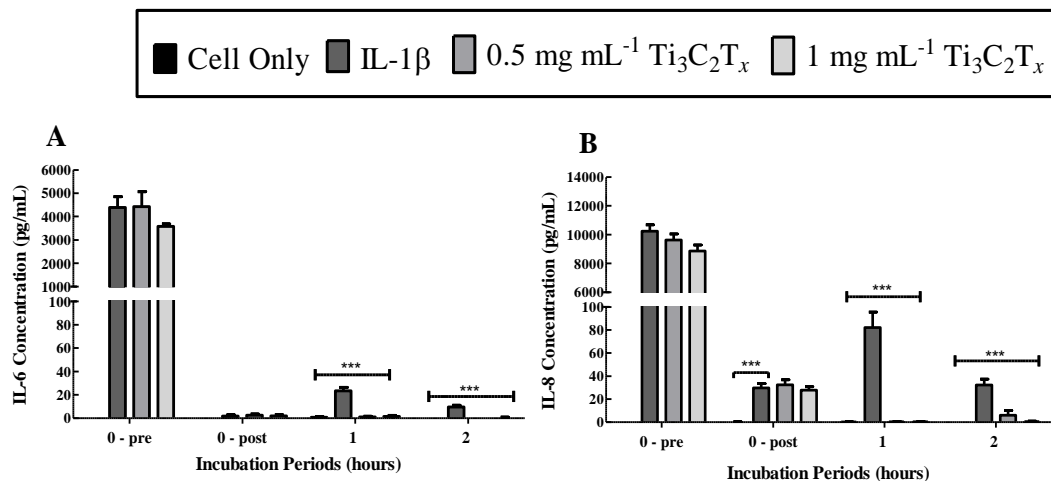
Figure 3.13: Release of pro-inflammatory cytokines by IL-1β-primed human lens epithelial (HLE-B3) cells treated with $Ti_3C_2T_x$. Cells were spiked with IL-1β followed by 0.5 and 1 mg mL^{-1} $Ti_3C_2T_x$. Samples were collected at 24 (0 – pre) and 0 (0 – post), 1 and 2 hours after the wells

were washed and given fresh media. $Ti_3C_2T_x$ significantly suppressed IL-6 and IL-8 release after 1 h incubation ($p \leq 0.001$). Significance was determined using a two-way ANOVA and post-hoc Bonferroni's multiple comparison test. ***$p \leq 0.001$. (Cell only: cells alone; IL-1β: cells treated with IL-1β; 0.5 mg mL^{-1} $Ti_3C_2T_x$ (MXene): cells incubated with 0.5 mg mL^{-1} $Ti_3C_2T_x$ colloidal solution; 1 mg mL^{-1} $Ti_3C_2T_x$ (MXene): cells incubated with 1 mg mL^{-1} $Ti_3C_2T_x$ colloidal solution) (Mean $\pm$ SEM; n=4).

3.3.7 Release of interleukin-6 after incubation with $Ti_3C_2T_x$ (MXene) solution and coatings

PBS spiked with IL-6 and treated with $Ti_3C_2T_x$ solution showed no detection of IL-6 after 24-hour incubation. PBS treated with $Ti_3C_2T_x$ coatings and IL-6 showed no significant downregulation of IL-6. Both $Ti_3C_2T_x$ treatments did not produce or release any IL-6 (**Fig. 3.14**).
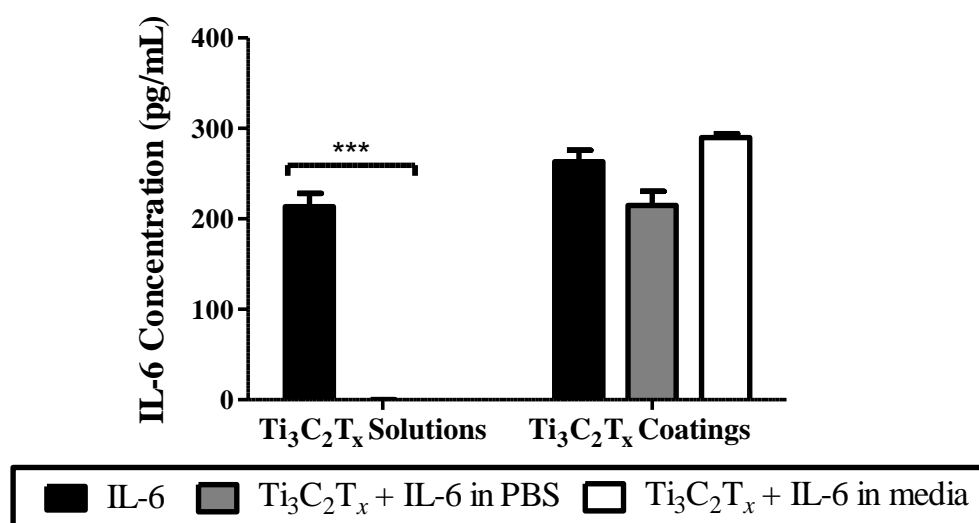
Figure 3.14: Detection of IL-6 in IL-6-spiked PBS or MEM treated with $Ti_3C_2T_x$ solution or coatings. PBS was spiked with IL-6 (1000 pg mL^{-1}) and treated with either $Ti_3C_2T_x$ solution or coatings (5 mg mL^{-1}) to elicit any removal of IL-6 by $Ti_3C_2T_x$. Post-incubation with $Ti_3C_2T_x$ solution, there was no detectable IL-6. Significance was determined using a two-way ANOVA and post-hoc Bonferroni's multiple comparison test. ***$p \leq 0.001$. (IL-6: PBS spiked with IL-6; $Ti_3C_2T_x$ + IL-6 in PBS: PBS spiked with IL-6 incubated with $Ti_3C_2T_x$ solution/coatings; $Ti_3C_2T_x$

+ IL-6 in media: MEM media spiked with IL-6 incubated with $Ti_3C_2T_x$ solution/coatings) (Mean $\pm$ SEM; n=3)

3.3.8 Release of interleukin-6, and -1 beta by interleukin-1 beta-primed human lens epithelial cells post-treatment with $Ti_3C_2T_x$ (MXene) coatings

The cell only control and cells treated with $Ti_3C_2T_x$ coatings showed low IL-6 and IL-1β release. Cells treated with IL-1β showed a significant upregulation in IL-1β and IL-6 ($p \leq 0.001$). Cells treated with $Ti_3C_2T_x$ and IL-1β showed reduced IL-1β and IL-6 release, although only a significant reduction in IL-1β was found ($p \leq 0.05$) (**Fig. 3.15**).
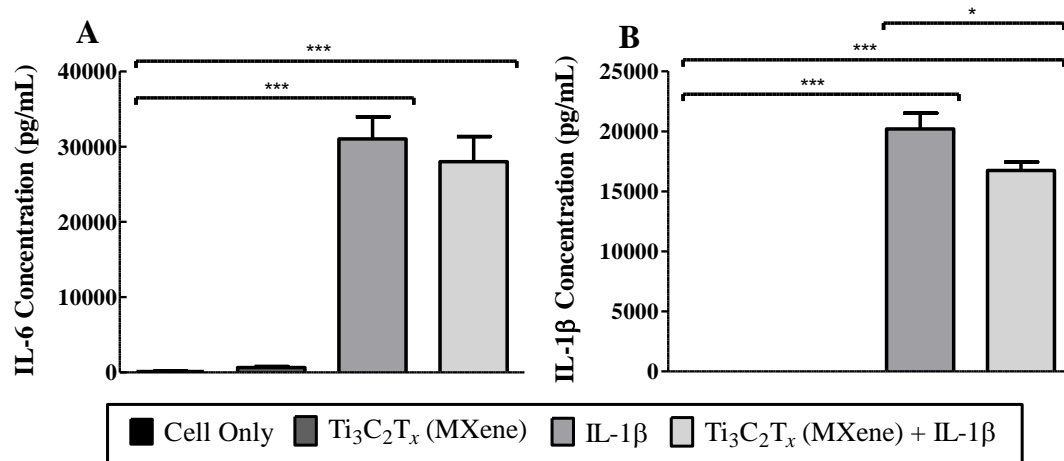
Figure 3.15: Release of pro-inflammatory cytokines by human lens epithelial (HLE-B3) cells grown on $Ti_3C_2T_x$ coatings. Release of IL-6 (**Fig. 3.15 A**) and IL-1β (**Fig. 3.15 B**) was quantified by ELISA. IL-1β (50 ng mL^{-1}) was used to prime the cells to induce an inflammatory response as a positive inflammation control and as a treatment with $Ti_3C_2T_x$ (5 mg mL^{-1}) to elicit any suppression of cytokine release by $Ti_3C_2T_x$. IL-1β-treated media background values were subtracted from all conditions. Significance was determined using a one-way ANOVA and post-hoc Bonferroni's multiple comparison test. *p $\leq$0.05, ***p $\leq$ 0.001. (Cell only: cells alone; $Ti_3C_2T_x$ (MXene): cells grown on $Ti_3C_2T_x$ coatings; IL-1β: cells treated with IL-1β; $Ti_3C_2T_x$ (MXene) + IL-1β: cells grown on $Ti_3C_2T_x$ coatings treated with IL-1β) (Mean $\pm$ SEM; n=3)

3.3.9 Upregulation in gene fold change of interleukin-6, -1 beta and CXCL1 in interleukin-1 beta-primed human lens epithelial cells with $Ti_3C_2T_x$ (MXene) coatings

CXCL1, IL-6 and *IL-8* gene fold expression of cells grown on $Ti_3C_2T_x$ coatings were quantified for comparison to protein expression shown in **Fig. 3.15**. *CXCL1* is an innate immune response gene which was highly upregulated in mice LEC PCS (109). HLE-B3 cells showed good amplification of the housekeeping gene β-actin. $Ti_3C_2T_x$ did not significantly alter any of the three genes' expression relative to the cell only control. A 3152-fold change of *CXCL1* (**Fig. 3.16 A**), 307-fold change of *IL-6* (**Fig. 3.16 B**) and 2002-fold change of *IL-1β* (**Fig. 3.16 C**) in cells treated with IL-1β. Cells treated with $Ti_3C_2T_x$ and IL-1β showed a reduction in fold change across all the genes however, there was only a significant reduction in *IL-1β* expression, similar to the cytokine expression showed in ELISA analysis (*$p \leq 0.05$) (**Fig. 3.15**). RNA extraction of each technical repeat for each experimental repeat, delta-delta Ct and optimisation and standard curve of cDNA volume against housekeeping gene, β-actin is reported in **Fig. S5, 6** and **7**.
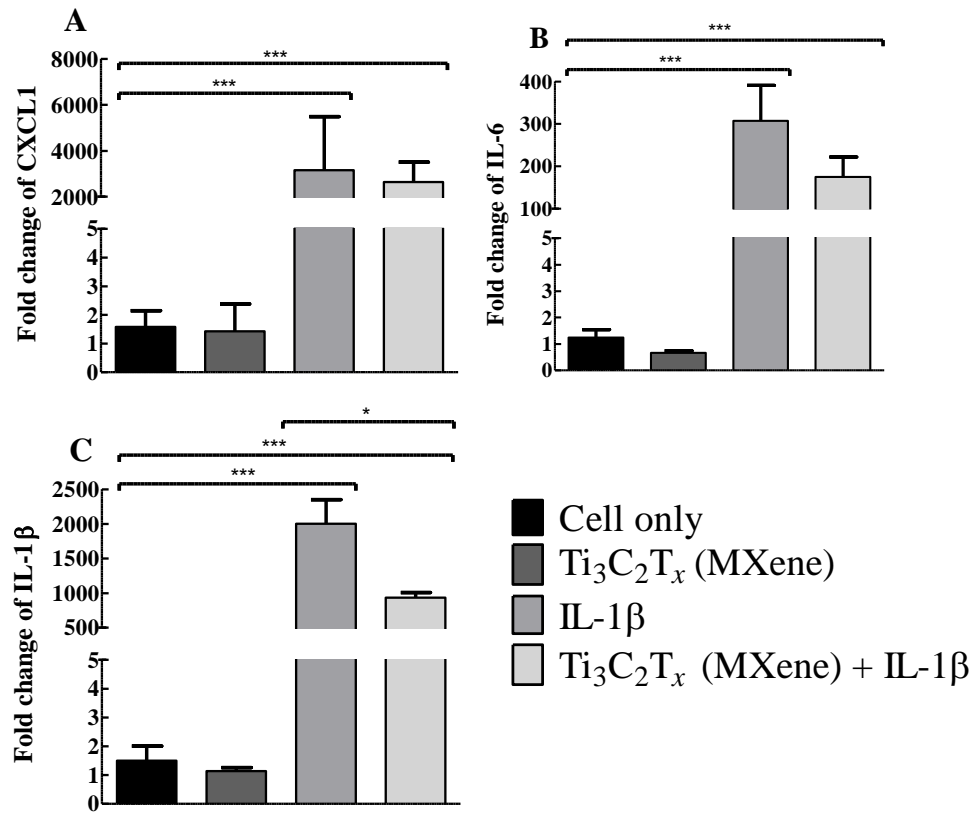
Figure 3.16: Expression of IL-1β, IL-6 and chemokine CXCL1 by human lens epithelial (HLE-B3) cells grown on $Ti_3C_2T_x$ coatings. rt-PCR amplification of *CXCL1* (**Fig. 3.16 A**), *IL-6* (**Fig. 3.16 B**) and IL-1β (**Fig. 3.16 C**) expression in cell only, $Ti_3C_2T_x$ and IL-1β samples. IL-1β was used to prime the cells to induce an inflammatory response as a positive inflammation control and as a treatment with $Ti_3C_2T_x$ to elicit any suppression of cytokine expression by $Ti_3C_2T_x$. Significance was determined using unpaired two-tailed t tests and F-tests for comparison of variance was used. $*p \leq 0.05$, $***p \leq 0.001$. (Cell only: cells alone; $Ti_3C_2T_x$ (MXene): cells grown on $Ti_3C_2T_x$ coatings; IL-1β: cells treated with IL-1β; $Ti_3C_2T_x$ (MXene) + IL-1β: cells grown on $Ti_3C_2T_x$ coatings treated with IL-1β) (Fold change ± SEM; n=5)

3.3.10 Migration of human lens epithelial cells grown on $Ti_3C_2T_x$ (MXene) coatings

The scratch assay was used to assess if the presence of $Ti_3C_2T_x$ coatings over the optic could increase PCO development by promoting cell migration across the optic. This method was

exploited to determine the migration rate of HLE-B3 cells across $Ti_3C_2T_x$-coated tissue culture wells in comparison to uncoated tissue culture wells. Cells grown on $Ti_3C_2T_x$-coated wells showed significant reduction in scratch width and total wound area from 24 and 48 hours, respectively (**Fig. 3.17 A, B**). A significant increased rate of wound closure was seen from 72 hours (**Fig. 3.17 C**). Time lapse light microscope images of stained scratches were taken of uncoated (**Fig. 3.17 D, F**) and $Ti_3C_2T_x$-coated wells (**Fig. 3.17 E, G**) at time of scratch (0 h) and end point (120 h).
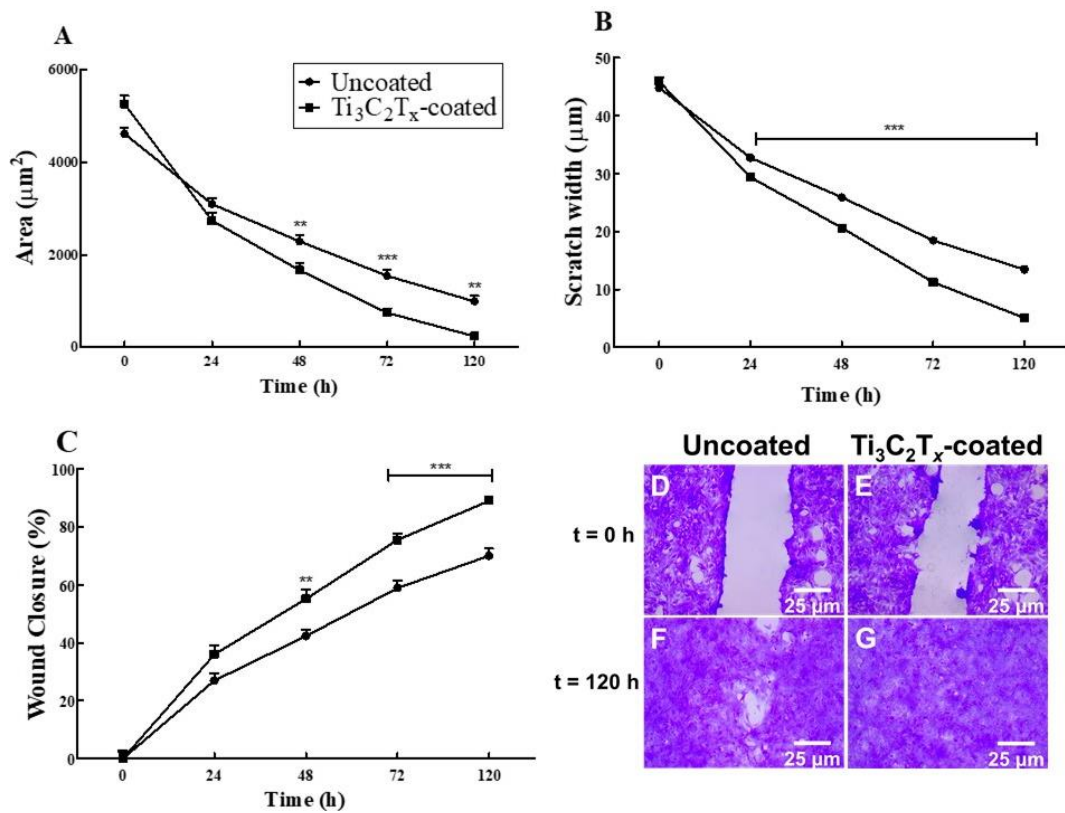
Figure 3.17: Human lens epithelial (HLE-B3) cells grown on uncoated and $Ti_3C_2T_x$-coated tissue grade 12-well plates. Wound area (**Fig. 3.17 A**), scratch width (**Fig. 3.17 B**) and wound closure (**Fig. 3.17 C**) was quantified using light microscope images taken at the selected time points. Light microscope images of HLE-B3 cells grown on uncoated (**Fig. 3.17 D, F**) and $Ti_3C_2T_x$-coated (**Fig. 3.17 E, G**) stained with crystal violet at t = 0 h (top) and t = 120 h (bottom). x50 magnification by light microscope (Zeiss Primovert HDcam, Germany). Scale bar: 25 µM. Measurements were calculated using Fiji Image J. Wound closure was calculated as the width

86

difference in the scratch across the cell monolayer at t = 0 h relative to the other time points. A two-way ANOVA was completed using GraphPad Prism 5. **p<0.01; ***p<0.001. (Uncoated: cells grown on tissue culture well; $Ti_3C_2T_x$-coated: cells grown on $Ti_3C_2T_x$-coated wells) (Mean ± SEM; n=6)

3.3.11 Expression of EMT markers in human lens epithelial cells grown on $Ti_3C_2T_x$ (MXene) coatings quantified by immunocytochemistry

FHL124 cells without treatment showed limited fluorescence for all three markers (**Fig. 3.18 A, E, I**). $Ti_3C_2T_x$ treatment alone did not upregulate EMT marker expression indicating no tendency to promote EMT (**Fig. 3.18 B, F, J**). TGF-β2 was used to prime the LEC to undergo myofibroblast differentiation. Cells exposed to TGF-β2 showed morphological changes, changing from rounded clusters of cells to elongated branch-like structures (**Fig. 3.18 C, G**). Intensity of α-SMA, SMAD2/3 and vimentin staining were increased in cells treated with TGF-β2 (**Fig. 3.18 C, G, K**). Following quantification of antibody staining using ImageJ, a significant reduction in vimentin expression was found (p ≤ 0.01) (**Fig. 3.18 N**) and a marked but not statistically significant reduction in α-SMA and SMAD2/3 expression was found in cells treated with $Ti_3C_2T_x$ and TGF-β2 compared to the TGF-β2 stimulated control (**Fig. 3.18 M, O**). No significant difference in cell number was found between control and treated conditions as quantified by DAPI stain (**Fig. 3.19**).
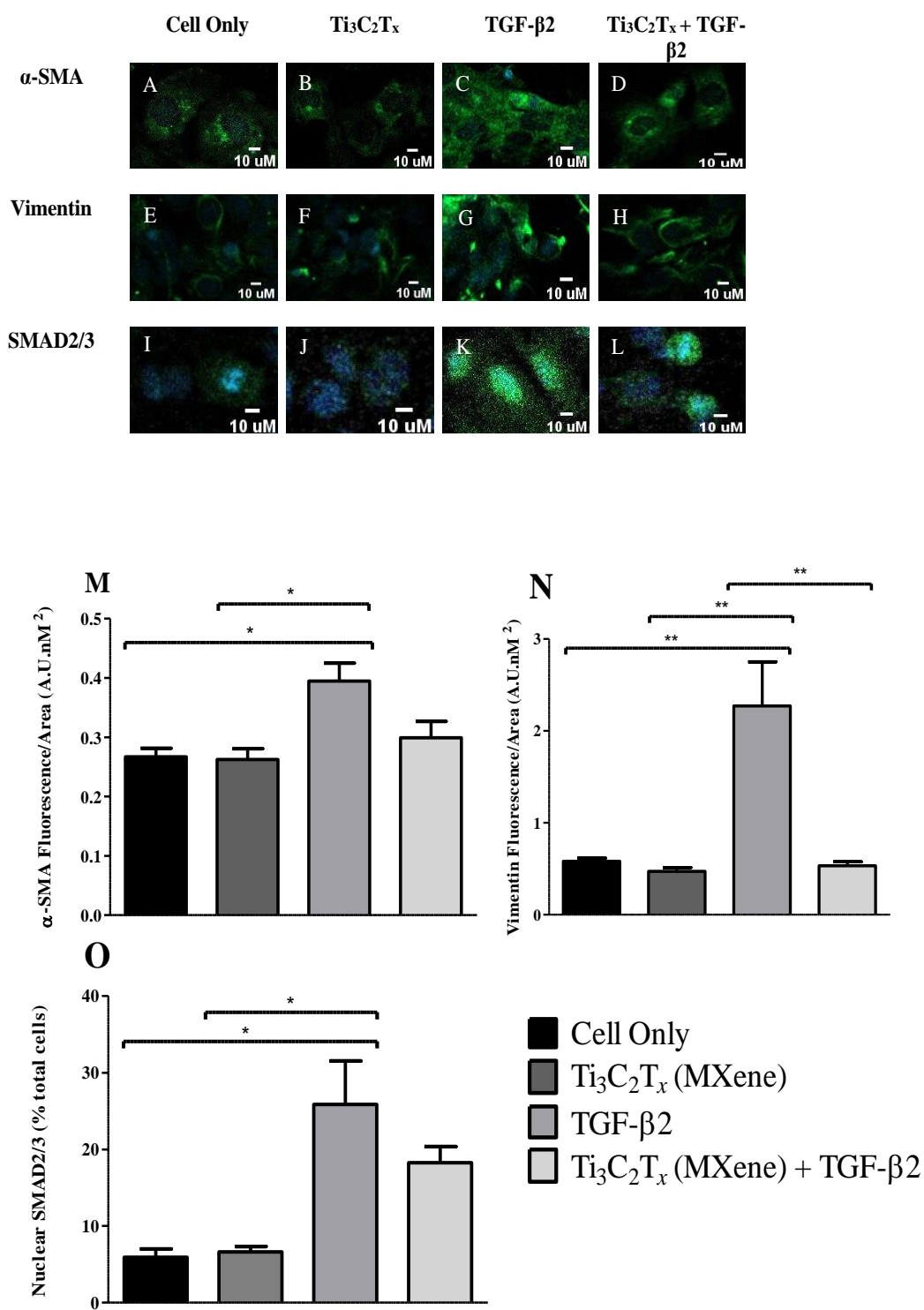
Figure 3.18: Alpha smooth muscle (α-SMA), vimentin and SMAD2/3 stain of FHL124 cells treated with 2 mg mL^{-1} Ti$_3$C$_2$T$_x$ and TGF-β2 quantified by immunocytochemistry. Expression of α-SMA by cell only (**Fig. 3.18 A**), cells with Ti$_3$C$_2$T$_x$ (**Fig. 3.18 B**), cells with TGF-β2 (**Fig. 3.18 C**) and cells with TGF-β2 and Ti$_3$C$_2$T$_x$ (**Fig. 3.18 D**). Expression of vimentin by cell only (**Fig.**

3.18 E), cells with $Ti_3C_2T_x$ (**Fig. 3.18 F**), cells with TGF-β2 (**Fig. 3.18 G**) and cells with TGF-β2 and $Ti_3C_2T_x$ (**Fig. 3.18 H**). Expression of SMAD2/3 by cell only (**Fig. 3.18 I**), cells with $Ti_3C_2T_x$ (**Fig. 3.18 J**), cells with TGF-β2 (**Fig. 3.18 K**) and cells with TGF-β2 and $Ti_3C_2T_x$ (**Fig. 3.18 L**). Images were quantified using Fiji: Image J by the fluorescence of each protein across the area of the cell sample for α-SMA (**Fig. 3.18 M**) and vimentin (**Fig. 3.18 N**). SMAD2/3 nuclei stain was normalised across the conditions against the DAPI cell count (**Fig. 3.18 O**). Cells were primed with TGF-β2 as a positive control for mesenchymal differentiation. A one-way ANOVA and Bonferroni's multiple comparison test was completed using GraphPad Prism 5. $*p \geq 0.05$, $**p \geq 0.01$. (Cell only: cells alone; $Ti_3C_2T_x$ (MXene): cells grown on $Ti_3C_2T_x$ coatings; TGF-β2: cells treated with TGF-β2; $Ti_3C_2T_x$ (MXene) + TGF-β2: cells grown on $Ti_3C_2T_x$ coatings treated with TGF-β2) (Mean ± SEM; n=3)
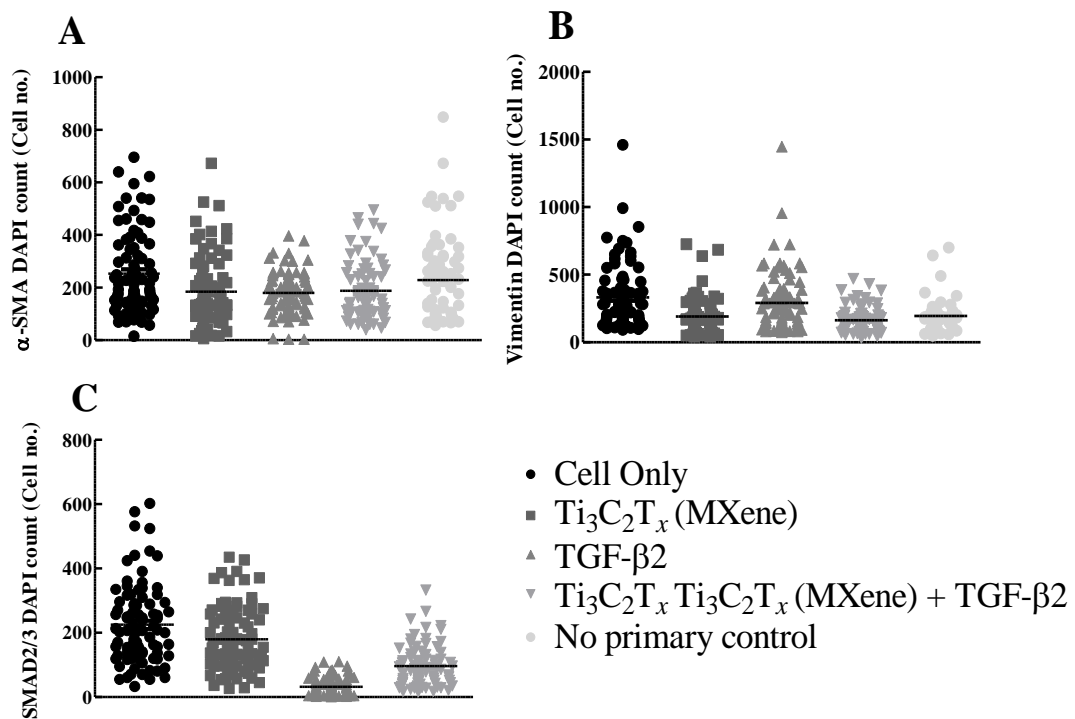
Figure 3.19: DAPI normalisation count of control and treated conditions in immunocytochemistry. Cell number was quantified by DAPI nuclei stain using Fiji Image J. Cell number was not significantly different between the cell control and cells treated with $Ti_3C_2T_x$ or TGF-β2 for α-SMA (**Fig. 3.19 A**), vimentin (**Fig. 3.19 B**) and SMAD2/3 (**Fig. 3.19 C**) (n=3).

3.3.12 Expression of EMT markers in human lens epithelial cells grown on $Ti_3C_2T_x$ (MXene) coatings quantified by western blot analysis

Western blot analysis found the cell control showed low expression of α-SMA, vimentin and SMAD2/3 normalised to its actin expression. Cells treated with $Ti_3C_2T_x$ did not show a significant change in protein expression. TGF-β2 showed a significant increase in the EMT markers, mirroring the immunocytochemistry analysis (**Fig. 3.20**). No significant difference in α-SMA and SMAD2/3 expression was found in cells treated with TGF-β2 and $Ti_3C_2T_x$. However, protein expression of vimentin was significantly downregulated in cells treated with TGF-β2 and $Ti_3C_2T_x$ ($p \leq 0.05$), similar to **Fig. 3.18**.
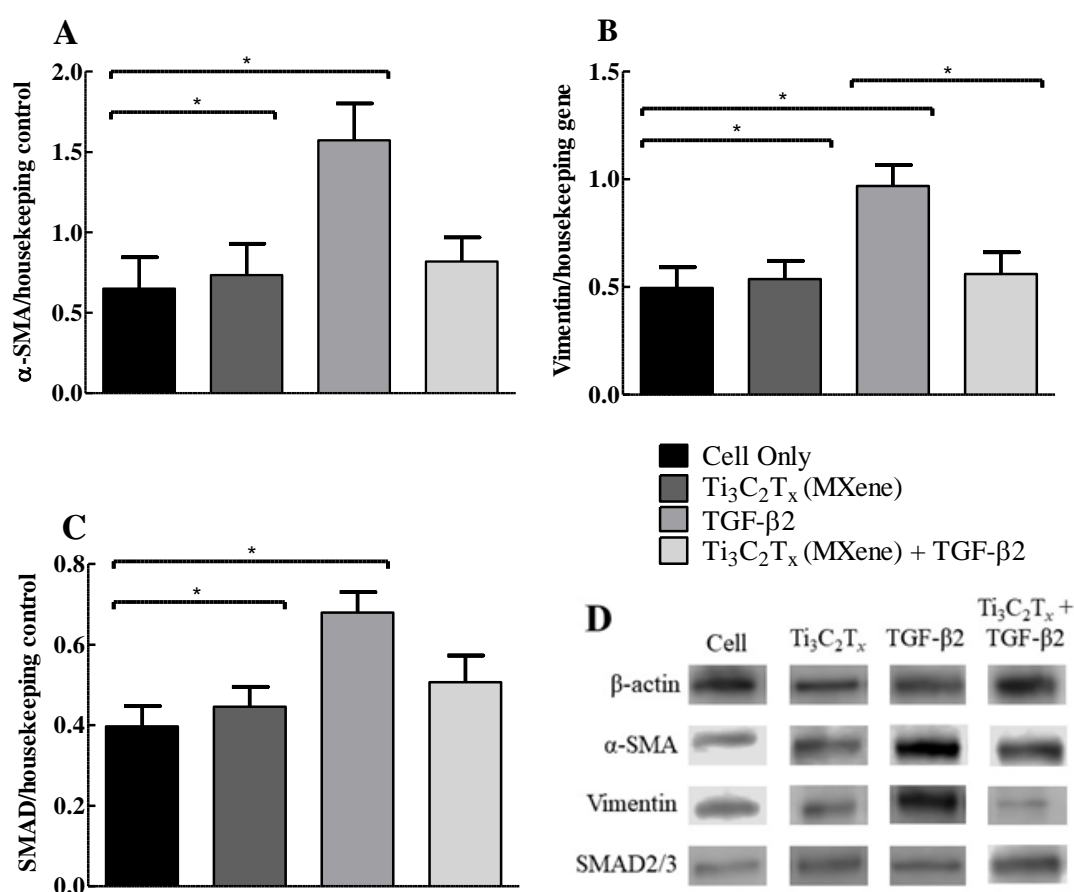
Figure 3.20: Western blot analysis for the expression of α-SMA, vimentin and SMAD in FHL124 cells treated with 2 mg mL^{-1} $Ti_3C_2T_x$. Net protein expression of α-SMA (**Fig. 3.20 A**), vimentin (**Fig. 3.20 B**) and SMAD (**Fig. 3.20 C**). was normalised and quantified as ratio to its beta-actin

(β-actin) expression. Images of the visualised protein bands (20 µG) in each of the control and treatment groups against their beta-actin (β-actin) expression (**Fig. 3.20 D**). TGF-β2 was used as a positive control for epithelial-mesenchymal transition. A one-way ANOVA and Bonferroni's multiple comparison test was conducted using GraphPad Prism 5. *p ≥ 0.05. (Cell only: cells alone; $Ti_3C_2T_x$ (MXene): cells grown on $Ti_3C_2T_x$ coatings; TGF-β2: cells treated with TGF-β2; $Ti_3C_2T_x$ (MXene) + TGF-β2: cells grown on $Ti_3C_2T_x$ coatings treated with TGF-β2) (Mean ± SEM; n=5).

Table 3.2: Chapter 3 experiments with experimental conditions and summary of data. LEC: lens epithelial cells; IL: interleukin; PBS: phosphate buffer saline; EMT: epithelial-mesenchymal transition.

Experiment no.	$Ti_3C_2T_x$ properties ($mg\ ml^{-1}$)	Cell type	Experiment type	Description of data
3.3.1	Coatings 0.18	HLE-B3	Live/Dead™; MTS; LDH	$Ti_3C_2T_x$ did not significantly impact LEC viability
3.3.2	Coatings 0.18	HLE-B3	ELISA	$Ti_3C_2T_x$ did not significantly upregulate IL-6 and IL-8 release from LEC
3.3.3	n/a	HLE-B3	ELISA	IL-1α and IL-1β treatment induces IL-6 and IL-8 release from LEC relative to cell control. IL-1β significantly increases IL-6 and IL-8 release in LECs relative to IL-1α. A treatment of IL-1β at 50 ng mL^{-1} for 24 hours is sufficient to induce a pro-inflammatory state in the LECs.
3.3.4	n/a	HLE-B3	ELISA	Untreated LECs do not express IL-1β. IL-1β can significantly induce release of IL-1β by LECs. IL-1α (50 ng mL^{-1}) can significantly upregulate IL-1β release after 24 hours.

3.3.5	Solution 1	HLE-B3	ELISA	$Ti_3C_2T_x$ did not significantly upregulate IL-6, IL-8 or IL-1β release in LEC. Positive controls IL-1α and LPS upregulated IL-6 and IL-8 release. Only IL-1α upregulated IL-1β release from LECs.
3.3.6	Solution 0.5, 1	HLE-B3	ELISA	IL-1β-primed cells upregulated IL-8 and IL-6 release which was significantly repressed after 1-hour incubation with $Ti_3C_2T_x$
3.3.7	Coatings, solution 5	n/a	ELISA	$Ti_3C_2T_x$ solution removed all IL-6 from both the PBS and media sample. $Ti_3C_2T_x$ coatings did not significantly remove IL-6 from either conditions. The slight reduction in IL-6 shown in the PBS condition was negated in the media condition, suggesting $Ti_3C_2T_x$ will bind proteins non-specifically.
3.3.8	Coatings 5	HLE-B3	ELISA	IL-1β significantly upregulated IL-6 and IL-1β release from LECs. LECs treated with IL-1β and $Ti_3C_2T_x$ showed a marked reduction in IL-6 release and a significant downregulation in IL-1β release.
3.3.9	Coatings 5	HLE-B3	qPCR	IL-1β significantly upregulated *IL-6* and *IL-1β* gene fold expression from LECs. LECs treated with IL-1β and $Ti_3C_2T_x$ showed a marked reduction in *IL-6* and *CXCL1* gene fold expression and a significant downregulation in *IL-1β* gene fold expression.

3.3.10	Coatings 2	HLE-B3	Scratch	$Ti_3C_2T_x$ significantly increased LEC wound closure rates, from 48 hours post-scratch.
3.3.11 3.3.12	Coatings 2	FHL124	Immunocyto-chemistry Western blots	$Ti_3C_2T_x$ did not significantly upregulate EMT markers. TGF-β2 significantly increased the expression of all EMT markers. $Ti_3C_2T_x$ significantly downregulated the expression of vimentin in TGF-β2-treated LECs.

3.4   Discussion

This chapter investigated the impact of $Ti_3C_2T_x$ on the wound healing response of residual LEC contributing to the development of PCO. This was achieved by focusing on the two fundamental intracellular pathways leading to PCO formation, hyperinflammation and EMT. This chapter has shown no significance difference between hydrophobic, hydrophilic and $Ti_3C_2T_x$-coated hydrophobic IOLs in ability to induce cell toxicity or inflammation. This chapter established a cell-based model of the cytokine-induced inflammation pathway-initiated PCS, aiming to investigate the impact of $Ti_3C_2T_x$ on suppressing the upregulation of pro-inflammatory cytokines and genes by HLE-B3 cells. $Ti_3C_2T_x$ significantly repressed IL-1β and markedly reduced IL-6 release and expression at protein and gene level. A reduction in the chemokine *CXCL1* gene was also observed when pro-inflamed cells were treated with $Ti_3C_2T_x$. Relative to the cells undergoing EMT upon treatment with TGF-β2, cells treated with $Ti_3C_2T_x$ did not significantly upregulate their expression of vimentin, α-SMA or SMAD2/3 proteins. Indeed, cells treated with $Ti_3C_2T_x$ and TGF-β2 showed a significant reduction in vimentin filament abundance. This work shows $Ti_3C_2T_x$ may promote a positive resolution of the LEC wound healing response by suppressing pro-inflammatory cytokines, supporting cell growth and adhesion whilst preventing overexpression of cytoskeletal filaments involved in EMT.

The impact of IOL base material on cell viability and propensity to inflammation has yet to be explored despite several studies reporting the great influence that IOL base material has on PCO rates (94,191,192). This chapter has shown that IOL base material and the presence of $Ti_3C_2T_x$ coatings on the optic have no impact on cell viability and cytokine production. Although cell viability was lower for hydrophobic acrylic IOLs (82.35 %) than hydrophilic acrylic IOLs (99 %), this was not significant and cell growth over the optic was not noted to be different across the two IOL types (p ≥ 0.05) **(Fig. 3.7)**. The presence of $Ti_3C_2T_x$ coatings on hydrophobic acrylic IOLs had a 96.3 % cell survival. This trend matches the contact angle analysis of the three IOL types (**Chapter 2.3.7**) and provides evidence indicating that the presence of $Ti_3C_2T_x$ coatings on

hydrophobic IOLs increases wettability. Consequently, $Ti_3C_2T_x$ coatings may increase the propensity of residual LECs in the capsule bag to settle over the optic which may be expected from its hydrophilic nature. However, as these results found no significance in loss of cell viability across the IOL types, it can be suggested that the presence of $Ti_3C_2T_x$ will not greatly increase propensity towards PCO development relative to the other IOL materials. Additionally, ELISA immunoassay analysis showed that IOL material did not significantly impact LEC release of IL-6 and IL-8 (**Fig. 3.8**). Once more, hydrophobic acrylic IOLs showed higher release of IL-6 (65 pg mL^{-1}) and IL-8 (42 pg mL^{-1}) which could be induced by the relative hydrophobic surface causing stress-induced inflammation to the adhered cells. $Ti_3C_2T_x$ coatings on hydrophobic IOLs reduced cytokine release to 16 pg mL^{-1} and 26 pg mL^{-1} for IL-6 and IL-8, respectively. This follows the trend seen in the viability of cells grown on hydrophobic and $Ti_3C_2T_x$-coated hydrophobic IOLs, supporting the hypothesis that $Ti_3C_2T_x$ increases the hydrophilicity of the hydrophobic optic surface, allowing for greater viability and reduced inflammatory response in LECs.

To mimic *in vitro* cytokine-induced inflammatory pathways, LPS has been used as a model for neuroinflammation, cornea and DED, retinal dystrophy and endotoxin-induced uveitis (193–195). Nevertheless, as LPS is used to model blood-borne infections, LPS may not be a suitable in an ocular model of inflammation and wound healing (196). Nishi et al., (119) found rabbits treated with human recombinant IL-1 receptor antagonist (IL-1ra) during phacoemulsification had reduced intensity in aqueous flare and fibrin deposition relative to the control rabbits, suggesting IL-1 plays a role in surgically-induced inflammation. Moreover, Planck et al., (158) showed human retinal pigment epithelial cells synthesised IL-1β on exposure to IL-1α. Therefore, IL-1α and IL-1β were investigated for their ability to induce release of pro-inflammatory cytokines IL-6, IL-8 and TNF in LECs. Both IL-1 cytokines induced IL-6 and IL-8 release (**Fig. 3.9**). IL-1β incited a significantly greater release of pro-inflammatory cytokines relative to IL-1α ($p \leq 0.01$). This may be as a result of the role of IL-1β in promoting a cascade of inflammatory pathways on release relative to its progenitor giving it greater potency (111). These results

support those found in the literature and confirmed the use of IL-1 as an appropriate immunostimulant to incite IL-6 and IL-8 release by LEC in this body of work. IL-1β was selected rather than IL-1α due to the significantly greater upregulation of IL-6 and IL-8 production, ensuring a significant response in the positive control (**Fig. 3.9**). Optimisation of incubation time and dose indicated that a dose of 50 ng mL^{-1} over 24 hours induced the greatest cytokine response by the LECs and any further uses of IL-1β was applied under these conditions (**Fig. 3.10**). TNF was not expressed by HLE-B3 cells alone or by IL-1β-treated cells and was not investigated further within this study. This was in contrast to the literature (197).

Upon spiking with IL-1β, HLE-B3 cells began to express IL-1β, potentially as a result of autocrine signalling which then provided a positive feedback mechanism to amplify IL-1β release and potentially upregulate inflammation pathways (**Fig. 3.11 A**). This is supported by Eskan et al., (169), who found that IL-1β promoted inflammation in human gingival epithelial cells by autocrine signalling. Moreover, these results showed that HLE-B3 cells treated with IL-1α expressed low levels of IL-1β, supporting literature (158,159,163) (**Fig. 3.11 B**). This IL-1-induced inflammation pathway provides a model whereby the effect of $Ti_3C_2T_x$ can be investigated.

MXene is a relatively new biomaterial and therefore studies investigating the impact of $Ti_3C_2T_x$ on inflammatory and EMT associated genetic expression profile are limited. The impact of $Ti_3C_2T_x$ on cytokine-induced inflammation has been explored by Ward et al., (14) and Ozulumba et al., (64). Ozulumba et al., (64) showed ML and DL $Ti_3C_2T_x$ (12.5 mg) did not induce IL-6, IL-8 or TNF release by THP-1 monocytes which was supported by Ward et al., (14) who found similar results on incubating THP-1 monocytes with $Ti_3C_2T_x$ coated hydrophobic acrylate IOLs. Building on these studies, this body of work investigated IL-6, IL-8 and TNF release by HLE-B3 cells when incubated with $Ti_3C_2T_x$ colloidal solution and coatings in order to investigate any impact by $Ti_3C_2T_x$ on PCO associated hyperinflammation pathways. ELISA analysis found HLE-B3 cells incubated with $Ti_3C_2T_x$ colloidal solution did not incite release of IL-6, IL-8 or IL-1β relative to the positive pro-inflammatory controls IL-1α and LPS (**Fig. 3.12**). Indeed, the

presence of $Ti_3C_2T_x$ completely suppressed all IL-6 and IL-8 release relative to the cell control (p ≤ 0.01, p ≤ 0.001 respectively) (**Fig. 3.12**). LPS did not induce release of IL-1β by HLE-B3 cells (**Fig. 3.12**). LPS is an endotoxin that induces inflammation and IL-1β release in monocytes (198). Xie et al., (199) showed that LPS/ATP treatment on murine macrophages triggered IL-1β release. However, in intestinal epithelial cells LPS did not induce IL-1β mRNA (200). This suggests that LPS may not play a role in IL-1β release in epithelial cell lines.

This suppressive action by $Ti_3C_2T_x$ was also found in IL-1β-stimulated cells where complete cytokine suppression occurred after 1-hour incubation with $Ti_3C_2T_x$ colloidal solution (**Fig. 3.13**). The results indicate that $Ti_3C_2T_x$ does not instigate upregulation of pro-inflammatory cytokine production and that in IL-1β stimulated cells, as would occur on activation of the inflammatory response during wound healing following surgical IOL implantation, suppression of inflammatory cytokine occurs. Potential mechanisms by which down regulation of inflammatory cytokine release by LECs may occur include the selective binding of $Ti_3C_2T_x$ with cell membrane receptors, blocking the activation of IL-6 and IL-8 release or the direct absorption of these cytokines by $Ti_3C_2T_x$ surface groups, 'trapping' them. MXene can easily intercalate organic molecules due to its hydrophilic properties and high negative zeta potential (201). Absorbance of cytokines by $Ti_3C_2T_x$ was determined by measuring IL-6 concentration with and without treatment with both $Ti_3C_2T_x$ coatings and solution. $Ti_3C_2T_x$ colloidal solution removed all IL-6 within the PBS after 24-hour incubation (**Fig. 3.14**). There was no significant reduction in IL-6 concentration in PBS incubated with $Ti_3C_2T_x$ coatings. This suggests that the surface contact of $Ti_3C_2T_x$ available to the cytokines impacts adsorption of IL-6 as when $Ti_3C_2T_x$ coatings are applied, there is a significant reduction in efficacy to remove cytokines. Additionally, when this experiment was repeated using culture media, the slight reduction in IL-6 concentration was lost. This suggests that the proteins within the media out-competed the binding of IL-6 to $Ti_3C_2T_x$ and that any removal of cytokines by $Ti_3C_2T_x$ may be due to non-specific binding of the cytokines to $Ti_3C_2T_x$. Moreover, as $Ti_3C_2T_x$ coatings did not significantly remove IL-6 from PBS or MEM but did significantly reduce IL-6 release in LEC, it can be suggested that $Ti_3C_2T_x$ coatings may

be also interacting with the cells' receptors or cytokine-release mechanisms to induce a repression in cytokine release. It can be more greatly suggested that $Ti_3C_2T_x$ induces cytokine repression through interacting with pro-inflammatory gene transcription machinery using **Figure 3.13**. IL-1β-primed cells would have not shown a suppression of IL-6 and IL-8 after $Ti_3C_2T_x$ treatment if the cytokine-repression mechanism was due to $Ti_3C_2T_x$ blocking the TLRs or IL1βRs as the cells were releasing IL-6 and IL-8 prior to $Ti_3C_2T_x$ treatment, at which point, blocking the receptors would not prevent cytokine release. Therefore, an alternative mechanism of $Ti_3C_2T_x$ interacting within the gene transcription machinery to repress hyperinflammation was explored.

The mechanisms behind the ability of $Ti_3C_2T_x$ to suppress cytokine production as transparent coatings was explored further by q-PCR, in order to investigate any repression of inflammation associated gene transcription in addition to the down regulation of inflammatory cytokine proteins. IL-1β and IL-6 were selected due to their prevalence in PCO literature, ocular-based inflammation and our previously observed cytokine profile by the HLE-B3 cells. IL-1β protein expression and *IL-1β* gene fold expression was significantly reduced in cells treated with $Ti_3C_2T_x$ and IL-1β relative to cells treated with IL-1β alone ($p \leq 0.05$) (**Fig. 3.15 B, 3.16 C**). A similar distinct yet not significant reduction was observed in the IL-6 protein and gene fold expression of cells treated with $Ti_3C_2T_x$ and IL-1β (**Fig. 3.15 A, 3.16 B**). The lack of significance may be due to the concentration of $Ti_3C_2T_x$ that the cells were exposed to. This is supported by Ozulumba et al., (64) who showed suppression of IL-8 with delaminated $Ti_3C_2T_x$ in colloidal suspension at a concentration of ≥ 5 mg mL^{-1}, IL-6 with ≥ 10 mg mL^{-1} and TNF-α with ≥ 50 mg mL^{-1}. An alternative mechanism could be due to the two-step activation of IL-1β, to cleave the pro-IL-1β into its bioactive form. $Ti_3C_2T_x$ may only interact with the secondary step of IL-1β release, preventing the formation of capsase-1 inflammasomes, which subsequently represses IL-1β release and not IL-6 release. The inflammasome complex NLRP3 is involved in this second step in the activation of IL-1β release (**Fig. 3.2**). $Ti_3C_2T_x$ may block TLRs which prevents the 'priming' of NLRP3 and subsequent release of IL-1β (202), suppress NLRP3 by inducing an efflux of K$^+$ or upregulate small interfering RNA (siRNA) which silences NLRP3 (199). During

the NLRP3 inflammasome complex formation, ASC must translocate from the nucleus to achieve a functional inflammasome complex with caspase-1, acting as a checkpoint to prevent harmful inflammation. It could be that $Ti_3C_2T_x$ prevents this translocation, by upregulating positive inflammation pathways which stops the redistribution of ASC (199). However, these suggested mechanisms cannot explain how $Ti_3C_2T_x$ significantly reduces IL-1β gene expression. The interaction by $Ti_3C_2T_x$ on gene fold change suggests $Ti_3C_2T_x$ may directly interact with pro-inflammatory gene transcription machinery which leads to repression of IL-6 and IL-1β production. One such mechanism may be the repression of transcription factors NF-κB, STAT3 or C/EBP β in LECs by $Ti_3C_2T_x$ which reduces the release of IL-1β and IL-6. This can be investigated further by comparing the gene expression of LECs treated with the inhibitors of these transcription factors to identify if LECs have a similar reduction in gene expression in comparison to the LECs treated with $Ti_3C_2T_x$. To further investigate if $Ti_3C_2T_x$ interacts with gene transcription machinery to suppress cytokine release, IL-1β and IL-6 gene knock-out species can be used to explore if $Ti_3C_2T_x$ can still induce repression of pro-inflammatory cytokines.

The impact of $Ti_3C_2T_x$ on the expression of *CXCL1*, part of the chemokine subfamily involved in the requirement of monocytes was also investigated. Jiang et al., (109) showed 3866-fold upregulation of *CXCL1* in rat primary LEC amongst other genes involved in cataractogenous and innate inflammation pathways-initiated PCS. HLE-B3 cells treated with $Ti_3C_2T_x$ showed no significant upregulation in *CXCL1* nor any suppression (**Fig. 3.16 A**). As the wound-healing response of LEC PCS has been shown to play a key role in the initial phase of PCO development, the suppression of IL-1β, IL-6 and IL-8 and lack of *CXCL1* activation by $Ti_3C_2T_x$ suggests that the application of $Ti_3C_2T_x$ within the capsule bag will not worsen the inflammatory response incited by surgical trauma and may aid in the suppression of the response.

MXene nanosheets has been exploited for use in wound dressings (62,203). Mao et al., (203) developed a bacterial cellulose MXene hydrogel (rBC/MXene hydrogel) which significantly enhanced the wound closure in a rat full-thickness defect model. EMT is an established part of the cell migration contributing to wound closure. The acquisition by residual

LEC to migrate across the posterior capsule and IOL is the final phase of PCO that results in the fibrous obscuration. The role of $Ti_3C_2T_x$ on the EMT pathway and upregulation of key intracellular filaments had yet to be investigated. Scratch wound assays are used to measure the wound-healing response and cell migration, specifically in testing therapeutical agents for clinical use in PCO patients (70,191,204). Smith et al., (70) found that lens epithelial FHL124 cells exposed to resveratrol, a polyphenolic phytoalexin compound that has been shown to inhibit fibrotic events, significantly reduced their migration rate in comparison to untreated samples. This work exploited this technique to establish the impact of $Ti_3C_2T_x$ coatings on HLE-B3 cell migration. The findings from the scratch wound assays showed $Ti_3C_2T_x$ significantly increased migration rate of HLE-B3 cells, reducing the time for complete wound closure (**Fig. 3.17**). This is likely as a result of the hydrophilic properties of $Ti_3C_2T_x$ providing a synonymous surface for cells to adhere and grow over. Although a positive interaction of cells to $Ti_3C_2T_x$ is highly favourable for implantation of medical devices, it could potentially worsen the development of PCO by increasing rate of migration of the residual transformed LEC across the posterior capsule. The application of $Ti_3C_2T_x$ coatings on the outer optic surface of the implanted IOL may increase rate of optic coverage and PCO formation.

The impact of $Ti_3C_2T_x$ coatings on the EMT pathway was further investigated by immunocytochemistry and western blot analysis to quantify the expression of key EMT protein markers vimentin, α-SMA and SMAD2/3 (174). These proteins become highly upregulated in residual LECs undergoing EMT. Vimentin is a cytoskeletal filament protein which is activate within the remodelling and migration of transformed myofibroblasts (173,178,183,184). α-SMA filaments are an isoform of actin filaments, which are also involved in cell motility (25). Myofibroblasts will greatly express α-SMA therefore, α-SMA can be used as marker for LEC differentiation (174). TGF-β2 promotes EMT during PCO development using SMAD2/3 signalling pathways. Therefore, SMAD2/3 proteins can be used to indirectly measure the presence of TGF-β2-induced EMT. These markers are commonly used to quantify EMT PCS as exemplified by Joseph et al., (25) who developed a method to examine the different markers of

EMT in a mouse LEC model by reprogramming mesenchymal cells into induced stem cells then differentiating them into an epithelial cell type. It was found that upon losing their mesenchymal phenotype, the mouse cells decreased their expression of α-SMA, vimentin and increased their levels of E-cadherin.

Immunocytochemistry and western blot analysis both confirmed no significant difference in expression of vimentin, α-SMA and SMAD2/3 in cells treated with $Ti_3C_2T_x$ relative to the cell only control (**Fig. 3.18; 3.20**). FHL124 alone showed low expression of all markers which is expected as these filaments are normally present in LEC (184,205). This is influenced by the addition of 5 % FBS to the culture media which is different to physiological conditions (85). The addition of TGF-β2 significantly increased the abundance of vimentin and α-SMA filaments and SMAD2/3 protein signalling. Moreover, changes were observed in cell morphology, from rounded cells with packed ECM to an elongated irregular structure with branched-like ECM. The upregulation in EMT markers and changes in cell morphology by TGF-β2 provides support to the use of TGF-β2 as a positive control to induce EMT in LECs (70). $Ti_3C_2T_x$ did not significantly upregulate any of the markers. Cells treated with $Ti_3C_2T_x$ and TGF-β2 showed a marked but not significant reduction in α-SMA and SMAD2/3 expression. However, the expression of vimentin was significantly reduced in cells treated with $Ti_3C_2T_x$ and TGF-β2 in comparison to cells treated with TGF-β2 alone. As vimentin is involved in lens epithelium repair and wound closure, this suggests $Ti_3C_2T_x$ may not upregulate cell migration or wound repair. However, **Fig. 3.17** showed the presence of $Ti_3C_2T_x$ coatings did increase cells' propensity to migrate and increased wound closure rate. Therefore, this evidence suggests that $Ti_3C_2T_x$ promotes wound closure whilst suppressing overexpression of cytoskeletal filaments to prevent the initiation of EMT differentiation pathways, promoting a positive resolution of the wound healing response in LEC.

In this chapter, an *in vitro* LEC inflammation model has been developed and has shown that with the addition of $Ti_3C_2T_x$ coatings into this model, no significant upregulation of these pro-inflammatory cytokines at protein and gene level was found. Indeed, the presence of $Ti_3C_2T_x$ significantly suppressed expression of IL-1β and markedly reduced the expression of IL-6 and

CXCL1. Moreover, this work showed that $Ti_3C_2T_x$ did not promote EMT pathways, shown by the lack of upregulation in EMT markers and the suppression of vimentin expression. This chapter has shown for the first time the ability of $Ti_3C_2T_x$ to suppress pro-inflammatory cytokine production and repress overexpression of EMT markers whilst increasing wound closure rate thereby promoting a positive resolution of the LEC wound healing response. The mechanism(s) of action behind the suppression of cytokine-induced inflammation and EMT markers in LEC by $Ti_3C_2T_x$ were explored further using genomic and lipidomic profiling of IL-1β and $Ti_3C_2T_x$-treated LECs in **Chapter 4**.

Chapter 4: Genomic and lipidomic

profiling of lens epithelial cells

incubated with $Ti_3C_2T_x$ (MXene)

4.1   Introduction

4.1.1 Genomic analysis

In **Chapter 3** it was shown that $Ti_3C_2T_x$ suppressed cytokine-induced inflammation and EMT markers in LEC. However, the mechanisms by which this process occurs are unknown. A genomics and lipidomics analysis was carried out in order to investigate potential routes by which $Ti_3C_2T_x$ may cause alterations in the LEC transcriptome and lipid membrane composition using the *in vitro* LEC inflammation model. RNA sequencing (RNA-Seq) provides insight into the gene transcriptome of cells upon a drug treatment or within a disease by identifying any differentially expressed genes (DEGs). Bulk RNA-Seq refers to the RNA sequencing technique where the total source of RNA within a sample is used for analysis. It is used to compare DEGs between sample conditions and to understand molecular mechanisms underpinning a condition (206,207). RNA sequencing begins with RNA isolation (**Fig. 4.1**). Single stranded RNA is unstable therefore RNA quality is assessed by its RNA Integrity Number (RIN[e]). A RIN[e] value above seven is considered suitable for sequencing. Freezing samples over an extended period of time or samples obtained from biopsies or paraffin imbedded tissues can negatively impact RNA quality (206). Specific RNA types can be targeted to be enriched. Denaturing the RNA samples maintains all RNA types; messenger (m)-RNA, pre-mRNA and non-coding (nc)-RNA. At this point, the samples are prepared for library sequencing. RNA is fragmented, converted to the more stable double standard complimentary (c)-DNA by reverse transcription and specialised adaptors for sequencing are added to the end of each strand via ligation (206). PCR enrichment is used to amplify the adaptor ligated cDNA. cDNA libraries are prepared, and index nucleotide barcodes are added to the libraries. The cDNA libraries are checked for purity, adaptor contamination and to quantify concentration. The libraries are pooled and sequenced (206). Bioinformatics are performed to identify and analyse DEGs.
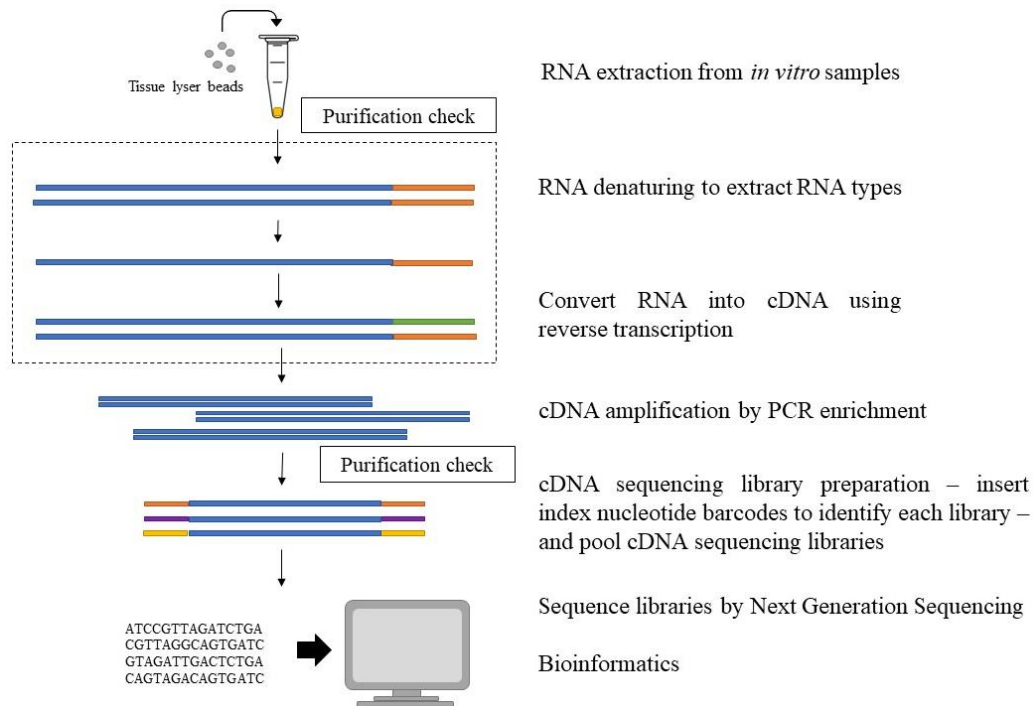
Figure 4.1: Overview of bulk RNA sequencing. Process begins with cell lysis to extract RNA. The RNA is converted to complimentary (c)-DNA. cDNA is amplified and the cDNA sequencing library is prepared. cDNA sequenced libraries are pooled and sequencing. Data is collected for bioinformatics (206,208).

4.1.2 Genomic bioinformatics in ocular conditions

RNA Seq has been used to characterise the origin and global gene expression of *in vitro* immortalised LEC lines. Weatherbee et al., (209) used RNA Seq to molecularly characterise the SRA01/04 cell line. The study found that SRA01/04 expressed several important genes in lens development and had key differences relative to the mouse LEC line, authenticating its human origin. RNA sequencing has also been used to identify DEGs associated with cataracts to provide insight into the disease's mechanism (109,210–212). Zhou et al., (212) used DNA microarray to investigate the effect of glucocorticoid (GCs) steroid hormones on posterior subcapsular cataract development for therapeutic targeting. Prolonged exposure to GCs has been linked to cataract formation by indirectly inducing oxidative stress and glutathione depletion in the lens. Upon GC treatment to LEC, the GC receptor begins regulating the MAPK and PI3/Akt pathways. These pathways have been linked to induction of EMT in LEC (8,170). The study identified 13

significant gene oncology (GO) functions of which the most common DEGs were CCL2, DUSP1 and FAS. These genes were suggested for therapeutic targeting, alongside their common transcription factor, c-Jun.

RNA-Seq has been previously used in PCO research to investigate the inflammation response PCS in LEC and the discrepancy between young and elderly cataract patients developing PCO (85,109). It is generally understood that TGF-β signalling induces EMT of residual LEC, culminating to the migration of fibrotic cells across the posterior visual axis. However, how this activation of latent TGF-β in the AH occurs was poorly understood. Jiang et al., (109) performed RNA-Seq on LECs obtained from mouse cataract surgery models to elucidate the initial pathways that contribute to the onset of TGF-β-induced EMT. The study found that 48 hours PCS was required to pass before there was detection of pSMAD2/3, one of the markers for TGF-β signalling. Despite this, the mRNA of key fibrotic markers such as α-SMA and fibronectin were detected at 24 hours PCS, with protein expression detected at 48 hours PCS, suggesting the progenitor pathways triggering EMT ($\leq$ 48 hours PCS) are initiated independently of TGF-β signalling. Therefore, the induction of these fibrotic pathways prior to TGF-β signalling was investigated. The study showed the DEGs in the LECs isolated 24 hour-PCS were linked to cataract-associated genes and chronic autoimmune and autoinflammatory conditions. Of the 132 Kyoto Encyclopaedia of Genes and Genomes (KEGG) defined pathways that were identified, the top 10 affected pathways included actin cytoskeletal regulation, inflammatory response and cell adhesion molecules. The greatest upregulated DEGs were linked to the cytokine-cytokine receptor pathway interactions and innate immune response genes such as *CXCL1* and other members of the CXC subfamily (**Fig. 4.2**). Coimmunostaining for α-SMA and pro-inflammatory markers showed a good overlap of pro-inflammatory cytokines within α-SMA-positive LECs. This suggests the immediate innate immune response of LEC PCS may play a significant role in combination with TGF-β signalling to induce later onset fibrotic pathways contributing to PCO development.
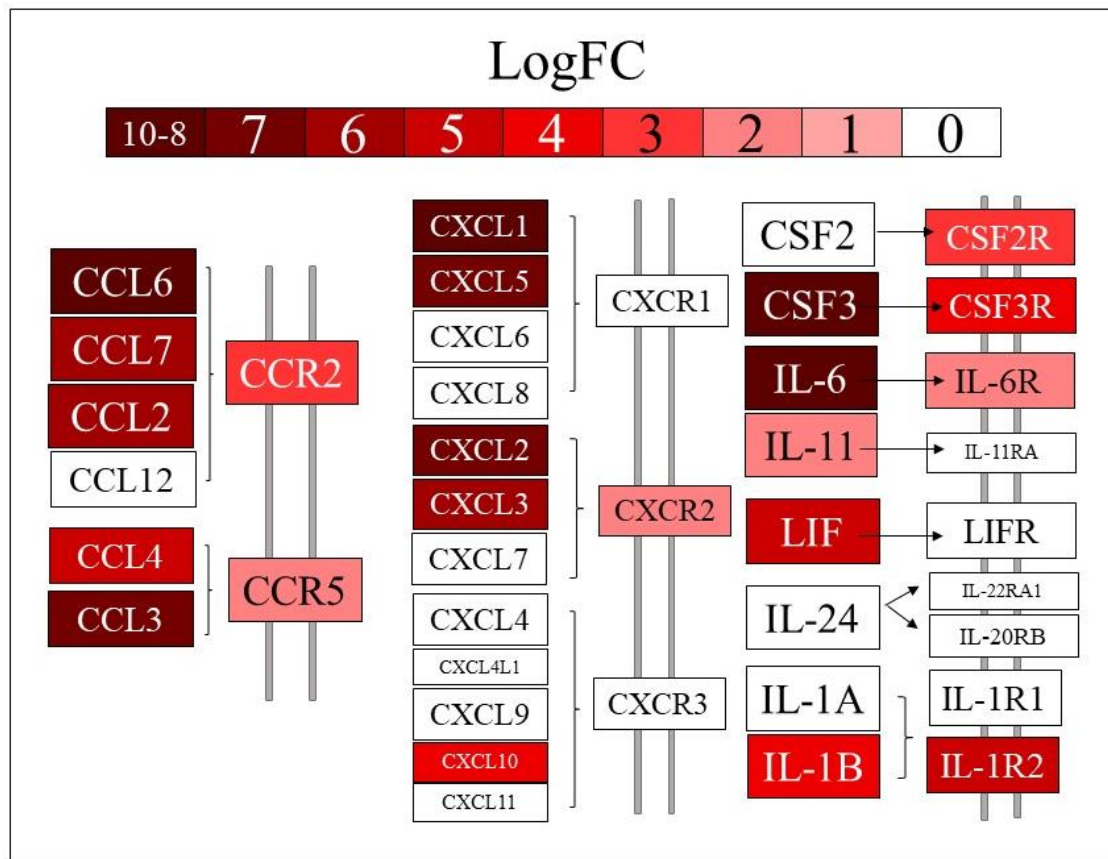
Figure 4.2: Cytokine-cytokine receptor interaction pathway post-cataract surgery in mouse cataract models. Log fold change of CXC, CCL, hematopoietins and IL-1-like subfamily genes in mouse LECs 24-hour post-cataract surgery involved in cytokine-cytokine receptor interaction, as defined by Kyoto Encyclopaedia of Genes and Genomes (KEGG) (213). Adapted from Jiang et al., (109).

The EMT pathway has been explored further using RNA-Seq in a young vs aged LECs model. The greater prevalence rate of PCO in younger patients in comparison to older patients was examined by Wei et al., (85) who used *in vitro* FHL124 cells and *in vivo* mouse cataract surgery models to compare the expression of DEGs between young (P15) and aged (P42) LECs. DEGs in the aged LECs were associated with the upregulation of the immune response, cell stress response, oxidative phosphorylation and p53 pathway as the cells adapt to the elevated stress. For the young LECs, the DEGs were associated with pathways linked to maintaining cell viability and proliferation such as the unfolded protein response (UPR), EMT, downregulated UV

response, hypoxia and hedgehog signalling. Focusing on hallmark EMT genes, aged LECs showed a downregulation in ECM, cell adhesion molecules such as cadherin 11 and 6, vimentin and α-SMA genes relative to the young LECs. It was also shown that the aged LECs suppressed TGF-β-induced EMT. This study provided insight into mechanisms behind the increased PCO risk for younger patients by showing the greater proliferative and pro-EMT phenotype of young LECs relative to aged LECs. These studies exemplify the usefulness and validity of RNA Seq in exploring the underlying inflammation and EMT pathways contributing to PCO development and was exploited to investigate the initial suppression of pro-inflammatory cytokines by $Ti_3C_2T_x$ discussed in **Chapter 3**. A potential mechanism of action underlying this anti-inflammatory effect by $Ti_3C_2T_x$ was also investigated using lipidomic analysis.

4.1.3 Role of lipids in ocular diseases

Light passing through the lens that converges at the retina must pass through 2,800 cellular membranes (214). These membranes help maintain lens clarity by modulating water content via aquaporins and by regulating calcium, sodium and potassium homeostasis (214). Unlike typical cell membranes, lens membranes consist primarily of dihydrosphingomyelin and most of the lipids are associated with crystallin proteins, significantly reducing the fluidity of the lens membrane relative to a typical membrane (**Fig. 4.3**). As the lens ages and there is lipid degradation, these crystallins become more embedded within the membrane leading to age-related changes. Degradation of membrane lipids contributes to cataract development. This is attributed to phospholipid oxidation (214,215). A decrease of < 1,000 of the total lens lipids can cause a deregulation in lipid composition, affecting membrane signalling and permeability, leading to cataractogenesis (214). Oxidative stress, drug-induced downregulation in cholesterol synthesis and fatty acids in the AH can also contribute to lipid oxidation and cataract formation (214).

Lipid composition in immortalised ocular lines has been reported (214,216). HLE-B3 cells had a lipid composition of, from highest to lowest, phosphatidylcholine (PC) (~ 52 %),

109

phosphatidylethanolamine (PE) (~ 17 %), sphingomyelin (SM) (~ 11 %), lyso-PC (LPC) (~ 7 %) and phosphatidylserine (PS) (~ 5 %) (215). Dihydro-SM was not detected, most likely as a result of these lipids being more abundant with age and HLE-B3 cells are an infant-derived lens cell line. Human corneal epithelial (HCE) cells were found to consist predominantly of PC (~ 39 %), PE (~ 21 %) and SM lipids (~ 13%) with low levels of plasmenyl-PC (~ 4 %) and PS (~ 2%) lipids (216).
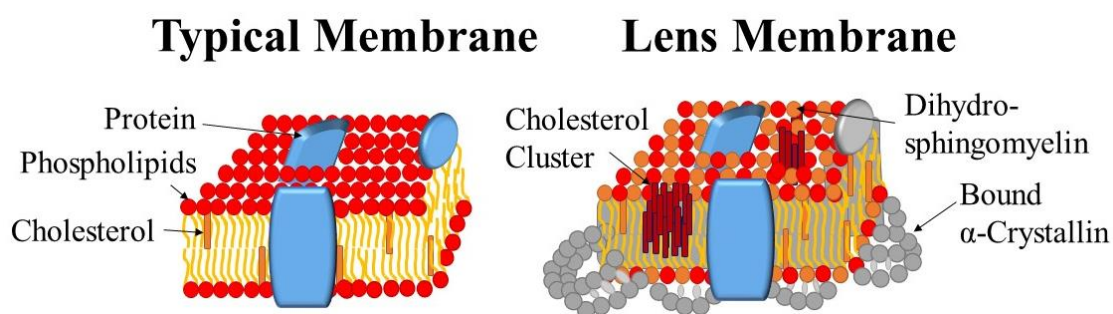
Figure 4.3: Structural differences between a typical cell membrane and a lens membrane. Human lens lipid membranes consist mostly of dihydrosphingomyelin. The membranes are associated with α-crystallins. Most of the composite lipids are bound to proteins, for example aquaporins (214).

Lipid oxidation has been linked within cataractogenesis (215). More than 30 % of the lens phospholipids are degraded over a human lifetime, creating ROS products contributing to cataract formation (214,215). This can be modelled with immortalised LEC lines. Huang et al., (215) showed in a hyperoxic environment, there was an increase in LPCs and a decrease in PC lipids. The ratio of PC lipids to SM lipids was 28 % lower in which corresponded with a 10-fold decrease in growth rate in LECs relative to cells grown in normal oxygen levels. These lipid composition changes contributed to a more ordered, saturated and stiffer membrane, consistent with *ex vivo* aged LECs.

The role of lipids in ocular diseases can be explored using lipidomics. Lysophosphatidic acid (LPA), a serum phospholipid found in the AH, was investigated in rabbit AH following

corneal injury (217). LPA was targeted due to its role in rabbit corneal epithelial cell' migration, inducing calcium influx in mechanosensitive ion channels during cataract surgery and in the stimulation of rabbit corneal keratocytes and epithelial cell proliferation. LPA levels were detected in the AH from normal and injured eyes using liquid chromatography-tandem mass spectrometry (LC-MS-MS). The study found that LPA was elevated in injured eyes although endogenous levels were not. Zumwalt et al., (218) investigated LPC for its potential role as a secondary messenger for IL-1β. LPC and PC lipids levels were detected using high performance thin layer chromatography (HPTLC). Exogenous LPC stimulated IL-6 in C6 glioma cells. With the addition of norepinephrine to LPC spiking, IL-6 expression was comparable to IL-6 levels produced upon IL-1β and norepinephrine treatment, suggesting a similar affinity to induce inflammation in neurodegenerative processes. Upon IL-1β treatment, glioma cells had higher levels of LPC 18:0 and showed a decrease in its parent lipid, PC, suggesting that increased levels of LPC 18:0 in glioma cells may indicate the presence of IL-1β-inflammation.

Significant alterations in gene expression have been shown during cataract formation (109,209,210). Nevertheless, the genomic profile of LEC in PCO development is relatively unexplored. Following on from the previous findings, alterations in genomic profile of LEC treated with $Ti_3C_2T_x$ was investigated in order to elicit any further potential mechanisms contributing to PCO development. Moreover, the ability of $Ti_3C_2T_x$ treatment to suppress gene fold change infers an interaction of $Ti_3C_2T_x$ with the cell membrane. Lipidomic analysis provides insight into the cell lipid composition and integrity, allowing for the investigation of a potential mechanism of action behind the ability of $Ti_3C_2T_x$ to enter the cell and promote anti-inflammatory pathways. Therefore, lipidomic analysis was also completed to show any changes in lipid membrane profile of cells when treated with $Ti_3C_2T_x$.

4.1.4 Aims and Objectives

This chapter aims to understand the underlying mechanisms behind the initial suppression of pro-inflammatory cytokines by $Ti_3C_2T_x$ that was observed in **Chapter 3**. In **Chapter 3** it was

found that $Ti_3C_2T_x$ suppressed gene fold change in pro-inflammatory cytokine expression. This chapter aimed to characterise the biological process (BP) and molecular function (MF) pathways contributing to the pro-inflammatory cytokine suppression by gene set enrichment analysis (GSEA) and explore the impact of $Ti_3C_2T_x$ on other hallmark inflammation gene sets. Moreover, the interaction by $Ti_3C_2T_x$ with the LEC gene transcriptome would require some interaction by $Ti_3C_2T_x$ with the lipid cell membrane. Therefore, this chapter also aims to determine if $Ti_3C_2T_x$ impacted lipid membrane composition, as a potential mechanism to explain in part the ability of $Ti_3C_2T_x$ to interfere with cell processes and repress gene transcription.

4.2   Methods

4.2.1 RNA Sequencing (RNA-Seq)

FHL124 cells were seeded into the wells of a 12 well tissue culture plate at a concentration of 6×10^5 cells mL^{-1}. Treatment and control groups were set up to include cells only, $Ti_3C_2T_x$-treated cells (5 mg mL^{-1} coatings), IL-1β-treated cells (100 ng mL^{-1}) and cells treated with $Ti_3C_2T_x$ and IL-1β. Samples were prepared in triplicate and were incubated for 24 hours at 37 °C, 5 % CO_2. Cells were trypsinised and centrifuged at 11600 rpm for 5 minutes. RNA extraction was performed using an miRNeasy Mini Kit (Qiagen, UK). All extracted RNA was quality checked using the RNA screen tapes and the Agilent TapeStation 4200 instrument. All had a RIN[e] above 7.9. mRNA purification from 200 ng of total RNA input was performed, as per the NEBNext® Poly(A)mRNA Magnetic Isolation Module (New England Biolabs, UK). Library preparation from purified mRNA was performed using the NEBNext® Ultra™ II Directional RNA Library Prep Kit for Illumina® (New England Biolabs, UK) protocol. Libraries were quality checked using the D100 High Sensitivity kit and the TapeStation 4200 instrument. The DNA from each library was quantified using the Qubit v2 fluorometer and all libraries were normalized to 2 nM final concentration before pooling. The library pool was quantified by qPCR using NEBNext® Library Quant Kit for Illumina® (New England Biolabs, UK) and sequenced on NextSeq 500 sequencer High Output kit 150 cycle 2x75 PE. The library preparation was repeated for two

technical repeats in the IL-1β-treated cells and cells treated with $Ti_3C_2T_x$ and IL-1β conditions. **Table 4.1** shows the index number, condition and replicate for each sample.

Table 4.1: Samples in experiment with index number, sample condition and the replicate number with its sequence run number.

Sample	Index	Condition	Replicate	Seq.run
1_C1	1	Cell only	1	1
2_C2	2	Cell only	2	1
3_C3	3	Cell only	3	1
4_M1	4	Cells with $Ti_3C_2T_x$	1	1
5_M2	5	Cells with $Ti_3C_2T_x$	2	1
6_M3	6	Cells with $Ti_3C_2T_x$	3	1
7_I1	7	Cells with IL-1β	1	1
7_I1_R	7	Cells with IL-1β - repeat	1	2
8_I2	8	Cells with IL-1β	2	1
9_I3	9	Cells with IL-1β	3	1
9_I3_R	9	Cells with IL-1β - repeat	3	2
10_MI1	10	Cells with $Ti_3C_2T_x$ and IL-1β	1	1
10_MI1_R	10	Cells with $Ti_3C_2T_x$ and IL-1β - repeat	1	2
11_MI2	11	Cells with $Ti_3C_2T_x$ and IL-1β	2	1

12_M13	12	Cells with $Ti_3C_2T_x$ and IL-1β	3	1
12_M13_R	12	Cells with $Ti_3C_2T_x$ and IL-1β - repeat	3	2

Approximately 30-40 million sequencing read pairs were obtained per sample. These were subjected to adapter and quality threshold trimming using trimgalore (219,220) and transcripts in the human genome (GRCh38) were quantified from the trimmed reads using salmon (221). The transcript count data were summarised to the gene-level and analysed for differential expression using DESeq2 (222). Gene set enrichment analysis and functional over-representation analysis of lists of significantly differentially expressed genes (FDR <=0.05) was performed using clusterProfiler (223). DEGs were identified then differential expression analysis of individual genes and related genes sets were performed.

4.2.2 Lipid extraction and sample preparation for mass spectrometry

FHL124 cells were seeded into the wells of a 12 well tissue culture plate at a concentration of 6 x 10^5 cells mL^{-1}. Treatment and control groups were set up to include cells only, $Ti_3C_2T_x$-treated cells (5 mg mL^{-1} coatings), IL-1β-treated cells (100 ng mL^{-1}) and cells treated with $Ti_3C_2T_x$ and IL-1β. Samples were prepared in triplicate and were incubated for 24 hours at 37 °C, 5 % CO_2. Cells were trypsinised, centrifuged at 11600 rpm for 5 minutes. Lipids were extracted from the cell samples using the Bligh-Dyer protocol (224). The cell pellet was resuspended in 800 µl of aqueous NaCl solution (0.9 wt%) with 10 µl of SPLASH LipidoMIX internal standard (Avanti Polar lipids) and vortexed to mix. Chloroform (1 mL), methanol (2 mL), chloroform (1 mL) and DI water (1 mL) were added and vortexed to mix. Samples were centrifuged at 1500 rpm for 10 mins at RT. The bottom organic layer was transferred to a glass culture tube and dried under nitrogen at 40 °C. Dried lipids were dissolved in *circa* 100 µl of chloroform into amber 2 mL HPLC vials, fitted with glass insert vials. Lipids were dried again under the same conditions and stored at -20 °C. Prior to analysis samples were resuspended by vortexing in 100 µl isopropanol:

methanol (1: 1). Samples were analysed by HLPC MS/MS spectrometry as described in Bahja et al., (225).

4.2.3 Bioinformatic lipid identification and analysis

Thermofisher raw format (.raw) files were converted to mzXML files using MSConvert (Proteowizard) (226). Filtering was performed using the peak picking 'Vendor' algorithm at MS level 1. HPLC alignment files were generated using MZMine (227). The negative and positive ionisation .raw files were analysed separately. Features were detected using the Mass detection algorithm (MS level 1, noise level 1×10^5). Chromatograms were constructed using the ADAP Chromatogram Builder (228,229) with a minimum group scan size (3), minimum group intensity (1×10^3), minimum highest intensity (1×10^5) and mass/ charge (m/z) tolerance of 0.005 m/z or 10 ppm. Chromatogram deconvolution was performed using a local minimum search algorithm with the following settings: chromatographic threshold (0.02%), search minimum in retention time (RT) threshold (0.05 min), minimum relative height (0.02%), minimum absolute height (5 $\times 10^5$), minimum ration of peak/ top edge (3) and peak duration range (0.05 to 1.5 min). Isotopic peak grouping was performed (m/z tolerance 0.005 m/z or 10 ppm, RT tolerance 0.05 min, maximum charge 2) the most intense isotope used as representative. Join alignment was performed (m/z tolerance 0.005 m/z or 10 ppm, m/z weight 20, RT tolerance 0.1 min, weight for RT 20). Gap filling was performed using the same RT and m/z range gap filler with an m/z tolerance of 0.005 m/z or 10 ppm. After filtering using the feature list rows filter, minimum peaks in a row (0.75), minimum peaks in an isotope pattern (2), data was exported as .csv file.

Lipid identities were assigned using Lipidex software (230), using the Lipidex_HCD_Formic, Lipidex_HCD_ULCFA and Lipidex_Splash_ISTD_Formic spectral libraries. Spectral searching was performed with MS1 search tolerance (0.01 m/z), MS2 search tolerance (0.01 m/z) and MS2 low mass cut-off of 61.00. Peak finding was performed using separate polarity files outputted from MZmine (.csv files). MS/MS filtering parameter were set at min lipid spectral purity (75 %), min MS2 search dot product (500), min MS2 search reverse

dot product (700). Feature association parameters were full width half maximum (FHWM) window multiplier (2.0) and max mass difference (15 ppm). The individual .csv files for each sample was uploaded to the spectrum searcher with identify Chromatographic peaks selected. A final results file (.csv file) was produced and lipid composition was analysed as described.

Lipids were analysed on a lipid class basis. Fatty ether/ ester compositions were calculated as the percentage of the peak area of the individual lipid relative to the sum of the peak areas of the entire lipid class. PE, PE(OH), Plasmanyl-PE and Plasmenyl-PE species were quantified to the PE standard 15:0-18:1(d7) PE ($5.3\,\mu g\,mL^{-1}$), PC, PC(OH), Plasmanyl-PC and Plasmenyl-PC were quantified to the PC standard 15:0-18:1(d7) PC ($150.6\,\mu g\,mL^{-1}$). DG, TAG, PI, PG and SM lipids were quantified relative to peak areas corresponding to 15:0-18:1(d7) DG ($8.8\,\mu g\,mL^{-1}$), 15:0-18:1(d7)-15:0 TAG ($52.8\,\mu g\,mL^{-1}$), 15:0-18:1(d7) PI ($8.5\,\mu g/mL^{-1}$), 15:0-18:1(d7) PG ($26.7\,\mu g\,mL^{-1}$) and d18:1-18:1(d9) SM ($29.6\,\mu g\,mL^{-1}$), respectively. Lyso PE and Lyso PC were quantified relative to peak areas corresponding to 18:1(d7) Lyso PE ($4.9\,\mu g\,mL^{-1}$) and 18:1(d7) Lyso PC $23.8\,\mu g\,mL^{-1}$).

4.3   Results

4.3.1 Quality checking and identification of differentially expressed genes in FHL124 cells

The genomic samples were quality checked prior to analysis in order to ensure that the DNA within the samples had been amplified to the necessary read number and had sufficient purity to ensure valid conclusions could be drawn from the data. The purification stages for the post-RNA extraction and post-cDNA libraries synthesis passed quality checks. All RNA extractions had a RIN[e] above 7.9 mRNA purification from 200 ng of total RNA input (**Fig. 4.4**). DNA library quantification mostly showed the required peak at 300 bp with no adaptor contamination (**Fig. S8**). Initial sequencing read quality control was performed using fastqc (version 0.11.9) (231) and multiqc (version 1.8) (219). Trimming was performed

using TrimGalore using a minimum quality threshold of 20 and discarding any trimmed reads shorter than 20 nucleotides. All samples passed these quality checks. The proportion of duplicate reads was high for all samples; however, this is not uncommon. High duplication can arise from either over-amplification of the libraries or over-sequencing of the highly expressed transcripts in the library. The latter is desirable to be able to observe low expression transcripts, so observing high duplication levels is not considered automatically to be an issue for further analysis.
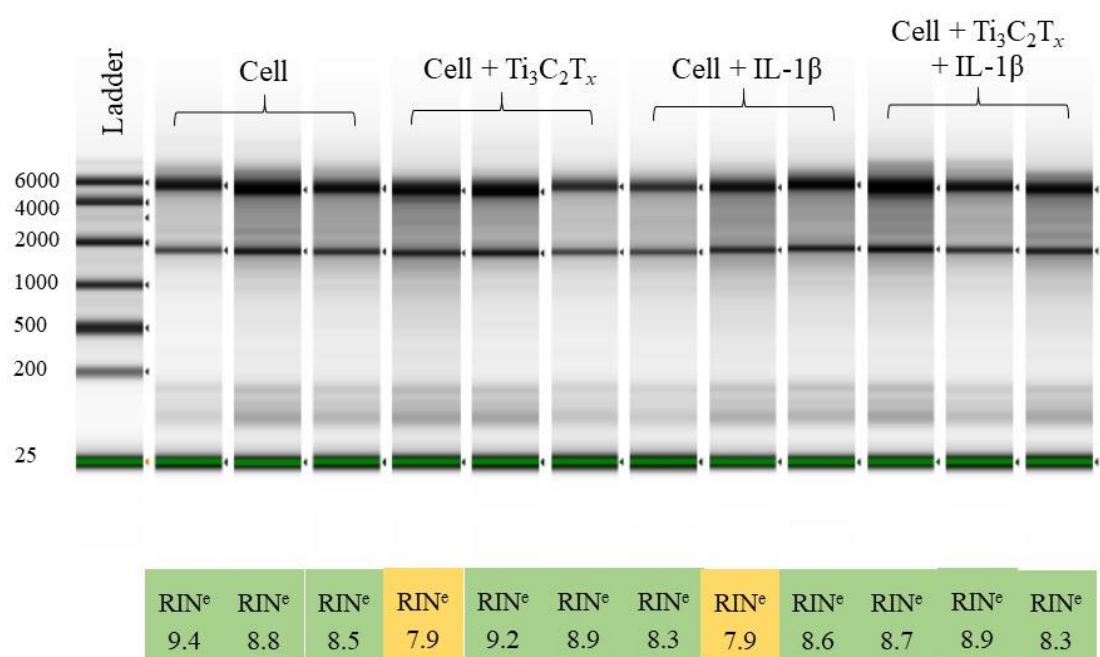
Figure 4.4: Purity check of extracted RNA using eukaryotic RNA analysis. All the samples achieved the required RIN^e of 7, confirming the sufficient purity of the extracted RNA from each sample.

Target gene mapping compares the test samples to a model genome to ensure good alignment. It tests for the quality of the sequencing, determines the proportion of reads aligned to introns or ribosomal RNA (r-RNA) and additionally checks for possible issues with genomic DNA or rRNA contamination. Quality control to assess read composition was performed by mapping to the GRCh38 human genome (ensembl) using hisat2 (220) (**Fig. S9, 10**). In the first sequencing "all data", all samples exhibited very high alignment rates, although sample *12_MI3* had generated markedly fewer sequencing reads than the other samples (~ 11

117

million compared to > 30 million). The libraries for MI3 were repeated to boost the reads of the sample to the same read number of the other samples. I1, I3 and MI1 were also repeated to ensure the repeats were balanced to avoid batch effect and allow for the repeated samples to be added to the previous analysis. In the second sequencing "new minimal data", all samples exhibited very high alignment rates, and the new repeat samples were comparable to the majority of the data previously sequenced "all data". Results of the mappings were additionally assessed using picard (version 2.21.8) (232) and rseqc (version 3.0.1) (233) (**Fig. S11, 12**). The proportion of reads mapping to r-RNA was reassuringly low (**Fig. S11 A, S12 A**) and the rate of mapping to CDS exons was reassuringly high (**Fig. S11 B, S12 B**). To generate data for differential expression testing, gene transcripts were quantified using salmon (version 1.5.2) (221). Only the "new minimal set" of samples referred to above were used.

The transcriptome data for all samples was imported into R, and the data summarized at the gene-level. The data was normalized and analysed using the DESeq2 pipeline (222). Assessment via principal component analysis (PCA) performed unsupervised clustering of the processed data, suggesting some variability in sample generation (**Fig. S13**). **Fig. S13 C** highlights the three technical replicate 1 samples as potential outliers in the experiment (*1_C1*, *4_M1*, *10_M1*). Of the remaining samples, those from the *C* and *M* treatments tend to cluster separately from the *I* and *MI* samples.

Statistical analysis of DEGs between sample conditions was completed. Over 34,000 transcripts were normalised and compared between the conditions. Cells treated with $Ti_3C_2T_x$ (*M*) had 2 up-regulated DEGs and 4 down-regulated DEGs relative to the cell only control (*C*). A total of 948 up-regulated DEGs and 896 down-regulated DEGs were identified in LECs treated with IL-1β (*I*) in comparison to LECs alone (*C*). Cells treated with $Ti_3C_2T_x$ and IL-1β (*MI)* had 816 up-regulated DEGs and 697 down-regulated DEGs relative to the cell only control (*C*) and 7 up-regulated and 1 down-regulated DEGs in comparison to the cells treated with IL-1β (*I*).

4.3.2 Functional analysis of DEGs in interleukin-1β primed cells

Functional analysis of LECs treated with IL-1β (*I*) was performed to test the validity of using IL-1β as a positive control for pro-inflammatory induction leading to PCO development. The DEGs were summarised into their Gene Ontology (GO), Biological Process (BP), Molecular Function (MF), Cellular Component (CC), and the KEGG and Reactome pathways for these genes.

A total of 64 up-regulated and 35 down-regulated MF pathways were identified and a total of 811 up-regulated and 371 down-regulated BP pathways were identified in LECs treated with IL-1β (*I*) in comparison to LECs alone (*C*). The significant DEGs between the cells treated with IL-1β (*I*) and cell only (*C*) group can be summarised into several key BP (**Fig. 4.5**) and MF (**Fig. 4.6**) pathways contributing towards PCO. These pathways include protein biosynthesis, immune response activation, endoplasmic reticulum (ER) stress response, interleukin signalling and ECM re-organisation.

In the CC pathways, 56 up-regulated and 112 down-regulated pathways were identified. The upregulated CC pathways include the ER stress response, ER chaperones complex and upregulation of collagen-containing ECM. A key downregulated CC pathway in IL-1β-primed cells was the loss of cell adhesion and cell-cell junctions. A total of 49 up-regulated and 3 down-regulated Reactome pathways were identified. Upregulated Reactome pathways include UPR, ECM organisation, interleukin signalling and chemokine receptor binding. In the KEGG pathways, 66 up-regulated and 8 down-regulated pathways were identified in cells treated with IL-1β (*I*) relative to cell only (*C*). KEGG pathways upregulated in IL-1β-primed cells include protein processing in ER, cytokine-cytokine receptor interaction and JAK-STAT signalling pathways. Downregulated KEGG pathways included focal adhesion and regulation of the actin cytoskeleton. These pathways are consistent with induction of an effective inflammation response.

119
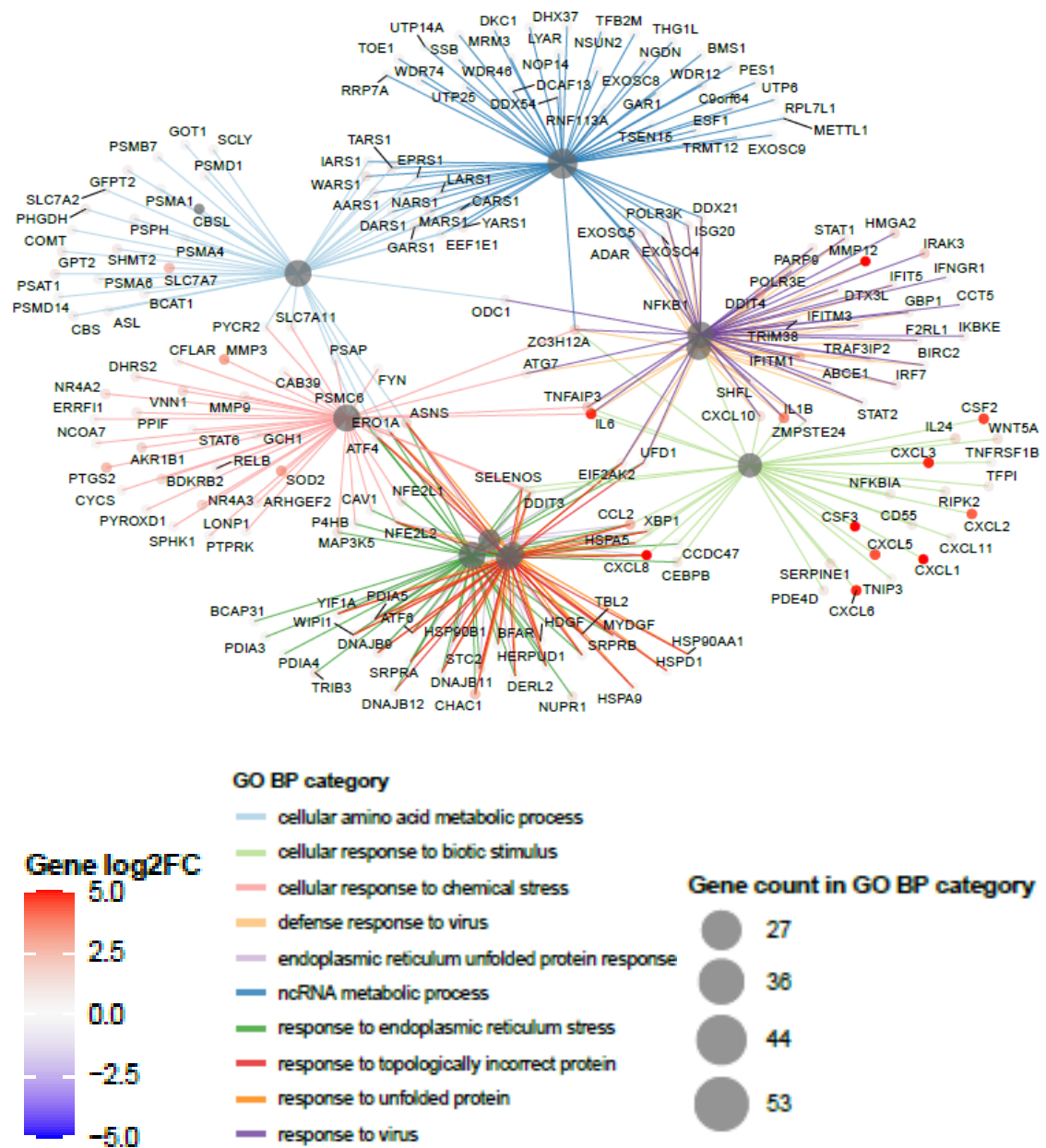
Figure 4.5: Simplified view of gene ontology (GO) biological process (BP) categories significantly enriched in the significantly upregulated genes in the cells treated with IL-1β relative to the cell control.
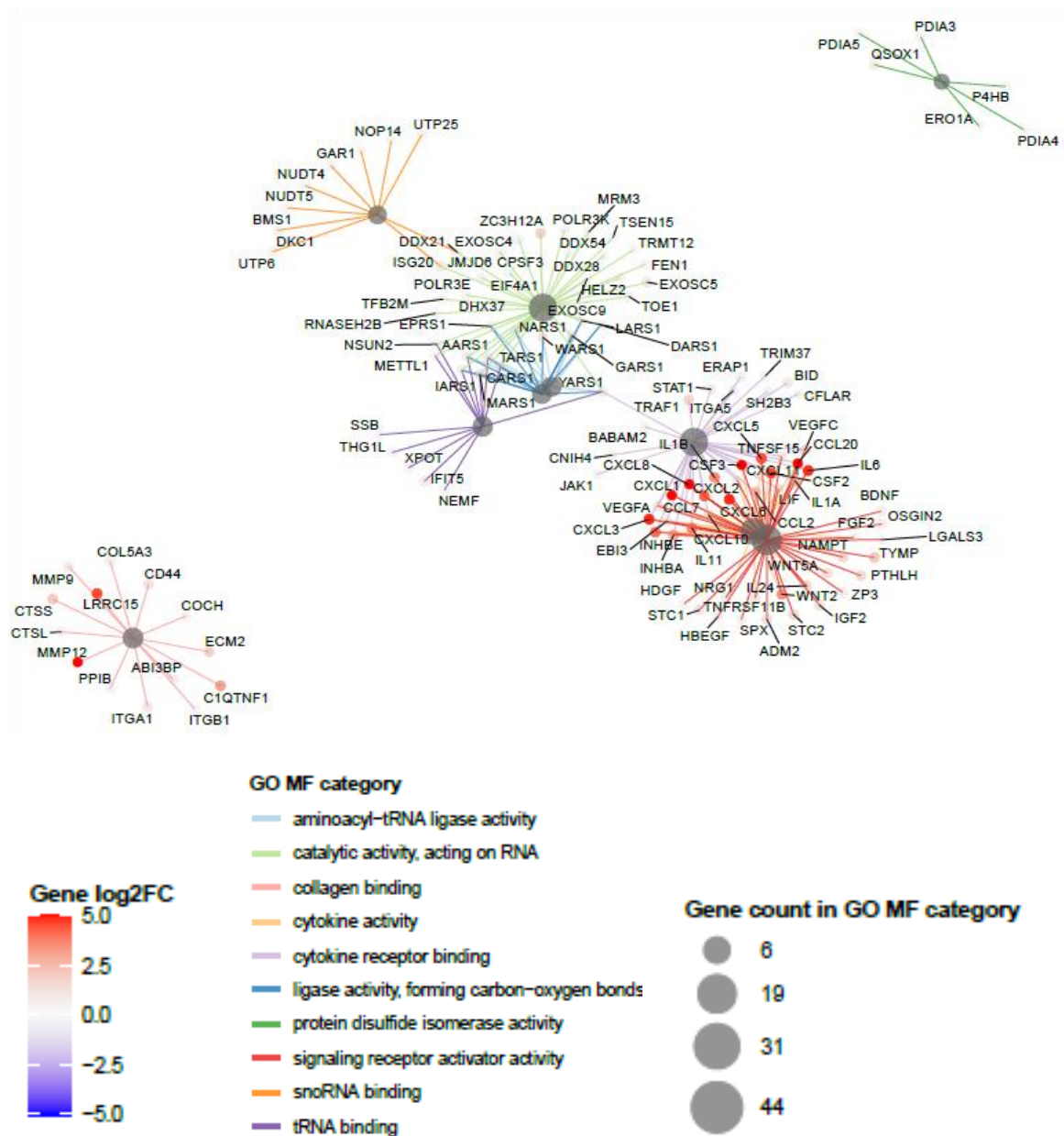
Figure 4.6: Simplified view of GO molecular function (MF) categories significantly enriched in the significantly upregulated genes in the cells treated with IL-1β relative to the cell control.

4.3.3 Gene set enrichment profile of IL-1β-primed and $Ti_3C_2T_x$-treated cells

Gene set enrichment analysis (GSEA) was performed between all conditions to consider coordinated changes in the expression of large functionally or positionally related sets of genes. The genes studied by the q-PCR (**Chapter 3.3.9**) showed similar results in the RNA-Seq. For

CXCL1, *IL-1β* and *IL-6* gene expression, there was significant upregulation in the IL-1β-treated cells (*I*) and Ti$_3$C$_2$T$_x$ and IL-1β-treated cells (*MI*) samples relative to the cell control (*C*) (*I_v_C; MI_v_C*) although no significant suppression was found between the I and MI samples (*I_v_MI*) (**Fig. 4.7**).
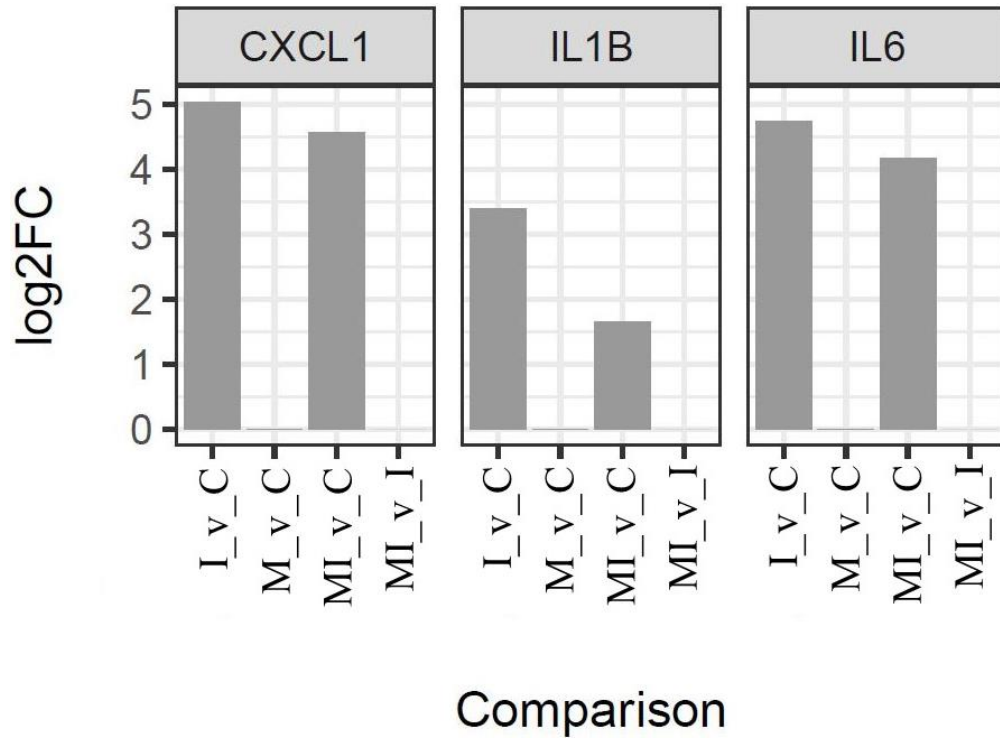
Figure 4.7: Log2Fc values of genes in IL-1β-primed and Ti$_3$C$_2$T$_x$-treated cells relative to cell only control. Genes previously studied by q-PCR were significant in the I and MI samples relative to C controls. (*C*: cell only; *M*: cells with Ti$_3$C$_2$T$_x$; *I*: cells with IL-1β; *MI*: cells with Ti$_3$C$_2$T$_x$ and IL-1β).

The hallmark inflammatory gene sets were explored further, mapping to previous work (**Chapter 3**). The inflammatory response genes sets were co-ordinately up-regulated in the *I* and *MI* samples relative to *C* samples. The hallmark inflammatory gene sets also appear to be up-regulated in the *I* sample in comparison to the *MI* samples. This was mirrored in a downregulation of hallmark inflammation gene sets between the *M* samples and *C* samples (**Fig. 4.8**), but the fold-changes on which these are based appear weaker (**Fig. 4.9**). Nevertheless, a side-by-side view of individual inflammatory response genes reveals several that may be more weakly induced

by *MI* than *I* e.g., *PDPN, CXCL10, CXCL11, CCL7, LAMP3, IL1A, IL1B* and *RNF144B* (**Fig. 4.10**).
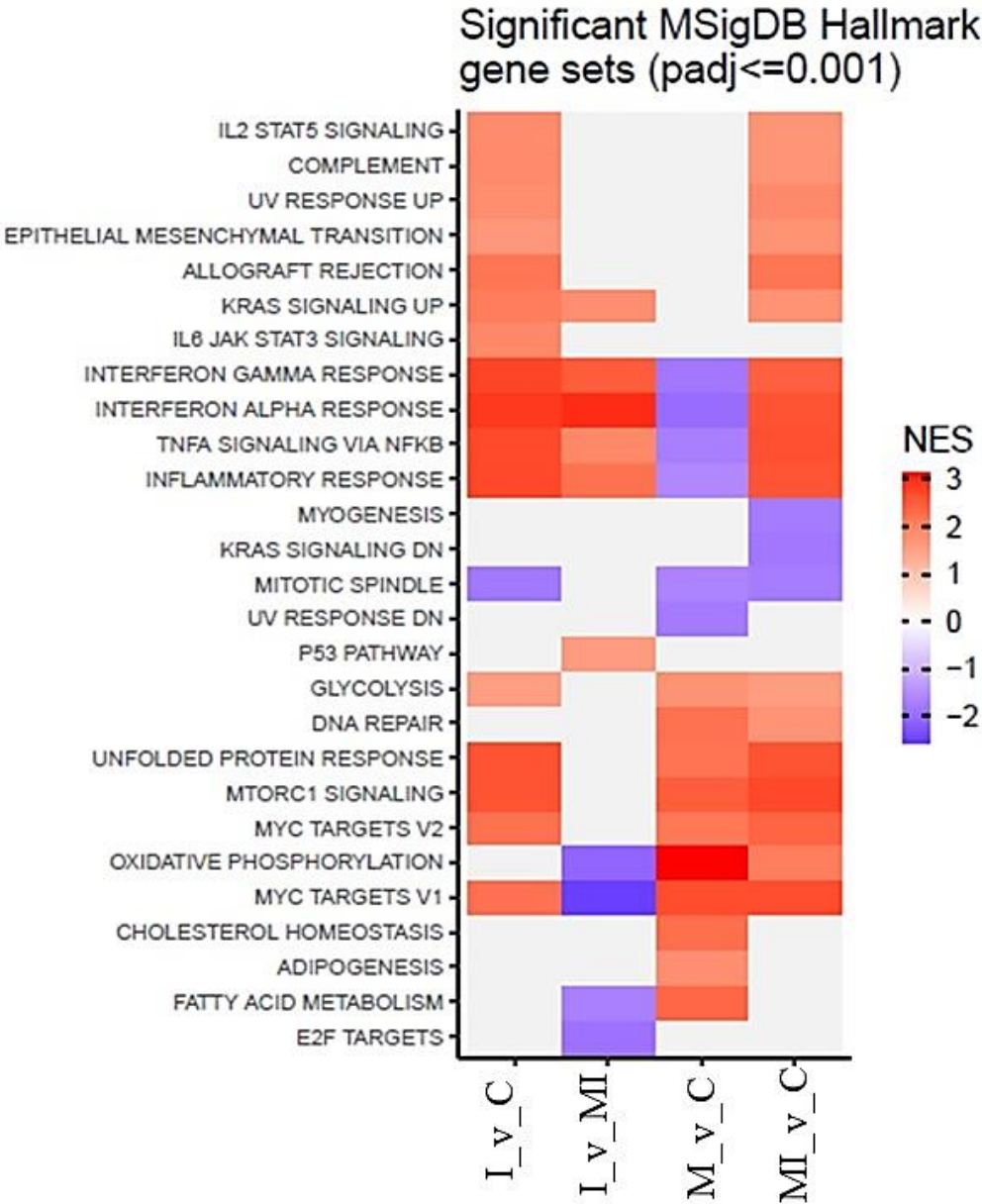
Figure 4.8: Hallmark inflammation gene set pathways upregulated in cells treated with IL-1β and Ti$_3$C$_2$T$_x$. Significant MSigDB Hallmark gene sets (padj<=0.05) across each comparison of interest. Only sets significant in at least one comparison are shown. A negative NES score in the context of these analyses indicates lower expression in the first of the named samples compared to the second whilst a positive NES indicates higher expression in the first samples. (*C*: cell only; *M*: cell and Ti$_3$C$_2$T$_x$; *I*: cell and IL-1β; *MI*: cell, Ti$_3$C$_2$T$_x$ and IL-1β).
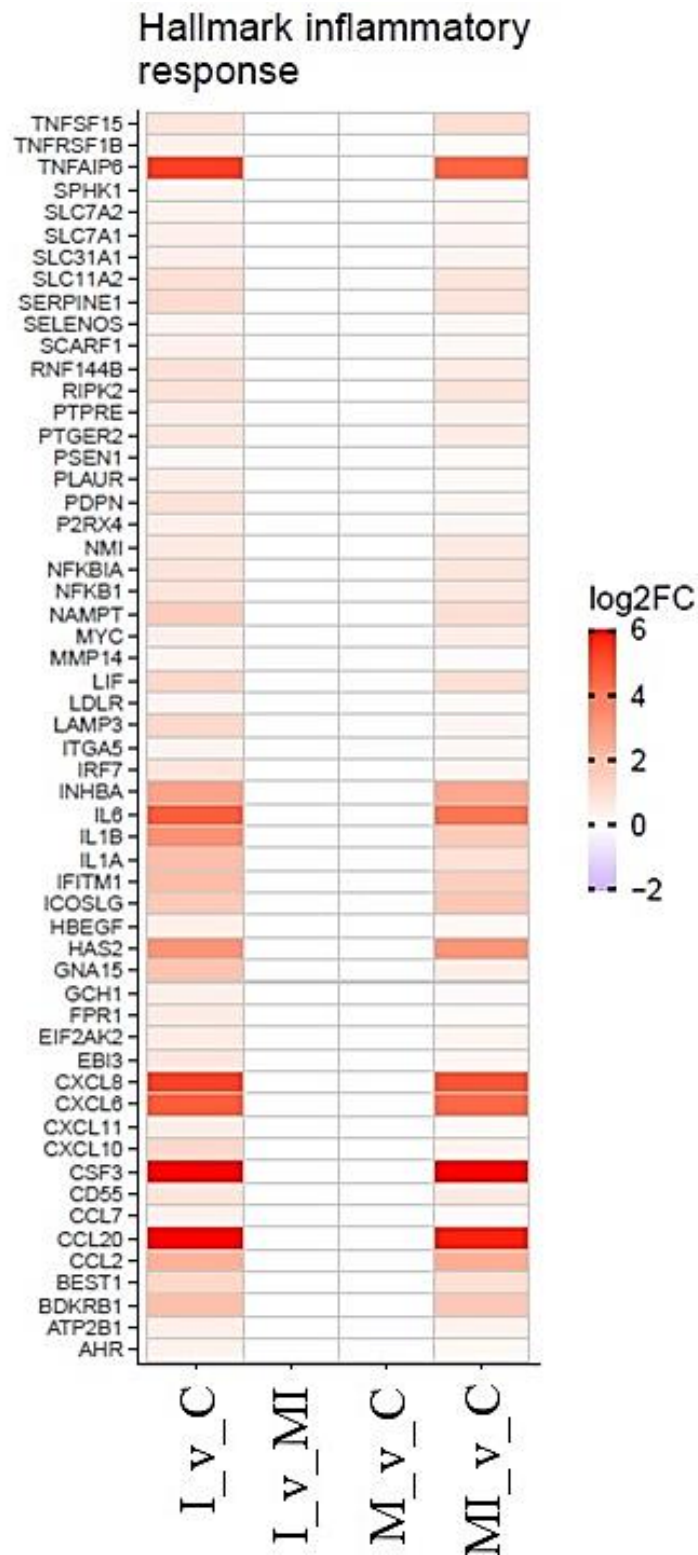
Figure 4.9: GSEA core enrichment genes in the hallmark inflammatory response. (*C*: cell only; *M*: cell and Ti₃C₂Tₓ; *I*: cell and IL-1β; *MI*: cell, Ti₃C₂Tₓ and IL-1β).
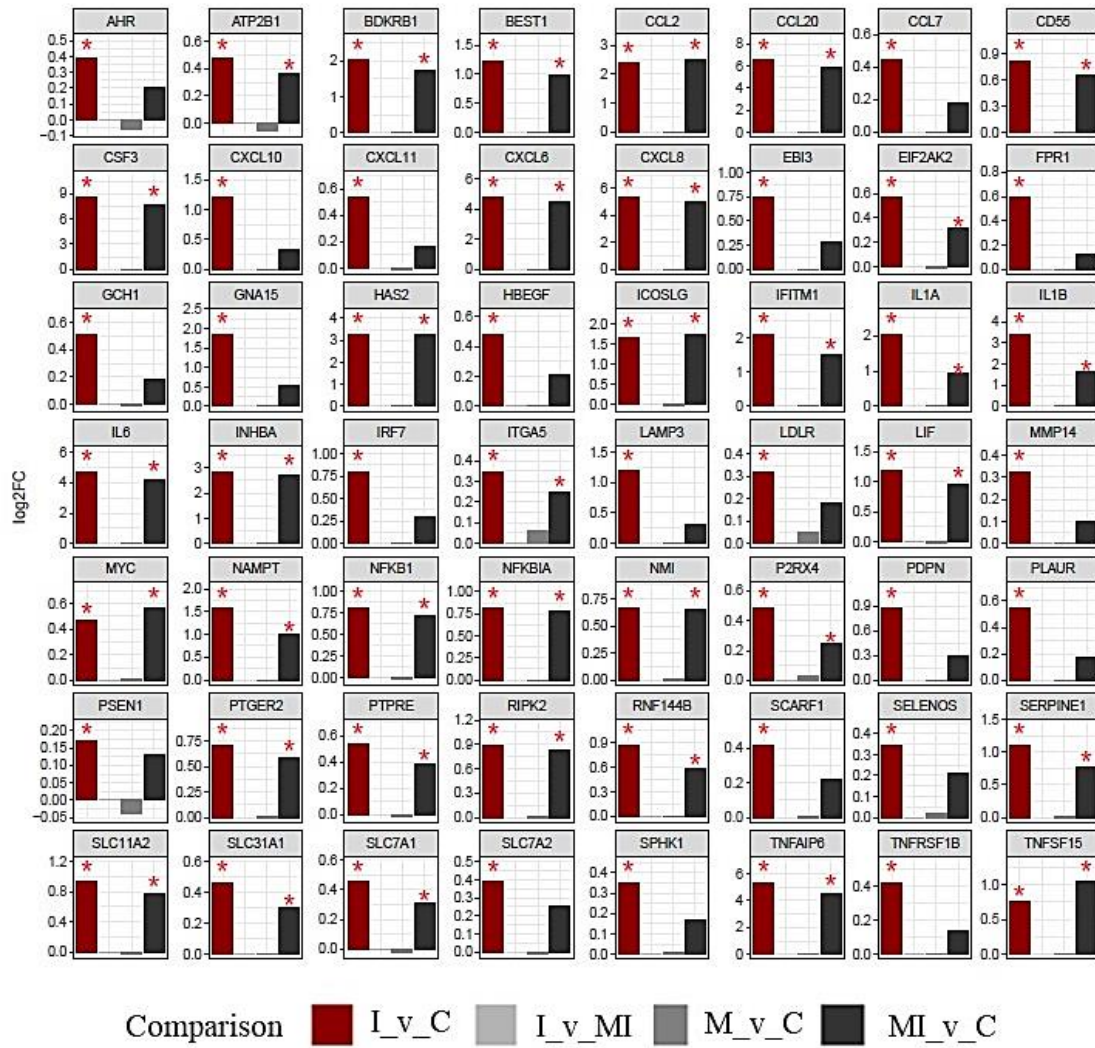
Figure 4.10: Specific comparison of individual inflammatory response genes in the *I* and *MI* samples. Genes identified as significantly differently expressed are marked by an asterisk. (*C*: cell only; *M*: cell and Ti$_3$C$_2$T$_x$; *I*: cell and IL-1β; *MI*: cell, Ti$_3$C$_2$T$_x$ and IL-1β).

The cytokine-cytokine receptor interaction KEGG pathway was found to be upregulated in the *I* samples relative to the *C* samples. Moreover, Jiang et al., (109) found this KEGG pathway was significantly upregulated in mouse eyes undergoing cataract surgery. Therefore, the individual gene fold changes in the *I_v_C* and *MI_v_C* samples were mapped onto the cytokine-cytokine receptor interaction. The *I* samples showed an up-regulation in the chemokine CC and CXC subfamilies, hematopoietins and IL-1 family (**Fig. 4.11 A**). A weakened but not significant reduction was found in these genes in the *MI* samples (**Fig. 4.11 B**).
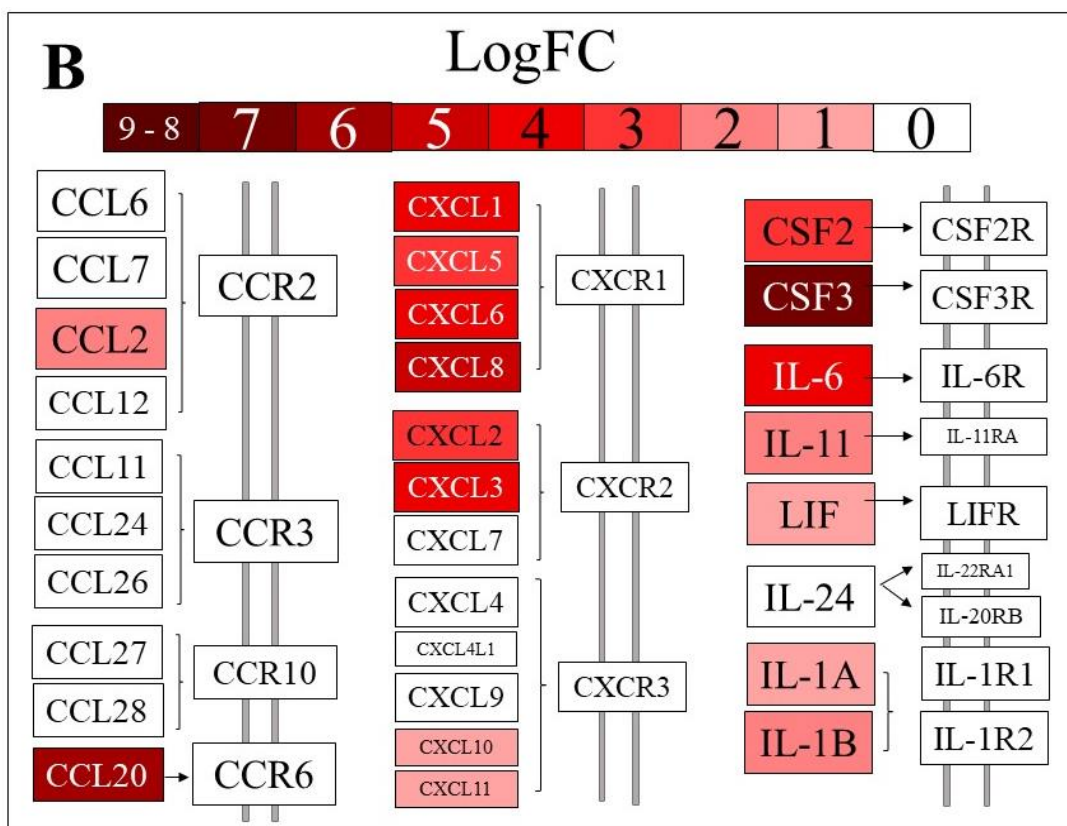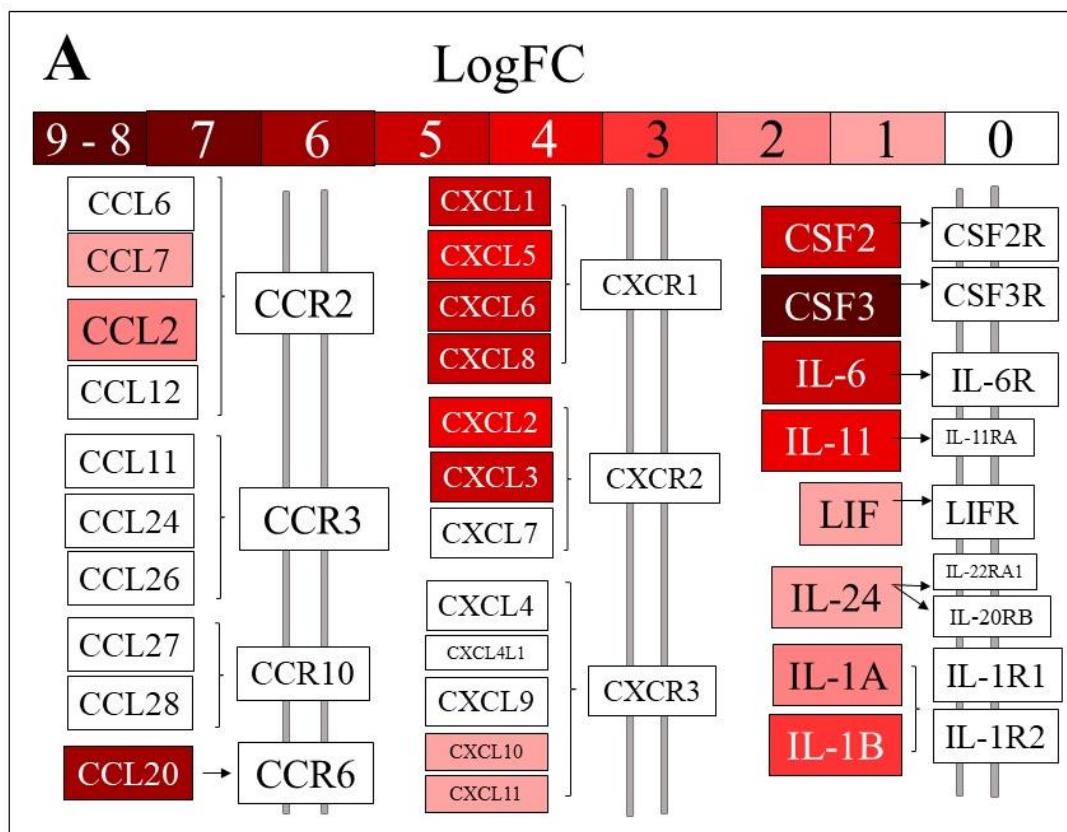
Figure 4.11: Cytokine-cytokine receptor interaction pathway of cells treated with IL-1β and Ti₃C₂Tₓ. Log fold change of CXC, CCL, hematopoietins and IL-1-like subfamily genes in

FHL124 cells treated with IL-1β (*I*) (**Fig. 4.11 A**) and FHL124 cells treated with $Ti_3C_2T_x$ and IL-1β (*MI*) (**Fig. 4.11 B**) involved in cytokine-cytokine receptor interaction, as defined by Kyoto Encyclopaedia of Genes and Genomes (KEGG) (213). All upregulated genes in cells treated with the positive inflammatory control showed a reduction in fold change when treated with $Ti_3C_2T_x$.

The hallmark EMT gene sets were also explored further to show any difference in DEGs of cells treated with $Ti_3C_2T_x$ (*M*) and cells treated with $Ti_3C_2T_x$ and IL-1β (*MI*). The EMT genes sets were co-ordinately up-regulated in the *I* and *MI* samples relative to *C* samples (**Fig. 4.12**). A side-by-side view of individual EMT genes reveals several that may be more weakly induced by *MI* than *I* eg. *MMP14, MMP2, PPIB, SDC4, PMEPA1* and *TF5SF12A* (**Fig. 4.13**).
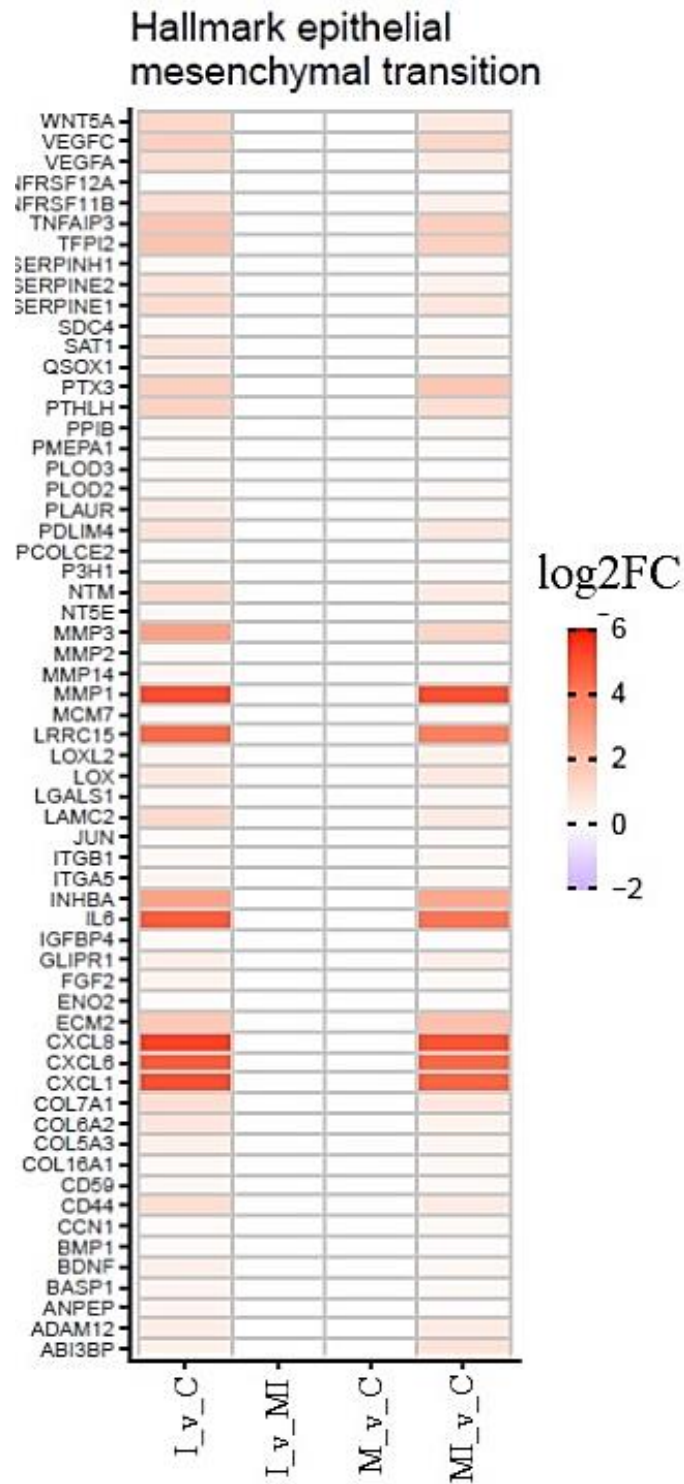
Figure 4.12: Hallmark epithelial mesenchymal transition gene set pathways upregulated in cells treated with IL-1β and Ti₃C₂Tₓ. GSEA core enrichment genes in the hallmark epithelial mesenchymal transition gene sets. (*C*: cell only; *M*: cell and Ti₃C₂Tₓ; *I*: cell and IL-1β; *MI*: cell, Ti₃C₂Tₓ and IL-1β).
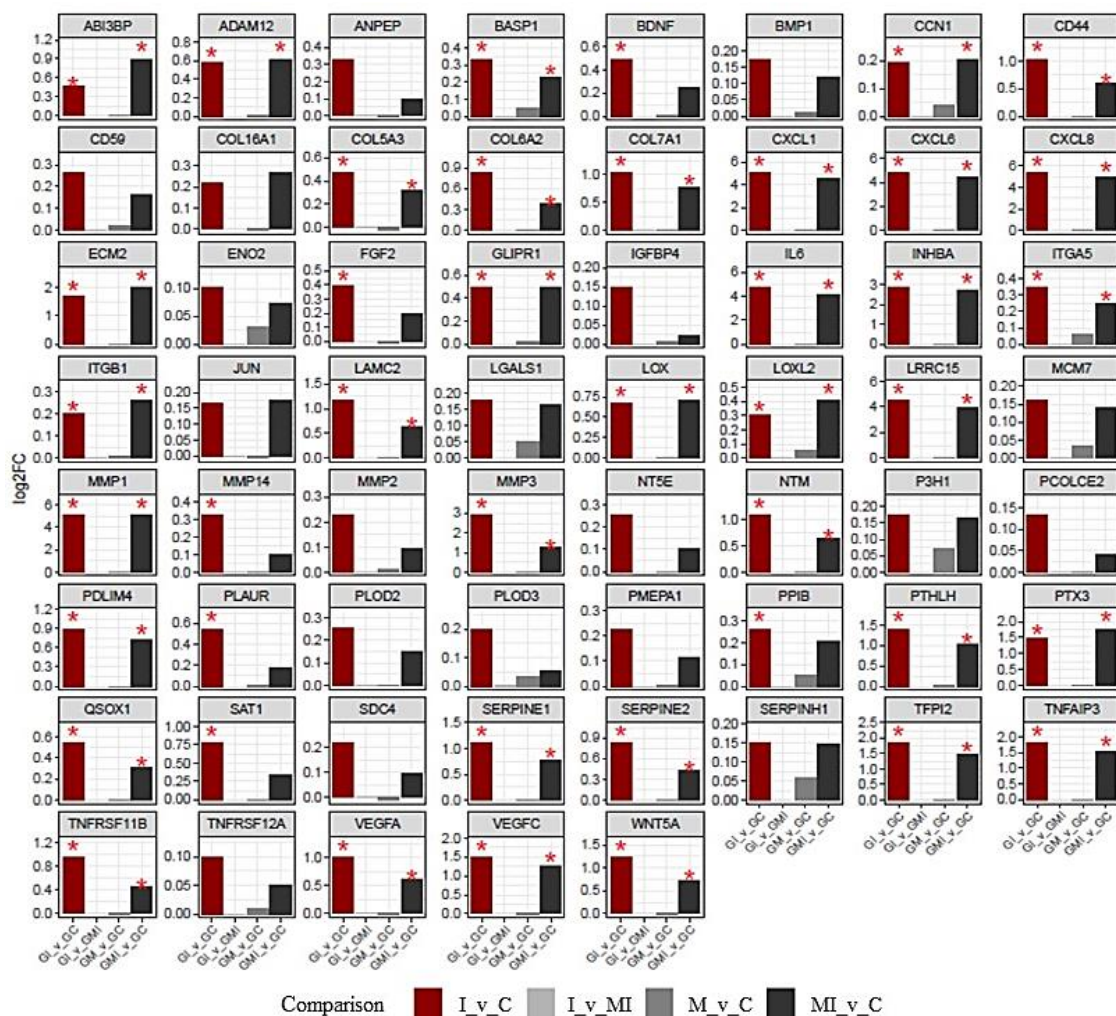
Figure 4.13: Specific comparison of individual EMT-related genes in the I and MI samples. Genes identified as significantly differently expressed are marked by an asterisk. (*C*: cell only; *M*: cell and $Ti_3C_2T_x$; *I*: cell and IL-1β; *MI*: cell, $Ti_3C_2T_x$ and IL-1β).

4.3.4 Lipidomic profile of IL-1β-primed and $Ti_3C_2T_x$-treated cells

Cells were grown in the presence and absence of $Ti_3C_2T_{x,}$ in addition to the pro-inflammatory stimulant IL-1β. The total quantified lipid composition was classified into 12 different lipid classes (**Fig. 4.14 A**). PC lipids were the most dominant lipid, such that PC and plasmenyl-PC lipid were collectively *circa* 60 % of total quantified lipid. PE and plasmenyl-PE lipids were the second most abundant at 20 % of the total quantified lipid. These values agree with the lipidome of LECs cells reported (215) where PC and PE are roughly 50 % and 20 %,

129

respectively (**Fig. 4.14 B**). No statistically significant changes in the total amount of individual lipid classes of LECs cells were observed in the presence of $Ti_3C_2T_x$.
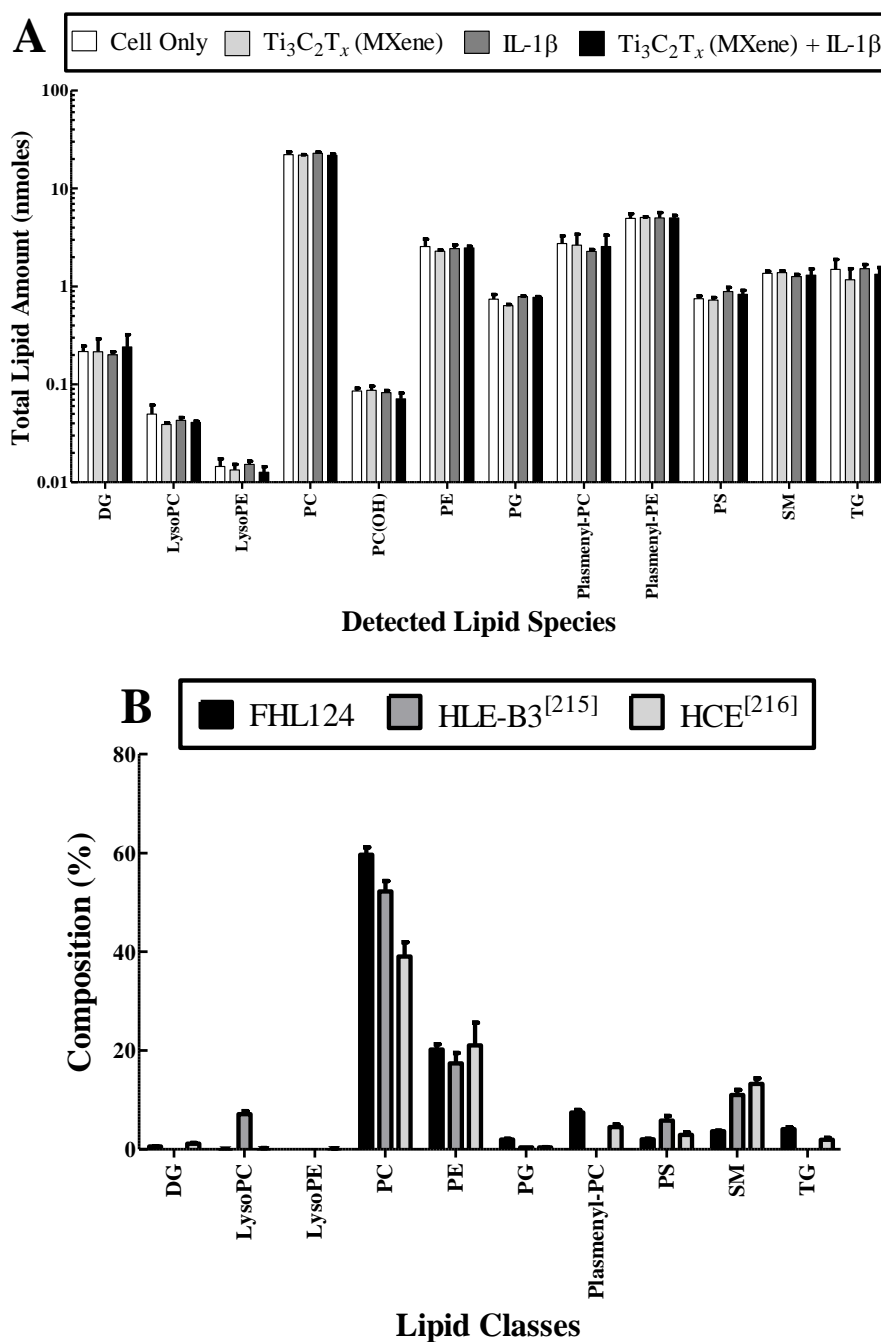
Figure 4.14: Detected lipid classes in FHL124 cells exposed to pro-inflammatory stimulus, IL-1β and $Ti_3C_2T_x$. Total quantified lipid composition of the major lipid classes found in FHL124 cells (**Fig. 4.14 A**). Comparison of lipid classes of FHL124, HLE-B3 and HCE cells (**Fig. 4.14 B**) (215,216). Individual lipid classes identified were diacyl glycerides (DG),

lysophosphatidylcholines (LysoPC), lysophosphatidylcholines (LysoPE), phosphatidylcholines (PC), hydroxy phosphatidylcholines (PC(OH)), phosphatidylethanolamines (PE), phosphatidylglycerols (PG), plasmenyl phosphatidylcholines (Plasmenyl-PC), plasmenyl phosphatidylethanolamines (Plasmenyl-PE), phosphatidylserines (PS), sphingomyelins (SM) and triacylglycerols (TG). (Cell only: cells alone; $Ti_3C_2T_x$ (MXene): cells grown on $Ti_3C_2T_x$ coatings; IL-1β: cells treated with IL-1β; $Ti_3C_2T_x$ (MXene) + IL-1β: cells grown on $Ti_3C_2T_x$ coatings treated with IL-1β) (Mean ± SD; n=3)

Figures S14-20 show the fatty acid distribution of the individual lipid classes, in order of highest compositional abundance. Lipids containing saturated and monounsaturated fatty acids such as palmitic acid (16:0), stearic (18:0) and oleic acid (18:1) were the most abundant in each of the different lipid classes observed. In general, only small compositional changes in the fatty acid profile of the individual lipid classes were observed, which are probably not significant. Exceptions to this were PG lipids, which were compositionally richer in PG 16:0_18:1 (**Fig. 4.18)** and DG lipids, that were compositionally reduced in DG 16:0_18:1 and DG 18:1_18:1 (**Fig. 4.15**) when incubated with IL-1β and $Ti_3C_2T_x$ with IL-1β. Similarly, LPC lipids were richer in LPC 16:0 but reduced in LPC 18:0 in the presence of IL-1β and $Ti_3C_2T_x$ with IL-1β (**Fig. 4.16**) and PC lipids were richer in PC 32:0 (possibly PC 16:0_16:0) in the presence of $Ti_3C_2T_x$ with IL-1β (**Fig. 4.17**). Finally, SM was compositionally richer in SM 34:0 (possibly SM 18:0_16:0) in the presence of IL-1β and $Ti_3C_2T_x$ with IL-1β and reduced in SM 42:3 in the presence of IL-1β (**Fig. 4.19**).
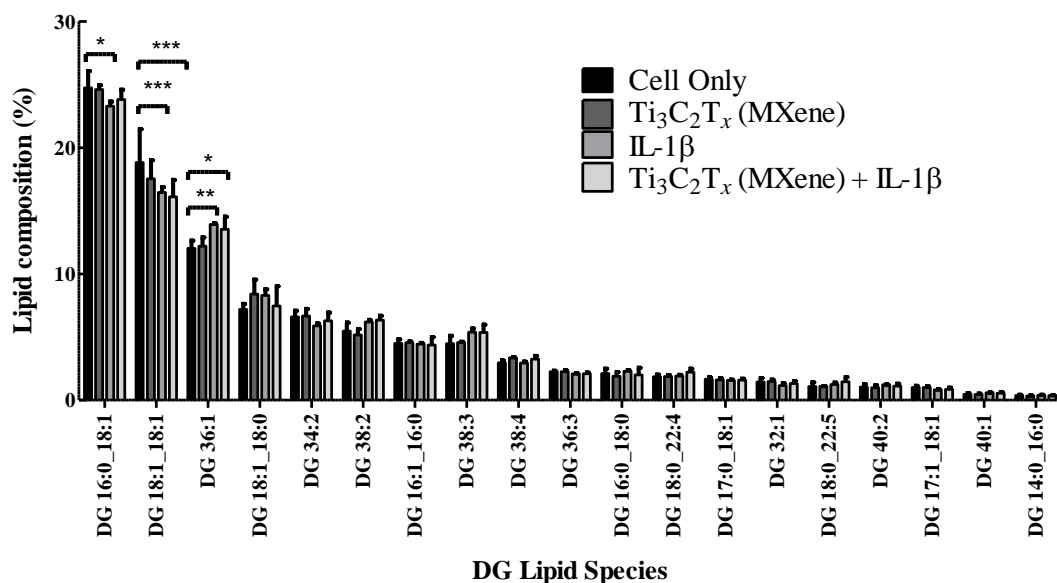
Figure 4.15: Fatty acid composition (%) in diglycerides (DG) lipid species in cells treated with Ti₃C₂Tₓ and IL-1β. A significant downregulation in DG 16:0_18:1 and DG 18:1_18:1 and a significant upregulation in DG 36:1 was found in cells treated with IL-1β relative to the cell only. Significance was determined using a two-way ANOVA and post-hoc Bonferroni's comparison of all conditions to one condition '**Cell only**'. *p $\leq$0.05, ** p $\leq$ 0.01, ***p $\leq$ 0.001. Lipid identifications are described using the Lipidmaps specification (294). Species in order of highest compositional abundance. (Cell only: cells alone; Ti₃C₂Tₓ (MXene): cells grown on Ti₃C₂Tₓ coatings; IL-1β: cells treated with IL-1β; Ti₃C₂Tₓ (MXene) + IL-1β: cells grown on Ti₃C₂Tₓ coatings treated with IL-1β) (Mean $\pm$ SD; n=3)
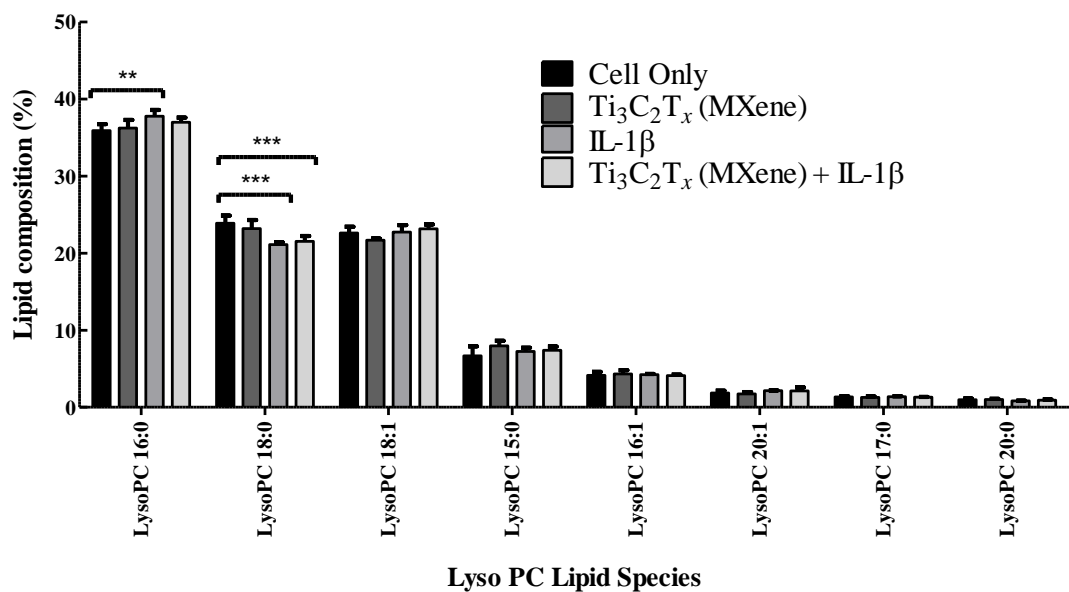
Figure 4.16: Fatty acid composition (%) in lysophosphatidylcholine (LysoPC), lipid species in cells treated with $Ti_3C_2T_x$ and IL-1β. A significant upregulation in Lyso PC 16:0 and a significant downregulation in Lyso PC 18:0 was found in cells treated with IL-1β relative to the cell only. Significance was determined using a two-way ANOVA and post-hoc Bonferroni's comparison of all conditions to one condition '**Cell only**'. ** $p \leq 0.01$, ***$p \leq 0.001$. Lipid identifications are described using the Lipidmaps specification (294). Species in order of highest compositional abundance. (Cell only: cells alone; $Ti_3C_2T_x$ (MXene): cells grown on $Ti_3C_2T_x$ coatings; IL-1β: cells treated with IL-1β; $Ti_3C_2T_x$ (MXene) + IL-1β: cells grown on $Ti_3C_2T_x$ coatings treated with IL-1β) (Mean ± SD; n=3)

Figure 4.17: Fatty acid composition (%) in phosphatidylcholine (PC) lipid species in cells treated with $Ti_3C_2T_x$ and IL-1β. A significant upregulation in PC 32:0 was found in cells treated with $Ti_3C_2T_x$ + IL-1β relative to the cell only. Significance was determined using a two-way ANOVA and post-hoc Bonferroni's comparison of all conditions to one condition '**Cell only**'. ** $p \leq 0.01$. Lipid identifications are described using the Lipidmaps specification (294). Species in order of highest compositional abundance. (Cell only: cells alone; $Ti_3C_2T_x$ (MXene): cells grown on $Ti_3C_2T_x$ coatings; IL-1β: cells treated with IL-1β; $Ti_3C_2T_x$ (MXene) + IL-1β: cells grown on $Ti_3C_2T_x$ coatings treated with IL-1β) (Mean ± SD; n=3)

134

Figure 4.18: Fatty acid composition (%) in phosphatidylglycerols (PG) lipid species in cells treated with Ti$_3$C$_2$T$_x$ and IL-1β. A significant upregulation in PC 32:0 was found in cells treated with Ti$_3$C$_2$T$_x$ + IL-1β relative to the cell only. Significance was determined using a two-way ANOVA and post-hoc Bonferroni's comparison of all conditions to one condition '**Cell only**'. ** p ≤ 0.01. Lipid identifications are described using the Lipidmaps specification (294). Species in order of highest compositional abundance. (Cell only: cells alone; Ti$_3$C$_2$T$_x$ (MXene): cells grown on Ti$_3$C$_2$T$_x$ coatings; IL-1β: cells treated with IL-1β; Ti$_3$C$_2$T$_x$ (MXene) + IL-1β: cells grown on Ti$_3$C$_2$T$_x$ coatings treated with IL-1β) (Mean ± SD; n=3)

Figure 4.19: Fatty acid composition (%) in sphingomyelin (SM) species in cells treated with $Ti_3C_2T_x$ and IL-1β. A significant upregulation in SM 34:0 and a significant downregulation in SM 42:3 was found in cells treated with IL-1β and $Ti_3C_2T_x$ + IL-1β relative to the cell only. Significance was determined using a two-way ANOVA and post-hoc Bonferroni's comparison of all conditions to one condition '**Cell only**'. ** $p \leq 0.01$, *** $p \leq 0.001$. Lipid identifications are described using the Lipidmaps specification (294). Species in order of highest compositional abundance. (Cell only: cells alone; $Ti_3C_2T_x$ (MXene): cells grown on $Ti_3C_2T_x$ coatings; IL-1β: cells treated with IL-1β; $Ti_3C_2T_x$ (MXene) + IL-1β: cells grown on $Ti_3C_2T_x$ coatings treated with IL-1β) (Mean ± SD; n=3)

4.4 Discussion

This chapter has presented the genomic and lipidomic profiling of FHL124 cells on exposure to $Ti_3C_2T_x$ and IL-1β. Cells were treated with $Ti_3C_2T_x$ to investigate the effect of $Ti_3C_2T_x$ alone and then with $Ti_3C_2T_x$ and IL-1β to mimic inflammatory upregulation following cataract surgery and the impact of $Ti_3C_2T_x$ on this. It has shown for the first time that $Ti_3C_2T_x$ does not significantly upregulate DEGs in hallmark inflammatory and EMT gene sets relative to the LECs alone and that $Ti_3C_2T_x$ can markedly reduce the gene fold transcription of key genes involved in

the cytokine-cytokine receptor interaction pathway in IL-1β-primed cells. This work has also mapped with the gene expression profiles of *CXCL1, IL-6* and *IL-1β* as quantified by q-PCR presented in **Fig. 3.16** (**Fig. 4.7**). This chapter also investigated the impact of $Ti_3C_2T_x$ on the lipid cell membrane composition, as a potential mechanism behind the ability of $Ti_3C_2T_x$ to enter the cell and repress pro-inflammatory gene transcription. $Ti_3C_2T_x$ did not significantly impact lipid composition after 24-hour exposure, supporting the biocompatibility of $Ti_3C_2T_x$ shown previously in this *in vitro* LEC model. This suggests $Ti_3C_2T_x$ may have the ability to interact with the cell membrane without causing significant damage unlike when exposed to bacterial cells. An alternative mechanism of action may be that $Ti_3C_2T_x$ may not need to enter the cells to induce intracellular pathways but may simply interact with the cell receptors to induce such changes, supported by the RNA-Seq which showed the interaction of $Ti_3C_2T_x$ with the cytokine-cytokine receptor interaction pathway.

FHL124 cells have been previously shown to be suitable for use in lens biology studies and RNA-Seq to investigate the developmental pathways of PCO (85). All samples passed sequencing data quality control checks. Functional analysis of significant DEGs were analysed in cells treated with IL-1β (*I_v_C*) (**Fig. 4.5, 4.6**). This was done for two reasons. The first was to validate the use of IL-1β as a positive control for pro-inflammatory response in LECs by investigating the intracellular pathways that were upregulated in IL-1β-primed LECs to key pathways in PCO development. Secondly, there were few DEGs between the *M_v_C* and *I_v_MI* comparisons. As there was only 6 DEGs between *I* and *MI* samples, it suggests that many of the upregulated pathways in the *MI_v_C* would overlap with the *I_v_C*. Therefore, the functional analysis of *I_v_C* alone was completed.

The upregulated BP, MP and KEGG pathways further supported the use of IL-1β in the stimulation of LECs to provide a positive control for upregulation of cellular inflammatory pathways linked to PCO development. Of those pathways which were upregulated, the ER stress response and UPR was the most upregulated and unexpected. In PCO development, surgically induced trauma induces a wound-healing response in any remaining LEC within the capsule bag,

137

promoting a cascade of pro-inflammatory and EMT pathways. In the event of cellular stresses, the ER and UPR is activated. UPR is part of the homeostatic response to maintain correct synthesis, folding and secretion of proteins (234–236). This process can be preventative or pathogenic; chronic UPR leads to ER stress and the onset of protein misfolding diseases (236). Within the eye, retinitis pigmentosa, the breakdown of photoreceptor rods leading to loss in vision, is commonly caused by a mutation in rhodopsin that increases the UPR which in turn has been linked to the degeneration of the photoreceptor rods (236). During cataract development, misfolded proteins aggregate contributing to the symptoms of the conditions. This process has been linked to ER stress and subsequent UPR, induced by the damaged chaperones α-crystallins, cryAA and cryAB (235,236). Therefore, IL-1β could be used to mimic the wound-healing response of LEC by its ability to incite the ER stress and UPR in the FHL124 cells.

Additionally, as part of the synthesis and secretion of proteins, amino acid structures will enter the ER for further processing and folding into their secondary and tertiary structures. These processes are supported by chaperones (237). During stress, ER chaperones can be affected, leading to an accumulation of unfolded proteins which activates the UPR response, as discussed previously (234–237). Chaperones are highly upregulated in the UPR response to prevent aggregation of unfolded proteins and to allow for proper folding. Key chaperones include BiP (HSPA5), heat shock protein (Hsp) families, GrpE and DnaJ (237). Several Hsp chaperones were upregulated in the *I* samples (**Fig. 4.5**). Hsp90 is a Hsp involved in protein homeostasis in physiological and pathological conditions (238). In tumour cells, Hsp90 plays a role in cell proliferation and EMT (239). Moreover, the chaperone has shown to promote skin wound repair by upregulating keratinocyte migration in primary neonatal keratinocytes and a diabetic wound murine model (240,241). The wound-healing response and LEC migration are established pathways contributing to PCO development. Therefore, Li et al., (242) investigated the impact of Hsp90 in key developmental pathways of PCO. In LECs extracted from an *ex vivo* rat capsule model, Hsp90 and other chaperones were detected. Inhibition of Hsp90 by 17-AAG prevented epithelial-growth factor receptor (EGFR) signalling and TGF-β-induced SMAD2/3 signalling

pathways which initiates proliferation, migration and differentiation of residual LEC PCS, respectively. This suggests Hsp90 induces proliferation and EMT of residual LEC as part of the wound-healing response and as a potential marker for these pathways. This further supports the use of IL-1β in *in vitro* cell models to induce ER stress pathways contributing to PCO development by its ability to incite key ER chaperones contributing to EMT of LEC.

The ER stress response has also been linked to promotion of the EMT pathway in various cell types (243–245). Zhou et al., (234) treated human LEC line SRA01/4 with thapsigargin (TG) and tunicamycin (TM) to induce ER stress. TG- and TM-treated cells displayed spindle-like morphology, loss of epithelial marker E-cadherin partnered with an increased expression of vimentin, fibronectin and α-SMA with greater migration rates, indicative of cells undergoing EMT. The ER stress response has also been targeted for PCO prevention. Sulforaphane (SFN), an organic isothiocyanate found in cruciferous vegetables, has been linked to promoting ER stress and UPR signalling leading to cell apoptosis (246,247). Liu et al., (246) investigated SFN to induce cell death in human capsule bags and FHL124 cell line. Treatments above 10 µM showed a significant reduction in cell viability and migration. The study also examined the impact of SFN on autophagy, the process of removing damaged cells that plays a role in lens maintenance and fibre differentiation (248,249). Western blot analysis showed significant increase in autosomal marker protein LC3 and TEM imaging displayed increased numbers of autophagosomes in cells treated with SFN above 10 µM. The exploitation of the ER stress and response and UPR in LECs should be explored further as a tool to prevent PCO development.

The use of IL-1β as a positive control to induce the developmental pathways of PCO was further supported by the identification of DEGs for long non-coding RNA (lncRNA). In recent investigation, lncRNA has been identified to play a role in eye development (250–252). These lncRNA are part of a family of circulating nucleic acids (CNA) that regulate physiological and pathologically conditions (251,253). Altered levels of CNA have been linked to diabetic retinopathy and age-related macular degeneration (250,252). CNA typically enters blood circulation due to the apoptosis of cells (254). During cataract formation, LEC undergo apoptosis

(251,253). Therefore, Shen et al., (251) investigated lncRNA expression in cataractous lenses. Of those most abundant, lncRNA-MIAT was shown to be highly elevated in patients' plasma and AH. MIAT knockdown in SRA01/04 significantly decreased viability, migration and proliferation. The study continued by investigating the wound-healing response of LEC during PCO development and the impact of lncRNA-MIAT. SRA01/04 cells treated with TNF alpha increased viability, proliferation and migration whereas cells with MIAT knockdown was shown to attenuate these changes.

The treatment of IL-1β to FHL124 cells also upregulated collagen binding pathways. Collagen is a main component of the ECM in the capsule bag and in LEC. MMPs are enzymes involved in the regulation of the ECM, including collagen and may remodel the ECM PCS leading to capsule wrinkling (255). IL-1β upregulated the expression of *MMP-9* and *MMP-12* mRNA (**Fig. 4.6**). Both these MMPs have been linked to the regulation of collagen (256,257). Positive resolution of the wound-healing response is a balance to ensure the injury has been resolved without inducing chronic inflammatory responses. MMP-9 is induced by pro-inflammatory cytokines and has been linked to play a role in this balance (258). LeBert et al., (256) examined the impact of MMP-9 in an acute and chronic inflammation zebrafish model. In the acute inflammation model, MMP-9 was essential for tissue regeneration, leukocyte recruitment and collagen fibre thickening for wound resolution. Conversely, in the chronic inflammation model MMP-9 exposure led to collagen fibre disorganisation, suggesting MMP-9 has an important role in collagen fibre remodelling. MMP-9 acts the same to maintain corneal transparency (259). MMPs have also shown to play a role in cancer and cell migration (258,260). High levels of MMPs have been found in sham cataract surgery models and treatment of MMP inhibitors have prevented LEC migration and lens capsule contraction (260). Moreover, TGF-β2 also induces MMP-2 and MMP-9 linked to cell migration and ECM remodelling (106). This highly supports the role of MMPs in PCO development and the ability of IL-1β to induce their expression in the FHL124 cell line further supports the use of IL-1β as a positive control for inflammatory pathways contributing to PCO development.

GSE analysis was performed to determine the enrichment of gene sets between cells treated with IL-1β (*I*) and cells treated with $Ti_3C_2T_x$ (*MI*) treatment, specifically focussed on the hallmark inflammation and EMT gene sets. The GSEA of IL-1β-primed cells was similar to literature (85,109,212). The upregulation of genes within the cytokine-cytokine receptor pathway by IL-1β-treated cells (*I*) (**Fig. 4.11**) was comparable to mouse LEC from sham cataract surgery (**Fig. 4.2**). Both displayed high upregulation in the CXC subfamily, an innate immune response family. There was also a high log fold change in CCL2 found in cells treated with IL-1β (*I*) and cells treated with $Ti_3C_2T_x$ and IL-1β (*MI*) (**Fig. 4.9, 10**). CCL2 is a monocyte chemotactic protein-1 which has been detected in samples obtained from cataract surgery patients. Moreover, enriched hallmark inflammation genes in the FHL124 cells treated with $Ti_3C_2T_x$ or IL-1β (**Fig. 4.8**) were similar to young and aged FHL124, respectively (85). Young FHL124 cells showed a negative NES in the gene sets for the UPR, EMT and UV response down, mirrored in the cells treated with $Ti_3C_2T_x$ (*M_v_C*). These pathways have been linked to the young cells' focus on maintaining cell viability and proliferation (85). Both aged FHL124 cells and FHL124 cells treated with IL-1β (*I_v_C*) showed a positive NES for inflammatory response, interferon gamma and alpha response, TNFA signalling via NFβ and UV response up. These pathways are indicative with cells managing under stress, either due to age or injury (85). This provides confidence that the positive inflammatory control IL-1β was suitable to mimic LEC inflammation PCS and the presence of $Ti_3C_2T_x$ did not significantly impact normal physiological processes of the LECs.

Cells treated with $Ti_3C_2T_x$ alone had 8 DEGs relative to the cell only control (*M_v_C*). None of these DEGs have been linked to the wound-healing response or EMT of LECs. $Ti_3C_2T_x$-treated cells (*M*) did not significantly upregulate any genes involved in the hallmark inflammation pathways in comparison to the cell control (*C*) (**Fig. 4.8**). Of note was the high NES for oxidative phosphorylation in $Ti_3C_2T_x$-treated cells. However, it has been previously shown that $Ti_3C_2T_x$ did not upregulate ROS production in THP-1 cell line and no lipid peroxidation was detected in the lipidomic profile (**Fig. 4.14**) (14). It could be suggested that despite the upregulation of oxidative phosphorylation genes by $Ti_3C_2T_x$ this may not present in intracellular processes. There was no

significant upregulation in core enrichment genes in the *M_v_C* comparison supporting that the presence of $Ti_3C_2T_x$ with the LEC does not promote pro-inflammatory pathways (**Fig. 4.8**).

Cells treated with IL-1β significantly upregulated hallmark inflammation gene sets in comparison to the cell only control (*I_v_C*) (**Fig. 4.8, 9, 10**). Cells treated with $Ti_3C_2T_x$ and IL-1β did not show significant suppression of pro-inflammatory gene sets relative to the *I* samples (*MI_v_C*) (**Fig. 4.8, 9, 10**). Nevertheless, in **Fig. 4.8**, there are several gene sets in the *I_v_MI* comparison that have a higher NES score which corresponds with a negative NES in the *M_v_C* comparison. Using the 'inflammatory response' gene set as an example (**Fig. 4.8**), the *I_v_C* comparison show a NES of +3 and the *MI_v_C* show a NES of +2 which correlates with the -1 NES of *M_v_C* and the +1 NES in the *I_v_MI*. Side-by-side view of individual inflammatory response genes and the cytokine-cytokine receptor interaction pathway also suggests that there is marked reduction in these genes in cells treated with $Ti_3C_2T_x$ and IL-1β (*MI*) relative to cells treated with IL-1β alone (*I*) (**Fig. 4.11**). This supports the initial findings that were discussed in **Chapter 3** and suggests that $Ti_3C_2T_x$ has anti-inflammatory effects at optimised concentrations and surface area contact.

There was a significant upregulation in the hallmark EMT gene sets in cells treated with IL-1β relative to cell only (*I_v_C*) and in cells treated with $Ti_3C_2T_x$ and IL-1β relative to the cell only (*MI_v_C*) (**Fig. 4.12**). $Ti_3C_2T_x$ treatment did not significantly suppress any hallmark EMT gene transcription. Nevertheless, the several EMT genes identified to be more weakly induced by IL-1β-primed cells treated with $Ti_3C_2T_x$ (*MI_v_C*) are linked to immune upregulation, cytoskeletal remodelling, TGF-β-induced SMAD signalling and positive regulation of wound healing response (**Fig. 4.13**). This suggests that LEC inflammation incited by IL-1β could influence the activation of EMT pathways, which could be dampened in the presence of $Ti_3C_2T_x$.

The lipidomic profile of FHL124 cells treated with $Ti_3C_2T_x$ was investigated to explore if the interaction of $Ti_3C_2T_x$ with the LEC gene transcription requires some interaction by $Ti_3C_2T_x$ with the lipid cell membrane for $Ti_3C_2T_x$ to first enter the cell. The lipid class composition of the

FHL124 cells was similar to literature, providing confidence that the experimental set-up and isolation of lipids was valid (**Fig. 4.14**) (215,216). Several studies suggest that MXene nanosheets exert anti-bacterial properties by penetrating the bacteria membrane using 'nano thermal blades' (60,261). $Ti_3C_2T_x$ did not cause any significant changes in lipid class composition (**Fig. 4.14**). This suggests $Ti_3C_2T_x$ does not act as an ocular irritant and has good biocompatibility in the ocular environment, at the concentrations studied. Incubation in the presence of IL-1β can cause increases in diacylglycerol lipids but these are typically transient occurring within a few minutes of initiation (262). IL-1β did not cause significant changes in the total lipid profile at 24 hrs. Further work would include using a shorter incubation profile with IL-1β to confirm any transient changes in lipid composition. For instance, Zumwalt et al., (218) treated glioma cells with IL-1β for 30 minutes prior to analysis.

Lipids like SM, PC, PS, LPC, DG and PG are lipid messengers involved in mediating inflammation and wound healing in other non-ocular cell lines (161,217,263). The composition changes seen in the lipids in the cells treated with IL-1β (*I*) and cells treated with $Ti_3C_2T_x$ and IL-1β (*MI*) may reflect an inflammatory response in a small subset of saturated/ monounsaturated lipids containing 16:0 and 18:1 fatty acids **(Fig. 4.15 – 19)**. Interestingly, an upregulation in LPC 16:0 and downregulation in LPC 18:0 was observed (**Fig. 4.16**). This was not expected as it has been previously reported that IL-1β and LPC 18:0 work in synergy to promote IL-6 expression in rabbit glioma cells (218). PC lipids are parent lipids to LPC. PC is hydrolysed by phospholipase A activity which can be activated as part of the defence mechanism during bacterial infection and by IL-1β treatment (217,218). It was found that cells treated with IL-1β showed an increase in PC 32:0 whilst there was an increase LysoPC 16:0 (**Fig. 4.16, 4.17**). Therefore, in human LEC lines, LysoPC 16:0 may act as a secondary messenger for IL-1β. Further work will be required to support this hypothesis and elucidate the significance of this. Moreover, during the protected release mechanism of IL-1β by THP-1 monocytes, the PS lipids are remodelled to the outer leaflet of the plasma membrane (161). Further work should explore the impact of this and how $Ti_3C_2T_x$ may affect the location of lipids within the plasma membrane.

In this chapter, the mechanism of action underlying the cytokine suppression by $Ti_3C_2T_x$ was investigated using genomic and lipidomic analysis. In consideration of both the genomic and lipidomic profiles of FHL124 cells treated with $Ti_3C_2T_x$, a suggested mechanism of action behind the ability of $Ti_3C_2T_x$ to induce intracellular pathways without causing damage to the lipid membrane may be as a result of the ability of $Ti_3C_2T_x$ to interact with the cells at a receptor-level, specifically the cytokine-cytokine interaction response pathway, to induce cell transcriptome changes. The genomic profile showed an upregulation in NF-κβ proteins in cells treated with IL-1β and cells treated with $Ti_3C_2T_x$ and IL-1β, suggesting that $Ti_3C_2T_x$ does not impact this transcription factor to repress pro-inflammatory gene transcription. The expression of STAT3 and STAT1 transcription factors did not differ between cells treated with IL-1β and cells treated with $Ti_3C_2T_x$ and IL-1β. However, STAT2 and STAT6 were not detected in cells treated with $Ti_3C_2T_x$ and IL-1β whereas an upregulation in these transcription factors was shown in cells treated with IL-1β alone. Both STAT2 and STAT6 are involved in the formation of the NLRP3 inflammasome complex (264,265). STAT2 is involved in interferon (IFN-γ) signalling, mediating antiviral activity (265). STAT6 predominantly acts to induce IL-4 biological responses, involving IL-4-induced macrophage polarisation occurring during fibrosis and other pathological inflammatory conditions. Czimmerer et al., (264) showed that IL-4-activated STAT6 directly repressed macrophage polarisation by decreasing line-age-determining transcription factor, p300 and RNA polymerase II binding which dampened IL-1β release. The study was also able to show that STAT6 acted on the NF-κβ p65 binding sites which reduced macrophage responsiveness to LPS. The significance of $Ti_3C_2T_x$ downregulating STAT6 gene expression and RNA polymerase II subunit J3 to limit the activation of the NLRP3 inflammasome complex should be explored further as a potential mechanism behind the repression of IL-1β release by $Ti_3C_2T_x$.

In conclusion, the functional analysis and GSEA showed that the experimental controls used in this *in vitro* FHL124-based inflammation model were suitable. It was established that the use of IL-1β as a positive control to induce pro-inflammatory pathways leading to PCO

development in the *in* vitro cell model was valid. Although IL-1β did not induce any significant changes in lipid composition after 24 hours, the effect of IL-1β is transient and may have been detected if a shorter incubation period had been used. However, the lipidomics analysis confirmed the biocompatibility of LEC when incubated with $Ti_3C_2T_x$. It can be suggested based on the evidence demonstrated in **Chapter 3** and **4** that $Ti_3C_2T_x$ does not induce a pro-inflammatory response in LEC and may act to repress cytokine expression at optimum concentrations, with no deleterious effect on lens cells' lipid composition or increased propensity towards EMT. These chapters have demonstrated that $Ti_3C_2T_x$ represses inflammation and EMT associated pathways which are known to contribute to PCO development through mechanisms which promote a positive resolution of the wound healing response within an *in vitro* LEC model. It was observed in the RNA Seq analysis that there were some downregulation in cyclin-dependent kinases (CDK), regulators of the cell cycle and p53 inducible proteins. The potential involvement of senescence associated pathways in the induction of the hyperinflammation and fibrotic events that contribute to PCO development and the impact of $Ti_3C_2T_x$ to induce cellular senescence was therefore investigated in a preliminary study in **Chapter 5**.

Chapter 5: The role of senescence and addition of $Ti_3C_2T_x$ (MXene) on fibrotic pathways contributing to posterior capsule opacification

5.1 Introduction

5.1.1 The role of senescence in age-related conditions

Senescence has been suggested to play a role in age-related conditions including cataracts (266). Several pathways that are upregulated in cell senescence are pathways involved in inflammation and fibrosis of LECs leading to PCO development such as the PI3K/AKT and JAK/STAT pathways (267). Nevertheless, the role of senescence in inducing fibrosis and inflammation contributing to PCO development and how $Ti_3C_2T_x$ may impact cellular senescence is unknown. Cellular senescence is the stable and permanent arrest of the cell cycle following extended culture (132,266). It can occur randomly in the cell at any time it undergoes division, potentially as a result of unfavourable conditions at G_1 (268). This stage is known as G_0. The cell cycle is the life cycle of a cell which consist of processes that allow the duplication of the original cell into two identical daughter cells. DNA duplication and cell division occurs in the synthesis (S) phase and mitosis (M) phase, respectively (131). There are two growth stages within the cycle, G_1, between the M phase and the S phase, and G_2, between the S phase and M phase. The first growth phase (G_1) is used to monitor the external and internal environment of the cell to check that the conditions are optimum for cell division (131). A second growth phase (G_2) is required to check errors in replication to ensure the cell is ready to enter the M phase. During mitosis, the sister pairs of chromosomes line up on the mitotic spindle and then separate into two new daughter cells known as cytokinesis (**Fig. 5.1**).

Senescent cells leave the cell cycle from the G_1 phase and undergo alternations in their gene transcriptome (268). Cells favour a senescence-associated secretory phenotype (SASP) over an apoptotic state and begin to express pro-inflammatory ligands (132,269). Fibroblasts have shown altered gene expression of *ICAM-1, MCP-1* and *IL-1β* leading to an upregulation of pro-inflammatory growth factors and cytokines IL-6, IL-8 and MCP-2 (270). These cytokines then maintain the senescent state, by generating DNA damage. This transformation to a pro-inflammatory profile is believed to promote its own elimination by the immune system (132).

Senescence is a necessary stage of the cell cycle and is used as a preventative tool against malignancy. It is the extent to which the senescent cells are present within a tissue that influences the benefit/harmful balance (132). When senescent cells accumulate over a period of time in the surrounding tissues, this promotes pro-inflammatory pathological conditions such as cataracts, corneal disorders and potentially, PCO (132,266,271).
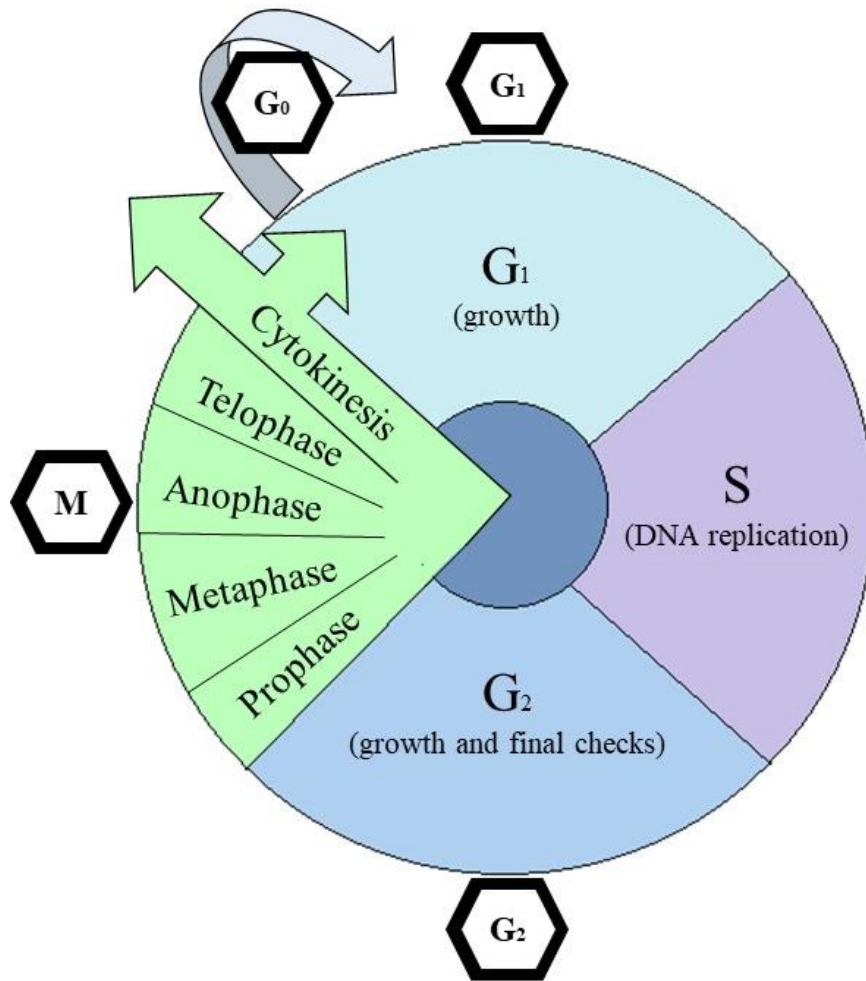
Figure 5.1: Life cycle of a cell. Cells are either within interphase or division stage. Cells will undergo mitosis to separate into two identical daughter cells. Senescence (G_0) can occur after division. (G_1: first growth phase; G_2: second growth phase; S: synthesis phase; M: mitosis stage) (131).

There are several triggers for cell senescence including telomere loss, oxidative stress and cell-cell fusion (**Fig. 5.2**) (132). Severely stressed cells will undergo apoptosis whereas under

milder stresses, cells will commence senescence. Cells that have experienced DNA damage will remove themselves from the cell cycle in order to repair the DNA damage. At this point, if there is extensive damage, the cell will enter senescence (132). The accumulation of the p53 gene upregulates the cyclin-dependent kinase inhibitor (CDKi), p21, which then binds to CDK2, 4 and 6 complexes, dephosphorylating retinoblastoma (RB) and preventing the activation of E2F-dependent gene expression. Activation of these pathways contribute to cell cycle arrest and cellular senescence (132). Long term DNA damage response (DDR) upregulates p16(INK4a), leading to permanent cell cycle arrest. The senescent cells develop SASP which promotes positive feedback loops that maintain the senescent state by dysregulating mitochondria function, upregulating cytokine release such as IL-6 and -8 and expressing ECM-degrading proteins (132,269). This SASP state promotes immune cell infiltration and removal of the senescent cells, similar to a wound healing response. Pathologies occur when there is poor removal of the senescent cells, leading to an accumulation in tissue contributing to age-related conditions (269).
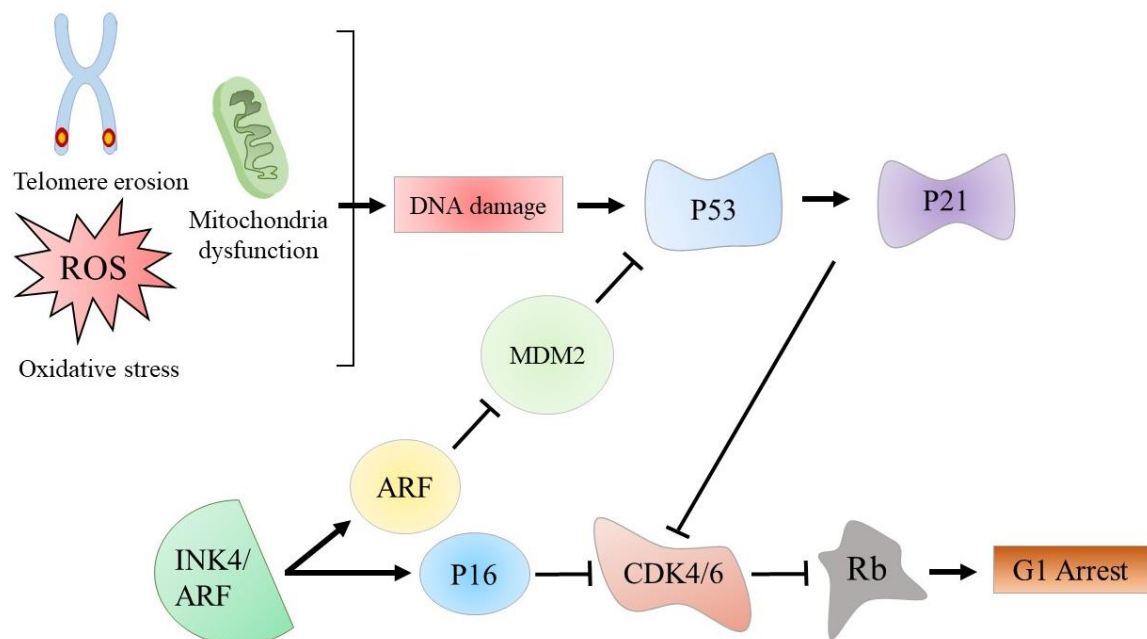
Figure 5.2: Signalling pathways of senescence. The repression of CDK4/6 is regulated by p53/p21 accumulation and p16 pathways, leading to the cell cycle arrest and induction of senescence. Adapted from Zhu et al., (267).

5.1.2 Senescence-induced ocular conditions and senotherapy

Ageing is the greatest risk factor for cataracts (266,272). Age-related cataracts (ARCs) represents over half of all cataract cases (266). The pathological mechanism is still relatively unknown. Senescence is a hallmark of ageing and it has been strongly suggested to induce ARC formation (70,266,272,273). Lens stem progenitor cells (LSCs) are a small subpopulation of LEC that proliferate and differentiate into lens fibre cells. LSCs dysfunction has been linked to cataractogenesis. Fu et al., (266) showed that functional human LSCs declined with age and an increased rate of senescence occurred in the terminally differentiated cells could contribute to ARCs. There is also some suggestion that senescent lens cells increase the dysregulation and aggregation of crystallins that then contribute to lens opacification (273). Telomerase is a ribonucleoprotein which maintains telomere length, a process which is believed to prevent senescence. Colitz et al., (274) showed in the canine lens that telomerase was highly present in the central, germinative and equatorial regions of the lens but not present in the lens fibre cells. The role of telomerase in these regions were hypothesised to be as part of the recovery of UV radiation damaged LECs and due to the high mitosis rate in the germinative region. Interestingly, telomerase activity was greatly increased in cataractous lens comparatively to normal lens which could be attributed to a protective mechanism against UV-induced DNA damage or as a response to the increased proliferation of cells compensating for the cataract-induced dysfunction. In the lens capsule, there were no senescent cells present immediately after dissection. Over time, the senescent cell population increased which mapped with the subsequent decrease in telomerase found within the cells. Wang et al., (275) also found a greater accumulation of senescent cells present in a 28-day D-galactose-induced cataract rat model relative to the control lenses. After treatment with senolytic drugs, dasatinib and quercetin, the expression of p16 and γH2AX, a histone variant abundant during the DNA damage response (DDR), was significantly lower. These studies suggests that senescence may contribute to cataract formation which may then contribute to the developmental pathways of PCO within the remaining LEC residing in the capsule PCS.

Cells that have experienced DNA damage-induced senescence will undergo cell cycle arrest and release of pro-inflammatory mediators, referred to as the hyper secretory SASP. These SASP pathways are similar to the PCS environment of the capsule bag (**Fig. 1.9**). The significant alteration in the gene transcriptome and release of cytokines culminating to an altered phenotype and morphology of a senescent cell from its progenitor cell is mirrored in the inflammation and EMT of LEC PCS. However, the role of senescence within PCO is still relatively unexplored. Senolytic drugs have been used to target key pathways in PCO development. Senolytic drugs, along with SASP inhibitors, are part of a novel treatment against senescence, known as senotherapy. Senolytic drugs can selectively target senescent cells for apoptosis and removal such as dasatinib and quercetin which eliminate senescent cells and reduce the SASP (267). Resveratrol (RESV) targets the SIRT1/NF-κβ pathway and has been shown to reverse senescence in liver epithelial cells (276) (Heidari et al., (133) (*manuscript in preparation*) and inhibit cell migration in cancer and retinal epithelial cells (70,267). Smith et al., (70) showed that RESV significantly suppressed TGF-β2-induced EMT in FHL124 cells. RESV reverted TGF-β2 induced transdifferentiation of LECs and significantly reduced α-SMA expression. It was also shown to prevent capsule wrinkling, contributed to by the suppression of MMP-2 and prevention of ECM remodelling and cell attachment (70). The p38 MAPK inhibitor SB203580 has been shown to inhibit cataract formation and downregulate the EMT response, linking SASP to both cataracts and PCO (277,278). This is further developed by exploring the targeted mechanisms of senolytic drugs and SASP inhibitors (**Fig. 5.3**). Dasatinib and 17-DMAG both target HSP90 and PI3K/AKT, cell machinery that has been linked within the development of PCO (127,242,267). SASP inhibitors such as Ruxolitinib inhibit inflammation by targeting the JAK pathway (267). The JAK/STAT3 pathway has implicated within IL-6 signalling (110) and the genomics analysis within this body of work has shown how JAK1 is upregulated by IL-1β treatment (**Chapter 4**). These findings collectively support the investigation of the role of senescence in PCO development. It is unknown whether the residual LEC within the capsule bag PCS could be remnants of senescent cells that contributed to the development of the cataract, then becoming progenitor cells for PCO development. Senescence may also be triggered in residual LEC by the

surgical trauma, generating DNA damage which then initiates the SASP, cascading towards PCO development.
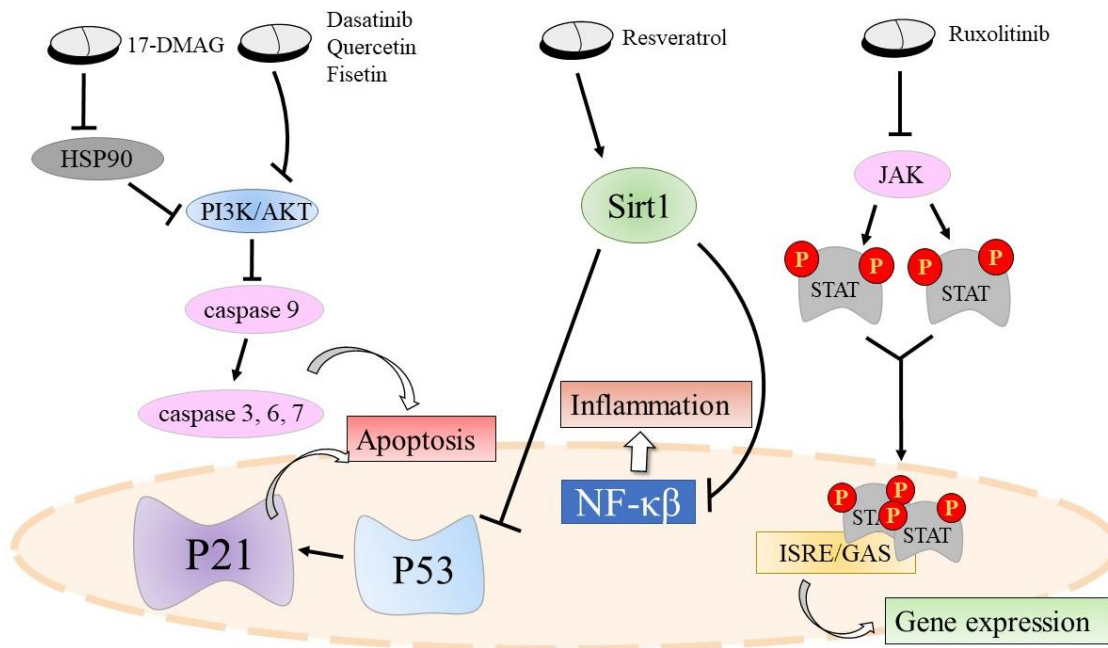
Figure 5.3: Targeted signalling pathways of senolytic and SASP inhibitors. Adapted from Zhu et al., (267).

5.1.3 Chapter aims

This chapter aimed to explore the role of senescence within the inflammatory and fibrotic pathways contributing towards PCO development and how the presence of $Ti_3C_2T_x$ coatings may impact the induction of cellular senescence. Firstly, a positive control to induce senescence in FHL124 cells was established. Secondly, the ability of IL-1β and TGF-β2 to induce upregulation of key senescence markers in the lens cells relative to the established positive control was compared. The findings were then used alongside the genomics analysis to establish any potential link between trauma-induced lens cell senescence triggered PCS resulting in the induction of developmental pathways leading to PCO.

5.2   Methods

5.2.1 Optimisation of etoposide treatment to induce senescence in lens epithelial cells

To investigate the impact of etoposide treatment to induce senescence pathways in FHL124 cells, the cells were first treated with etoposide for 8 hours and then collected. FHL124 cells were seeded into the wells of a 12 well tissue culture plate at a concentration of 6×10^5 cells mL^{-1}. Treatment and control groups were set up to include cells only, $Ti_3C_2T_x$-treated cells (5 mg mL^{-1} coatings), cells with etoposide (10 µm mL^{-1}), IL-1β-treated cells (100 ng mL^{-1}), cells treated with $Ti_3C_2T_x$ and IL-1β, cells treated with TGF-β2 (20 ng mL^{-1}), and cells treated with $Ti_3C_2T_x$ and TGF-β2. Each treatment and control group were prepared in duplicate and incubated for 24 hours at 37 °C, 5 % CO_2 prior to their treatment then incubated for a further 8 hours at 37 °C, 5% CO_2.

To investigate if the etoposide treatment induces senescence over time, FHL124 cells were exposed to etoposide treatment for 8 hours, and then incubated in fresh media for a further 48 hours. FHL124 cells were seeded at a concentration of 5×10^4 mL^{-1} and incubated at 37 °C, 5% CO_2 for 24 hours prior to treatment. Treatment and control groups were set up to include cells only, $Ti_3C_2T_x$-treated cells (2 mg mL^{-1} coatings), cells with etoposide (10 µm mL^{-1}), cells treated with TGF-β2 (20 ng mL^{-1}), and cells treated with $Ti_3C_2T_x$ and TGF-β2. Cells were treated for 8 hours then washed in 1 mL PBS thrice and allowed to incubate in media for 48 hours at 37 °C, 5 % CO_2.

5.2.2 Gene fold change of p16 and p21 in interleukin-1 beta and transforming growth factor beta 2-treated human lens epithelial cells with $Ti_3C_2T_x$ (MXene) coatings

Samples were treated for 8 hours and then immediately used as described in **5.2.1**. Cells were collected using trypsin into Eppendorf's, centrifuged at 11600 rpm for 5 minutes. Expression of primers (**Table 5.1**) were quantified as described in **3.2.9**.

Table 5.1: Primers for senescence marker genes of interest (Qiagen, UK).

Gene Name	Protein Encoded	Catalog Number
CDKN1A_va.1	p21	QT02588621
CDKN2A_vb.1	p16	QT00998459

5.2.3 EdU staining of interleukin-1 beta and transforming growth factor beta 2-treated human lens epithelial cells with $Ti_3C_2T_x$ (MXene) coatings

EdU was performed on both conditions described in **5.2.1**, with the exception of the cells were seeded at a concentration of 5×10^4 cells mL^{-1}. For the first group of samples, after the 8-hour treatment, 10 µM of EdU (5-ethynyl-2'-deoxyuridine) was added for 18 hours. For the second group of samples, 10 µM of EdU was added after the additional 48-hour incubation. Cells were fixed and permeabilised as described in **3.2.12**. The cells were incubated in 500 µL Click-iT® reaction cocktail for 30 minutes, protected from the light then washed thrice in 3 % BSA diluted in PBS. The samples were counterstained with 1 µg mL^{-1} DAPI for 5 minutes then washed thrice. Cells were visualised using a Zeiss LSM800 Confocal Microscope (Carl Zeiss Microscopy GmBh, Germany). Images were analysed using Fiji: Image J analysis. EdU positive cells was quantified by cell counting of the stained nuclei over the total cell count quantified by DAPI nuclei staining.

5.2.4 Release of interleukin-6 and interleukin-8 by human lens epithelial cells grown on $Ti_3C_2T_x$ coatings spiked with etoposide and transforming growth factor beta 2

Samples were treated for 8 hours then incubated for a further 48 hours in fresh media as described in **5.2.1**. At 8 and 48 hours, media samples were collected in Eppendorf tubes, centrifuged at 11600 rpm for 5 minutes and the media was stored in fresh Eppendorf tubes.

Samples were kept at -20°C until required. Detection of IL-6 and -8 release were undertaken following the BD Bioscience protocol as described in **3.2.3**. Samples were analysed neat.

5.2.5 Senescence beta-galactosidase staining of interleukin-1 beta-primed human lens epithelial cells with $Ti_3C_2T_x$ (MXene) coatings

Samples were treated for 8 hours then immediately used as described in **5.2.1**, with the exception of the cells were seeded at a concentration of 1×10^5 cells mL^{-1}. Samples were stained using the Senescence β-Galactosidase Staining Kit (Cell Signalling Technology, UK). The β-Galactosidase Staining Solution was prepared by adding 1X Staining Solution to 20 mg mL^{-1} X-Gal dissolved in DMSO and Solution A and B. Wells were washed in PBS then 1 mL of Fixative Solution was added for 10 minutes. The wells were rinsed in PBS and 500 µL β-Galactosidase Staining Solution was added. The plate was covered in parafilm to avoid evaporation and incubated at 37 °C, no CO_2. Light microscopy images were taken at four weeks.

5.2.6 Statistical analysis

Statistical analysis was performed in Graph Pad Prism version 5 (GraphPad Software, US). For the standard curves, the known concentration standards and wavelength absorbance was compared using linear regression analysis. Parametric statistical significance was determined using a one-way ANOVA. $P \le 0.05$ was considered statistically significant.

5.3   Results

5.3.1 Gene fold change of p16 and p21 in interleukin-1 beta and transforming growth factor beta 2-treated human lens epithelial cells with $Ti_3C_2T_x$ (MXene) coatings

There was no significant upregulation of *CDKN1a* (p21) (**Fig. 5.4 A**) and *CDKN2a* (p16) (**Fig. 5.4 B**) expression in $Ti_3C_2T_x$ and IL-1β treated LECs relative to the cell only control. TGF-β2 treatment did markedly increase gene fold expression of both genes however, this was no

significant. Ti$_3$C$_2$T$_x$ treatment did reduce *CDKN1a* gene fold upregulation after IL-1β priming and *CDKN2a* gene fold upregulation after TGF-β2 treatment. Etoposide treatment induced significant upregulation of both genes in the lens cells.
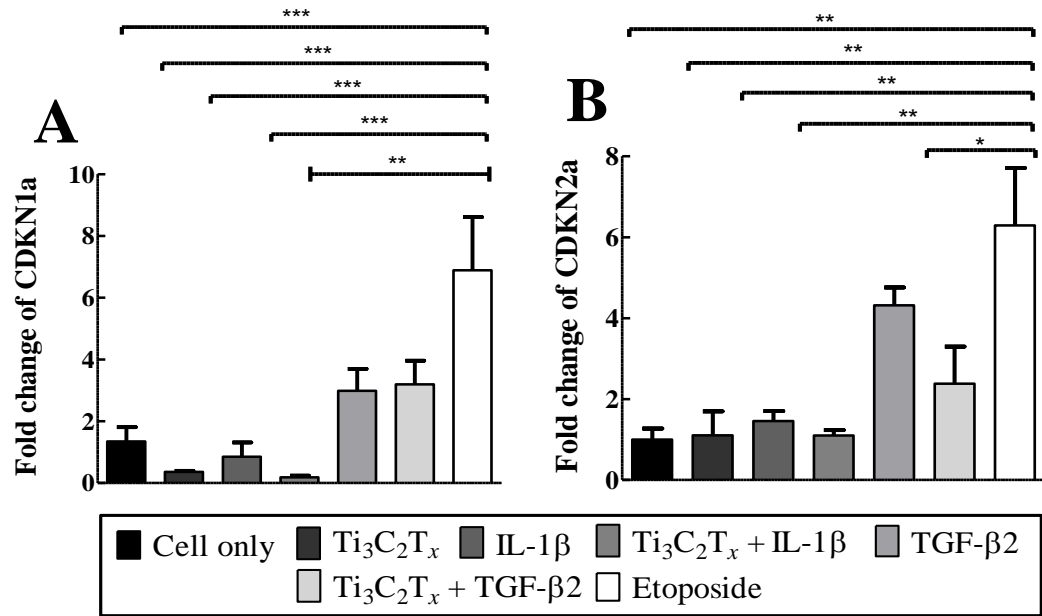
Figure 5.4: Expression of CDKN1a (p21) and CDKN2a (p16) by FHL124 cells grown on Ti$_3$C$_2$T$_x$ coatings. q-PCR amplification of *CDKN1a* (**Fig. 5.4 A)** and *CDKN2a* (**Fig. 5.4 B**) expression in cell only, Ti$_3$C$_2$T$_x$, IL-1β, TGF-β2 and etoposide-treated samples. A one-way ANOVA and Bonferroni's multiple comparison test was completed using GraphPad Prism 5. *p ≤ 0.05, **p ≤ 0.01, ***p ≤ 0.001. (Cell only: cells alone; Ti$_3$C$_2$T$_x$ (MXene): cells grown on Ti$_3$C$_2$T$_x$ coatings; IL-1β: cells treated with IL-1β; Ti$_3$C$_2$T$_x$ (MXene) + IL-1β: cells grown on Ti$_3$C$_2$T$_x$ coatings treated with IL-1β); TGF-β2: cells treated with TGF-β2; Ti$_3$C$_2$T$_x$ (MXene) + TGF-β2: cells grown on Ti$_3$C$_2$T$_x$ coatings treated with TGF-β2; Etoposide: cells treated with etoposide) (Mean ± SEM; n=3)

5.3.2 EdU staining of interleukin-1 beta and transforming growth factor beta 2-treated human lens epithelial cells with $Ti_3C_2T_x$ (MXene) coatings

After the 8-hour incubation, $Ti_3C_2T_x$, IL-1β and TGF-β2 treatment did not alter the cell division of FHL124 cells, as quantified by EdU expression (**Fig. 5.5**). Etoposide treatment of just 8 hours showed an impact on cell proliferation and had significantly downregulated cell division rate in comparison to the untreated cells ($p \geq 0.05$).
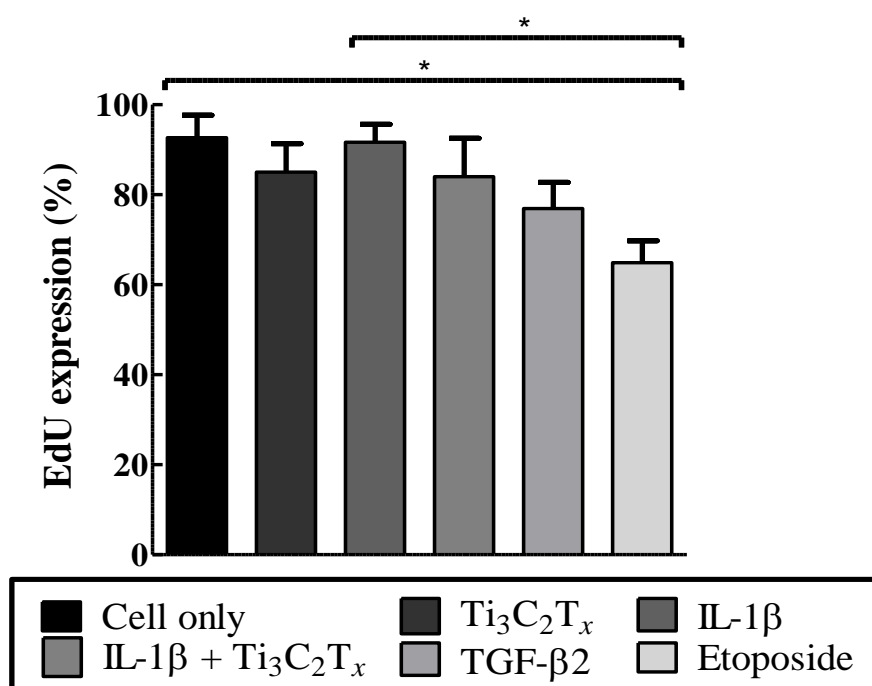
Figure 5.5: EdU expression of FHL124 cells treated with $Ti_3C_2T_x$, IL-1β, TGF-β2 and etoposide for 8 hours. Etoposide treatment significantly downregulated cell proliferation. *$p \leq 0.05$. (Cell only: cells alone; $Ti_3C_2T_x$ (MXene): cells grown on $Ti_3C_2T_x$ coatings; IL-1β: cells treated with IL-1β; $Ti_3C_2T_x$ (MXene) + IL-1β: cells grown on $Ti_3C_2T_x$ coatings treated with IL-1β); TGF-β2: cells treated with TGF-β2; Etoposide: cells treated with etoposide) (Mean ± SEM; n=3)

Cells treated for 8 hours then incubated in fresh media for a further 48 hours showed a greater downregulation in cell proliferation in cells treated with etoposide and TGF-β2 treatment relative to the cell control (**Fig. 5.6**). Cells treated with $Ti_3C_2T_x$ did not show any changes in cell proliferation relative to the cell control (**Fig. 5.7**). Etoposide treatment significantly reduced cell

proliferation ($p \geq 0.001$) but this significance was lessened when cells were treated with etoposide and $Ti_3C_2T_x$ coatings ($p \geq 0.01$) (**Fig. 5.8**). TGF-β2-treated cells did markedly reduce cell proliferation relative to the cell control although, this was not significant (**Fig. 5.9**).
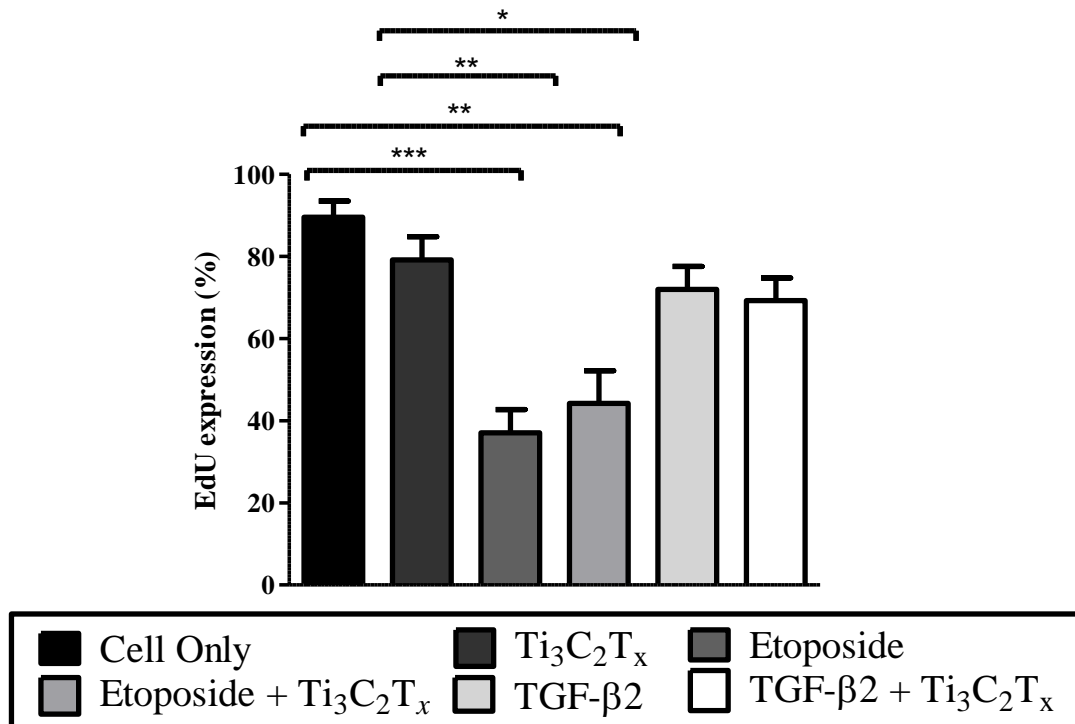
Figure 5.6: EdU expression of FHL124 cells treated with $Ti_3C_2T_x$, IL-1β, TGF-β2 and etoposide for 8 hours, then incubated in fresh media for a further 48 hours. Etoposide treatment significantly downregulated cell proliferation. *$p \leq 0.05$, **$p \leq 0.01$, ***$p \leq 0.001$. (Cell only: cells alone; $Ti_3C_2T_x$ (MXene): cells grown on $Ti_3C_2T_x$ coatings; Etoposide: cells treated with etoposide; $Ti_3C_2T_x$ (MXene) + etoposide: cells grown on $Ti_3C_2T_x$ coatings treated with etoposide); TGF-β2: cells treated with TGF-β2; $Ti_3C_2T_x$ (MXene) + TGF-β2: cells grown on $Ti_3C_2T_x$ coatings treated with TGF-β2;) (Mean ± SEM; n=3)
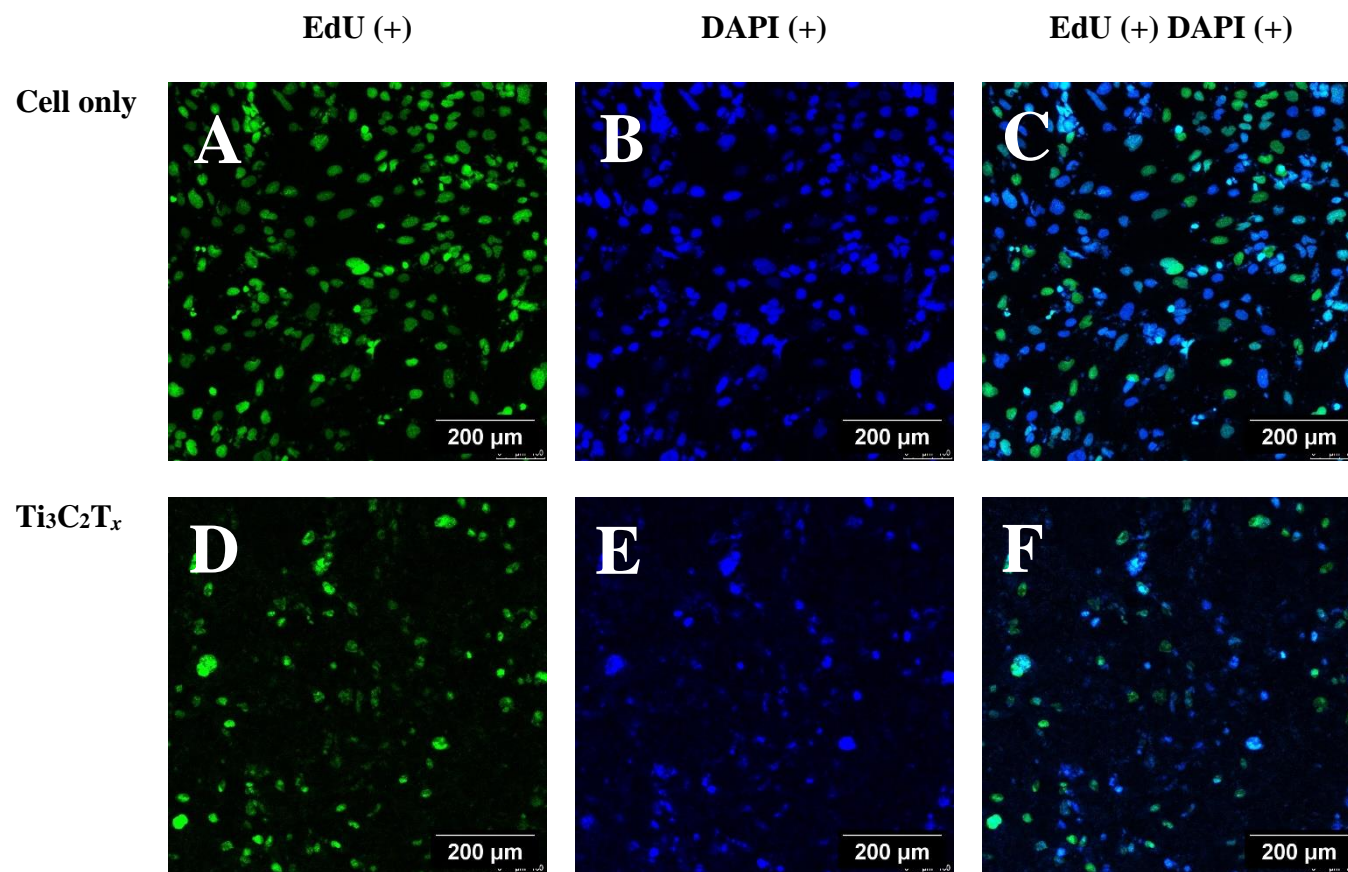
Figure 5.7: Micrographs of EdU expression in cell controls (**Fig. 5.7. A – C**) and Ti₃C₂Tₓ treated cells (**Fig. 5.7 D – F**) post 8-hour treatment and 48-hour incubation. EdU nuclei stain was normalised across the conditions against the DAPI cell count. Cells were visualised using a Zeiss LSM800 Confocal Microscope (Carl Zeiss Microscopy GmBh, Germany). Mag x100. (n=3)
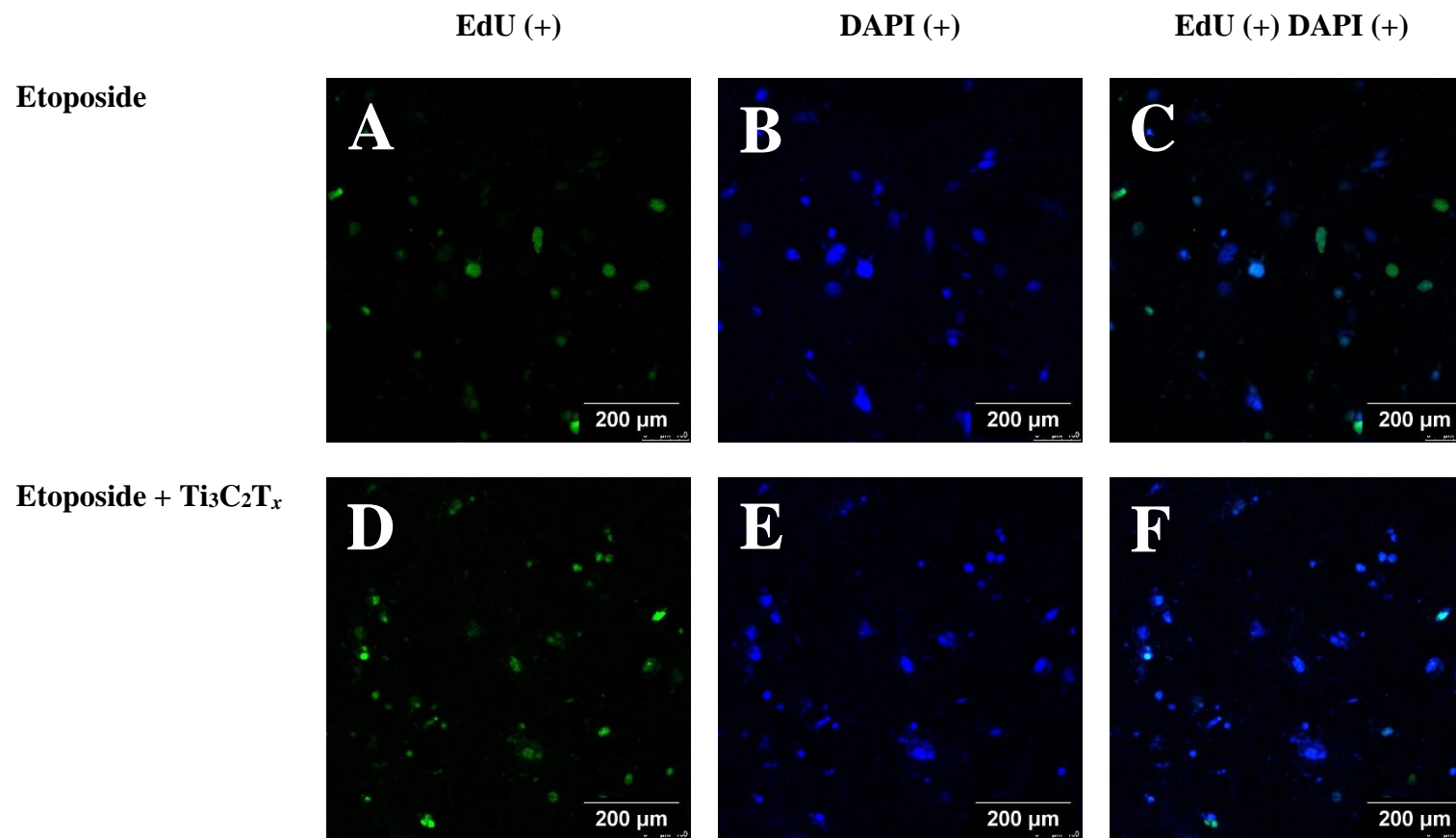
Figure 5.8: Micrographs of EdU expression in etoposide treated cells (**Fig. 5.8. A – C**) and etoposide and $Ti_3C_2T_x$ treated cells (**Fig. 5.8 D – F**) post 8-hour treatment and 48-hour incubation. EdU nuclei stain was normalised across the conditions against the DAPI cell count. Cells were visualised using a Zeiss LSM800 Confocal Microscope (Carl Zeiss Microscopy GmBh, Germany). (n=3)
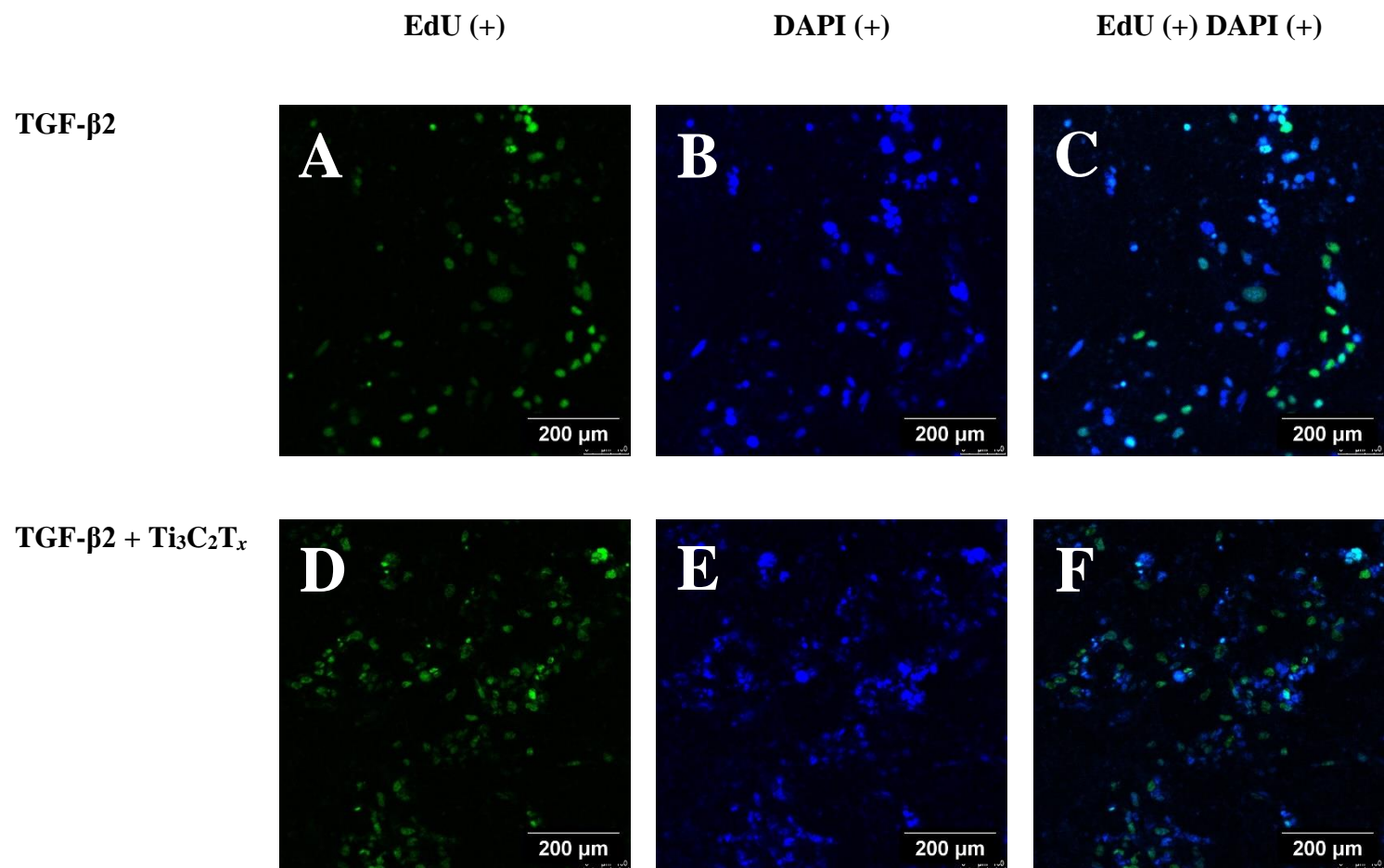
Figure 5.9: Micrographs of EdU expression in TGF-β2 treated cells (**Fig. 5.9. A – C**) and TGF-β2 and $Ti_3C_2T_x$ treated cells (**Fig. 5.9 D – F**) post 8-hour treatment and 48-hour incubation. EdU nuclei stain was normalised across the conditions against the DAPI cell count. Cells were visualised using a Zeiss LSM800 Confocal Microscope (Carl Zeiss Microscopy GmBh, Germany). (n=3)

5.3.3 Release of interleukin-6 and interleukin-8 by human lens epithelial cells grown on

Ti$_3$C$_2$T$_x$ coatings spiked with etoposide and transforming growth factor beta 2

Etoposide and TGF-β2-treated cells showed a greater release of IL-6 and IL-8 after the 48-hour incubation in fresh media (**Fig. 5.10 C, D**) in comparison to immediately after the 8-hour treatment (**Fig. 5.10 A, B**). Etoposide-treated cells showed a significant upregulation in release of IL-6 at 8 and 48 hours and IL-8 at 48 hours relative to the cell control. IL-6 release was markedly reduced in etoposide-treated cells grown on Ti$_3$C$_2$T$_x$ coatings compared to etoposide-treated cells alone, at both time points (**Fig. 5.10 A, C**). IL-8 release was significantly reduced in etoposide-treated cells grown on Ti$_3$C$_2$T$_x$ coatings relative to cells treated with etoposide alone, at 48 hours (p ≤ 0.01) (**Fig. 5.10 D**). TGF-β2-treated cells showed a significant upregulation in IL-6 release relative to the cell control, which was then significantly reduced in TGF-β2 and Ti$_3$C$_2$T$_x$-treated cells at 48 hours (p ≤ 0.01) (**Fig. 5.10 C**). TGF-β2-treated cells did not significantly release IL-8 in comparison to the cell control.
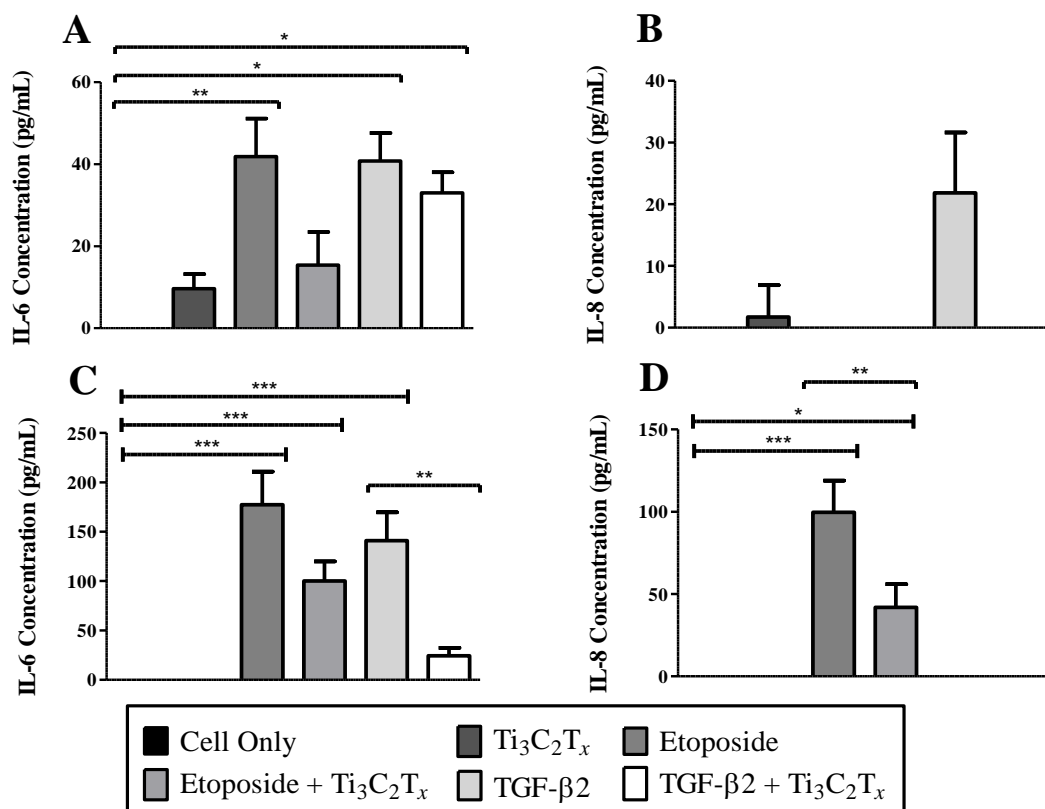
Figure 5.10: Release of IL-6 and IL-8 by etoposide and TGF-β2-treated FHL124 cells grown on Ti$_3$C$_2$T$_x$ coatings after 8-hour (**Fig. 5.10 A, B**) and 48-hour incubation (**Fig. 5.10 C, D**). Release of IL-6 (**Fig. 5.10 A, C**) and IL-8 (**Fig. 5.10 B, D**) was quantified by ELISA. Cells were treated with either etoposide (10 μM mL^{-1}) or TGF-β2 (20 μm mL^{-1}) and grown on 2 mg mL^{-1} Ti$_3$C$_2$T$_x$ coatings. Significance was determined using a one-way ANOVA and post-hoc Bonferroni's multiple comparison test. *p ≤ 0.05, ** p ≤ 0.01 ***p ≤ 0.001. (Cell only: cells alone; Ti$_3$C$_2$T$_x$: cells grown on Ti$_3$C$_2$T$_x$ coatings; Etoposide: cells treated with etoposide; Etoposide + Ti$_3$C$_2$T$_x$: cells grown on Ti$_3$C$_2$T$_x$ coatings treated with etoposide; TGF-β2: cells treated with TGF-β2; TGF-β2 + Ti$_3$C$_2$T$_x$: cells grown on Ti$_3$C$_2$T$_x$ coatings treated with TGF-β2) (Mean ± SEM; n=3)

5.3.4 Senescence beta-galactosidase staining of interleukin-1 beta-primed human lens epithelial cells with Ti₃C₂Tₓ (MXene) coatings

β-galactosidase expression was higher in cells treated with $Ti_3C_2T_x$ (**Fig. S21 B, D**) and etoposide (**Fig. S21 E**) in comparison to cells alone (**Fig. S21 A**). IL-1β treatment did not increase the expression of β-galactosidase (**Fig. S21 C**).

5.4   Discussion

This chapter aimed to establish a model of etoposide induced senescence in order to assess the potential role senescence may play in upregulation of fibrotic and inflammatory pathways in LECs leading to PCO development. It did this in order to consider the potential role of $Ti_3C_2T_x$ in repression of senescence associated inflammatory and fibrotic response. The results within this chapter show for the first time that etoposide can be used to activate senescence pathways in LECs and that $Ti_3C_2T_x$ did not upregulate senescence associated pathways on interaction with LECs. This chapter showed that whilst IL-1β didn't upregulate these pathways, TGF-β2 did promote *p21* and *p16* gene upregulation, IL6 release and downregulated cell proliferation as quantified by reduced EdU incorporation. It has also shown under the experimental conditions, that $Ti_3C_2T_x$ does not upregulate key senescence markers and downregulated etoposide and TGF-β2-mediated release of IL-6 and IL-8, indicating a potential repression of SASP associated activity.

Etoposide is a DNA-damaging drug that has been used to induce senescence via telomere erosion (279,280). In this body of work, H_2O_2 and etoposide were tested for their ability to induce senescence in FHL124 cells. Even at concentrations of 100 µM, H_2O_2 did not induce senescence in the LECs (data not shown). However, after 8-hour treatment of 10 µM etoposide, the presence of sen-β-galactosidase activity was detected. At 24 hours, the etoposide treatment had activated cell death in the FHL124 cells. Therefore, the treatment period was set at 8 hours and samples were quantified for *p21* and *p16* gene expression, cell proliferation rate and sen-β-gal expression.

Whilst the q-PCR data indicated activation of *p21* and *p16* and induction of senescence associated pathways, this was not demonstrated in the EdU data for an 8-hour incubation or in the associated cytokine expression data. However, further incubation with etoposide beyond 8 hours induced cell death. Therefore, the etoposide treatment method was altered by removal of etoposide treatment at 8 hours followed by a further 48 hr incubation period in fresh media. Samples then demonstrated a more reflective reduction in EdU expression and upregulation in cytokine production suggestive of SASP, indicating a significant impact by etoposide incubation.

The upregulation of CDKN1a (p21) and CDKN2a (p16) causes cell cycle arrest contributing towards senescence and these markers were therefore used to determine the onset of senescence. The first group of samples that were treated for 8 hours were then immediately quantified for analysis. $Ti_3C_2T_x$ and IL-1β did not significantly upregulate *p21* or *p16* fold change (**Fig. 5.4**). TGF-β2 showed a marked increase in fold change of *p21* and *p16* although this was not significant when compared to the cell control. This could be as a result of the short exposure time and with an extended incubation period, this upregulation of *p21* and *p16* may be significant. Whilst it was not possible to repeat the extended incubation for the qPCR data it is likely that on using an extended incubation period a significant upregulation of *p21* and *p16* would occur based on the difference in the EdU and cytokine expression profile following the further 48 hr incubation on removal of etoposide. $Ti_3C_2T_x$ treatment did not suppress *p21* or *p16* expression in both IL-1β and TGF-β2 treated cells, suggesting that under these experimental conditions, $Ti_3C_2T_x$ does not have the potential to downregulate cell cycle arrest pathways. However, a longer incubation cycle may increase the difference between samples incubated with $Ti_3C_2T_x$ and those without $Ti_3C_2T_x$ treatment, since this was the case for the subsequent cytokine expression study (**Fig. 5.10 C, D**). Etoposide significantly upregulated *p21* and *p16* gene expression, supporting its use as the positive control to induce senescence in LECs.

Incorporation of the modified nucleotide EdU into replicating DNA can be used to determine if a cell has undergone cell cycle arrest, a marker for a cell undergoing senescence (281). A reduction in the incorporation of EdU indicates a cell is no longer replicating DNA and

in combination with an upregulation of other senescence markers, shows if a cell population has commenced senescence. For the first group of samples that were quantified for EdU expression immediately after the 8-hour treatment, $Ti_3C_2T_x$ did not show a significant reduction of EdU relative to the cell control, suggesting that $Ti_3C_2T_x$ did not alter cell division or proliferative ability (**Fig. 5.5**). This supports the findings of **3.3.1** which showed that the presence of $Ti_3C_2T_x$ does not negatively impact cell viability. Cells treated with IL-1β or TGF-β2 treatment showed no significant changes in cell division in comparison to the cell control. Etoposide treatment did show a significant reduction in EdU incorporation although this reduction was much lower than anticipated (**Fig. 5.5**).

For the second group of samples that were quantified for EdU expression after a 48-hour incubation in fresh media post-8-hour treatment, it was shown that the additional 48-hour incubation period produced a stronger impact of the treatment on cell proliferation. Etoposide treatment significantly downregulated cell proliferation relative to the cell control and the cells treated with etoposide for only 8 hours ($p \geq 0.001$) (**Fig. 5.6**). This suggests that the 8-hour treatment is sufficient to cause DNA damage, potentially leading to cell cycle arrest and then the removal of etoposide and addition of fresh media removes the excess stimulus leading to cell death. The impact of the TGF-β2 on cell proliferation was also more impactful after the additional 48-hour incubation. TGF-β2 treatment markedly reduced proliferation in cells relative to cell control and cells treated with TGF-β2 after 8-hour treatment alone. Further work is required to optimise the concentration and incubation period of TGF-β2 to show any significant impact of TGF-β2 on the induction of senescence.

Senescent cells develop SASP which promotes positive feedback loops, maintaining the senescent state, including the release of IL-6 and IL-8 (132,269). This is distinct from the inflammation response which typically involves an upregulation in cytokine release and resolution within a 24-hour period (282). Therefore, the samples were also quantified for IL-6 and IL-8 release at the 8-hour and 48-hour time point. Etoposide and TGF-β2-treated cells had a greater inflammatory cytokine release after the 48-hour incubation in comparison to 8-hour,

suggesting that the treatment period was sufficient to induce a pro-inflammatory state in the LECs. Etoposide treatment induced the release of IL-6 and IL-8 (**Fig. 5.10**). However, further work is required to determine if this is a result of cell death or cells promoting a SASP. Etoposide-treated cells incubated with $Ti_3C_2T_x$ coatings showed a significant downregulation of IL-8 at the 48-hour time point (**Fig. 5.10 C**). The $Ti_3C_2T_x$ coatings could potentially be adsorbing etoposide, preventing it from binding to the cells relative to the etoposide-treated cells alone. TGF-β2 treatment only led to the upregulation of IL-6 in the LECs. This was expected as IL-6 and TGF-β2 has been suggested to work in synergy in EMT pathways contributing to PCO development (110). IL-6 release was significantly downregulated by the presence of $Ti_3C_2T_x$ coatings at the 48-hour time point (**Fig. 5.10 D**). This work has shown that $Ti_3C_2T_x$ coatings significantly downregulated vimentin expression, a marker of TGF-β2 signalling. Further work is required to establish if the presence of $Ti_3C_2T_x$ impacts the signalling pathways of TGF-β2.

The increase of sen-β-galactosidase activity is indicative of the presence of senescent cells (281). The higher presence of sen-β-galactosidase catalyses the hydrolysis of β-galactosidases to monosaccharides which can be targeted by its substrate 5-bromo-3-chloro-3-indolyl-β-D-glucopyranoside (X-gal) to form a blue precipitate. The first group of samples were used for this experiment. These results showed that $Ti_3C_2T_x$ coatings increased the formation of blue precipitate, suggesting that $Ti_3C_2T_x$ increases the induction of senescence in LECs (**Fig. S21**). This does not support the previously reported data and may have caused by $Ti_3C_2T_x$ interacting with the colorimetric assay. Nevertheless, the cell control and IL-1β treated-cells showed low to no blue precipitate and etoposide-treated cells showed a higher presence of the blue precipitate, supporting the EdU and qPCR analysis.

The potential role of senescence associated pathways in IL-1β upregulation of pro-inflammatory state in the FHL124 cells was considered with regard to its potential relationship with SASP. IL-1β and -1α have been shown in previous studies to induce SASP contributing to tumour progression by upregulating the release of IL-6 and IL-8 via NF-κβ signalling (283). The FHL124 genomic profile showed that IL-1β-treated cells did upregulate NF-κβ. Nevertheless,

the findings from the EdU and qPCR analysis were also supported by the RNA-Seq analysis. IL-1β treatment downregulated *CDKN2C* (p18), which acts on CDK4 and 6 to regulate the cell cycle. However, IL-1β treatment also increased *CDK2AP2*, which inhibits the G1 and S phase by repressing CDK2. IL-1β treatment also downregulated *PERP* and *TP52INP1*, involved in promoting apoptosis. Together, these results suggests that IL-1β did not induce senescence in LECs and that potentially IL-1β/NF-κβ pathway may not play a role in the induction of senescence in LECs.

The TGF family have been linked to several age-related conditions through its downstream signalling pathways instigating processes such as DDR, ROS production and the UPR (284,285). There have been some suggestions that these processes are as a result of a relationship between TGF-β2 signalling and cellular senescence (286,287). TGF-β2 represses proliferation in favour for differentiation by inducing CDK inhibitors p15^{Ink4b}, p21 and p27 via Smad-dependent signalling (285,288) and has been implicated within senescence-induced bronchial epithelial cells, hepatocellular carcinoma cells and fibroblasts (286,287). TGF-β2 has been linked to the induction of EMT within tumour progression and PCO development and has been used in this body of work to induce EMT in FHL124 cells (7,115,173). Smith et al., (70) found that TGF-β2-induced fibrosis in FHL124 cells was subdued by a known senolytic RESV. Such evidence supports the hypothesis that TGF-β2 may act via senescence associated pathways in residual LECs as part of the fibrotic response. The results of the qPCR and EdU analysis did not provide a conclusive role for TGF-β2 in the induction of senescence in LECs, potentially due to the shortened exposure period, although an upregulation in key senescence markers was shown. Evidence to date suggests that senescence plays a role in PCO development. For instance, senolytic drugs target HSP90, PI3K/AKT and several pathways that are upregulated during the developmental pathways of PCO. Therefore, it would be opportune to continue this work by optimising TGF-β2 concentration and incubation period to determine the effects of long-term exposure of TGF-β2 on upregulation of cellular senescence associated pathways in LECs.

In conclusion, this work aimed to investigate the potential activation of senescence associated pathways and their possible role in LEC induction of inflammation and fibrosis linked to PCO. In addition, the influence of $Ti_3C_2T_x$ upon these pathways was also considered. This work showed for the first time that senescence of FHL124 cells can be induced by etoposide stimulus and that this effect was mirrored by a marked upregulation of TGF-β2 associated p21 and p16 mRNA expression but not by IL-1β inflammatory stimulus (**Fig. 5.4**). Preliminary data also showed no induction of senescence by $Ti_3C_2T_x$ in the *in vitro* LEC model with no upregulation of *p21* and *p16* gene expression or effect on EdU proliferating cell fraction. Interestingly, whilst $Ti_3C_2T_x$ did not appear to repress induction of senescence by etoposide, it did appear to slow TGF-β2 induced effects and particularly to limit the SASP-like sustained upregulation of IL-6 at the 48-hour time point following TGF-β2 exposure. An inflammation associated initial rise in IL-6 expression would be expected to decline rather than increase at this time point (282). This preliminary data supports the hypothesis that $Ti_3C_2T_x$ may slow senescence associated fibrotic events, in part, through downregulation of SASP. Further work is required to consider in full the intracellular mechanisms by which this potential effect may occur. These findings were derived using 2D *in vitro* cell culture experiments which are known to restrict cell behaviour in comparison to 3D and *in vivo* models. Capsule bag models provide the cell and tissue spatial environment similar to those observed clinically. However, access to animal and human donor capsules can be expensive, limited by tissue availability and time constraints. An approach to develop a silicone-based 3D *in vitro* capsule bag model was therefore investigated for use as an alternative artificial capsule bag for PCO research in **Chapter 6**.

Chapter 6: Development of an *in vitro* capsule bag model for the preliminary investigation of Ti$_3$C$_2$T$_x$ coatings

6.1 Introduction

6.1.1 Capsule bag models

Ex vivo models for PCO research utilises human and animal capsule bags due to their similarities in cell and tissue spatial arrangement relative to clinical observation. The capsule bag is removed from human, chick or canine donors and suspended within a culture disk (8,286). In human donor eyes, the cornea and iris are removed to prevent any visual obstruction to the lens. A capsulorhexis is performed and the lens is removed by hydrodissection where an IOL can then be implanted (289). To maintain the shape of the capsule bag during experimentation, pins are used to secure the capsule bag to the culture disk (290,291). Penetrating the capsules' walls can induce an injury response and can influence cell growth over the anterior capsule due to the new stretched-out surface (289). Cleary et al., (291) developed an improved model which pinned the ciliary zonules and body attached to the capsule bag to a silicone ring (**Fig. 6.1**). Maintaining the capsule bags in serum-free media better mimics the low-protein physiological environment of the AH (289).
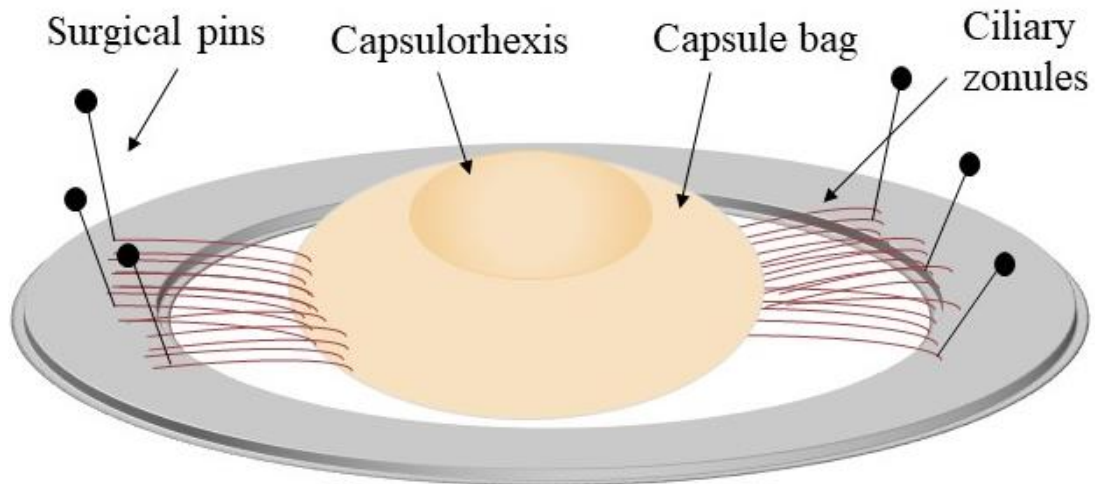
Figure 6.1: Schematic of human donor capsule bag model, ciliary body pinned to a silicone ring (289,291).

Capsule bag models can be used for investigation into the molecular mechanism driving PCO development and have elicited the role of many growth factors, predominantly the influence of TGF-β. Taiyab et al., (117) explanted a rat lens epithelium on its basement membrane to investigate the role of TGF-β in the EMT pathway contributing to PCO development. In their first study, the explant models were treated with TGF-β with or without SIS3, a Smad3 inhibitor. The untreated lens epitheliums showed low α-SMA and stress F-actin fibre expression whereas lens explants treated with TGF-β displayed a greater staining of these markers. The explants treated with TGF-β and SIS3 showed a reduction in the expression of α-SMA and stress F-actin fibre expression. Following on from this work, the study investigated the E-cadherin/β-cadherin complex within the cell periphery that undergoes rearrangement during EMT-related PCO. On treating the explants with TGF-β, a reduction in E-cadherin and increased nuclear translocation of β-catenin was observed which led to a loss in cell structure. With the addition of SIS3, the staining of E-cadherin did not alter in comparison to the untreated control explants and only a partial reduction in β-catenin nuclear translocation was seen.

Capsule bag models can also be used for IOL implantation to test therapeutic agents to prevent or manage PCO. Pot et al., (292) used harvested lens capsules from canine eyes to investigate the impact of selenium functionalised IOL on cell migration. Poly (HEMA) IOL were pre-treated with an activation solution, creating covalent bonding sites on the IOL surface to allow the binding of selenocystamine (SeIOL). The lens capsules were divided into three groups: no implanted lens, control IOL or SeIOLs. PCO scores were graded at day 1, 3, 6, 9 and 10. At day 10, the control capsules reached confluence and the experiment was terminated. PCO scores were significantly lower in SeIOL-implanted capsules in comparison to the control and empty capsules at day 3 ($p \leq 0.05$ and $p \leq 0.01$ respectively) and at day 10 ($p \leq 0.05$ and $p \leq 0.001$, respectively). Histology sections showed the SeIOLs had significantly lower cell coverage than the control IOL. Masson's trichrome staining showed the greatest collagen deposition was in the empty capsules without IOL implantation and the least deposition was found in the SeIOL-

implanted capsule. The study concluded that selenium bound IOLs could potentially be used as a long-term prevention against PCO development.

Capsule bag models do not restrict cell behaviour as the model recaptures the same spatial cell and tissue arrangement as observed clinically (12). This cannot be mimicked to the same standard in 2D cell culture models especially when monitoring cell migration and recolonisation of the capsule PCS in the assessment of different IOL types. Nagamoto et al., (293) observed LEC migration across human and rabbit posterior capsules using a phase-contrast microscope and time-lapse videomicroscopy. This method allowed for the observation of factors influencing the direction of cell migration and expansion such as the contact inhibition of cell movement by other cells and capsule folding. Nagamoto et al., (294) used this method to evaluate a new sharp ridge IOL design against commercially available IOLs. This work contributed to the current understanding of how contact pressure between the optic edge and the posterior capsule inhibits cell migration. Despite the advantages of using a capsule bag models within PCO research, the time-limits when using human and animal tissue and the lack of accessibility for many laboratories highlights a requirement for an artificial capsule bag model.

6.1.2 Artificial capsule bag models

Artificial capsule bag models are primarily used in research to examine biomechanical properties of newly developed IOL technology. Silicone has been investigated as a composite material for an artificial capsule bag model. Silicone is used in the development of capsule devices, enclosed rings which are implanted during cataract surgery to improve capsule bag stability and IOL centration (78,79). Moreover, silicone has elastic properties which mimic the capsule bag behaviour (107). Therefore, using silicone for an artificial capsule bag model would be appropriate.

Silicone-based capsule bag models have been developed. Beck et al., (295) constructed a 3D silicone capsule bag model to investigate the capsule bag deformation by different IOL types. Wei et al., (107) used an artificial lens capsule with a lens radial stretching system (LRSS) to

mimic the biomechanical properties of the capsule bag in the design of new AIOL technology. The LRSS was used to mimic accommodation by replicating the muscle contractions that deform the capsule bag shape to allow a change in lens' shape. This deformation was characterised in a 'stretched' and 'non-stretched' state in the lens' shape, changing focal length and providing a change in refractive index. Plastic arms attached to the capsule halves, attached to the LRSS by metal shims acted as a ciliary body (**Fig. 6.2**). The deformation of the silicone capsules (0.7 – 1.5 MPa) was similar to *ex vivo* (0.4 – 1.5 MPa) capsules. The silicone capsules along the axial distance was at the lower limit of the human capsule stiffness (0.5 MPa) post-stretching. There was some disparity in the uniaxial tension between the human capsule and the silicone capsule, likely due to the greater thickness of the silicone capsule walls which would require great radial force to induce the same equatorial displacement. Despite these noted similarities between the human capsule and silicone capsules, artificial capsule bags have yet to be explored for use within biological models as an alternative approach to human and animal tissue which can be challenging to acquire.
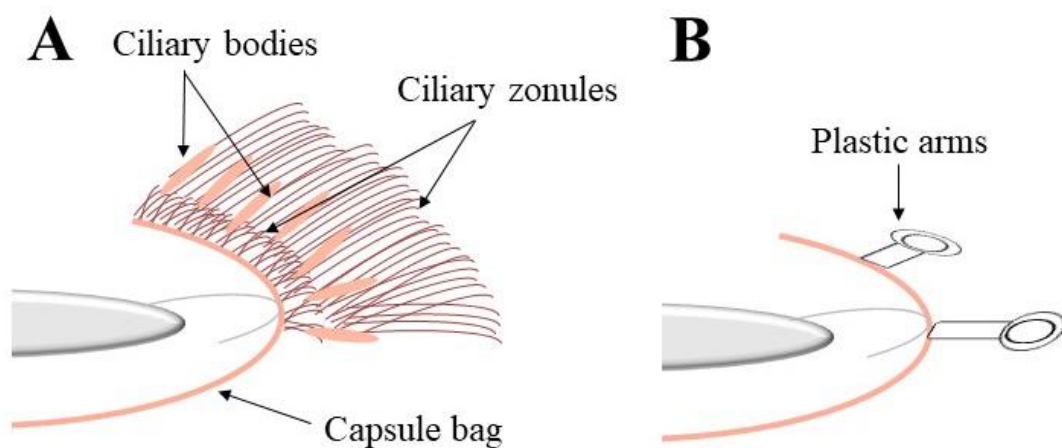
Figure 6.2: Schematic comparison of human donor ciliary body vs artificial ciliary body. The human capsule bag model utilises the natural ciliary body to pin the capsule bag securely (**Fig. 6.2 A**). The artificial capsule bag replicates this by using plastic arms, glued to the silicone capsule halves (**Fig. 6.2 B**) (107).

There are several challenges in applying a silicone-based artificial capsule bag for use in biological assessments and PCO models. Silicone is a hydrophobic material which is not routinely used to culture cells and tissues. The silicone would require pre-treatment to mimic the human capsule bag environment. Such treatments could include fibronectin and collagen coating to replicate the ECM on the capsule bag' lateral membrane (156). A further challenge is the lack of native cells. This would require seeding of *in vitro* LEC line(s). The seeding placement and density would need to be optimised. Nevertheless, this model provides a novel approach to extract and test individual mediators contributing to PCO development within an isolated environment, absent of other interacting factors that in human or animal tissue would be impossible. Moreover, this model could be used in industry or academic settings that have limited access to tissue and lack of institution-based ethical processes, greatly widening the use of the capsule bag model for PCO treatment and IOL development.

6.1.3 Chapter aims

This chapter aimed to produce an *in vitro* silicone capsule bag model to perform mock IOL implantation surgery.

6.2 Materials and methods

6.2.1 Silicone polymerisation

The silicone (MED-6820 NuSil™, US) was prepared by mixing the catalyst and base in equal parts. During polymerisation, the silicone mix was left under vacuum pump (BACOENG Vacuum Chamber, China) for 1 hour to remove air bubbles. The silicone was then left at 80 °C to cure overnight.

6.2.2 Gas chromatography/mass spectroscopy (GC/MS) of silicone

Silicone samples were cut to scale of a 48-well tissue culture plate well (Sarstedt, Germany). Samples were submerged in 250 μL 99.8 % ethanol for 48 hours. At 48 hours, the

samples were washed in dH20 water to remove excess ethanol. The samples were put in fresh wells and incubated in 250 μL dH2O water at 37 °C, 5 % CO_2 to extract leachable starting material that would elute under the experimental conditions. The water elution was collected in sterile Eppendorf tubes. Samples were analysed neat using gas chromatography and mass spectroscopy (GC/MS) (Clarus 690 GC, PerkinElmer, UK) at Rayner Intraocular Lenses Ltd, UK. The ethanol washes were also analysed to detect any potential leachable materials in the washes.

6.2.3 Construction of the silicone capsule bag model

Silicone was prepared as described in **6.2.1**. Silicone was deposited into the female mould of the anterior capsules at a weight of 0.03 – 0.04 g and the posterior capsules at a weight of 0.04 – 0.05 g of silicone. The female moulds were kept under vacuum for 1 hour then the male moulds were placed on top and left for 1 hour to centre (**Fig. 6.3 A**). The moulds were kept at 80 °C overnight then left at RT for at least an hour to cool. The excess material was trimmed using a scalpel under a light microscope then a capsulorhexis was performed using a hole punch with a diameter of 4.5 mm. The two capsule sections were glued to a plastic arm ring support using uncured silicone. The silicone was cured by applying a heat gun for 10 minutes then left to cool (**Fig. 6.3 B**). The capsule was washed in methanol for 48 hours, followed by a 24-hour dH2O wash. The complete capsule was plasma etched for 10 minutes at 11 sccm, 10 cm^3min^{-1} at atmospheric pressure then 100 - 120 μL of collagen I was added to the hollow capsule via the capsulorhexis for incubation at RT for 2 hours. Excess collagen was aspirated, and the capsule was pinned to a silicone ring in a 6-well plate for stability (**Fig. 6.3 C**). The capsule bag model was UV sterilised for 1 hour then incubated in cell media for 24 hours prior to cell seeding.
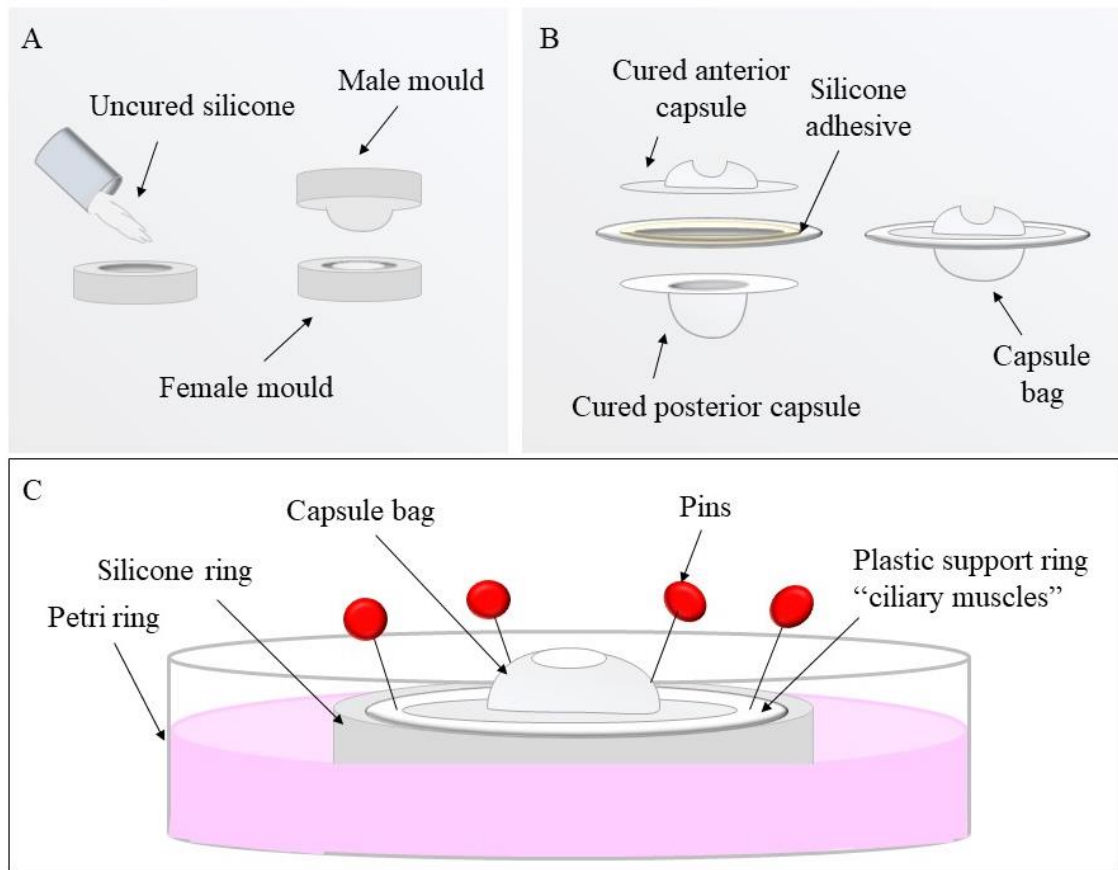
Figure 6.3: Development of silicone capsule bag model. Silicone components were mixed in equal parts and distributed into the female mould for the anterior and posterior capsule sections (**Fig. 6.3 A**). The silicone was kept under vacuum to remove air bubbles during polymerisation and left to cure overnight at 80 °C. Capsules were glued to a plastic arm ring support using silicone and cured using a heat gun for 10 minutes (**Fig. 6.3 B**). The complete capsule bag was pinned to a silicone ring within a 6-well plate and incubated for 24 hours in media prior to addition of cells and IOL (**Fig. 6.3 C**).

6.2.4 Cell seeding and IOL implantation within the silicone capsule bag model

FHL124 cells were cultured as described in **3.2.1**. The capsule bag was seeded with 100 µL of FHL124 cells at a concentration of 5 x 10^5 cells mL^{-1} and incubated overnight at 37 °C, 5 % CO_2. LECs removal was performed using an aspirator, mimicking capsule polishing. Individual IOL types were implanted, and cells were left to attach for 7 days. 9 mL of media was added to the well to prevent evaporation of media within the capsule bag. The capsule was fixed

in 100 µL 3.7 % formaldehyde diluted in PBS for 5 minutes then stained with 0.1 % crystal violet in PBS (Sigma Aldrich, UK) for 5 minutes. The IOL and capsule bag was imaged using VHX Digital Microscope (Keyence, USA), Ocular Coherence Tomography (OCT) (Atria® Series 1060 nm OCT Imaging System, THORlabs, USA), Carl Zeiss Primovert Microscope (Carl Zeiss Microscopy GmbH 415510-1104-000, Germany) and Leica EZ4 Microscope (Scientific Laboratory Supplies, UK).

6.3   Results

6.3.1 Characterisation of silicone castings

GC/MS was used to identify any leachable starting material from the silicone base material of the *in vitro* capsule bag model prior to cell work. Washing the pre-cast silicone in ethanol for 48 hours was sufficient to remove any leachable material **(Fig. 6.4)**. Leachable materials were removed during the first ethanol wash as shown in **Table 6.1**.
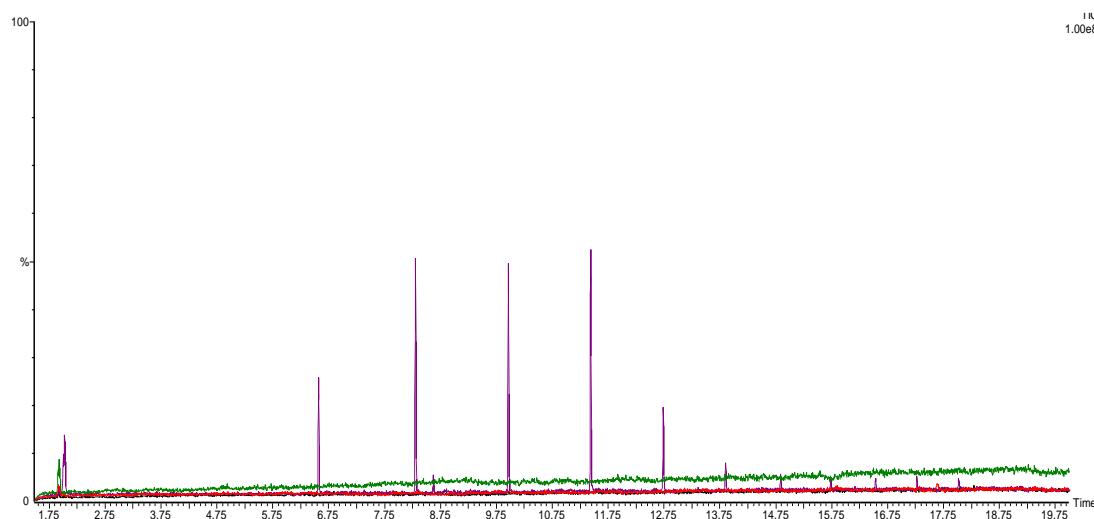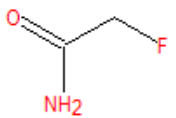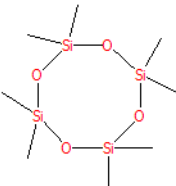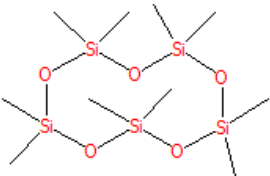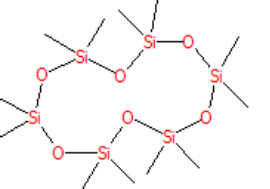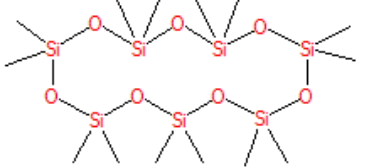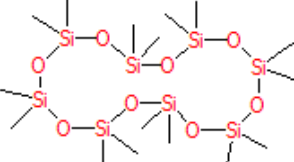
Figure 6.4: GC/MS analysis of the silicone extractables. Leachable material was detected in the first 24-hour ethanol wash (purple). No leachable material was detected in the 48-hour ethanol wash (black) or the 24-hour dH_2O wash (red). Methanol was used as a background control (green).

Table 6.1: GC/MS analysis of silicone extractables in the first ethanol wash.

Retention Time	R Match	Name	Chemical Structure
2.03	895	2-fluoro-acetamide	
6.57	889	Octamethylcyclotetrasiloxane	
8.31	854	Decamethylcyclopentasiloxane	
9.97	895	Dodecamethylcyclohexasiloxane	
11.44	841	Tetradecamethylcycloheptasiloxane	
12.74	874	Hexadecamethylcyclooctasiloxane	

6.3.2 Capsule bag model

Artificial capsule bags were constructed as described by Wei et al., (107). Once constructed, the bags were treated like *ex vivo* capsule bag explants and pinned to a silicone ring

by its 'ciliary muscle' plastic arms structure (**Fig. 6.5 A**). A good centration of the capsulorhexis was found, performed under a microscope for accuracy. A magnified view of the implanted IOL shows good centration within the capsule bag (**Fig. 6.5 B**). The haptics settled out flat within the capsule bag, the arms against the capsule walls applying tension to maintain the shape of the bag with little distortion.
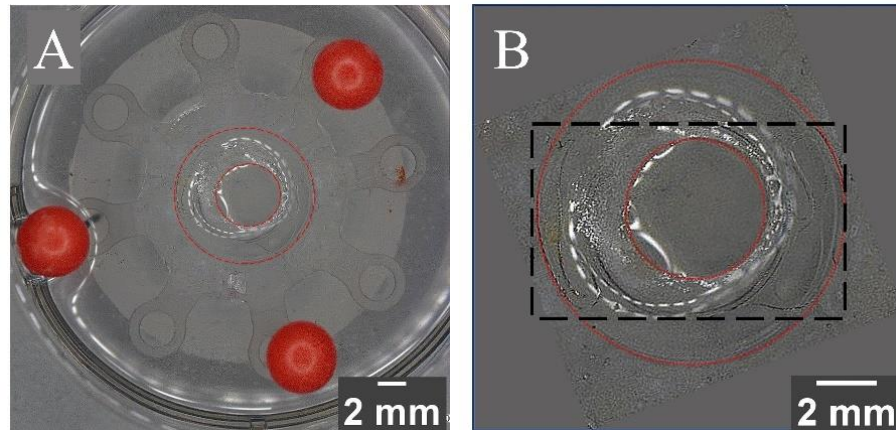
Figure 6.5: Digital microscope image of the aerial view of the capsule bag model. Full view of the capsule bag (**Fig. 6.5 A**) and magnified view, highlighting the capsule bag and implanted IOL (**Fig. 6.5 B**) VHX Digital Microscope (Keyence, USA) (Mag. x20). The silicone capsule bag was attached to the silicone ring by its plastic arms, held by pins. Red annotated lines indicate the circumference of the capsulorhexis and capsule bag. The black box indicates the position of the implanted IOL.

The orientation of the IOL was examined further by OCT imaging to achieve a cross-section of the IOL once implanted in the capsule bag. The cross-sectional view confirmed good centration of the implanted IOL; the central optic located over the visual axis of the posterior capsule (**Fig. 6.6 A**). Measurements of the capsule bag dimensions were taken (**Fig. 6.6 B**). The internal diameter and depth of the capsule bag cavity was 9.54 and 4.38 mm, respectively. The capsulorhexis measured at 4.38 mm. Average thickness of the capsule walls was 0.19 ± 0.05 mm.
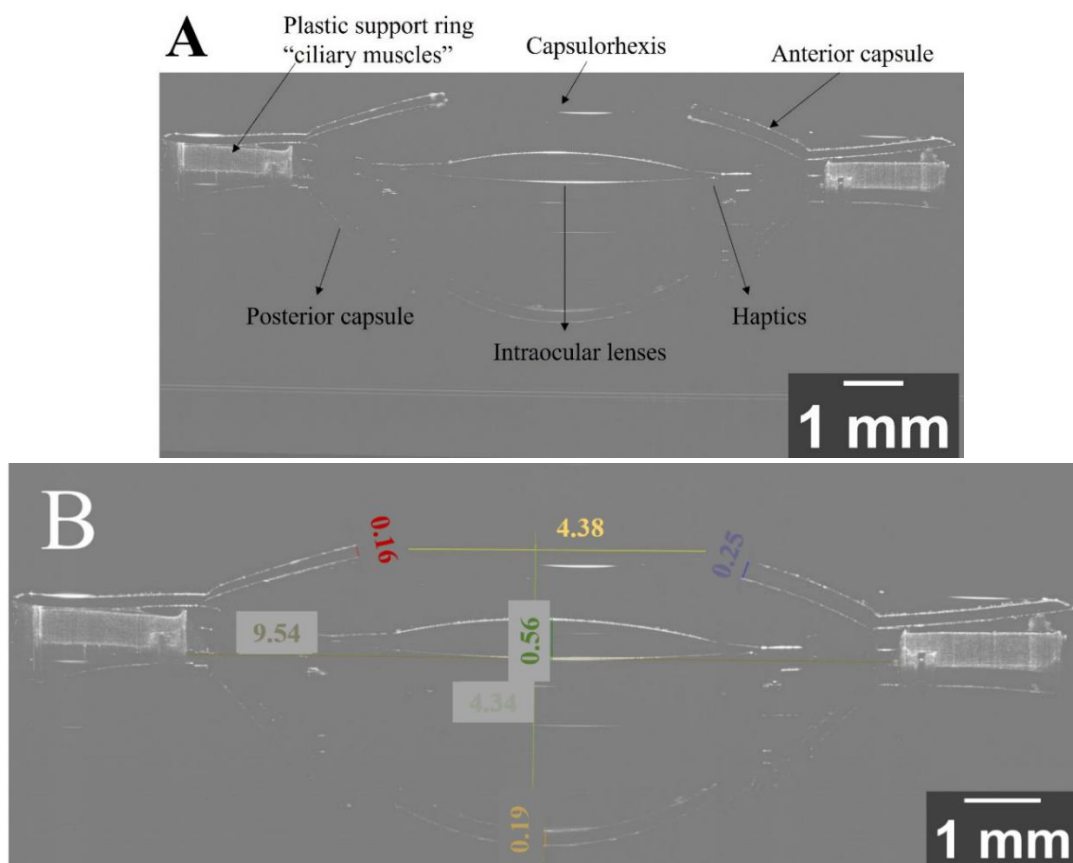
Figure 6.6: Ocular coherence tomography (OCT) of the cross section of the capsule bag attached to silicone ring (Ocular Coherence Tomography (OCT) (Atria® Series 1060 nm OCT Imaging System, THORlabs, USA). Annotated image to show location of IOL within the capsule bag (**Fig. 6.6 A**). Measurements of the capsule bag and IOL were taken (**Fig. 6.6 B**). Red and blue lines show measurements for the anterior capsule thickness. The yellow line shows the capsulorhexis width. The dark green line shows the central optic measurement. The gold line shows the diameter of the capsule, and the light green line shows the depth of the capsule. The orange line shows the posterior capsule thickness. All measurements are in mm.

6.3.3 Cell migration across the posterior capsule

FHL124 cells grew over the collagen-coated posterior capsule and had colonised the entire posterior surface after 24-hour incubation. Capsules implanted with an IOL had greater cell migration across the posterior capsule (**Fig. 6.7 – 6.10**). Repeat experiments are shown in **Figures S22-29.**

181
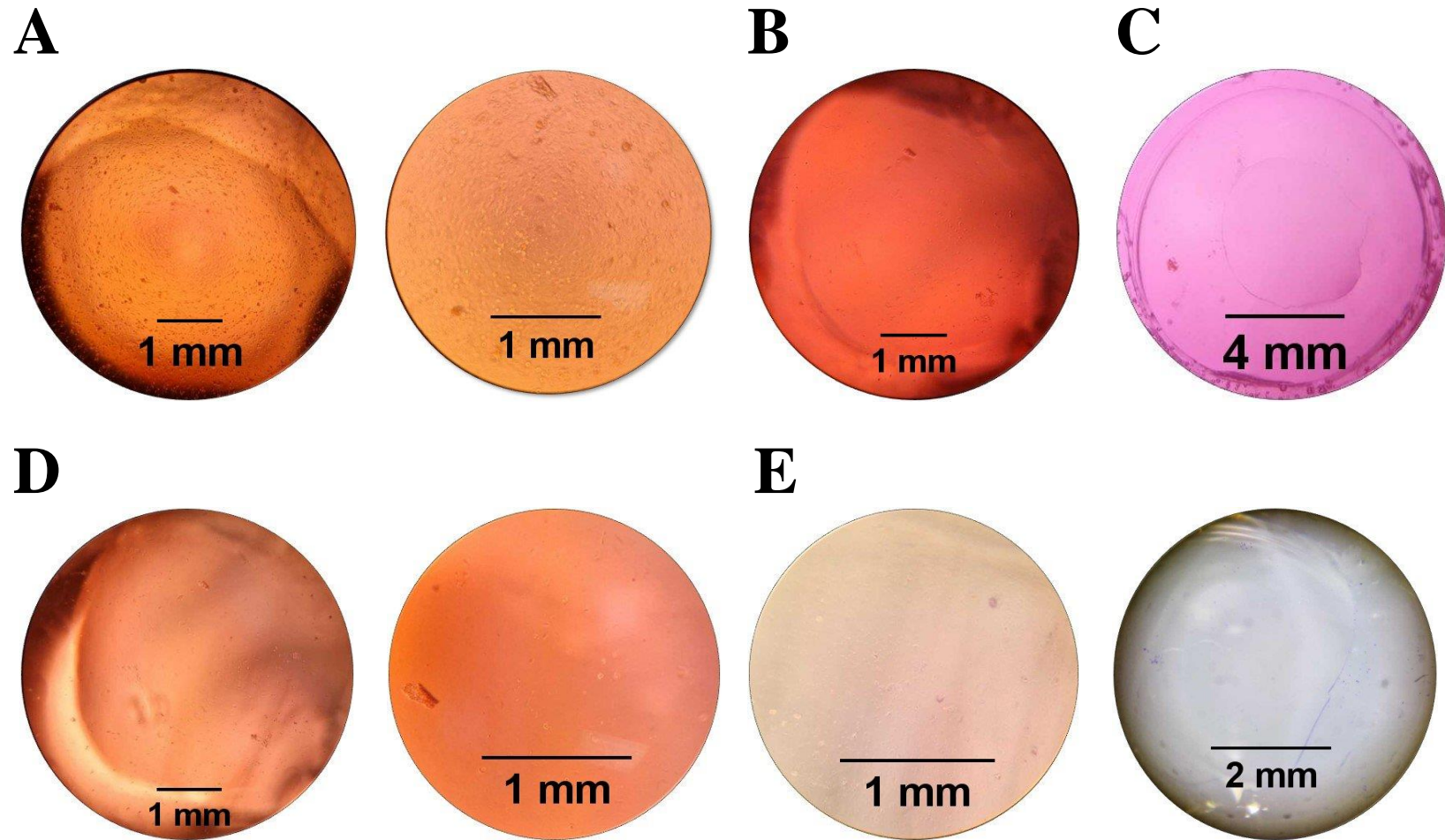
Figure 6.7: Light microscope images of capsule control. Capsule seeded with cells at 5 x magnification (left) and 10 x magnification (right) (**Fig. 6.7 A**), after LEC removal at 5 x magnification (**Fig. 6.7 B**) and 2 x magnification (**Fig. 6.7 C**), after 1-day incubation at 5 x magnification (left) and 10 x magnification (right) (**Fig. 6.7 D**) and day 7 at 10 x magnification (left) and 2 x magnification (right) stained with crystal violet (**Fig. 6.7 E**). (n=1 of 3)
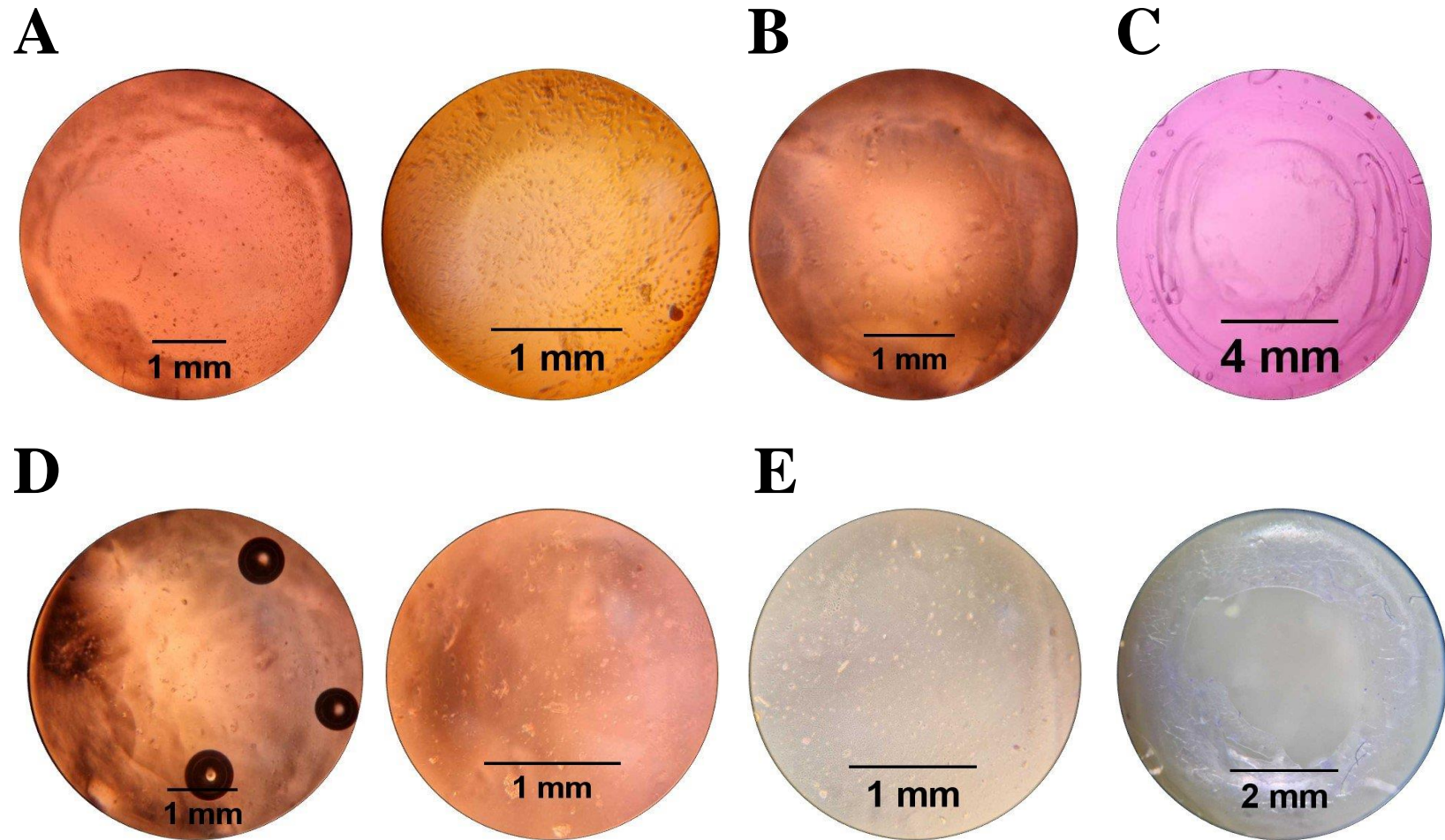
Figure 6.8: Light microscope images of an implanted hydrophobic IOL. Capsule seeded with cells at 5 x magnification (left) and 10 x magnification (right) (**Fig. 6.8 A**), after LEC removal at 5 x magnification (**Fig. 6.8 B**) and 2 x magnification (**Fig. 6.8 C**), after 1-day incubation at 5 x magnification (left) and 10 x magnification (right) (**Fig. 6.8 D**) and day 7 at 10 x magnification (left) and 2 x magnification (right) stained with crystal violet (**Fig. 6.8 E**). (n = 1 of 3)
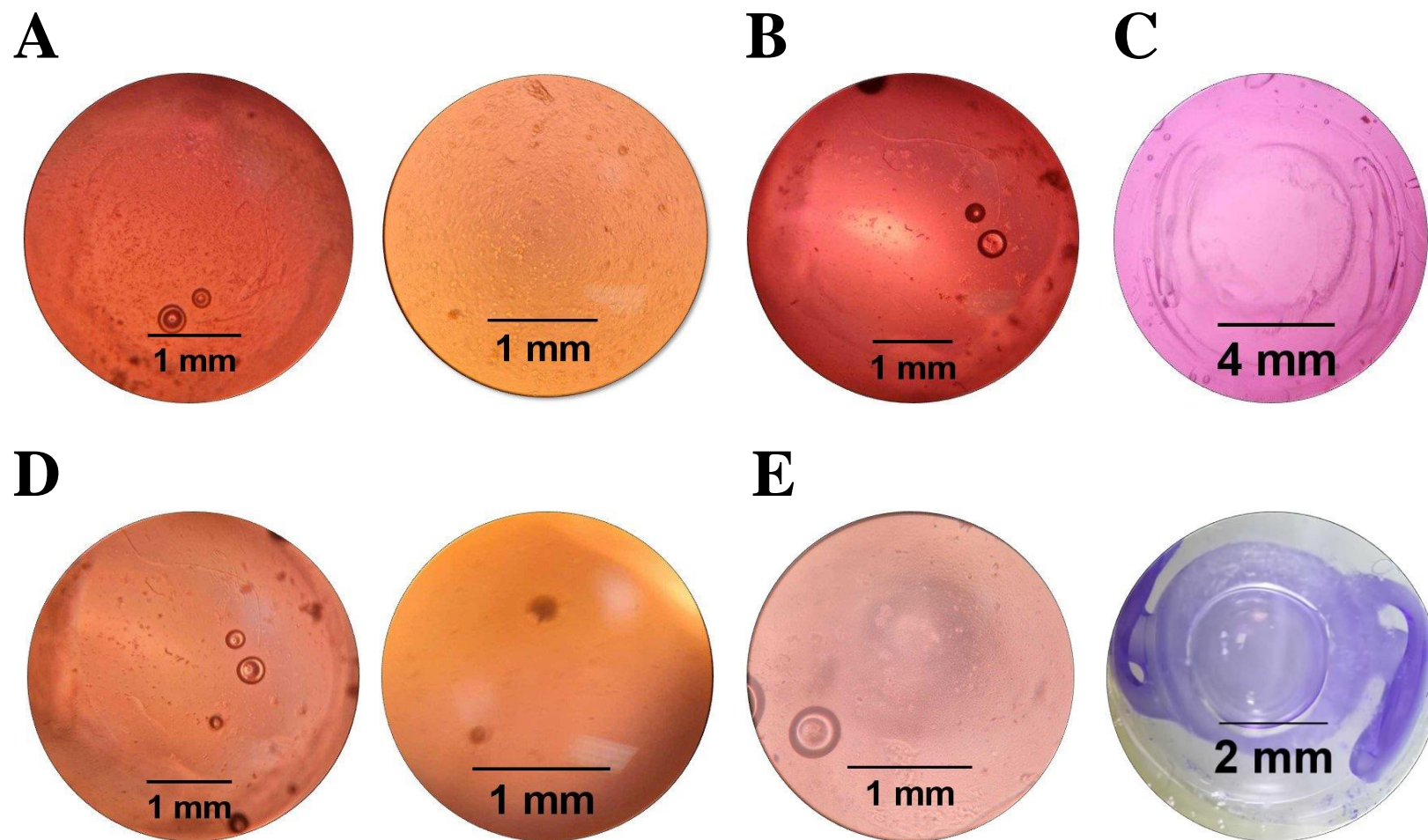
Figure 6.9: Light microscope images of an implanted hydrophilic IOL. Capsule seeded with cells at 5 x magnification (left) and 10 x magnification (right) (**Fig. 6.9 A**), after LEC removal at 5 x magnification (**Fig. 6.9 B**) and 2 x magnification (**Fig. 6.9 C**), after 1-day incubation at 5 x magnification (left) and 10 x magnification (right) (**Fig. 6.9 D**) and day 7 at 10 x magnification (left) and 2 x magnification (right) stained with crystal violet (**Fig. 6.9 E**). (n = 1 of 3)
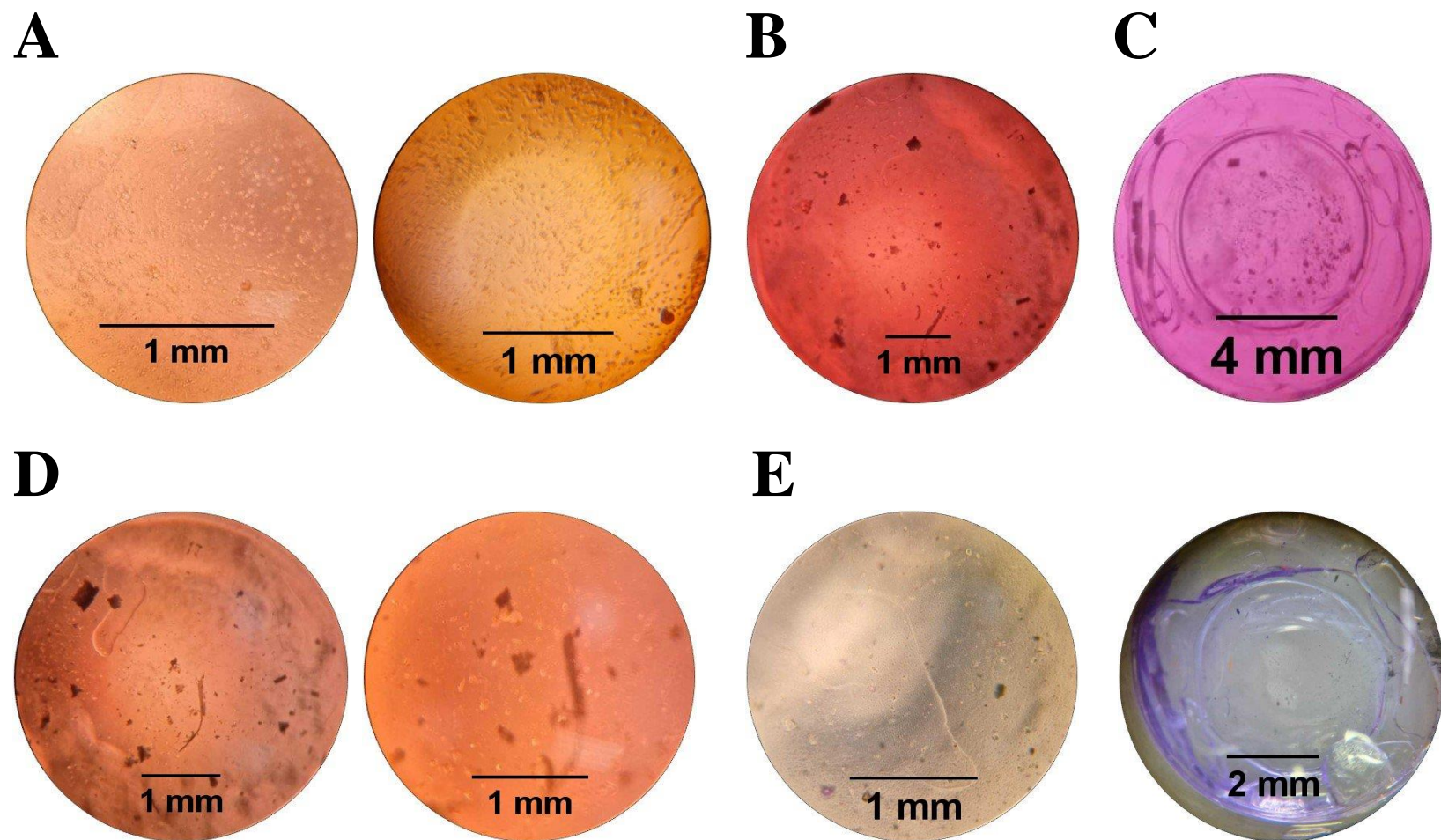
Figure 6.10: Light microscope images of an implanted Ti$_3$C$_2$T$_x$-coated hydrophobic IOL. Capsule seeded with cells at 5 x magnification (left) and 10 x magnification (right) (**Fig. 6.10 A**), after LEC removal at 5 x magnification (**Fig. 6.10 B**) and 2 x magnification (**Fig. 6.10 C**), after 1-day incubation at 5 x magnification (left) and 10 x magnification (right) (**Fig. 6.10 D**) and day 7 at 10 x magnification (left) and 2 x magnification (right) stained with crystal violet (**Fig. 6.10 E**). (n = 1 of 3)

6.4   Discussion

This chapter developed a novel silicone capsule bag model for exploitation within *in vitro* modelling of key developmental pathways of PCO. It has shown for the first time that a silicone capsule bag model could be applied to monitor cell migration of LEC across different IOL types. Capsule bag models have been employed within PCO research to explore the underlying mechanisms of its development, to test new IOL technology and evaluate potential therapeutic interventions delivered by IOL coatings. Animal and human donor tissue are commonly used. However, acquisition of tissue requires lengthy ethical protocols which presents challenges for time-limited projects and issues with accessibility for all laboratories. As yet, there is no artificial 3D capsule bag that has been optimised for use in *in vitro* cell culture. A silicone capsule bag model developed by Wei et al., (107) at Rayner Intraocular Lenses was exploited in this project for IOL implantation and for use as an alternative *in vitro* cell-based artificial capsule bag. This work has shown the silicone capsule bag model developed by Wei et al (107) can be modified to allow for cell seeding and observation of cell migration across the posterior capsule and IOL types.

In the initial investigation of the base material for material leachables, the silicone base material was investigated for any toxic elements. The material leachables from the first ethanol wash were mostly silicone-derivatives and consistent with material formed during the polymerisation reaction that had no hazardous information (**Table 6.1**). The presence of 2-fluoro-actemaide may be as a result of contamination from other equipment. It was found that a 24-hour ethanol wash was sufficient to remove all the material leachables from the silicone **(Fig. 6.4)**. Future silicone casting was washed for 48 hours for diligence.

The moulds used to make the capsule bag was based on the measurements of human capsule bags. The crystalline lens is estimated to be 4.5 mm thick. The capsule bag is 9.5 mm in diameter but increases to 10.5 mm when the lens is removed and the capsule bag collapses (296). A capsulorhexis of $4.5 - 5$ mm improves healing and minimises the post-operative complications.

The capsule bag model used in this project has similar measurements to human donor capsules (**Fig. 6.6 B**). OCT imaging is used by surgeons to diagnose ocular diseases such as macular and to review the post-operative outcomes of cataract surgery (297). OCT imaging of the IOLs implanted within the capsule bag showed good centration and alignment of the optic with the visual axis (**Fig. 6.6 A**). The full extension of the haptics caused little distortion of the capsule bag shape. The capsules' walls showed a greater thickness than what would be found *in vivo*, as a result of the design limitations within the moulds.

Silicone is a hydrophobic material which is inhibitory to cell adhesion and growth. It was possible to culture cells on the silicone capsules after the capsules were pre-treated with atmospheric oxygen to allow the binding of collagen and pre-equilibration with culture media. An aspirator can remove LECs within the capsule, similar to capsule polishing during cataract-surgery. The IOLs could be implanted manually using tweezers or by injection and situated centrally within the capsule (**Fig. 6.8 C, 6.9 C, 6.10 C**). Residual LECs could then be monitored through a phase contrast microscope. Capsules were observed over 7 days. It was possible to fix the contents of the capsule using formaldehyde and cells were stained with crystal violet to provide better contrast for cell visualisation against the capsule. Cell migration appeared to be greater in capsules implanted with IOLs in comparison to the capsule control. This was not expected as in literature, recolonisation of the posterior capsule tends to occur quicker in the capsule control (11). This could be potentially due to the surface treatment of the silicone capsules. The capsules were coated in collagen, a key component of the capsule's ECM however, there are other key components that was not included. Further work would include developing a more appropriate ECM coating for the capsules.

There were several limitations with this model. Firstly, the cells were not stained for cytoskeletal markers, so it is unclear how the culturing on the 3D collagen coated capsules impacted the phenotype expression of the LECs. Secondly, the IOL was difficult to remove without disturbing the cells upon its surface and the capsule' surface once the end point of the experiment had been reached. Lastly, as the silicone composite material would not behave as the

native capsule bag membrane would, this model would be limited to investigate how cell migration and ECM deposition affects the capsule structure. Nevertheless, this work has shown that a silicone 3D *in vitro* capsule bag model can be developed and has been shown as a proof-of-concept design to monitor cell migration across different IOL types. This approach allows for tunability of culture conditions, optimising culture media with the addition of cytokines and growth factors for investigation on how these factors contribute to PCO development which could not be isolated using animal or human tissue. This silicone capsule bag model could be used to provide valuable insight into new IOL designs or feasibility tests of new therapeutic interventions against PCO prior to using more expensive and time restrictive animal and human donor models.

Chapter 7: Thesis conclusions and

future work

7.1 Summary of findings and contribution to knowledge

Ti$_3$C$_2$T$_x$ has been shown to perform as a TCE in a proof-of-concept adaptive focus design however, the impact of Ti$_3$C$_2$T$_x$ within the capsule bag and the wound-healing response of LEC PCS is unknown. It was hypothesised that Ti$_3$C$_2$T$_x$ coatings would act to repress the excessive inflammation and fibrotic response linked to PCO. The impact of Ti$_3$C$_2$T$_x$ on hyperinflammation and the propensity of LEC to undergo EMT was assessed using an optimised LEC based model. Ti$_3$C$_2$T$_x$ was synthesised and processed to achieve sufficient yield, concentration, uniform flake sizes and stability across batches (**Table 2.2**). Uniform, conductive, and stable coatings were achieved using spray-coating deposition (**Fig. 2.9**). IL-1β was established as a positive control to stimulate cytokine-induced inflammation in LECs as measured by protein and RNA expression studies (**Fig. 3.9**; **Fig. 3.16**; **Section 4.3.2**). TGF-β2 was used as an effective positive control to upregulate expression of EMT markers, vimentin, α-SMA and SMAD2/3, measured by immunocytochemistry and western blot analysis (**Fig. 3.18; 3.20**). A novel contribution to knowledge was made by demonstrating the ability of Ti$_3$C$_2$T$_x$ to suppress pro-inflammatory cytokine production (**Fig. 3.15**) and repress overexpression of EMT markers (**Fig. 3.18; 3.20**) whilst increasing wound closure rate thereby promoting a positive resolution of LEC wound healing response (**Fig. 3.17**). It was also shown that Ti$_3$C$_2$T$_x$ coatings do not significantly impact the lipid composition of LECs under the experimental conditions used (**Fig. 4.14**). This work has tentatively suggested mechanisms of action leading to the cytokine suppression induced by Ti$_3$C$_2$T$_x$ coatings via the cytokine-cytokine receptor interaction pathway and the potential interaction of Ti$_3$C$_2$T$_x$ coatings to block the formation of the NLRP3 inflammasome complex, inhibiting the secondary activation required for IL-1β release. This work has shown that Ti$_3$C$_2$T$_x$ does not upregulate key senescence markers and downregulates release of cytokines potentially linked to SASP (**Fig. 5.6; 5.7**). It has also shown that fibrotic events induced by TGF-β2 treatment may also be linked to the induction of senescence and SASP in LECs. This work has presented for the first time the use of a silicone-based capsule bag model to investigate cell migration across the posterior capsule and IOL types (**Fig. 6.7 – 6.10**).

Using an *in vitro* LEC model for inflammation and fibrosis, this work mimicked key developmental pathways of PCO, including the induction of IL-6, IL-8, IL-1β and other hallmark inflammation gene sets by LEC and the migration and differentiation of LEC seen during fibrosis. $Ti_3C_2T_x$ was added to these pathways to examine its effect on these pathways. The initial suppression of pro-inflammatory pathways by $Ti_3C_2T_x$ was investigated further by genomic and lipidomics analysis to infer a potential mechanism of action. This work evidenced senescence associated pathways may be upregulated by TGF-β2-induced fibrosis and that $Ti_3C_2T_x$ does not induce cellular senescence pathways and may reduce the SASP associated inflammatory cytokine release in LECs. The impact of IOL material and $Ti_3C_2T_x$ coatings on the IOL optic was investigated using immortalised LEC lines within a silicone-based capsule bag model. This work has provided evidence to support the hypothesis that MXene can be optimised as a coating for AIOL implantation in a design capable of reducing pathways associated with the development of PCO. Further work in this area will include investigating the potential of intercalating $Ti_3C_2T_x$ coatings with an inhibitory molecule of PCO to further support the production of an AIOL with reduced propensity towards PCO development (14).

7.1.1 IL-1β as a positive control to induce pro-inflammatory pathways contributing to PCO development

IL-6, IL-8 and IL-1 have all individually been linked to the developmental pathways of PCO. ELISA analysis was used to elucidate any potential interaction of these cytokines in HLE-B3 cells. Firstly, the role of IL-1 was investigated. Literature confirms the presence of IL-1 in the eye (111,119,120). The findings of the ELISA assays found IL-1β to be an appropriate immunostimulant to induce IL-6, IL-8 and further IL-1β release by HLE-B3 cells (**Fig. 3.9**). This was further supported by the functional analysis of DEGs in IL-1β-treated cells which identified the upregulated BP and MF pathways associated with these DEGs, also contributed towards PCO development (**Fig. 4.5; 4.6**). IL-1β was used as a positive pro-inflammatory mediator control in future experiments. However, as shown in this work, IL-1β is not produced by HLE-B3 cells

under physiological conditions. Current literature suggests IL-1α is expressed by damaged, stressed cells which leads to the release of IL-1β. This work confirmed that IL-1α treatment of HLE-B3 cells initiates IL-1β release (**Fig. 3.11**). Moreover, the results of the ELISA showed that the release of IL-1β amplifies its upregulated release via autocrine signalling and incites IL-6 and IL-8 release by HLE-B3 cells (**Fig. 3.9; 3.11**). This work has demonstrated a cell-based model of the cytokine-induced inflammation pathway-initiated PCS which could then be used to assess the impact of $Ti_3C_2T_x$ coatings on this response.

7.1.2 The positive resolution of the wound-healing response in lens epithelial cells by $Ti_3C_2T_x$ (MXene)

$Ti_3C_2T_x$ showed a positive resolution of the wound-healing response in the *in vitro* LEC model by significantly suppressing the release of IL-1β and promoting would closure whilst repressing the overexpression of cytoskeletal mesenchymal filament vimentin (**Fig. 3.15; 3.17; 3.18; 3.20**). ELISA analysis revealed that $Ti_3C_2T_x$ did not incite IL-6, IL-8, IL-1β or TNF release by HLE-B3 cells. At the LEC gene transcriptome level, $Ti_3C_2T_x$-treated cells did not induce gene expression of *CXCL1*, *IL-6* and *IL-1β* (**Fig. 3.16; 4.7**). RNA sequencing revealed that $Ti_3C_2T_x$ did not significantly upregulate any of the hallmark inflammation gene sets (**Fig. 4.9**). Indeed, this body of work has shown that the presence of $Ti_3C_2T_x$ may suppress cytokine-induced inflammation, supporting previous studies in THP-1 monocytes (14,64). Cells primed with IL-1β and treated with $Ti_3C_2T_x$ coatings showed a significant downregulation in IL-1β release, at protein and gene level (**Fig. 3.15; 3.16**). Other inflammatory response genes more weakly induced in IL-1β, and $Ti_3C_2T_x$-treated cells included *PDPN, CXCL10, CXCL11, CCL7, LAMP3, IL-1α, IL-1β* and *RNF144B,* of which several have been linked to the developmental pathways leading to PCO (**Fig. 4.9; 4.10**).

Furthermore, $Ti_3C_2T_x$ demonstrated no significant impact on the EMT pathway of LEC. The EMT pathway was induced in LECs via TGF-β2 treatment. $Ti_3C_2T_x$ coatings did not upregulate expression of key EMT markers, α-SMA, SMAD2/3 and vimentin relative to cells

treated with TGF-β2 (**Fig. 3.18; 3.20**). Although wound closure rate was significantly increased on cells grown on $Ti_3C_2T_x$ coatings as shown by scratch assay analysis (**Fig. 3.17**), $Ti_3C_2T_x$ suppressed vimentin overexpression in the LEC treated with TGF-β2. Additionally, no significant changes in lens lipid membrane composition were found suggesting $Ti_3C_2T_x$ coatings have good compatibility with the lens lipid membrane and does not induce lipid peroxidation (**Fig. 4.14**). A potential mechanism behind the compatibility of $Ti_3C_2T_x$ with LECs was investigated by genomics and lipidomics analysis in **Chapter 4**. RNA sequencing found that $Ti_3C_2T_x$ downregulated several sub-families within the cytokine-cytokine receptor interaction pathway. This work has contributed to knowledge by demonstrating the positive resolution of the wound-healing response in LECs by $Ti_3C_2T_x$, potentially preventing upregulation of chronic wound-healing pathways contributing to PCO. This body of work has suggested potential mechanisms of action by which $Ti_3C_2T_x$ may work via interaction with the cytokine-cytokine interaction response pathway (**Fig. 4.11**), or the formation of the NLRP3 inflammasome complex, blocking the secondary activation and release of IL-1β (**Fig. 3.2**), suppressing cell gene transcriptome changes which promote anti-inflammatory mechanisms to resolve the inflammation and EMT response of LECs.

7.1.3 The role of senescence in inflammation and fibrotic pathways leading to PCO and potential impact of $Ti_3C_2T_x$

A preliminary investigation to explore the role of senescence in the inflammatory and fibrosis pathways contributing to PCO development and how $Ti_3C_2T_x$ coatings may impact the induction of senescence in LECs was conducted. This work has demonstrated that the presence of $Ti_3C_2T_x$ coatings does not upregulate key markers of senescence in LECs. It has shown that $Ti_3C_2T_x$ coatings may slow the onset of senescence by downregulating SASP-related IL-6 and IL-8 release in senescence induced LECs (**Fig. 5.10**). It has shown that the induction of senescence in LECs can be optimised using etoposide treatment (**Fig. 5.5; 5.6**). This work has evidenced the significance of investigating the role of senescence within PCO development and

the relationship between TGF-β2 and its signalling pathways on the induction of senescence in residual LECs PCS (**Fig. 5.4**; **5.6**).

7.1.4 Establishment of capsule bag model

An alternative artificial capsule bag model has been designed, constructed, and used to monitor cell migration. The proof-of-concept silicone-derived 3D *in vitro* capsule bag model was modified to allow for cell seeding and was used to observe cell migration across different IOL types (**Fig. 6.7 − 6.10**). This work has contributed to knowledge by providing an alternative approach to the capsule bag model and on further optimisation, a model that gives insight into the cell and tissue spatial arrangement of the lens environment that does not rely on more expensive, harder to access and time constrained animal or human tissue.

7.2 Limitations

This body of work has shown that $Ti_3C_2T_x$ coatings promotes a positive resolution of the hyperinflammation and EMT-associated pathways contributing to the wound-healing response of LEC. There were several limitations to this work. Firstly, these conclusions are based on an *in vitro* immortalised cell model. The use of a primary cell strain could be used to better mimic the in vivo phenotype of the LEC but has limitations within the tissue culture environment in terms of growth characteristics and culture life span. Further development would include *in vivo* and *ex vivo* animal models. An ex vivo capsule bag model would allow for the consideration of cell response in a 3D environment which is known to better sustain phenotypic integrity. There was a limitation in the quantification of LEC lipid membrane composition. In quantifying the lens lipid membrane composition post-IL-1β and $Ti_3C_2T_x$ treatment, LC-MS analysis was used. This technique cannot detect cholesterol which is a key component in lens lipid membrane. Other techniques to detect cholesterol should be explored due to its predominance in lens membrane integrity. This work has demonstrated that a silicone-derived capsule bag model can be

developed. However, the impact of the collagen-coated silicone on cell phenotype and access to the IOL for analysis at the experimental endpoint requires more investigation.

7.3   Future work

This body of work has shown that $Ti_3C_2T_x$ coatings may suppress or markedly reduce pro-inflammatory cytokine pathways and fibrotic EMT markers through a mechanism linked to cytokine-cytokine receptor interactions. There is a requirement to optimise the specific concentrations and Ti_3C_2T composition the cells must be exposed for $Ti_3C_2T_x$ to induce significant suppression across all inflammation gene sets and fibrotic markers. However, this would additionally require a parallel investigation to ensure that this did not impact on transparency which would negatively affect its use as a coating within an AIOL device.

Approaches to explore the underlying mechanisms behind the ability of $Ti_3C_2T_x$ to suppress pro-inflammatory pathways could include comparing the gene expression of LECs treated with transcription factor inhibitors to the LECs treated with $Ti_3C_2T_x$ to identify any similar alterations in LEC gene transcriptome. To further investigate if $Ti_3C_2T_x$ interacts with gene transcription machinery to suppress cytokine release, IL-1β and IL-6 gene knock-out species can be used to explore if $Ti_3C_2T_x$ can still induce repression of pro-inflammatory cytokines. To explore if $Ti_3C_2T_x$ upregulates siRNA to interfere with the NLRP3 inflammasome complex machinery, an RNA interference study can be conducted by transfecting LECs with siRNAs targeting NLRP3 (199). Furthermore, the role of TGF-β2 and senescence inducing fibrotic events contributing to the development of PCO requires further investigation and offers an alternative approach to targeting PCO.

This work has shown a proof-of-concept silicone-derived 3D *in vitro* capsule bag model can be utilised to monitor cell migration across the posterior capsule. It requires further development into producing an improved ECM coating to better mimic the native environment for residual LECs. The culture condition can also be optimised by adding growth factors such as

TGF-β2 and cytokines to investigate how these factors impact cell migration and expression individually and in synergy, which cannot be achieved using animal or human tissue.

Further work to optimise the positive interaction of $Ti_3C_2T_x$ within the AIOL device for more significant repression of LEC propensity towards PCO could potentially be through drug elution mechanisms. Organic molecules intercalate easily within MXene flakes due to its hydrophilicity and high negative zeta potential of -80 to -30 mV (201). Resveratrol, a senolytic that represses EMT associated pathways in LECs, could be intercalated within MXene coatings applied as part of an AIOL device to target inflammatory and fibrotic pathways leading to PCO development (70).

7.4 Conclusion

This body of work has demonstrated for the first time, the ability of $Ti_3C_2T_x$ to interact with the inflammatory pathway machinery to promote the positive resolution of the LEC wound healing response, suppressing the hyperinflammation and EMT pathways contributing to PCO development. This work has established a novel silicone-based capsule bag for PCO research. Whilst this work has presented the assessment of $Ti_3C_2T_x$ coatings on LEC inflammation and EMT pathways, further work is required to optimise $Ti_3C_2T_x$ concentration for effective use as a preventative tool against PCO development prior to its application within an AIOL device.

Chapter 8: References

1.   Foster A. Cataract and "Vision 2020" - the "right to sight" initiative. Br J Ophthalmol. 2001;85(6):635–7.
2.   Zvornicanin J, Zvornicanin E. Premium intraocular lenses: The past, present and future . J Curr Ophthalmol. 2018;30:287–96.
3.   Wormstone IM, Wang L, Liu CSC. Posterior Capsule Opacification. Exp Eye Res. 2009;88:257–69.
4.   Ram J, Brar S. G, Brar S. G. Posterior Capsule Opacification: An Overview. DOS Times. 2006;12(4):285–8.
5.   Cooksley G, Dymond MK, Lacey J, Sandeman S. Factors Affecting Posterior Capsule Opacification in the Development of Intraocular Lens Materials. Pharmaceutics. 2021;13(6).
6.   Meacock WR, Spalton DJ, Stanford MR. Role of cytokines in the pathogenesis of posterior capsule opacification. Br J Ophthalmol. 2000;84:332–6.
7.   Wormstone IM, Tamiya S, Anderson I, Duncan G. TGF-β2-induced matrix modification and cell transdifferentiation in the human lens capsular bag. Investig Ophthalmol Vis Sci. 2002;43(7):2301–8.
8.   Nibourg M L, Gelens E, Kuijwe R, Hooymans JMM, Kooten G.van T, Koopmans A. S. Prevention of posterior capsular opacification. Exp Eye Res. 2015;136:100–15.
9.   Raj MS, Vasavada AR, Johar SR, Vasavadam AV, A. V, Vasavada A. Post-Operative Capsular Opacification: A Review. Int J Biomed Sci. 2007;3(4):237–50.
10.   Dawes LJ, Illingworth CD, Wormstone IM. A Fully Human In Vitro Capsular Bag Model to Permit Intraocular Lens Evaluation. Invest Ophthalmol Vis Sci. 2012;53(1):23–9.
11.   Eldred JA, Zheng J, Chen S, Wormstone IM. An in vitro human lens capsular bag model adopting a graded culture regime to assess putative impact of iols on pco formation. Investig Ophthalmol Vis Sci. 2019;60(1):113–22.
12.   Wormstone IM, Eldred JA. Experimental models for posterior capsule opacification research. Exp Eye Res. 2016;142:2–12.
13.   Alió JL, Barrio JLA del, Vega-Estrada A. Accommodative intraocular lenses: where are we and where we are going. Eye Vis. 2017;4(16).
14.   Ward EJ, Lacey J, Crua C, Dymond MK, Maleski K, Hantanasirisakul K, et al. 2D Titanium Carbide (Ti3C2Tx) in Accommodating Intraocular Lens Design. Adv Funct Mater. 2020;2000841:1–9.
15.   Lin H, Chen Y, Shi J. Insights into 2D MXenes for Versatile Biomedical Applications: Current Advances and Challenges Ahead . Adv Sci. 2018;5(1800518).
16.   Soleymaniha M, Shahbazi MA, Rafieerad AR, Maleki A, Amiri A. Promoting Role of MXene Nanosheets in Biomedical Sciences: Therapeutic and Biosensing Innovations. Adv Healthc Mater. 2019;8(1).
17.   Lipatov A, Lu H, Alhabeb M, Anasori B, Gruverman A, Gogotsi Y, et al. Elastic properties of 2D Ti3C2Tx MXene monolayers and bilayers. Sci Adv. 2018;4.
18.   Maleski K, Ren CE, Zhao MQ, Anasori B, Gogotsi Y. Size-Dependent Physical and Electrochemical Properties of Two-Dimensional MXene Flakes. ACS Appl Mater Interfaces. 2018;10(29):24491–8.
19.   Anasori B, Lukatskaya MR, Gogotsi Y. 2D metal carbides and nitrides (MXenes) for energy storage. Nat Rev Mater. 2017;2(16098).
20.   Zhang CJ, Anasori B, Seral-Ascaso A, Park SH, McEvoy N, Shmeliov A, et al. Transparent, Flexible, and Conductive 2D Titanium Carbide (MXene) Films with High Volumetric Capacitance. Adv Mater. 2017;29(36).
21.   Trent N. Global Intraocular Lens market 2019: size, share, demand, trends, growth and 2022 forecasts explored in latest research. Wise Guy Reports. 2018;(FBI101220):1–2.
22.   Vasavada A, Allen D, Vasavada A. Cataract and surgery for cataract. Br Med J. 2006;333(7559):128–32.
23.   Laser Eye Surgery Hub. Cataract Statistics & Resources [Internet]. 2018 [cited 2020 Nov 9]. p. 1. Available from: https://www.lasereyesurgeryhub.co.uk/cataract-statistics/
24.   Hejtmancik JF, Shiels A. Overview of the Lens. Prog Mol Biol Transl Sci. 2017;134:119–27.
25.   Joseph R, Bales K, Srivastava K, Srivastava O. Lens epithelial cells-induced pluripotent stem cells as a model to study epithelial-mesenchymal transition during posterior capsular

opacification. Biochem Biophys Reports. 2019;(100696).

26. Daszynski DM, Santhoshkumar P, Phadte AS, Sharma KK, Zhong HA, Lou MF, et al. Failure of Oxysterols Such as Lanosterol to Restore Lens Clarity from Cataracts. Sci Rep. 2019;9(8459).

27. Ray NJ. Biophysical chemistry of the ageing eye lens. Biophys Rev. 2015;7(4):353–68.

28. Davis G. The Evolution of Cataract Surgery. Mo Med. 2016;113(1):58–62.

29. Jaffe NS. History of Cataract Surgery. Ophthalmology. 1996;103(8):5–16.

30. Franzco EC, Mahroo OAR, Spalton DJ. Complications of cataract surgery. Clin Exp Optom. 2010;93(6).

31. Gupta RM, Ravishankar B. Etiopathogenesis of cataract: An apprasial. Indian J Ophthalmol. 2014;62(2):103–10.

32. Bellucci R. An Introduction to Intraocular Lenses: Material, Optics, Haptics, Design and Aberration. Cataract. 2013;3:38–55.

33. Saika S. Relationship between posterior capsule opacification and intraocular lens biocompatibility. Prog Retin Eye Res. 2004;23(3):283–305.

34. Pérez-Vives C. Biomaterial Influence on Intraocular Lens Performance: An Overview. J Ophthalmol. 2018;15(2687385).

35. Pepose JS, Burke J, Qazi MA. Benefits and barriers of accommodating intraocular lenses. Curr Opin Ophthalmol. 2017;28(1):3–8.

36. Strenk SA, Strenk LM, Guo S. Magnetic resonance imaging of the anteroposterior position and thickness of the aging, accommodating, phakic, and pseudophakic ciliary muscle. J Cataract Refract Surg. 2010;36(2):235–41.

37. Pardue MT, Sivak JG. Age-related changes in human ciliary muscle. Optom Vis Sci. 2000;77(4):204–10.

38. Sheppard AL, Davies LN. The effect of ageing on in vivo human ciliary muscle morphology and contractility. Investig Ophthalmol Vis Sci. 2011;52:1809–16.

39. Liang Y-L, Jia S-B. Clinical application of accommodating intraocular lens. Int J Ophthalmol. 2018;11(6):1028–37.

40. Nun J Ben. Accommodating Intraocular Lens (AIOL) Capsules. 2010. p. US20110112636A1.

41. Chattopadhyaym DN, Seal GN. Amplitude of accommodation in different age groups and age of on set of presbyopia in Bengalee population. Indian J Ophthalmol. 1984;32(2):85–7.

42. Alio JL, Simonov A, PLaza-Puche AB, Angelov A, Agelov Y, van Lawick W. Visual Outcomes and Accommodative Response of the Lumina Accommodative Intraocular Lens. Am J Ophthalmol. 2016;164:37–48.

43. Zhao J, Yu J, Wang T, Mban B. Ciliary sulcus implantation of intraocular lens in manual small incision cataract surgery complicated by large posterior capsule rupture. Exp Ther Med. 2018;17(2):1470–5.

44. Woo YS. Transparent Conductive Electrodes Based on Graphene-Related Materials. Micromachines. 2019;10(13).

45. Zhang Q, Z L, Yang J, Kim J. Graphene oxide-based transparent conductive films. Prog Mater Sci. 2014;64:200–47.

46. Lee S, Jo I, Kang S, Jang B, Moon J, Park JB, et al. Smart Contact Lenses with Graphene Coating for Electromagnetic Interference Shielding and Dehydration Protection. ACS Nano. 2017;11(6):5318–24.

47. Park J, Kim J, Kim SY, Cheong WH, Jang J, Park YG, et al. Soft, smart contact lenses with integrations of wireless circuits, glucose sensors, and displays. Sci Adv. 2018;4(1).

48. Kim J, Kim M, Lee MS, Kim K, Ji S, Kim YT, et al. Wearable smart sensor systems integrated on soft contact lenses for wireless ocular diagnostics. Nat Commun. 2017;8(14997).

49. Mahmoodi T, Hahn Y, Wang Y. Graphene and its derivatives for solar cells application. Nano Energy. 2018;47:51–65.

50. Choi C, Choi MK, Liu S, Kim MSM, Park OK, Im C, et al. Human eye-inspired soft optoelectronic device using high-density MoS2-graphene curved image sensor array. Nat Commun. 2017;8(1664).

51. Hantanasirisakul K, Zhao M, Urbankowski P, Halim J, Anasori B, Kota S, et al. Fabrication of Ti3C2TX MXene Transparent Thin Films with Tunable Optoelectronic Properties. Adv

Electron Mater. 2016;2.

52. Gou G, Li X, Jian J, Tian H, Wu F, Ren J, et al. Two-stage amplification of an ultrasensitive MXene-based intelligent artificial eardrum. Sci Adv. 2022;8(13).

53. Yin S, Zhao B, Wan J, Wang S, Yang J, Wang X, et al. MXene-contact enhanced broadband photodetection in centimeter level GeS films. J Physiscs D Appl Phys. 2022;55(26):265105.

54. Ma C, Yuan Q, Du H, Ma M-G, Si C, Wan P. Multiresponsive MXene (Ti 3 C 2 T x)-Decorated Textiles for Wearable Thermal Management and Human Motion Monitoring. ACS Appl Mater Interfaces. 2020;12(30):34226–34.

55. Hantanasirisakul K, Gogotsi Y. Electronic and Optical Properties of 2D Transition Metal Carbides and Nitrides (MXenes). Adv Mater. 2018;30(52).

56. Huang K, Li Z, Lin J, Han G, Huang P. Two-dimensional transition metal carbides and nitrides (MXenes) for biomedical application. Chem Soc Rev. 2018;47:5109–24.

57. Naguib M, Mochalin VN, Barsoum MW, Gogotsi Y. 25th Anniversary Article: MXenes: A New Family of Two-Dimensional Materials. Adv Mater. 2014;26(7):992–1004.

58. Gogotsi Y, Anasori B. The Rise of MXenes. ACS Nano. 2019;13(8):8491–4.

59. Lin H, Gao S, Dai C, Chen Y, Shi J. A Two-Dimensional Biodegradable Niobium Carbide (MXene) for Photothermal Tumor Eradication in NIR-I and NIR-II Biowindows. J Am Chem Soc. 2017;139(45):16235–47.

60. Rasool K, Helal M, Ali A, Ren CE, Gogotsi Y, Mahmoud KA. Antibacterial Activity of Ti3C2Tx MXene. ACS Nano. 2016;10:3674–84.

61. Alimohammadi F, Gh MS, Attanayake NH, Thenuwara AC, Gogotsi Y, Anasori B, et al. Antimicrobial Properties of 2D MnO2 and MoS2 Nanomaterials Vertically Aligned on Graphene Materials and Ti3C2 MXene. Langmuir. 2018;34:7192–200.

62. Zhou L, Zheng H, Liu Z, Wang S, Liu Z, Chen F, et al. Conductive Antibacterial Hemostatic Multifunctional Scaffolds Based on Ti3C2TxMXene Nanosheets for Promoting Multidrug-Resistant Bacteria-Infected Wound Healing. ACS Nano. 2021;15(2):2460–80.

63. Dai C, Lin H, Xu G, Liu Z, Wu R, Chen Y. Biocompatible 2D Titanium Carbide MXenes Composite Nanosheets for PH-Responsive MRI-Guided Tumor Hyperthermia. Chem Mater. 2017;29(20):8637–52.

64. Ozulumba T, Ingalve G, Gogotsi Y, Sandeman S. Moderating cellular inflammation using 2-dimensional titanium carbide MXene and graphene variants. Biomater Sci. 2021;9(5).

65. Ursell PG, Dhariwal M, Majirska K, Ender F, Klason-Ray S, Venerus A, et al. Three-year incidence of Nd:YAG capsulotomy and posterior capsule opacification and its relationship to monofocal acrylic IOL biomaterial: a UK Real World Evidence study. Eye. 2018;32:1579–89.

66. Ursell P., Dhariwal M, O'Boyle D, Khan J, Venerus A. 5 year incidence of YAG capsulotomy and PCO after cataract surgery with single-piece monofocal intraocular lenses: a real-world evidence study of 20,763 eyes. Eye. 2020;34:960–968.

67. Karahan E, Er D, Kaynak S. An Overview of Nd:YAG Laser Capsulotomy. Med hypothesis, Discov Innov Ophthalmol J. 2014;3(2):45–50.

68. Bhargava R, Kumar P, Phogat H, Chaudhary Kulbhushan P, Chaudhary Kulbhushan P. Neodymium-Yttrium Aluminium Garnet Laser Capsulotomy Energy Levels for Posterior Capsule Opacification . J Ophthalmic Vis Res. 2015;10(1):37–42.

69. Burq MA, Taqui AM. Frequency of retinal detachment and other complications after neodymium:YAG capsulotomy. J Cataract Refract Surg. 2008;58:550–2.

70. Smith, A, J O, Eldred JA, Wormstone IM. Resveratrol inhibits wound healing and lens fibrosis: A putative candidate for posterior capsule opacification prevention. Investig Ophthalmol Vis Sci. 2019;60(12):3863–77.

71. Awasthi N, Guo S, Wagner BJ. Posterior Capsular Opacification: A Problem Reduced but Not Yet Eradicated. JAMA Ophthalmol. 2009;127(4):555–62.

72. Ling R, Borkenstein E-M, Borkenstein AF. Evaluation of Nd:YAG Laser Capsulotomy Rates in a Real-Life Population. Clin Ophthalmol. 2020;14:3249–57.

73. Apple DJ, Peng Q, Visessook N, Werner L, Pandey, Suresh K, Escobar-Gomez M, et al. Eradication of Posterior Capsule Opacification: Documentation of a Marked Decrease in Nd:YAG Laser Posterior Capsulotomy Rates Noted in an Analysis of 5416 Pseudophakic Human Eyes Obtained Postmortem. Ophthalmology. 2020;127(4):S29–42.

74.   Fişuş AD, Findl O. Capsular fibrosis: a review of prevention methods and management. Eye. 2020;34:256–62.

75.   Sinha R, Shekhar H, Sharma N, Titiyal JS, Vajpayee RB. Posterior capsular opacification: A review. Indian J Ophthalmol. 2013;61(7):371–6.

76.   Paik J., Shiloach M, Macsai-Kaplan M. The Effect of Posterior Capsule Polishing on Posterior Capsule Opacification. Invest Ophthalmol Vis Sci. 2012;53(14):6668.

77.   Menapace R, Wirtitsch M, Findl O, Buehl W, Kriechbaum K, Sacu S. Effect of anterior capsule polishing on posterior capsule opacification and neodymium: YAG capsulotomy rates: three-year randomized trial. J Cataract Refract Surg. 2005;31(11):2067.

78.   Kramer GD, Werner L, Mamalis N. Prevention of postoperative capsular bag opacification using intraocular lenses and endocapsular devices maintaining an open or expanded capsular bag. J Cataract Refract Surg. 2016;42:469–84.

79.   Hasanee K, Butler M, Ahmed IIK. Capsular tension rings and related devices: current concepts. Curr Opin Ophthalmol. 2006;17(1):31–41.

80.   Kramer GD, Werner L, MacLean K, Farukhi A, Gardiner GL, Mamalis N. Evaluation of stability and capsular bag opacification with a foldable intraocular lens coupled with a protective membrane in a rabbit model. J Cataract Refract Surg. 2015;41:1738–44.

81.   Batur M, Gül A, Seven E, Can E, Yaşar T. Posterior capsular opacification in preschool- and school-age patients after pediatric cataract surgery without posterior capsulotomy. Turk Oftalmoloiji Derg. 2016;46(5):205–8.

82.   Wormstone IM, Liu CS, Rakic JM, Marcantonio JM, Vrenson GF, Duncan G. Human lens epithelial cell proliferation in a protein-free medium. Invest Ophthalmol Vis Sci. 1997;38(2):396–404.

83.   Tokko HA, Hussain F, Al-Awadi A, Mei F, Zeiter JH, Kim C, et al. Factors Associated with the Development of Posterior Capsule Opacification Requiring Yttrium Aluminum Garnet Capsulotomy. Optom Vis Sci. 2019;96(7):492–9.

84.   Wu S, Tong N, Pan L, Jiang X, Li Y, Guo M, et al. Retrospective Analyses of Potential Risk Factors for Posterior Capsule Opacification after Cataract Surgery. J Ophthalmol. 2018;(9089285).

85.   Wei Z, Gordon P, Hao C, Huangfu J, Fan E, Zhang X, et al. Aged Lens Epithelial Cells Suppress Proliferation and Epithelial–Mesenchymal Transition-Relevance for Posterior Capsule Opacification. Cells. 2022;11(13).

86.   Kiziltoprak H, Tekin K, Inanc M, Goker YS. Cataract in diabetes mellitus. World J Diabetes. 2019;10(3):140–53.

87.   Zukin LM, Pedler MG, Groman-Lupa S, Pantcheva M, Ammar DA, Mark Petrash J. Aldose reductase inhibition prevents development of posterior capsular opacification in an in vivo model of cataract surgery. Investig Ophthalmol Vis Sci. 2018;59(18):3591–8.

88.   Praveen MR, Vasavada AR, Shah GD, Shah AR, Khamar BM, Dave KH. A prospective evaluation of posterior capsule opacification in eyes with diabetes mellitus: A case-control study. Eye. 2014;28(6):720–7.

89.   Chen H-C, Lee C-Y, Sun C-C, Huang J-Y, Lin H-Y, Yang S-F. Risk factors for the occurrence of visual threatening posterior capsule opacification . J Transl Med. 2019;17(1).

90.   Gayton J L. Etiology, prevalence, and treatment of dry eye disease. Clin Ophthalmol. 2009;3:405–12.

91.   Wallin TR, Hinckley M, Nilson C, Olson RJ. A clinical comparison of single-piece and three-piece truncated hydrophobic acrylic intraocular lenses. Am J Ophthalmol. 2003;136(4):614–9.

92.   Bilge AH, Aykan U, Akin T, Unsal U. The Effects of Three-Piece or Single-Piece Acrylic Intraocular Lens Implantation on Posterior Capsule Opacification. Eur J Ophthalmol. 2004;14(5):375–80.

93.   Haripriya A, Chang DF, Vijayakumar B, Niraj A, Shekhar M, Tanpreet S, et al. Long-term Posterior Capsule Opacification Reduction with Square-Edge Polymethylmethacrylate Intraocular Lens: Randomized Controlled Study. Ophthalmology. 2017;124(3):295–302.

94.   Boureau C, Lafuma A, Jeanbat V, Berdeaux G, Smith AF. Incidence of Nd:YAG laser capsulotomies after cataract surgery: comparison of 3 square-edged lenses of different composition. Can J Ophthalmol. 2009;44(2):165–70.

95.   Bai L, Zhang J, Chen L, Ma T, Liang HC. Comparison of posterior capsule opacification at 360-degree square edge hydrophilic and sharp edge hydrophobic acrylic intraocular lens in diabetic patients. Int J Ophthalmol. 2015;8(4):725–9.

96.   Werner L, Mamalis N, Pandey SK, Izak AM, Nilson CD, Davis BL, et al. Posterior capsule opacification in rabbit eyes implanted with hydrophilic acrylic intraocular lenses with enhanced square edge. J Cataract Refract Surg. 2004;30:2403–2409.

97.   Kohnen T, Fabian E, Gerl R, Hunold W, Hütz W, Strobel J, et al. Optic Edge Design as Long-term Factor for Posterior Capsular Opacification Rates. Ophthalmology. 2008;115(8):1308–14.

98.   Nishi O, Nishi K, Akura J, Nagata T. Effect of round-edged acrylic intraocular lenses on preventing posterior capsule opacification. J Cataract Refract Surg. 2001;27(4):608–13.

99.   Hazra S, Palui H, Vemuganti GK. Comparison of design of intraocular lens versus the material for PCO prevention. Int J Ophthalmol. 2012;5(1):59–63.

100.   Yu N, Fang F, Wu B, Zeng L, Cheng Y. State of the art of intraocular lens manufacturing. Int J Adv Manuf Technol. 2018;98:1103–1130.

101.   Özyol P, Özyol E, Karel F. Biocompatibility of intraocular lenses. Turk Oftalmoloiji Derg. 2017;47(4):221–5.

102.   Cooke CA, McGimpsey S, Mahon G, Best RM. An In Vitro Study of Human Lens Epithelial Cell Adhesion to Intraocular Lenses with and without a Fibronectin Coating. Invest Ophthalmol Vis Sci. 2006;47(7):2985–9.

103.   Plüss CJ, Kustermann S. A Human Three-Dimensional In Vitro Model of Lens Epithelial Cells as a Model to Study Mechanisms of Drug-Induced Posterior Subcapsular Cataracts. J Ocul Pharmacol Ther. 2019;36(1):56–64.

104.   Andley U., Rhim J., Chylack Jr LT, Fleming TP. Propagation and Immortalization of Human Lens Epithelial Cells in Culture. Invest Ophthalmol Vis Sci. 1994;35(7):3094–102.

105.   Awasthi N, Wagner BJ. Suppression of Human Lens Epithelial Cell Proliferation by Proteasome Inhibition, a Potential Defense against Posterior Capsular Opacification. Invest Ophthalmol Vis Sci. 2006;47(10):4482–9.

106.   Eldred; JA, Hodgkinson; LM, Dawes; LJ, Reddan; JR, Edwards; DR, Wormstone IM. MMP2 Activity is Critical for TGFβ2-Induced Matrix Contraction—Implications for Fibrosis. Lens. 2012;53(7):4085–98.

107.   Wei H, Wolffsohn JS, Oliveira OG de, Davies LN. Characterisation and Modelling of an Artificial Lens Capsule Mimicking Accommodation of Human Eyes. Polymers (Basel). 2021;13(3916).

108.   Mohammadpour M, Jafarinasab MR, Javadi MA. Outcomes of acute postoperative inflammation after cataract surgery. Eur J Ophthalmol. 2007;17(1):20–8.

109.   Jiang J, Shihan MH, Wang Y, Duncan MK. Lens Epithelial Cells Initiate an Inflammatory Response Following Cataract Surgery. Invest Ophthalmol Vis Sci. 2018;59(12):4986–97.

110.   Ma B, Yang L, Jing R, Liu J, Quan Y, Hui Q, et al. Effects of Interleukin-6 on posterior capsular opacification. Exp Eye Res. 2018;172:94–103.

111.   Ferrick MR, Thurau SR, Oppenheim MH, Herbort CP, Ni M, Zachariae COC, et al. Ocular inflammation stimulated by intravitreal interleukin-8 and interleukin-1. Investig Ophthalmol Vis Sci. 1991;32(5):1534–9.

112.   Basu A, Krady JK, Levison SW. Interleukin-1: A master regulator of neuroinflammation. J Neurosci Res. 2004;78(2):151–6.

113.   Lewis AC. Interleukin-6 in the pathogenesis of posterior capsule opacification and the potential role for interleukin-6 inhibition in the future of cataract surgery. Med Hypotheses. 2013;80(4):466–74.

114.   Nishi O, Nishi K, Ohmoto Y. Synthesis of interleukin-1, interleukin-6, and Basic Fibroblast Growth Factor by Human Cataract Lens Epithelial Cells. J Cataract Refract Surg. 1996;22(1):852–8.

115.   Saika S. TGFbeta pathobiology in the eye. Lab Invest. 2006;86(2):106–15.

116.   Kubo E, Shibata T, Singh P D, Sasaki H. Roles of TGFB and FGF Signals in the Lens: Tropomyosin Regulation for Posterior Capsule Opacification. Int J Mol Sci. 2018;19(3093).

117.   Taiyab A, Holms J, West-Mays JA. β-Catenin/Smad3 Interaction Regulates Transforming

Growth Factor-β-Induced Epithelial to Mesenchymal Transition in the Lens. Int J Mol Sci. 2019;20(9):2078.

118. Walton KL, Johnson KE, Harrison CA. Targeting TGF-β mediated SMAD signaling for the prevention of fibrosis. Front Pharmacol. 2017;8(461).

119. Nishi O, Nishi K, Ohmoto Y. Effect of interleukin 1 receptor antagonist on the blood-aqueous barrier after intraocular lens implantation. Br J Ophthalmol. 1994;78:917–20.

120. Wilson SE, Esposito A. Focus on Molecules: Interleukin-1: A master regulator of the corneal response to injury. Exp Eye Res. 2009;89(2):124–5.

121. Ooi KGJ, Galatowicz G, Calder VL, Lightman SL. Cytokines and chemokines in uveitis - Is there a correlation with clinical phenotype? Clin Med Res. 2006;4(4):294–309.

122. Kubo E, Shibata S, Shibata T, Kiyokawa E, Sasaki H, Singh DP. FGF2 antagonizes aberrant TGFβ regulation of tropomyosin: role for posterior capsule opacity. J Cell Mol Med. 2017;21(5):916–28.

123. Tandon A, Tovey JCK, Sharma A, Gupta R, Mohan RR. Role of Transforming Growth Factor Beta in Corneal Function, Biology and Pathology. Curr Mol Med. 2012;10(6):565–78.

124. Nishi O, Nishi K, Wada K, Ohmoto Y. Expression of transforming growth factor (TGF)-α, TGF-β2 and interleukin 8 messenger RNA in postsurgical and cultured lens epithelial cells obtained from patients with senile cataracts. Graefe's Arch Clin Exp Ophthalmol. 1999;237:806–11.

125. Yamashita H. Functions of the transforming growth factor-β superfamily in eyes. J Japanese Ophthalmol Soc. 1997;101(12):927–47.

126. Lois N, Taylor JA, Forrester JV, Smith GC, Van't Hof R., McKinnon AD. Effect of TGF-(beta)2 and Anti-TGF(beta)2 antibody in a new in vivo rodent model of posterior capsule opacification. Invest Ophthalmol Vis Sci. 2005;46:4260–6.

127. Cho HJ, Baek KE, Saika S, Jeong MJ, Yoo J. Snail is required for transforming growth factor-beta-induced epithelial-mesenchymal transition by activating PI3 kinase/Akt signal pathway. Biochem Biophys Res Commun. 2007;353(2):337–43.

128. Pei C, Ma B, Kang Q-Y, Qin L, Cui L-J. Effects of transforming growth factor beta-2 and connective tissue growth factor on induction of epithelial mesenchymal transition and extracellular matrix synthesis in human lens epithelial cells. Int J Ophthalmol. 2013;6(6):752–7.

129. Gotoh N, Perdue NR, Matsushima H, Sage EH, Yan Q, Clark JI. An in vitro model of posterior capsular opacity: SPARC and TGF-β2 minimize epithelial-to-mesenchymal transition in lens epithelium. Investig Ophthalmol Vis Sci. 2007;48:4679–87.

130. Amoozgar B, Fitzpatrick SD, Sheardown H. Effect of anti-TGF-β2 surface modification of polydimethylsiloxane on lens epithelial cell markers of posterior capsule opacification. J Bioact Compat Polym. 2013;28(6):637–51.

131. Alberts B, Johnson A, Lewis J, Raff M, Roberts K, Walter P. An Overview of the Cell Cycle. Molecular Biology of the Cell. 2002. p. https://www.ncbi.nlm.nih.gov/books/NBK26869/.

132. Burton DGA, Faragher RGA. Cellular senescence: from growth arrest to immunogenic conversion. Age (Omaha). 2015;37(27).

133. Heidari N, Sandeman S, Faragher RGA. Hepatotoxic metabolites induce cellular senescence and loss of primary tissue specific functions in HepG2 cells: protection by resveralogues (manuscript in preparation). 2023;XX(XX).

134. Alhabeb M, Maleski K, Anasori B, Lelyukh P, Clark L, Sin S, et al. Guidelines for Synthesis and Processing of Two-Dimensional Titanium Carbide (Ti 3 C 2 T x MXene). Chem Mater. 2017;29(18):7633–7644.

135. Mohammadi AV, Rosen J, Gogotsi Y. The world of two-dimensional carbides and nitrides (MXenes). Science (80-). 2021;372(eabf1581).

136. Jiang L, Zhou D, Yang J, Zhou S, Wang H, Yuan X, et al. 2D single- and few-layered MXenes: synthesis, applications and perspectives. J Mater Chem A. 2022;10:13651–72.

137. Shekhirev M, Shuck CE, Sarycheva A, Gogotsi Y. Characterization of MXenes at every step, from their precursors to single flakes and assembled films. Prog Mater Sci. 2021;120(100757).

138. Abdolhosseinzadeh S, Jiang X, Zhang H, Qiu J, Zhang CJ. Perspectives on solution processing of two-dimensional MXenes. Mater Today. 2021;48:214–40.

139. Lei J, Zhang X, Zhou Z. Recent advances in MXene: Preparation, properties, and applications. Front Phys. 2015;10(107303).

140. Wu X, Tan F, Cheng S, Chang Y, Wang X, Chen L. Investigation of interaction between MXene nanosheets and human plasma and protein corona composition. Nanoscale. 2022;14:3777–87.

141. Ronchi RM, Arantas JT, Santos SF. Synthesis, structure, properties and applications of MXenes: Current status and perspectives. Ceram Int. 2019;45:18167–88.

142. Maleski K, Shuck CE, Fafarman AT, Gogotsi Y. The Broad Chromatic Range of Two-Dimensional Transition Metal Carbides. Adv Opt Mater. 2020;9(4):2001563.

143. Naguib M, Kurtoglu M, Presser V, Lu J, Niu J, Heon M, et al. Two-dimensional nanocrystals produced by exfoliation of Ti 3AlC 2. Adv Mater. 2011;23(37):4248–53.

144. Kwok DY, Neumann AW. Contact angle measurement and contact angle interpretation. Adv Colloid Interface Sci. 1999;81:167–249.

145. Yuan Y, Lee TR. Contact Angle and Wetting Properties. Bracco G, Holst B Surf Sci Tech Springer Ser Surf Sci. 2013;51:3–34.

146. Goldberg W. Dynamic light scattering. Am J Phys. 1999;67(1152).

147. Stetefeld J, McKenna S., Patel T. Dynamic light scattering: a practical guide and applications in biomedical sciences. Biophys Rev. 2016;8(4):409–427.

148. Xia Y, Mathis TS, Zhao M, Anasori B, Dang A, Zhou Z, et al. Thickness-independent capacitance of vertically aligned liquid-crystalline MXenes. Nature. 2018;557(7705):409–12.

149. Danaei M, Dehghankhold M, Ataei S, Hasanzadeh Davarani F, Javanmard R, Dokhani A, et al. Impact of particle size and polydispersity index on the clinical applications of lipidic nanocarrier systems. Pharmaceutics. 2018;10(2).

150. Quain E, Mathis TS, Kurra N, Maleski K, Van Aken KL, Alhabeb M, et al. Direct Writing of Additive-Free MXene-in-Water Ink for Electronics and Energy Storage. Adv Mater Technol. 2019;4(1800256).

151. Driscoll N, Richardson AG, Maleski K, Anasor B, Adewole O, Lelyukh P, et al. Two-Dimensional Ti3C2 MXene for High-Resolution Neural Interfaces. ACS Nano. 2019;12(10):10419–29.

152. Zhao S, Li L, Zhang H, Qian B, Luo J, Deng Z, et al. Janus MXene nanosheets for macroscopic assemblies. Mater Chem Front. 2020;(4):910–7.

153. Yuen ACY, Chen TBY, Lin B, Yang W, Kabir II, Cordeiro IMDC, et al. Study of structure morphology and layer thickness of Ti3C2 MXene with Small-Angle Neutron Scattering (SANS). Elsevier Compos Part C Open Access. 2021;5(100155).

154. Kruss Scientific. Contact Angle [Internet]. Kruss Scientific Online Resources. 2019 [cited 2020 Apr 24]. p. 1. Available from: https://www.kruss-scientific.com/services/education-theory/glossary/contact-angle/

155. Shinde PV, Singh MK. Synthesis, Characterization, and Properties of Graphene Analogs of 2D Material. Fundam Sens Appl 2D Mater. 2019;(9780081025772):91–143.

156. Wormstone IM, Wormstone YM, Smith AJO, Eldred JA. Posterior capsule opacification: What's in the bag? Prog Retin Eye Res. 2021;82(100905).

157. Kappelhof J., Vrenson G., de Jong P., Pameyer J, Willekens B. The ring of soemmering in man: an ultrastructural study. Graefe's Arch Clin Exp Ophthalmol. 1987;225:77–83.

158. Planck SR, Huang XN, Robertson JE, Rosenbaum JT. Retinal pigment epithelial cells produce interleukin-1 beta and granulocyte-macrophage colony-stimulating factor in response to interleukin-1 alpha. Curr Eye Res. 1993;12(3):205–12.

159. Kaneko N, Kurata M, Yamamoto T, Morikawa S, Masumoto J. The role of interleukin-1 in general pathology. Inflamm Regen. 2019;39(12).

160. Wan C, He C, Sun L, Egwuagu CE, Leonard WJ. Interleukin-1 Receptor Signaling is Critical for the Development of Autoimmune Uveitis. J immunol. 2015;196(2):543–6.

161. Lopez-Castejon G, Brough D. Understanding the mechanism of IL-1β secretion. Cytokine Growth Factor Rev. 2011;22:189–95.

162. GroB O, Yazdi AS, Thomas CJ, Masin M, Heinz LX, Guarda G, et al. Inflammasome Activators Induce Interleukin-1α Secretion via Distinct Pathways with Differential Requirement for the Protease Function of Caspase-1. Immunity. 2012;36(3):388–400.

163. Fettelschoss A, Kistowska M, LeibundGut-Landmann S, Beer HD, Johansen P, Senti G, et al. Inflammasome activation and IL-1β target IL-1α for secretion as opposed to surface expression. Proc Natl Acad Sci U S A. 2011;108(44):18055–60.
164. Di Paolo NC, Shayakhmetov DM. Interleukin 1α and the inflammatory process. Nat Immunol. 2016;17(8):906–13.
165. Karasawa T, Takahashi M. The crystal-induced activation of NLRP3 inflammasomes in atherosclerosis. Inflamm Regen. 2017;37(1).
166. Duann P, Lianos EA, Ma J, Lin P. Autophagy, Innate Immunity and Tissue Repair in Acute Kidney Injury. Int J Mol Sci. 2016;17(5):662.
167. Dutot M, Olivier E, Wakx A, Rat P. The Role of the P2X7 Receptor in Ocular Stresses: A Potential Therapeutic Target. Vis. 2017;1(2):14.
168. Dinarello CA. Overview of the IL-1 family in innate inflammation and acquired immunity. Immunol Rev. 2018;281(1):8–27.
169. Eskan MA, Benakanakere MR, Rose B., Zhang P, Zhao J, Stathpouloi P, et al. Interleukin-1β Modulates Proinflammatory Cytokine Production in Human Epithelial Cells. Infect Immun. 2020;76(5):2080–9.
170. Gonzalez DM, Medici D. Signalling mechanisms of the epithelial-mesenchymal transition. Sci Signal. 2015;7(344).
171. Shirai K, Tanaka SI, Lovicu FJ, Saika S. The murine lens: A model to investigate in vivo epithelial–mesenchymal transition. Dev Dyn. 2018;247(3):340–5.
172. Zeisberg M, Neilson EG. Biomarkers for epithelial-mesenchymal transitions. J Clin Invest. 2009;119(6):1429–37.
173. Usman S, Waseem NH, Nguyen TKN, Mohsin S, Jamal A, Teh M-T, et al. Vimentin Is at the Heart of Epithelial Mesenchymal Transition (EMT) Mediated Metastasis. Cancers (Basel). 2021;13(19):4985.
174. Anggorowati N, Kurniasari CR, Damayanti K, Cahyanti T, Widodo I, Ghozali A, et al. Histochemical and Immunohistochemical Study of α-SMA, Collagen, and PCNA in Epithelial Ovarian Neoplasm. Asian Pac J Cancer Prev. 2017;18(3):667–71.
175. Xiong W, Frasch SC, Thomas SM, Bratton DL, Henson PM. Induction of TGF-β1 Synthesis by Macrophages in Response to Apoptotic Cells Requires Activation of the Scavenger Receptor CD36. PLoS One. 2013;8(8).
176. Shihan MH, Kanwar M, Wang Y, Jackson EE, Faranda AP, Duncan MK. Fibronectin has multifunctional roles in posterior capsular opacification (PCO). Matrix Biol. 2020;90:79–108.
177. Chen X, Ye S, Xiao W, Wang W, Luo L, Liu Y. ERK1/2 pathway mediates epithelial-mesenchymal transition by cross-interacting with TGFbeta/Smad and Jagged/Notch signalling pathways in lens epithelial cells. Int J Mol Med. 2014;33:1664–70.
178. Gilles C, Polette M, Zahm J, Tournier J, Volders L, Foidart J, et al. Vimentin contributes to human mammary epithelial cell migration. J Cell Sci. 1999;112:4615–25.
179. Menko AS, Bleaken BM, Libowitz AA, Zhang L, Stepp MA, Walker JL. A central role for vimentin in regulating repair function during healing of the lens epithelium. Mol Biol Cell. 2014;25(6):776–90.
180. Walker JL, Zhai N, Zhang L, Bleaken BM, Wolff I, Gerhart J, et al. Unique precursors for the mesenchymal cells involved in injury response and fibrosis. PNAS. 2010;107(31):13730–5.
181. Nagamoto T, Eguchi G, Beebe DC. Alpha-Smooth Muscle Actin Expression in Cultured Lens Epithelial Cells. Lens. 2000;41:1122–9.
182. Kurosaka D, Kato K, Nagamoto T. Presence of alpha smooth muscle actin in lens epithelial cells of aphakic rabbit eyes. Br J Ophthalmol. 1996;80(10):906–10.
183. Danielsson F, Peterson MK, Araújo H., Lautenschläger F, Gad AK. Vimentin Diversity in Health and Disease. Cells. 2018;7(10):147.
184. Mendez MG, Kojima S, Goldman RD. Vimentin induces changes in cell shape, motility and adhesion during the epithelial to mesenchymal transition. FASEB J. 2010;24:1838–51.
185. Ivaska J. Vimentin - Central hub in EMT induction? Small GTPases. 2011;2(1):51–3.
186. Muller M, Bhattacharya SS, Moore T, Prescott Q, Wedig T, Herrman H, et al. Dominant cataract formation in association with a vimentin assembly disrupting mutation. Hum Mol Genet. 2009;18:1052–7.

187.	Cherng S, Young J, Ma H. Alpha-Smooth Muscle Actin (α-SMA) . J Am Sci. 2008;4(4):7–9.

188.	Suarez-Amedo A, Figueroa FT, Clavijo C, Arbeláez P, Cruz JC. An image J plugin for the high throughput image analysis of in vitro scratch wound healing assays. PLoS One. 2020;15(7):e0232565.

189.	Shihan MH, Novo SG, Marchand SJL, Wang Y, Duncan MK, Professor F. A simple method for quantitating confocal fluorescent images. Biochem Biophys Reports. 2021;25(100916).

190.	Pillai-Kastoori L, Schutz-Geschwender AR, Harford J. A systematic approach to quantitative Western blot analysis. Anal Biochem. 2020;593(113608).

191.	Wang GQ, Dang YL, Huang Q, Woo VCP, So KF, Lai JSM, et al. In Vitro Evaluation of the Effects of Intraocular Lens Material on Lens Epithelial Cell Proliferation, Migration, and Transformation. Curr Eye Res. 2017;42(1):72–8.

192.	Lundqvist B, Mönestam E. Ten-Year Longitudinal Visual Function and Nd: YAG Laser Capsulotomy Rates in Patients Less Than 65 Years at Cataract Surgery. Am J Ophthalmol. 2010;

193.	Satofuka S, Ichihara A, Nagai N, Yamashiro K, Koto T, Shinoda H, et al. Suppression of Ocular Inflammation in Endotoxin-Induced Uveitis by Inhibiting Nonproteolytic Activation of Prorenin. Invest Ophthalmol Vis Sci. 2006;47(6):2686–92.

194.	Simmons KT, Xiao Y, Pflugfleder SC, de Paiva CS. Inflammatory Response to Lipopolysaccharide on the Ocular Surface in a Murine Dry Eye Model. Invest Ophthalmol Vis Sci. 2016;57(6):2443–51.

195.	Noailles A, Maneu V, Campello L, Lax P, Cuenca N. Systemic inflammation induced by lipopolysaccharide aggravates inherited retinal dystrophy. Cell Death Dis. 2018;9(350 (2018)).

196.	Schwarz H, Gornicec J, Neuper T, Parigiani MA, Wallner M, Duschl A, et al. Biological activity of masked endotoxin. Sci Rep. 2017;7(44750).

197.	Ye Z, Huang Y, Li J, Ma T, Gao L, Huihui H, et al. Two-dimensional ultrathin Ti3C2 MXene nanosheets coated intraocular lens for synergistic photothermal and NIR-controllable rapamycin releasing therapy against posterior capsule opacification. Front Bioeng Biotechnol. 2022;10(989099).

198.	Parmentier M, Hirani N, Rahman I, Donaldson K, MacNee W, Antonicelli F. Regulation of lipopolysaccharide-mediated interleukin-1b release by N-acetylcysteine in THP-1 cells. Eur Respir J. 2000;16:933–9.

199.	Xie Q, Shen W-W, Zhong J, Huang C, Zhang L, Li J. Lipopolysaccharide/adenosine triphosphate induces IL-1β and IL-18 secretion through the NLRP3 inflammasome in RAW264.7 murine macrophage cells. Int J Mol Med. 2014;34(1):341–9.

200.	Waterhouse CCM, Stadnyk AW. Rapid Expression of IL-1B by Intestinal Epithelial Cells in Vitro. Cell Immunol. 1999;193:1–8.

201.	Ghidiu MJ, Naguib M, Barsoum MW, Anasori B, Gogotsi Y. Chemical and Electrochemical Intercalation of Ions and Molecules into MXenes. In: 2D Metal Carbides and Nitrides (MXenes). 2019. p. 161–75.

202.	Song N, Li T. Regulation of NLRP3 Inflammasome by Phosphorylation. Front Immunol. 2018;9(2305).

203.	Mao L, Hu S, Gao Y, Wang L, Zhao W, Fu L, et al. Biodegradable and Electroactive Regenerated Bacterial Cellulose/MXene (Ti3C2Tx) Composite Hydrogel as Wound Dressing for Accelerating Skin Wound Healing under Electrical Stimulation. Adv Healthc Mater. 2020;9(19).

204.	Kassumeh SA, Wertheimer CM, von Studnitz, A., Hillenmayer A, Priglinger C, Wolf A, Mayer WJ, et al. Poly(lactic-co-glycolic) Acid as a Slow-Release Drug-Carrying Matrix for Methotrexate Coated onto Intraocular Lenses to Conquer Posterior Capsule Opacification. Curr Eye Res. 2018;43(6):702–8.

205.	Garcia CM, Kwon GP, Beebe DC. α-Smooth muscle actin is constitutively expressed in the lens epithelial cells of several species. Exp Eye Res. 2006;83(4):999–1001.

206.	Hegenbarth J, Lezzoche G, Windt, L, J D, Stoll M. Perspectives on Bulk-Tissue RNA Sequencing and Single-Cell RNA Sequencing for Cardiac Transcriptomics. Front Mol Med. 2022;2(839338).

207.	Li X, Wang C. From bulk, single-cell to spatial RNA sequencing. Int Journey Oral Sci.

2021;13(36(2021)).

208. Haque A, Engel J, Teichmann SA, Lönnberg T. A practical guide to single-cell RNA-sequencing for biomedical research and clinical applications. Genome Med. 2017;9(75 (2017)).

209. Weatherbee BAT, Barton JR, Siddam AD, Anand D, Lachke SA. Molecular characterisation of the human lens epithelium-derived cell line SRA01/04. Exp Eye Res. 2019;188(107787).

210. Wang Z, Su D, Liu S, Zheng G, Zhang G, Cui T, et al. RNA sequencing and bioinformatics analysis of human lens epithelial cells in age-related cataracts. BMC Ophthalmol. 2021;21(152).

211. Lin X, Li H, Yang T, Liu X, Fan F, Zhou X, et al. Transcriptomics Analysis of Lens from Patients with PosteriorSubcapsular Congenital Cataract. Genes (Basel). 2021;12(1904).

212. Zhou D, Zhang L, Wang L, Sun Y, Liu P. Identification of genes and transcription factors associated with glucocorticoid response in lens epithelial cells. Mol Med Rep. 2015;11:4073–8.

213. Kanehisa M, Furumichi M, Tanabe M, Sato Y, Morishima K. KEGG: new perspectives on genomes, pathways, diseases and drugs. Nucleic Acids Res. 2017;45:D353–D361.

214. Borchman D, Yappert MC. Lipids and the ocular lens. J Lipid Res. 2010;51(9):2473–2488.

215. Huang L, Estrada R, Yappert MC, Borchman D. Oxidation-induced changes in human lens epithelial cells: 1. Phospholipids. Free Radic Biol Med. 2006;41(9):1425–32.

216. Magny R, Auzeil N, Olivier E, Kessal K, Regazzetti A, Dutot M, et al. Lipidomic analysis of human corneal epithelial cells exposed to ocular irritants highlights the role of phospholipid and sphingolipid metabolisms in detergent toxicity mechanisms. Biochimie. 2020;178:148–157.

217. Tokumura A, Taira S, Kikuchi M, Tsutsumi T, Shimizu Y, Watsky MA. Lysophospholipids and lysophospholipase D in rabbit aqueous humor following corneal injury. Prostaglandins Other Lipid Mediat. 2012;97(3–4):83–9.

218. Zumwalt JW, Thunstrom BJ, Spangelo BL. Interleukin-1β and Catecholamines Synergistically Stimulate Interleukin-6 Release from Rat C6 Glioma Cells in Vitro: a Potential Role for Lysophosphatidylcholine. Endocrinology. 1999;140(2):888–96.

219. Ewels P, Magnusson M, Lundin S, Käller. M. MultiQC: Summarize Analysis Results for Multiple Tools and Samples in a Single Report. Bioinformatics. 2016;32(19):3047–8.

220. Kim D, Paggi JM, Park C, Bennett C, Salzberg SL. MultiQC: Summarize Analysis Results for Multiple Tools and Samples in a Single Report. Nat Biotechnol. 2019;37:907–15.

221. Patro R, Duggal G, Love M, Irizarry R, Kingsford C. Salmon Provides Fast and Bias-Aware Quantification of Transcript Expression. Nat Methods. 2017;14:417–9.

222. Love MI, Huber W, Anders S. Moderated Estimation of Fold Change and Dispersion for RNA-Seq Data with DESeq2. Genome Biol. 2014;15(550).

223. Yu G, Wang L-G, Han Y, He Q-Y. clusterProfiler: An r Package for Comparing Biological Themes Among Gene Clusters. Omi A J Integr Biol. 2012;16(5):284–7.

224. Bligh EG, Dyer WJ. A rapid method of total lipid extraction and purification. Can J Biochem Physiol. 1959;37:911–7.

225. Bahja J, Stewart NA, Dymond MK. Oxidative stress is inhibited by plant-based supplements: A quantitative lipidomic analysis of antioxidant activity and lipid compositional change. Adv Redox Res. 2022;6(100054).

226. Kessner D, Chambers M, Burke R, Agus D, Mallick P. ProteoWizard: Open source software for rapid proteomics tools development. Bioinformatics. 2008;24:2534–6.

227. Katajamaa M, Miettinen J, Orešič M. MZmine: Toolbox for processing and visualization of mass spectrometry based molecular profile data. Bioinformatics. 2006;22:634–6.

228. Pluskal T, Castillo S, Villar-Briones A, Orešič M. MZmine 2: Modular framework for processing, visualizing, and analyzing mass spectrometry-based molecular profile data. BMC Bioinformatics. 2010;11.

229. Myers OD, Sumner SJ, Li S, Barnes S, Du X. One Step Forward for Reducing False Positive and False Negative Compound Identifications from Mass Spectrometry Metabolomics Data: New Algorithms for Constructing Extracted Ion Chromatograms and Detecting Chromatographic Peaks. Anal Chem. 2017;89:8696–8703.

230. Hutchins PD, Russell JD, Coon JJ. 'LipiDex: An Integrated Software Package for High-Confidence Lipid Identification. Cell Syst. 2018;6(5):621–5.

231. Andrews S, Krueger F, Segonds-Pichon A, Biggins L, Krueger C, Wingett S. FastQC [Internet]. Babraham, UK: Babraham Institute. 2012. Available from: https://www.bioinformatics.babraham.ac.uk/projects/fastqc/

232. Broad Institute. Picard Tools. Broad Institute, GitHub Repository. 2019. p. http://broadinstitute.github.io/picard/.

233. Wang L, Wang S, Li W. RSeQC: quality control of RNA-seq experiments. Bioinformatics. 2012;28(16):2184–85.

234. Zhou S, Yang J, Wang M, Zheng D, Liu Y. Endoplasmic reticulum stress regulates epithelial-mesenchymal transition in human lens epithelial cells. Mol Med Rep. 2020;21:173–80.

235. Yang J, Zhou S, Gu J, Wang Y, Guo M, Liu Y. Differences in Unfolded Protein Response Pathway Activation in the Lenses of Three Types of Cataracts. PLoS One. 2015;10(6).

236. Lindholm D, Korhonen L, Eriksson O, Kõks S. Recent Insights into the Role of Unfolded Protein Response in ER Stress in Health and Disease. Front Cell Dev Biol. 2017;5(48).

237. Ma Y, Hendershot LM. ER chaperone functions during normal and stress conditions. J Chem Neuroanat. 2004;28(1–2):51–65.

238. Schopf FH, Biebl MM, Buchner J. The HSP90 chaperone machinery. Nat Rev Mol Cell Biol. 2017;18:345–60.

239. Khandelwal A, Kent CN, Balch M, Peng S, Mishra SJ, Deng J, et al. Structure-guided design of an Hsp90β N-terminal isoform-selective inhibitor. Nat Commun. 2018;9(425).

240. Woodley DT, Fan J, Cheng C-F, Li Y, Chen M, Bu G, et al. Participation of the lipoprotein receptor LRP1 in hypoxia-HSP90α autocrine signaling to promote keratinocyte migration. J Cell Mol Med. 2009;122(10):1495–8.

241. Cheng C-F, Sahu D, Tsen F, Zhao Z, Fan J, Kim R, et al. A fragment of secreted Hsp90α carries properties that enable it to accelerate effectively both acute and diabetic wound healing in mice. J Clin Invest. 2011;121(11):4348–61.

242. Li J, Xue W, Wang X, Huang W, Wang X-X, Li H, et al. HSP90 as a novel therapeutic target for posterior capsule opacification. Exp Eye Res. 2019;189(107821).

243. Shen X, Xue Y, Si Y, Wang Q, Wang Z, Yuan J, et al. The unfolded protein response potentiates epithelial-mesenchymal transition (EMT) of gastric cancer cells under severe hypoxia conditions. Med Oncol. 2015;32(447).

244. Zeindl-Eberhart E, Brandl L, Liebmann S, Ormanns S, Scheel SK, Brabletz T, et al. Epithelial-mesenchymal transition induces endoplasmic-reticulum-stress response in human colorectal tumor cells. PLoS One. 2014;31(9):e87386.

245. Zhong Q, Zhou B, Ann DK, Minoo P, Liu Y, Banfalvi A, et al. Role of endoplasmic reticulum stress in epithelial-mesenchymal transition of alveolar epithelial cells: effects of misfolded surfactant protein. Am J Respir Cell Mol Biol. 2011;45(3):498–509.

246. Liu H, Smith AJ, Ball SS, Bao Y, Bowater RP, Wang N, et al. Sulforaphane promotes ER stress, autophagy, and cell death: implications for cataract surgery. J Mol Med. 2017;95:553–64.

247. Doudican NA, Wen SY, Mazumder A, Orlow SJ. Sulforaphane synergistically enhances the cytotoxicity of arsenic trioxide in multiple myeloma cells via stress-mediated pathways. Oncol Rep. 2012;28(5):1851–8.

248. Costello MJ, Brennan LA, Basu S, Chauss D, Mohamed A, Gilliland KO, et al. Autophagy and mitophagy participate in ocular lens organelle degradation. Exp Eye Res. 2014;116.

249. Basu S, Rajakaruna S, Reyes B, Bockstaele E Van, Menko AS. Suppression of MAPK/JNK-MTORC1 signaling leads to premature loss of organelles and nuclei by autophagy during terminal differentiation of lens fiber cells. Autophagy. 2014;10(7):1193–211.

250. Xu X-D, Li K-R, Li X-M, Yao J, Qin J, Yan B. Long non-coding RNAs: new players in ocular neovascularization. Mol Biol Rep. 2014;41(7):4493–505.

251. Shen Y, Dong L-F, Zhou R-M, Yao J, Song Y-C, Yang H, et al. Role of long non-coding RNA MIAT in proliferation, apoptosis and migration of lens epithelial cells: a clinical and in vitro study. J Cell Mol Med. 2016;20(3):537–48.

252. Yan B, Tao Z-F, Li X-M, Zhang H, Yao J, Jiang Q. Aberrant expression of long noncoding

RNAs in early diabetic retinopathy. Invest Ophthalmol Vis Sci. 2014;55(2):941–51.

253. Dunmire JJ, Lagouros E, Bouhenni RA, Jones M, Edward DP. MicroRNA in aqueous humor from patients with cataract. Exp Eye Res. 2013;108:68–71.

254. Suraj S, Dhar C, Srivastava S. Circulating nucleic acids: An analysis of their occurrence in malignancies. Biomed Rep. 2017;6(1):8–14.

255. Jabłońska-Trypuć A, Matejczyk M, Rosochacki S. Matrix metalloproteinases (MMPs), the main extracellular matrix (ECM) enzymes in collagen degradation, as a target for anticancer drugs. J Enzyme Inhib Med Chem. 2016;31(1):177–83.

256. LeBert DC, Squirrell JM, Rindy J, Broadbridge E, Lui Y, Zakrzewska A, et al. Matrix metalloproteinase 9 modulates collagen matrices and wound repair. Development. 2015;142(12):2136–46.

257. Taddese S, Jung MC, Ihling C, Heinz A, Neubert RHH, Schmelzer CEH. MMP-12 catalytic domain recognizes and cleaves at multiple sites in human skin collagen type I and type III. Biochim Biophys Acta. 2010;1804(4):731–9.

258. Kim YH, Kwon H-J, Kim D-S. Matrix Metalloproteinase 9 (MMP-9)-dependent Processing of βig-h3 Protein Regulates Cell Migration, Invasion, and Adhesion. J Biol Chem. 2012;287(46):38957–69.

259. Sandeman S, Faragher RGA, Allen MCA, Liu C, Lloyd AW. Does MMP-9 expression and secretion change with increasing serial passage of keratocyte in culture? Mech Ageing Dev. 2001;122:157–67.

260. Awasthi N, Wang-Su ST, Wagner BJ. Downregulation of MMP-2 and -9 by Proteasome Inhibition: A Possible Mechanism to Decrease LEC Migration and Prevent Posterior Capsular Opacification. Invest Ophthalmol Vis Sci. 2008;49(5).

261. Wu D, Zhao R, Chen Y, Wang Y, Li J, Fan Y. Molecular insights into MXene destructing the cell membrane as a "nano thermal blade". Phys Chem Chem Phys. 2021;23:3341–50.

262. Welsh N. Interleukin-1β-induced ceramide and diacylglycerol generation may lead to activation of the c-Jun NH2-terminal kinase and the transcription factor ATF2 in the insulin-producing cell line RINm5F. J Biol Chem. 1996;271(14):8307–12.

263. Knuplez E, Marsche G. An Updated Review of Pro- and Anti-Inflammatory Properties of Plasma Lysophosphatidylcholines in the Vascular System. Int J Mol Sci. 2020;21(12):4501.

264. Czimmerer Z, Daniel B, Horvath A, Rückerl D, Nagy G, Kiss M, et al. The Transcription Factor STAT6 Mediates Direct Repression of Inflammatory Enhancers and Limits Activation of Alternatively Polarized Macrophages. Immunity. 2018;48(1):75–90.

265. Choudhury SM, Ma X, Abdullah SW, Zheng H. Activation and Inhibition of the NLRP3 Inflammasome by RNA Viruses. J Inflamm Res. 2021;14:1145–63.

266. Fu Q, Qin Z, Yu J, Yu Y, Tang Q, Lyu D, et al. Effects of senescent lens epithelial cells on the severity of age-related cortical cataract in humans: A case-control study. Med. 2016;95(25):e3869.

267. Zhu M, Meng P, Ling X, Zhou L. Advancements in therapeutic drugs targeting of senescence. Ther Adv Chronic Dis. 2020;11:1–26.

268. Faragher RGA, Mulholland B, Tuft SJ, Sandeman S, Khaw PT. Aging and the cornea. Br J Ophthalmol. 1997;81:814–7.

269. Saul D, Kosinsky RL, Atkinson EJ, Doolittle ML, Zhang X, LeBrasseur NK, et al. A new gene set identifies senescent cells and predicts senescence-associated pathways across tissues. Nat Commun. 2022;13(4827).

270. Coppé J-P, Patil CK, Rodier F, Sun Y, Muñoz DP, Goldstein J, et al. Senescence-associated secretory phenotypes reveal cell-nonautonomous functions of oncogenic RAS and the p53 tumour suppressor. PLoS Biol. 2008;6(12):2853–68.

271. Sheerin AN, Smith SK, Jennert-Burston K, Brook AJ, Allen MC, Ibrahim B, et al. Characterization of cellular senescence mechanisms in human corneal endothelial cells. Aging Cell. 2012;11(2):234–40.

272. Zhang C, Chen M, Zhou N, Qi Y. Metformin Prevents H2O2-Induced Senescence in Human Lens Epithelial B3 Cells. Med Sci Monit Basic Res. 2020;26(e923391).

273. Chen M, Fu Y, Wang X, Wu R, Su D, Zhou N, et al. Metformin protects lens epithelial cells against senescence in a naturally aged mouse model. Cell Death Discov. 2022;8(8).

274. Colitz CMH, Davidson MG, McGahan MC. Telomerase Activity in Lens Epithelial Cells of Normal and Cataractous Lenses. Exp Eye Res. 1999;69:641–9.

275. Wang Y, Tseng Y, Chen K, Wang X, Mao Z, Li X. Reduction in Lens Epithelial Cell Senescence Burden through Dasatinib Plus Quercetin or Rapamycin Alleviates D-Galactose-Induced Cataract Progression. J Funct Mater. 2023;14(6).

276. Latorre E, Birar VC, Sheerin AN, Jeynes JC, Hooper A, Dawe HR, et al. Small molecule modulation of splicing factor expression is associated with rescue from cellular senescence. BMC Cell Biol. 2017;18(1):31.

277. Bai J, Zheng Y, Dong L, Cai X, Wang G, Liu P. Inhibition of p38 mitogen-activated protein kinase phosphorylation decreases H(2)O(2)-induced apoptosis in human lens epithelial cells. Graefes Arch Clin Exp Ophthalmol. 2015;253:1933–1940.

278. Nam M, Nagaraj RH. Matrix-bound AGEs enhance TGF-β2-mediated mesenchymal transition of lens epithelial cells via the noncanonical pathway: implications for secondary cataract formation. Biochem J. 2019;475(8):1427–40.

279. Nagano T, Nakano M, Nakashima A, Onishi K, Yamao S, Enari M, et al. Identification of cellular senescence-specific genes by comparative transcriptomics. Sci Rep. 2016;6(31758).

280. Teng Y-N, Chang H-C, Chao Y-Y, Cheng H-L, Lien W-C, Wang C-Y. Etoposide Triggers Cellular Senescence by Inducing Multiple Centrosomes and Primary Cilia in Adrenocortical Tumor Cells. Cells. 2021;10(6):1466.

281. González-Gualda E, Baker AG, Fruk L, Muñoz-Espín D. A guide to assessing cellular senescence in vitro and in vivo. FEBS J. 2020;288(1):56–80.

282. Fullerton JN, Gilroy DW. Resolution of inflammation: a new therapeutic frontier. Nat Rev Drug Discov. 2016;15:551–67.

283. Lau L, Porciuncula A, Yu A, Iwakura Y, David G. Uncoupling the Senescence-Associated Secretory Phenotype from Cell Cycle Exit via Interleukin-1 Inactivation Unveils Its Protumorigenic Role. Mol Cell Biol. 2019;39(12):e00586-18.

284. Ueda S, Tominaga T, Ochi A, Sakurai A, Nishimura K, Shibata E, et al. TGF-β1 is involved in senescence-related pathways in glomerular endothelial cells via p16 translocation and p21 induction. Sci Rep. 2021;11(21643).

285. Tominaga K, Suzuki HI. TGF-β Signaling in Cellular Senescence and Aging-Related Pathology. Int J Mol Sci. 2019;20(20):5002.

286. Senturk S, Mumcuoglu M, Gursoy-Yuzugullu O, Cingoz B, Akcali KC, Ozturk M. Transforming growth factor-beta induces senescence in hepatocellular carcinoma cells and inhibits tumor growth. Hepatology. 2010;52(3):966–74.

287. Minagawa S, Araya J, Numata T, Nojiri S, Hara H, Yumino Y, et al. Accelerated epithelial cell senescence in IPF and the inhibitory role of SIRT6 in TGF-β-induced senescence of human bronchial epithelial cells. Am J Physiol Lung Cell Mol Physiol. 2011;300(3):L391–401.

288. Zhang Y, Alexander PB, Wang X-F. TGF-β Family Signaling in the Control of Cell Proliferation and Survival. Cold Spring Harb Perspect Biol. 2017;9(a022145).

289. Wormstone IM. The human capsular bag model of posterior capsule opacification. Eye. 2020;34:225–31.

290. Hillenmayer A, Wertheimer C., Kassumeh S, von Studnitz A, Luft N, Ohlmann A, et al. Evaluation of posterior capsule opacification of the Alcon Clareon IOL vs the Alcon Acrysof IOL using a human capsular bag model. BMC Ophthalmol. 2020;20(77).

291. Cleary G, Spalton DJ, Zhang J, Marshall J. In vitro lens capsule model for investigation of posterior capsule opacification. J Cataract Refract Surg. 2010;36(8):1249–52.

292. Pot SA, Chandler HL, Colitz CMH, Bentley E, Dubielzig RR, Mosley TS, et al. Selenium functionalized intraocular lenses inhibit posterior capsule opacification in an ex vivo canine lens capsular bag assay. Exp Eye Res. 2009;89:728–34.

293. Nagamoto T, Hara E. Lens epithelial cell migration onto the posterior capsule in vitro. J Cataract Refract Surg. 1996;22(1):841–6.

294. Nagamoto T, Fujiwara T. Inhibition of lens epithelial cell migration at the intraocular lens optic edge: role of capsule bending and contact pressure. J Cataract Refract Surg. 2003;29(8):1605–12.

295.   Beck R, Stave J, Guthoff R. A 3-D capsular bag model to describe the biomechanical properties of new types of artificial lenses. The Opthalmologist. 2000;97:546–51.

296.   Assia EI, Apple DJ. Side-view analysis of the lens. I. The crystalline lens and the evacuated bag. Arch Ophthalmol . 1992;110(1):89–93.

297.   Nguyen P, Chopra V. Applications of optical coherence tomography in cataract surgery. Curr Opin Ophthalmol. 2013;24(1):47–52.

Chapter 9: Appendix

Appendix 1 - Supporting materials and results

2.3.1 Synthesis and Characterisation of $Ti_3C_2T_x$

Table S1: Optimisation requirements for synthesised $Ti_3C_2T_x$ (MXene) batches. (x2(S) represents centrifugation post-sonication.

Batch No.	Synthesis Period (h)	No. of Washes	Shaking (mins)	Centrifuge (3500rpm/h)	Sonication (mins)	Optimisation
1	24	4	15	1 (x2)	30,60	Low concentration Polydisperse solution
2	24	4	n/a	1 (x2)	60, 120	Good
3	48	5	n/a	1 (x2)	20	Low concentration Polydisperse solution
4	48	6	15 (x2)	1 (x2)	20	Low concentration Polydisperse solution
5	24	5	15	1 (x2(S)	20	Good
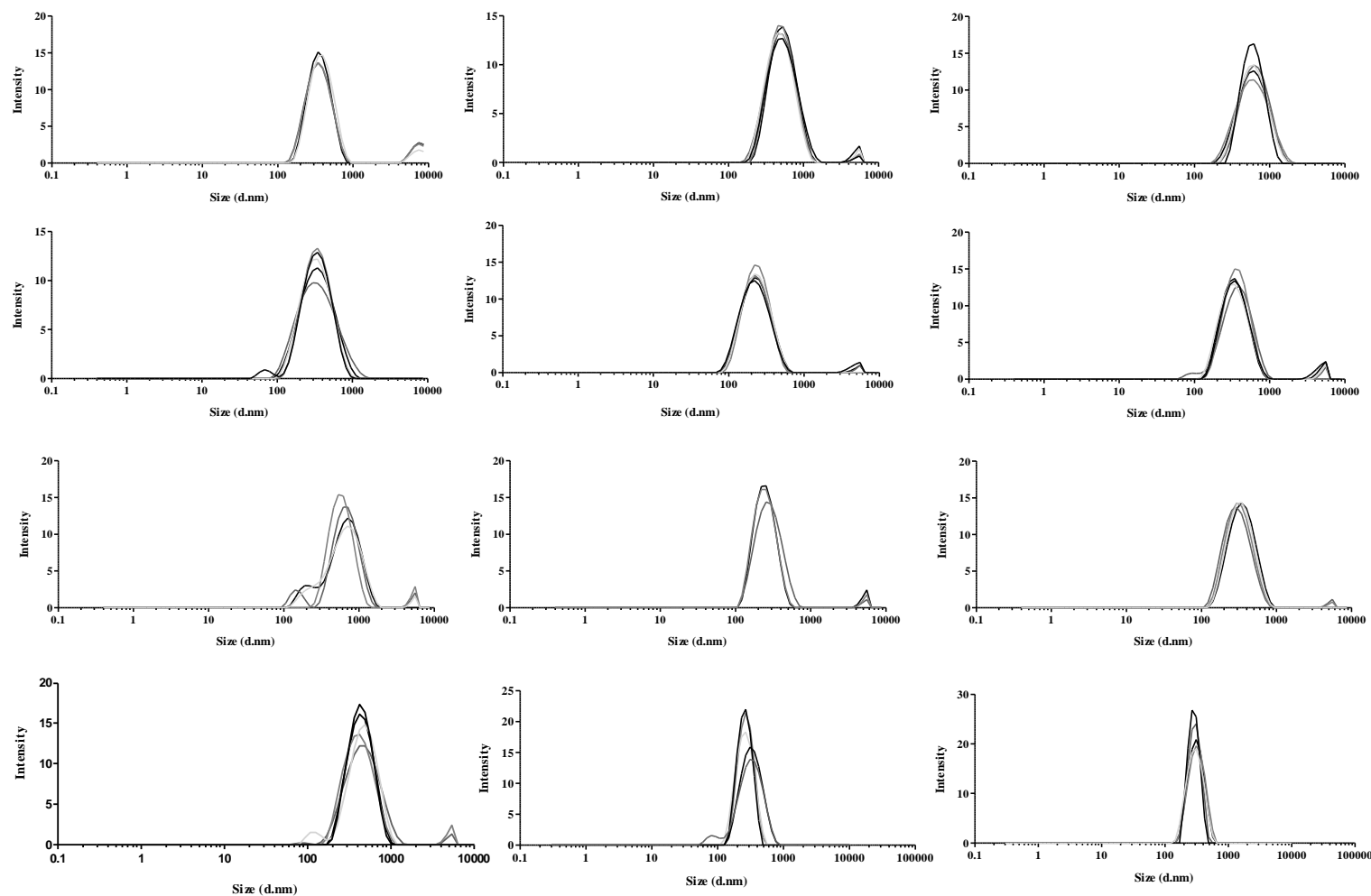
Figure S1: Dynamic light scattering analysis for the MXene batches synthesised and used during this project. From left to right, top to bottom, Batch 3, 5, 6, 7, 8, 9, 10, 11, 12, 13, 14, 15,16.

Figure S2: Ultraviolet spectroscopy analysis of all the synthesised MXene batches used during this project. From left to right, top to bottom, Batch 3, 5, 6, 7, 8, 9, 10, 11, 12, 13, 14, 15,16.

Table S2: $Ti_3C_2T_x$ (MXene) batches with characterisation techniques and application in experiments.

Batch No.	*Application*	*Location*
3	Live/Dead™ stain	3.2.2.1
X	IL-1α stimulated ELISA	3.2.8
5	LDH, MTS, IOLs' ELISA	3.2.3
6	IL-1β primed ELISA	3.2.8, 3.2.9
7	Scratch assay	3.2.11
8	QPCR	3.2.10
10	Immunocytochemistry	3.2.12
11	Genomics and Lipidomics	Chapter 4
12	Western blot	3.2.13
13	Coatings characterisation; IL-6 ELISA after $Ti_3C_2T_x$ incubation	2.2.1.7; 3.2.9
14	QPCR for p21 and p16; EdU; Sen B gal staining	Chapter 5
15	QPCR for p21 and p16; EdU; Sen B gal staining	Chapter 5
16	Coated IOLs for capsule bag	Chapter 6

3.3.2 Release of interleukin-6, and -8 by human lens epithelial cells grown on intraocular lens types
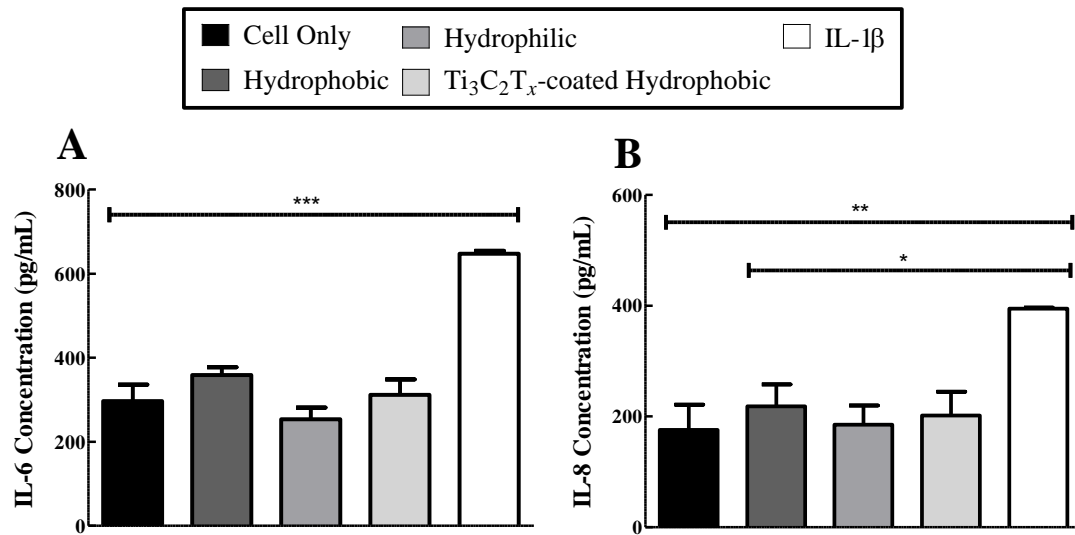
Figure S3: Expression of IL-6 and IL-8 by human lens epithelial cells (HLE-B3) grown on intraocular lens types with cell only background expression (Rayner Intraocular Lenses Ltd, UK). A one-way ANOVA was conducted to determine significance ($p \leq 0.05$) by comparing the positive control to untreated cells and cells grown on intraocular lens types. $*p \leq 0.05$ $** p \leq 0.01$ $***p \leq 0.001$. (Mean $\pm$ SEM; n=3)

3.3.3 Optimisation of interleukin-1 beta and -alpha treatment for detecting interleukin-6, -8 and tumour necrosis factor
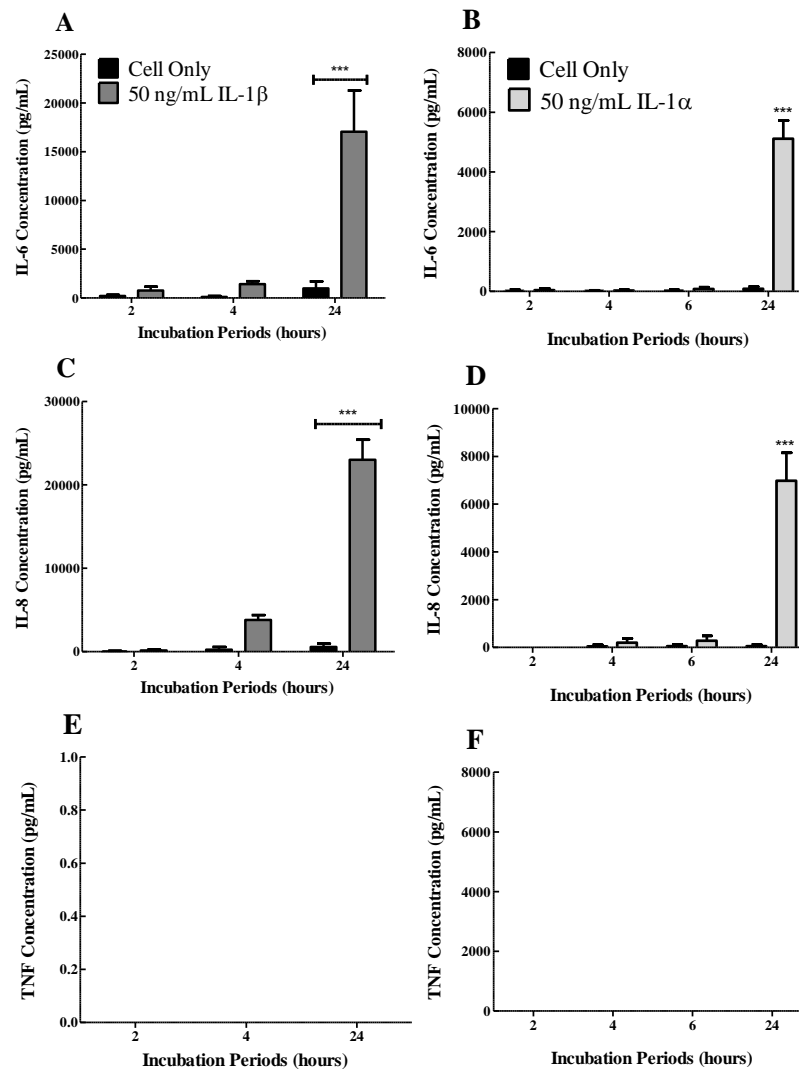
Figure S4: Expression of pro-inflammatory cytokines by human lens epithelial (HLE-B3) cells after spiking with IL-1α and IL-1β. Expression of IL-6 (**Fig. S4 A**), IL-8 (**Fig. S4 B**) and TNF (**Fig. S4 C**) of cells treated with IL-1β as quantified by ELISA. Expression of IL-6 (**Fig. S4 D**), IL-8 (**Fig. S4 E**) and TNF (**Fig. S4 F**) of cells treated with IL-1α as quantified by ELISA. Samples were taken at 2, 4 and 24 hour-periods. Cells treated with IL-1β (50 ng mL^{-1}) and IL-1α (50 ng mL^{-1}) showed significant upregulation in IL-6 and IL-8 after 24 h exposure, relative to cells alone

($p \le 0.001$). (Cell only: cells alone; 100 ng mL^{-1} IL-1β: cells treated with IL-1β; 50 ng mL^{-1}: cells treated with IL-1α) (Mean $\pm$ SEM; n=3)

3.3.9 Upregulation in gene fold change of interleukin-6, -1 beta and CXCL1 in interleukin-1 beta-primed human lens epithelial cells with Ti$_3$C$_2$T$_x$ (MXene) coatings
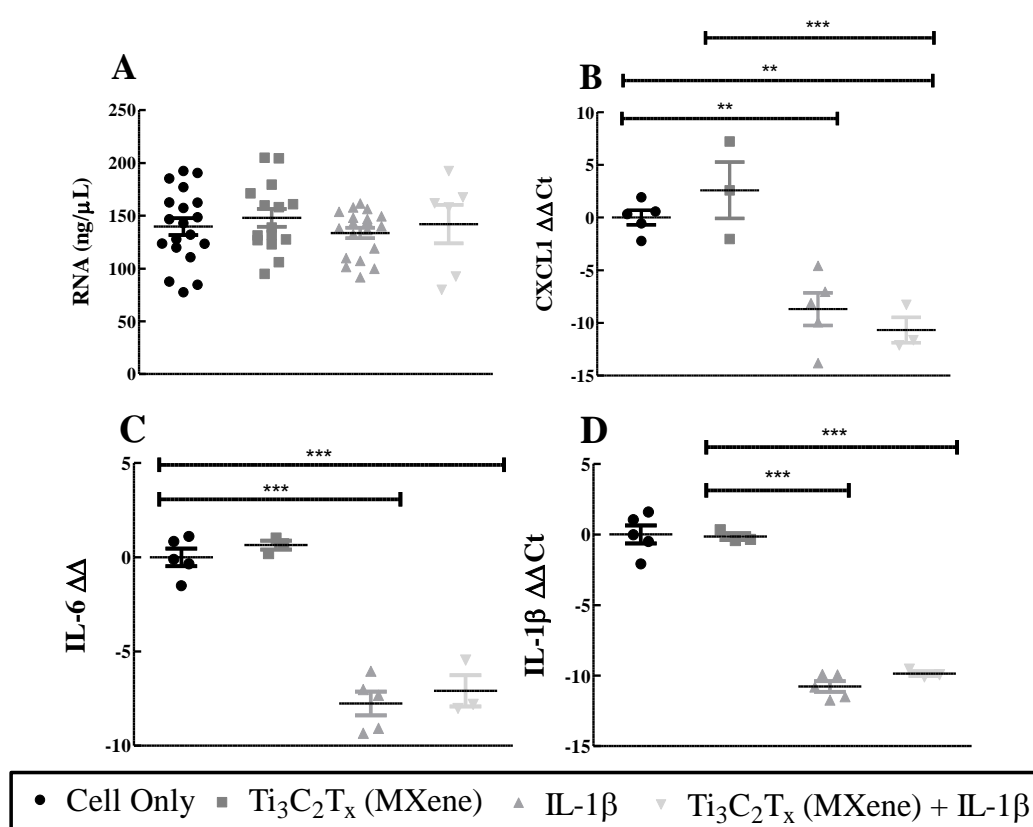
Figure S5: Scatter plot of extracted RNA and delta delta Ct ($\Delta\Delta$Ct) values from each technical repeat of each condition. RNA extraction of each technical repeat (ng µL^{-1}) (**Fig. S5 A**). $\Delta\Delta$Ct values for CXCL1 (**Fig. S5 B**), IL-6 (**Fig. S5 C**) and IL-1β (**Fig. S5 D**) used to calculate gene fold change. Significance was determined using unpaired two-tailed t tests and F-tests for comparison of variance was used. **p $\le$0.01, ***p $\le$ 0.001. (Cell only: cells alone; Ti$_3$C$_2$T$_x$ (MXene): cells grown on Ti$_3$C$_2$T$_x$ coatings; IL-1β: cells treated with IL-1β; Ti$_3$C$_2$T$_x$ (MXene) + IL-1β: cells grown on Ti$_3$C$_2$T$_x$ coatings treated with IL-1β) (Fold change $\pm$ SEM; n=5)
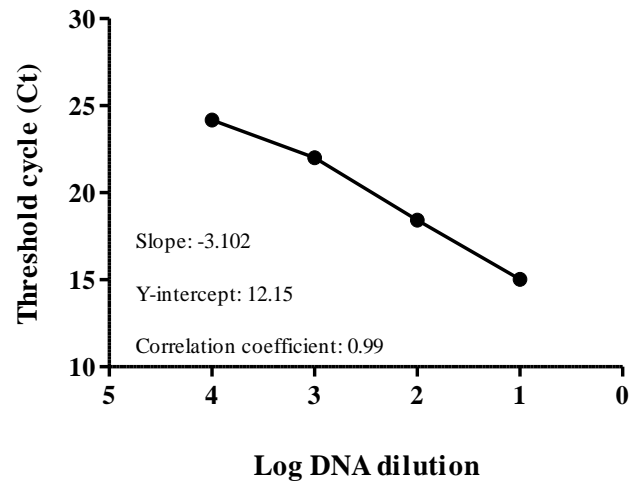
Figure S6: Calibration curve of serial dilution of β-actin housekeeping gene. Efficiency slope between -3.58 and -3.10. Y intercept ≥ 10 confirms reliable quantification.
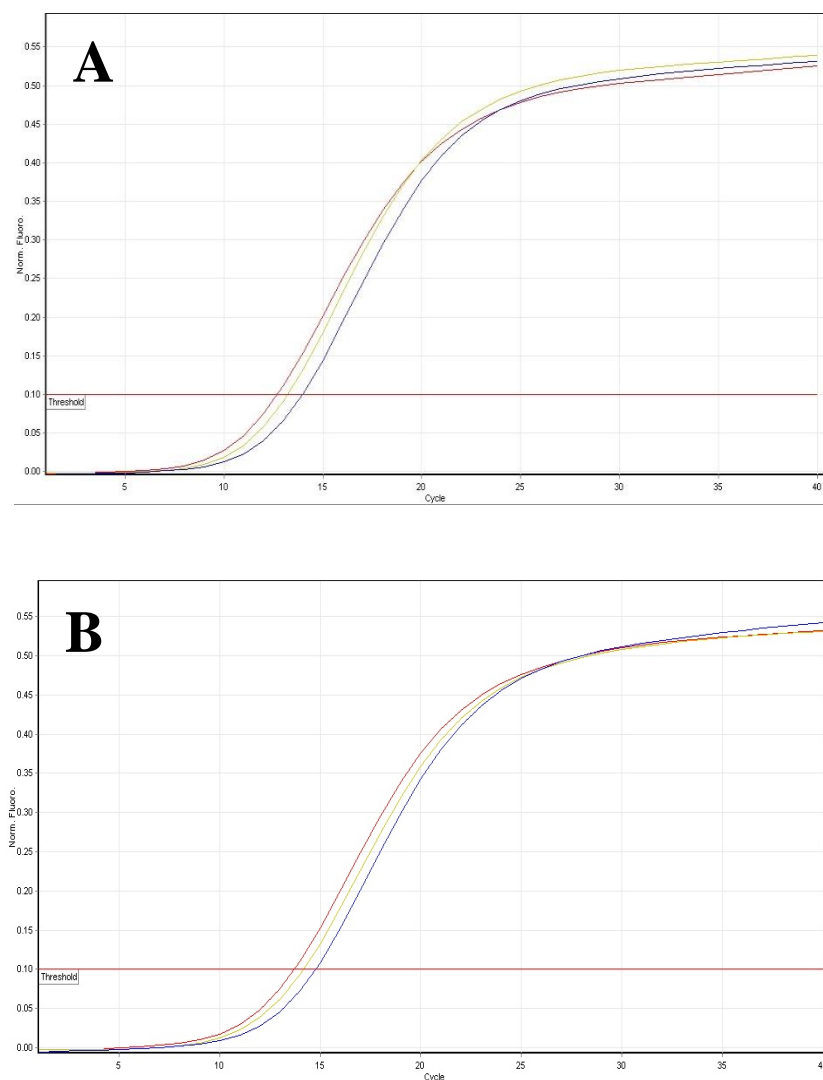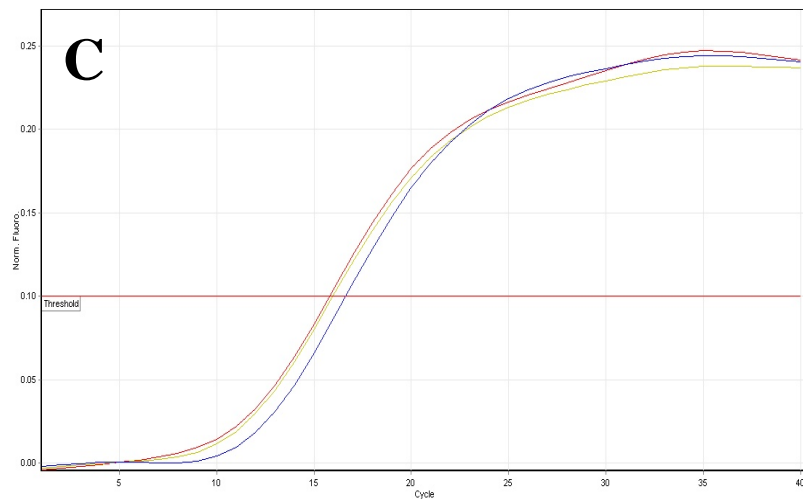
Figure S7: rt-PCR amplification cycle plot of actin housekeeping gene in cell only controls, (**Fig. S7 A**) 1 µL (**Fig. S7 B**) 2 µL and (**Fig. S7 C**) 3 µL (n=1).

4.3.1 Genomic profile of FHL124 cells
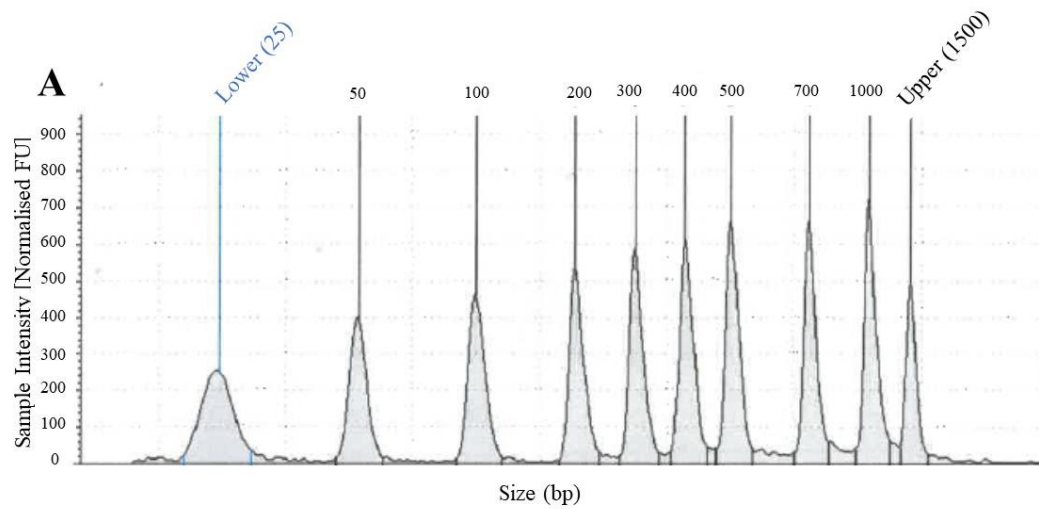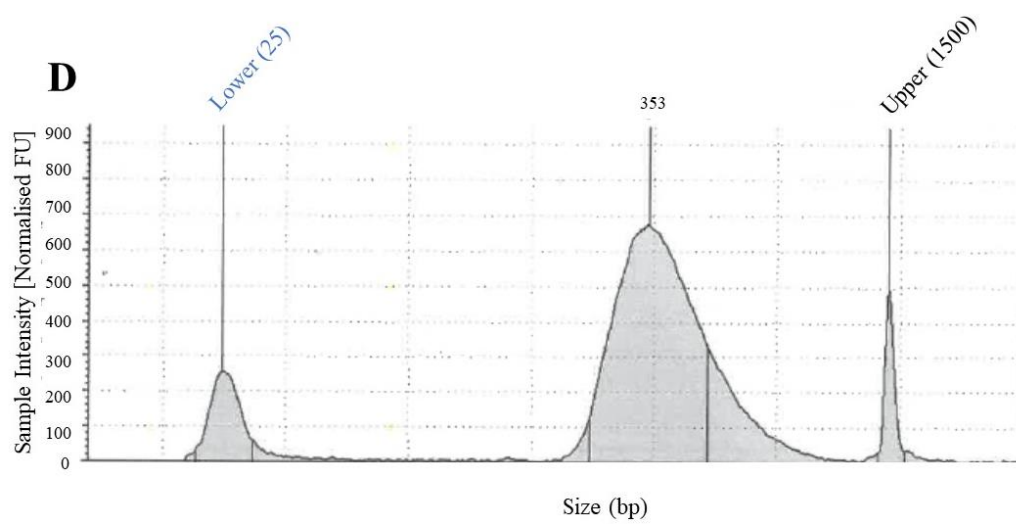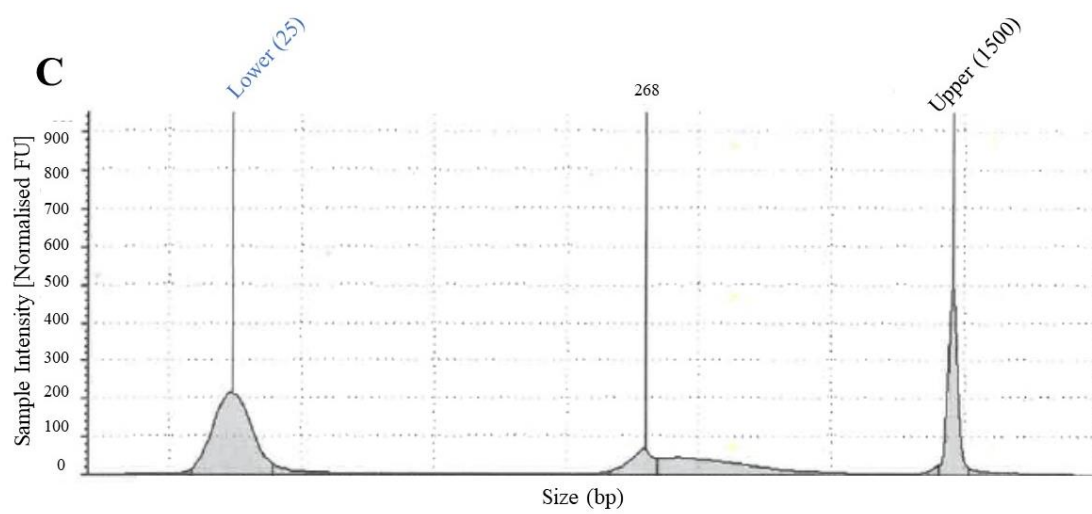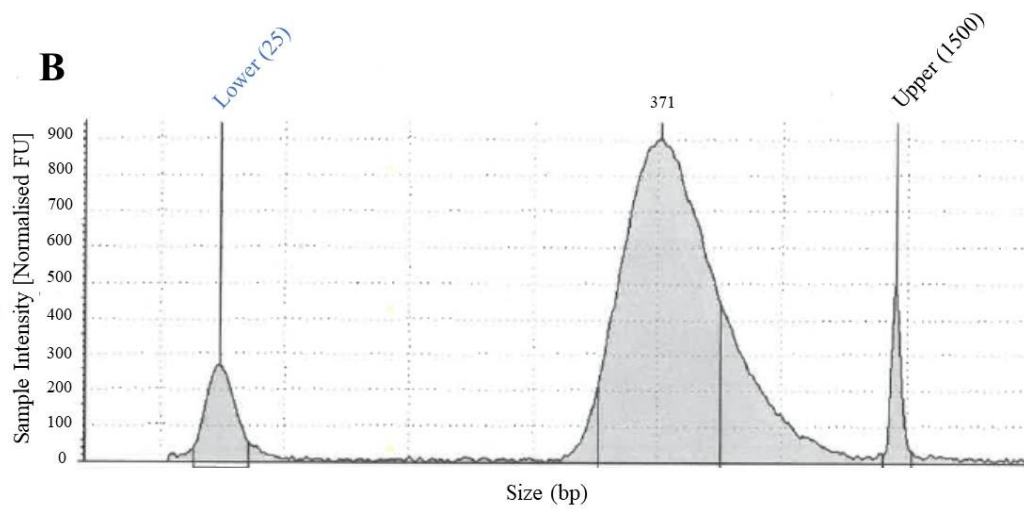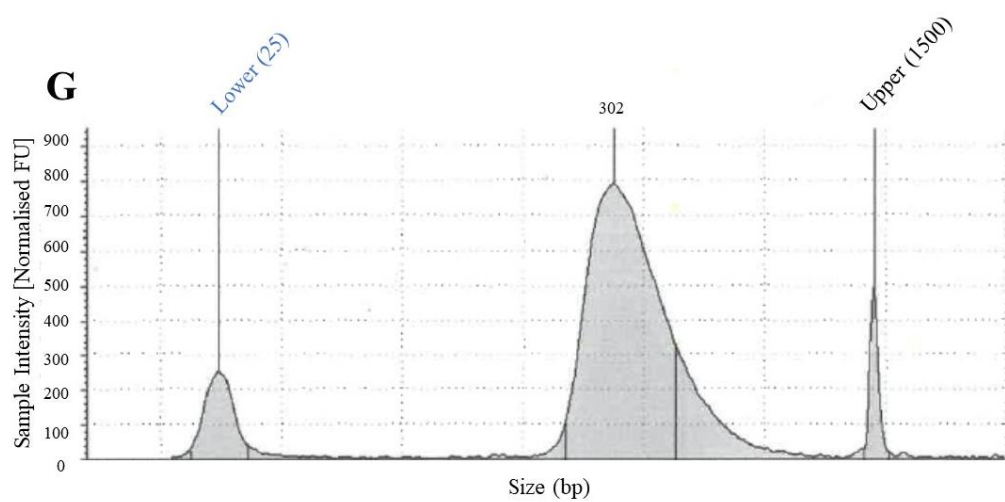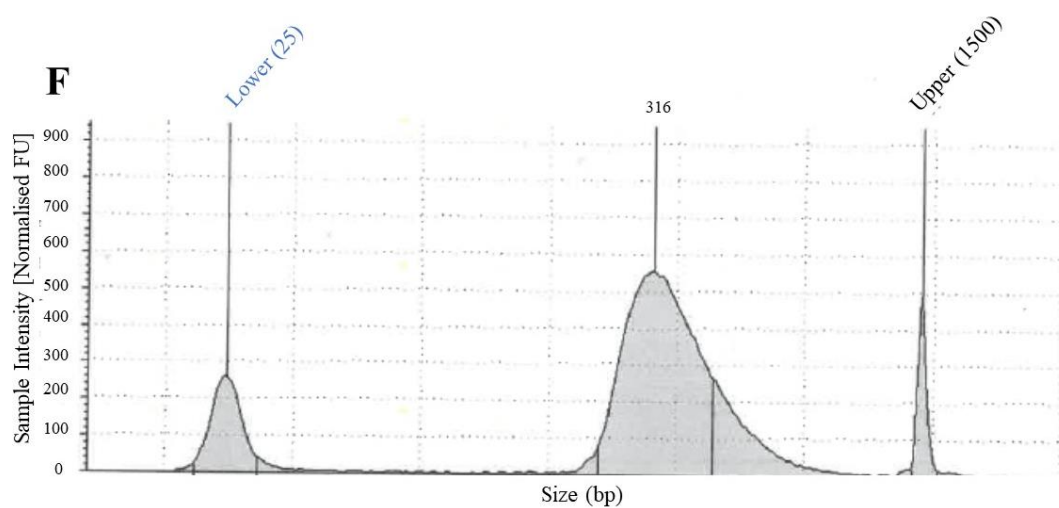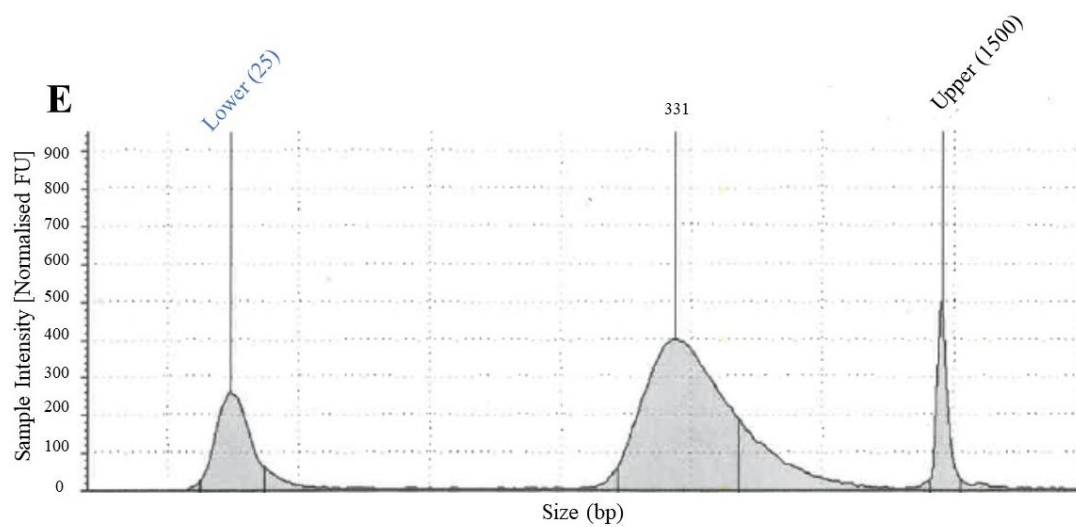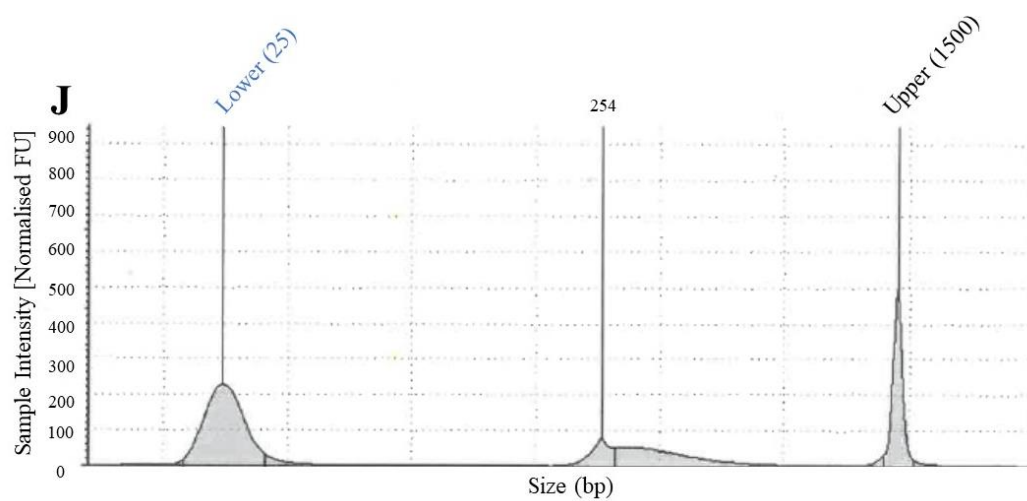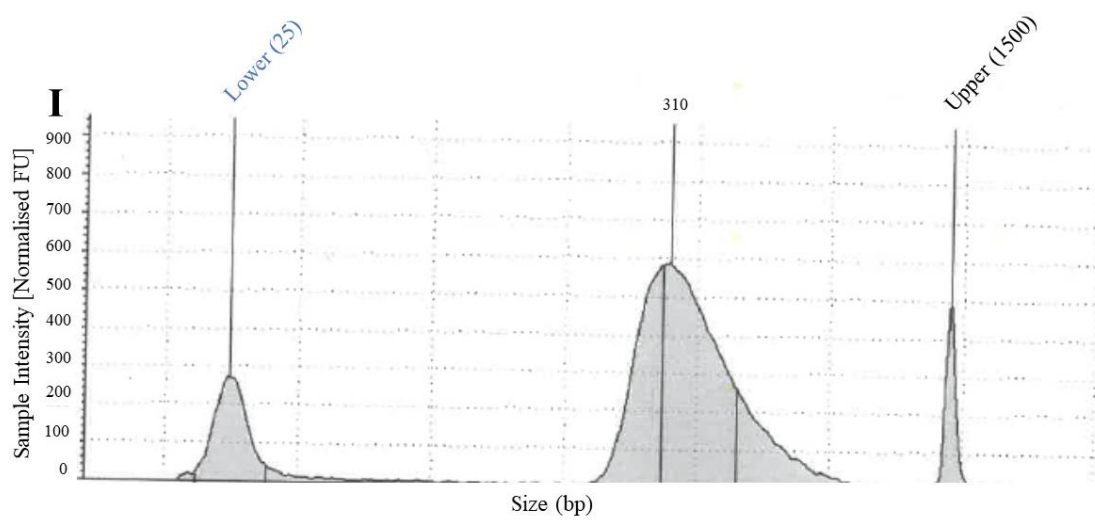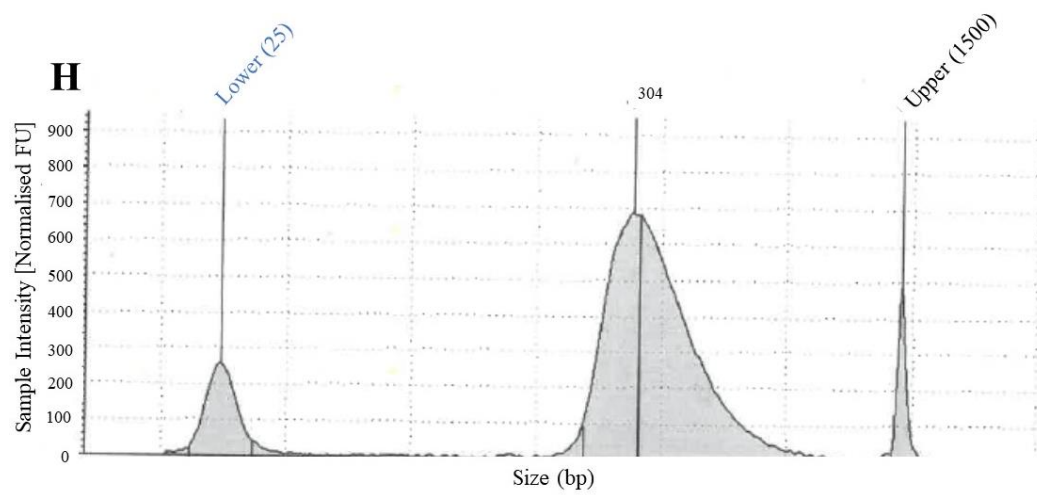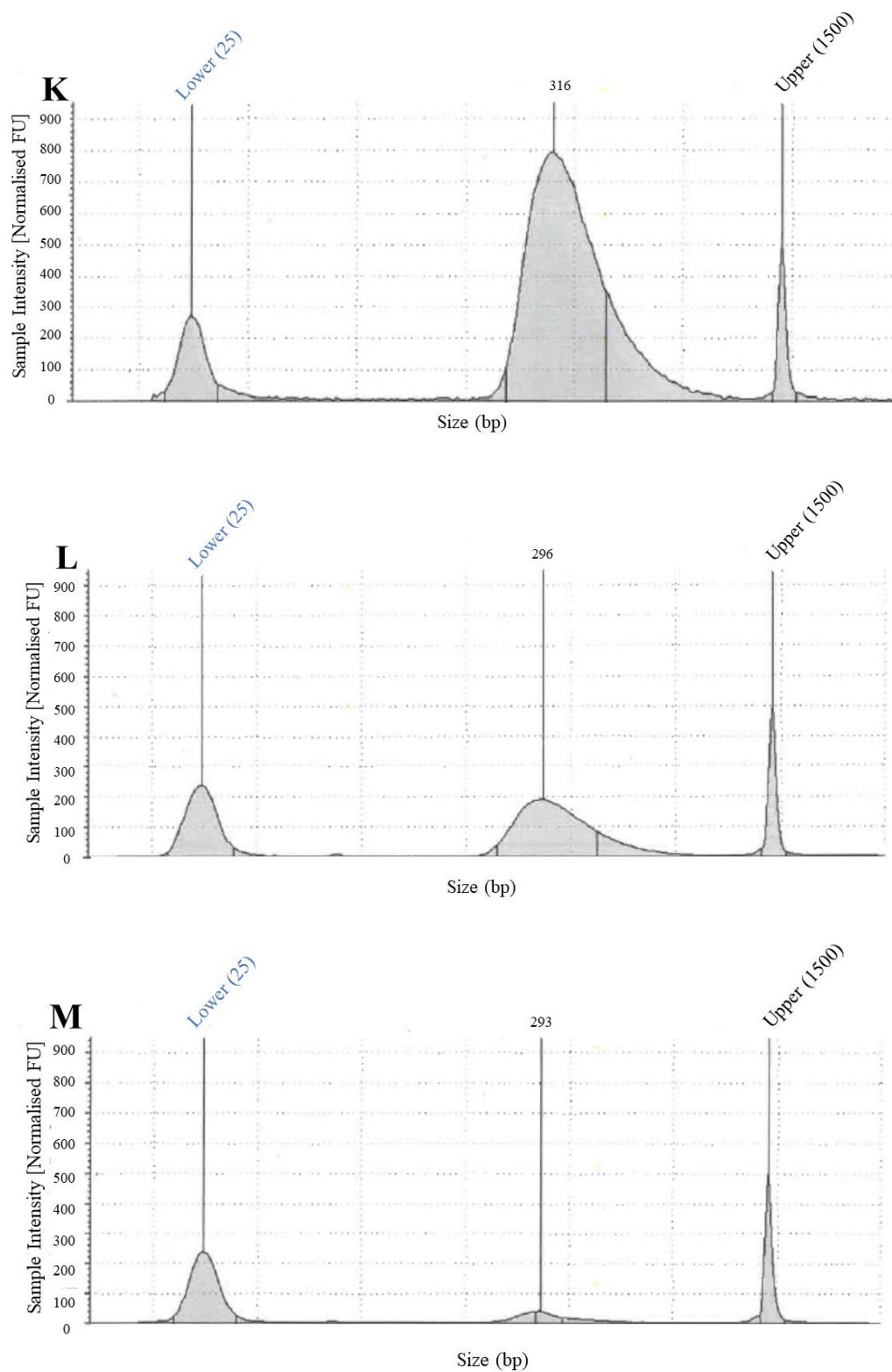
Figure S8: DNA library size distribution. Library quality was assessed using a Bioanalyzer (Agilent DNA 1000 Chip). Distribution for cell only (**Fig. S8 B, C, D**), cell with $Ti_3C_2T_x$ (**Fig. S8 E, F, G),** cell with IL-1β (**Fig. S8 H, I, J**) and cell with $Ti_3C_2T_x$ and IL-1β (**Fig. S8 K, L, M**). Ladder standard (**Fig. S8 A**).
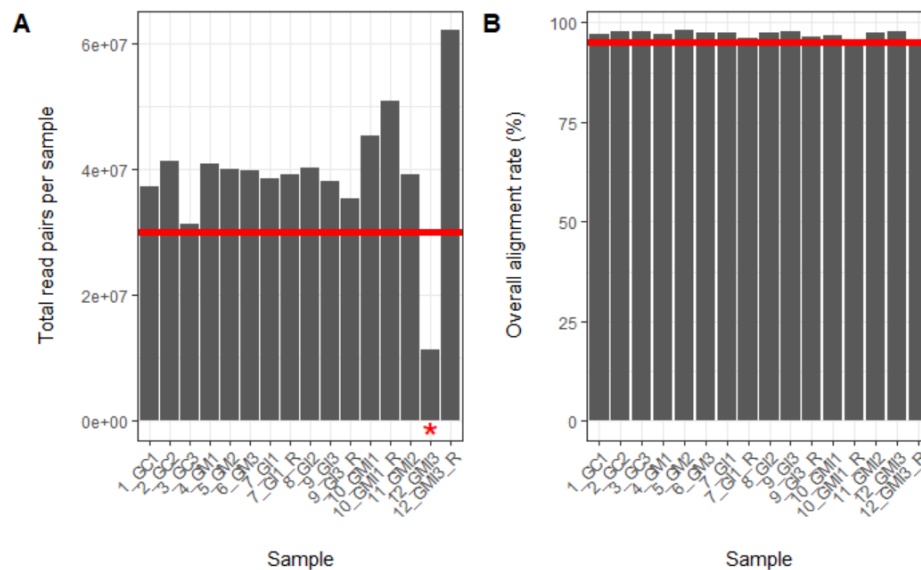
Figure S9: Summary of mapping to the GRCh38 genome: all data. Total raw reads per sample (red lines indicate 30 million read pairs) (**Fig. S9 A**). Proportion of the reads correctly aligning to the genome (red line indicates 95% alignment) (**Fig. S9 B**).
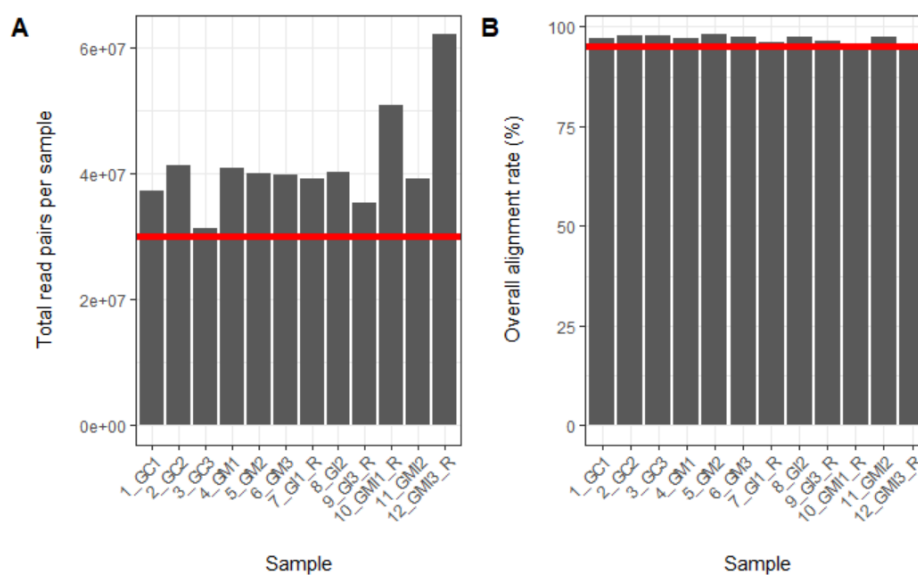
Figure S10: Summary of mapping to the GRCh38 genome; new minimal set (8 from Seq.run 1, 4 from Seq.run 2). Total raw reads per sample (red lines indicate 30 million read pairs (**Fig. S10 A**). Proportion of the reads correctly aligning to the genome (red line indicates 95% alignment) (**Fig. S10 B**).
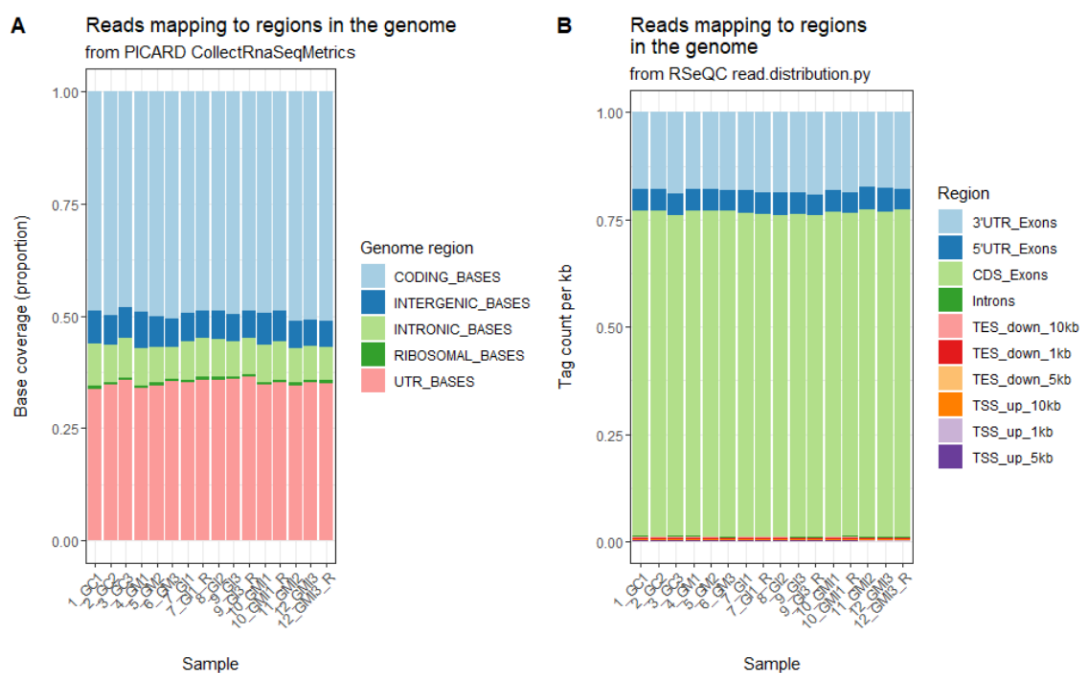
Figure S11: Summary of reads mapping to regions in the GRCh38 genome: all data. Proportion mapping to regions (PICARD output) (**Fig. S11 A**). Proportion mapping to regions (RSeQC output), normalised for total proportion of each region in the genome (**Fig. S11 B**).
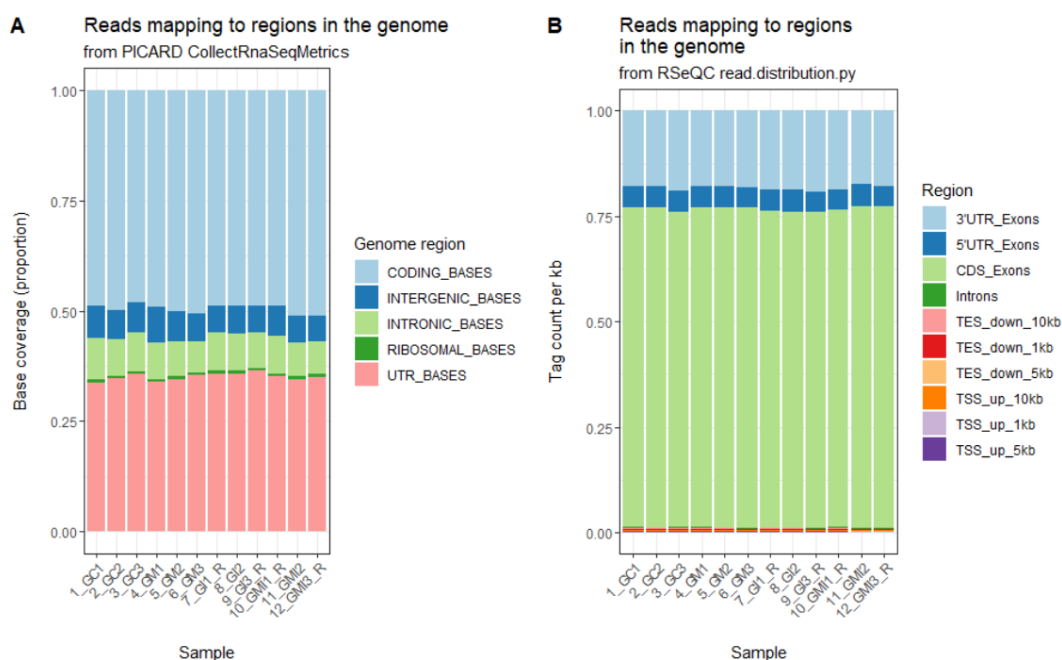
Figure S12: Summary of reads mapping to regions in the GRCh38 genome: new minimal set (8 from Seq.run 1, 4 from Seq.run 2). Proportion mapping to regions (PICARD output) (**Fig. S12**

A). Proportion mapping to regions (RSeQC output), normalised for total proportion of each region in the genome (**Fig. S12 B**).
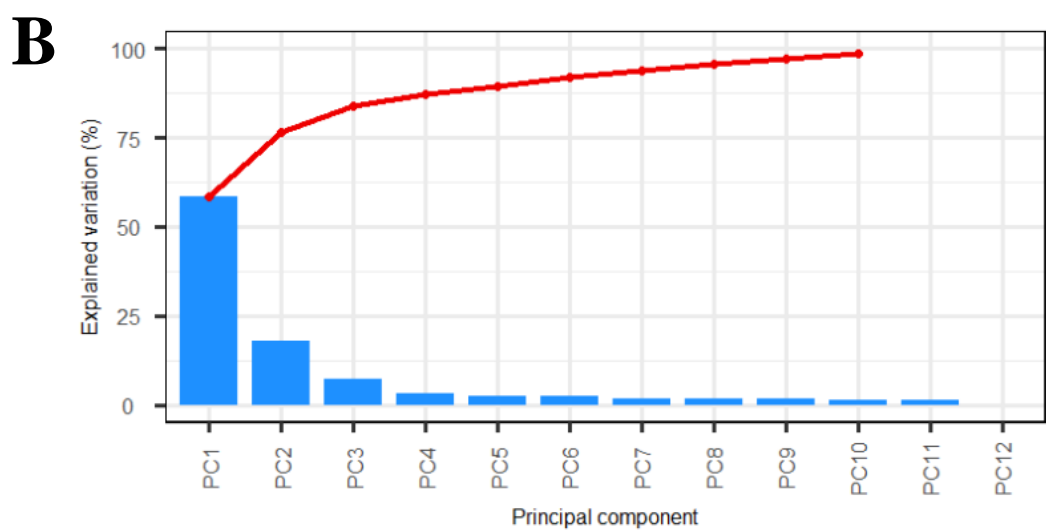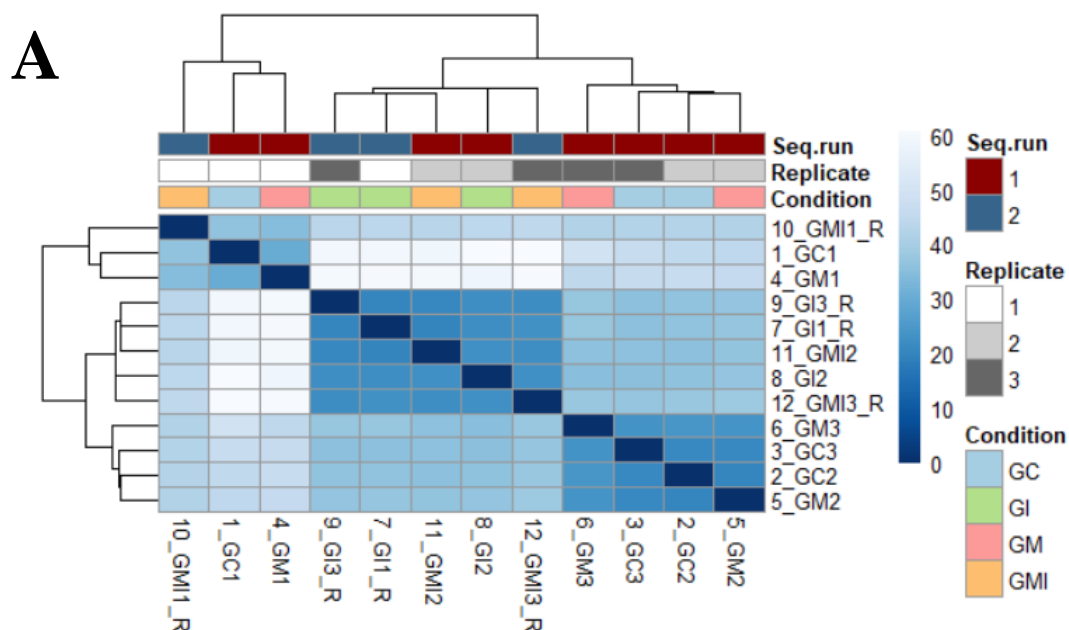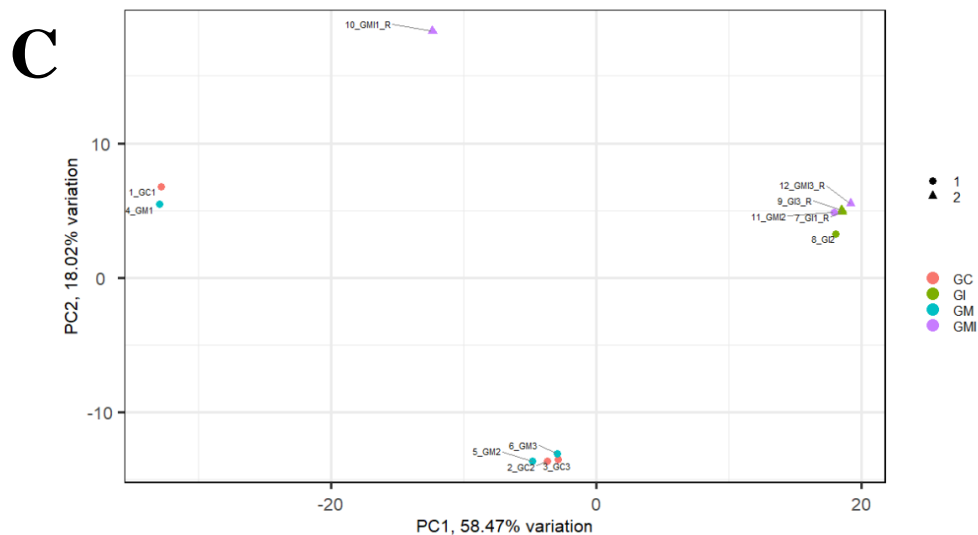
Figure S13: Principal component variance of the samples. Unsupervised clustering of samples based on their DESEq2 normalised gene-level counts. Heat map of inter-sample Euclidean distances, e darker blue colours indicate closer similarity (**Fig. S13 A**). Scree plot of variance explained ratio for each principal component showing distribution of variance across all twelve technical repeats (%) (**Fig. S13 B**). Principal components analysis of the clustered samples (**Fig. S13 C**).

4.3.5 Lipid profile of IL-1β-primed and $Ti_3C_2T_x$-treated cells
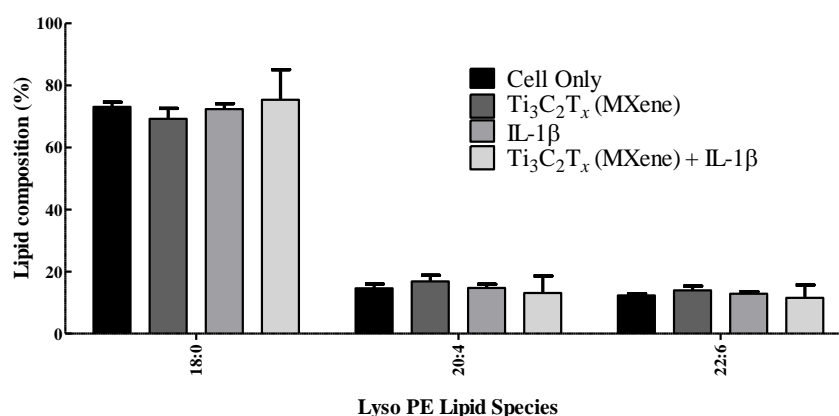
Figure S14: Fatty acid composition (%) in lysophosphatidylethanolamine (LysoPE) lipid species in cells treated with $Ti_3C_2T_x$ and IL-1β. Significance was determined using a two-way ANOVA and post-hoc Bonferroni's comparison of all conditions to one condition '**Cell only**'. Lipid

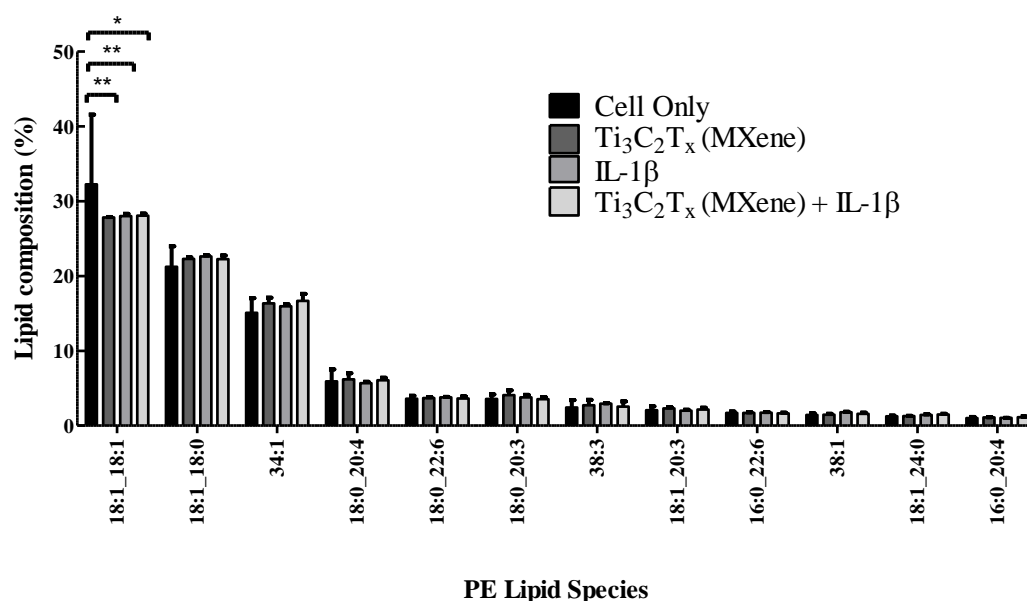identifications are described using the Lipidmaps specification (294). Species in order of highest compositional abundance. (Cell only: cells alone; $Ti_3C_2T_x$ (MXene): cells grown on $Ti_3C_2T_x$ coatings; IL-1β: cells treated with IL-1β; $Ti_3C_2T_x$ (MXene) + IL-1β: cells grown on $Ti_3C_2T_x$ coatings treated with IL-1β) (Mean $\pm$ SD; n=3)

Figure S15: Fatty acid composition (%) in phosphatidylcholine (PC[OH]) lipid species in cells treated with $Ti_3C_2T_x$ and IL-1β. A significant upregulation in PC 32:0 was found in cells treated with $Ti_3C_2T_x$ + IL-1β relative to the cell only. Significance was determined using a two-way ANOVA and post-hoc Bonferroni's comparison of all conditions to one condition '**Cell only**'. ** p $\leq$ 0.01. Lipid identifications are described using the Lipidmaps specification (294). Species in order of highest compositional abundance. (Mean $\pm$ SD; n=3)
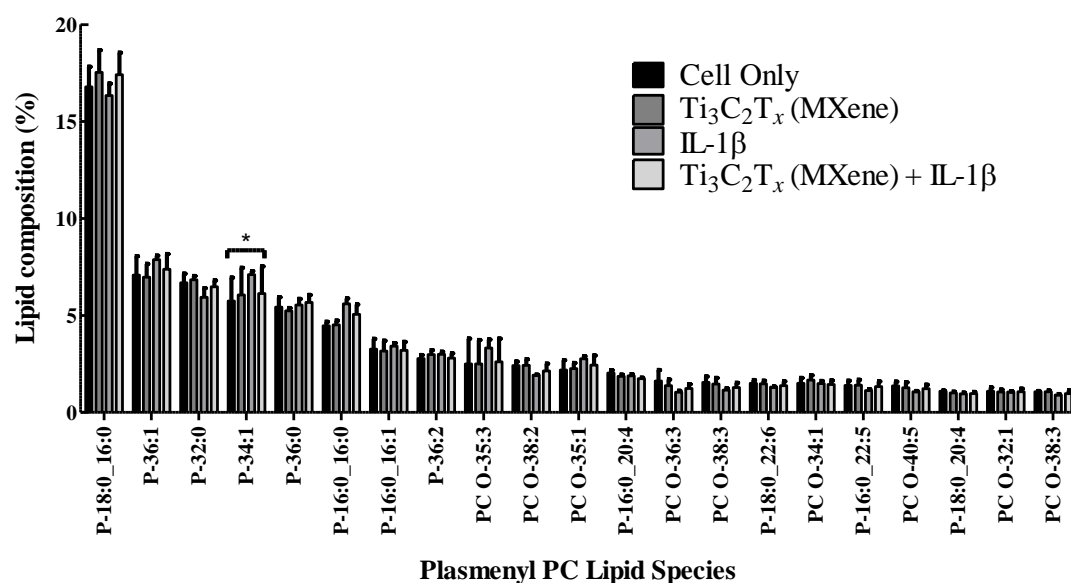
Figure S16: Fatty acid composition (%) in phosphatidylethanolamine (PE) species in cells treated with $Ti_3C_2T_x$ and IL-1β. A significant downregulation in PE 18:1_18:1 was found in all conditions relative to the cell only. Significance was determined using a two-way ANOVA and post-hoc Bonferroni's comparison of all conditions to one condition '**Cell only**'. * $p \leq 0.05$, ** $p \leq 0.01$. Lipid identifications are described using the Lipidmaps specification (294). Species in order of highest compositional abundance. (Mean ± SD; n=3)
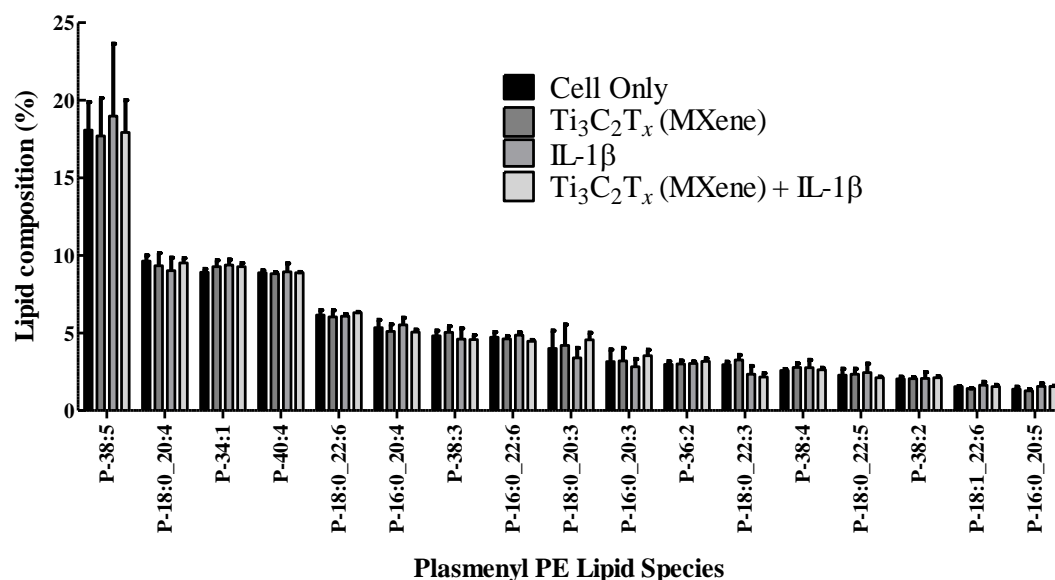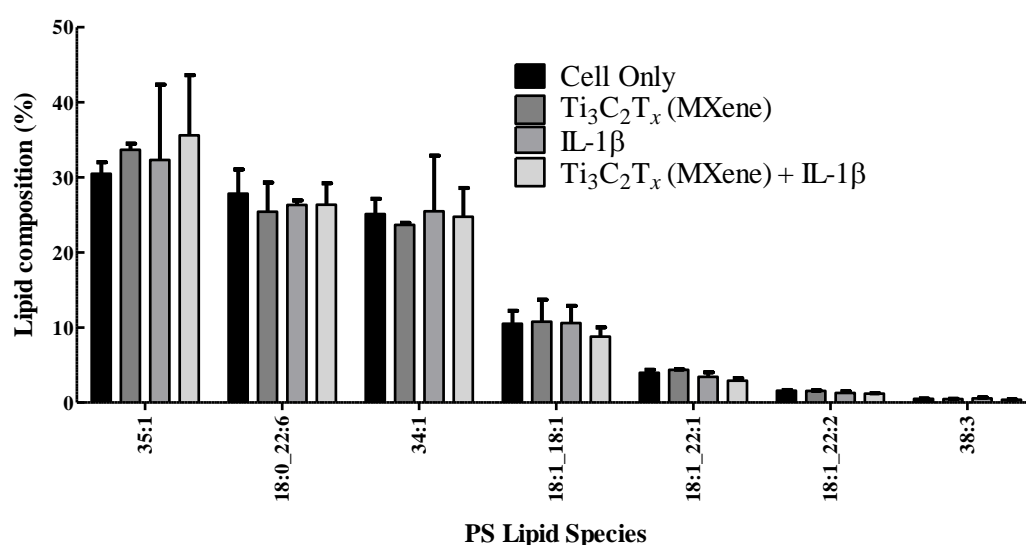

Figure S17: Fatty acid composition (%) in plasmenyl phosphatidylcholine (Plasmenyl-PC) species in cells treated with $Ti_3C_2T_x$ and IL-1β. A significant upregulation in Plasmenyl PC 34:1 was found in cells treated with IL-1β relative to the cell only. Significance was determined using

a two-way ANOVA and post-hoc Bonferroni's comparison of all conditions to one condition 'Cell only'. ** $p \leq 0.05$. Lipid identifications are described using the Lipidmaps specification (294). Species in order of highest compositional abundance. (Mean $\pm$ SD; n=3)

Figure S18: Fatty acid composition (%) in plasmenyl phosphatidylethanolamine (Plasmenyl-PE) species in cells treated with $Ti_3C_2T_x$ and IL-1β. Significance was determined using a two-way ANOVA and post-hoc Bonferroni's comparison of all conditions to one condition '**Cell only**'. Lipid identifications are described using the Lipidmaps specification (294). Species in order of highest compositional abundance. (Mean $\pm$ SD; n=3)
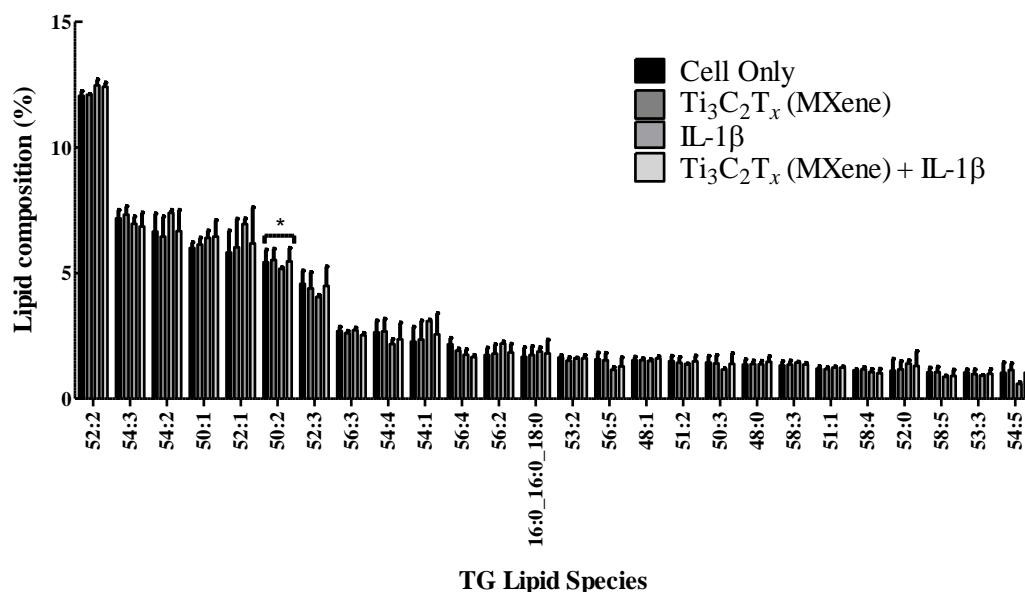

Figure S19: Fatty acid composition (%) in phosphatidylserine (PS) species in cells treated with $Ti_3C_2T_x$ and IL-1β. Significance was determined using a two-way ANOVA and post-hoc

Bonferroni's comparison of all conditions to one condition '**Cell only**'. Lipid identifications are described using the Lipidmaps specification (294). Species in order of highest compositional abundance. (Mean ± SD; n=3)

Figure S20: Fatty acid composition (%) in triglycerides (TG) species in cells treated with $Ti_3C_2T_x$ and IL-1β. A significant upregulation in TG 52:1 was found in cells treated with IL-1β relative to the cell only. Significance was determined using a two-way ANOVA and post-hoc Bonferroni's comparison of all conditions to one condition '**Cell only**'. ** $p \leq 0.05$. Lipid identifications are described using the Lipidmaps specification (294). Species in order of highest compositional abundance. (Mean ± SD; n=3)

5.3.4 Senescence beta-galactosidase staining of interleukin-1 beta-primed human lens epithelial cells with $Ti_3C_2T_x$ (MXene) coatings
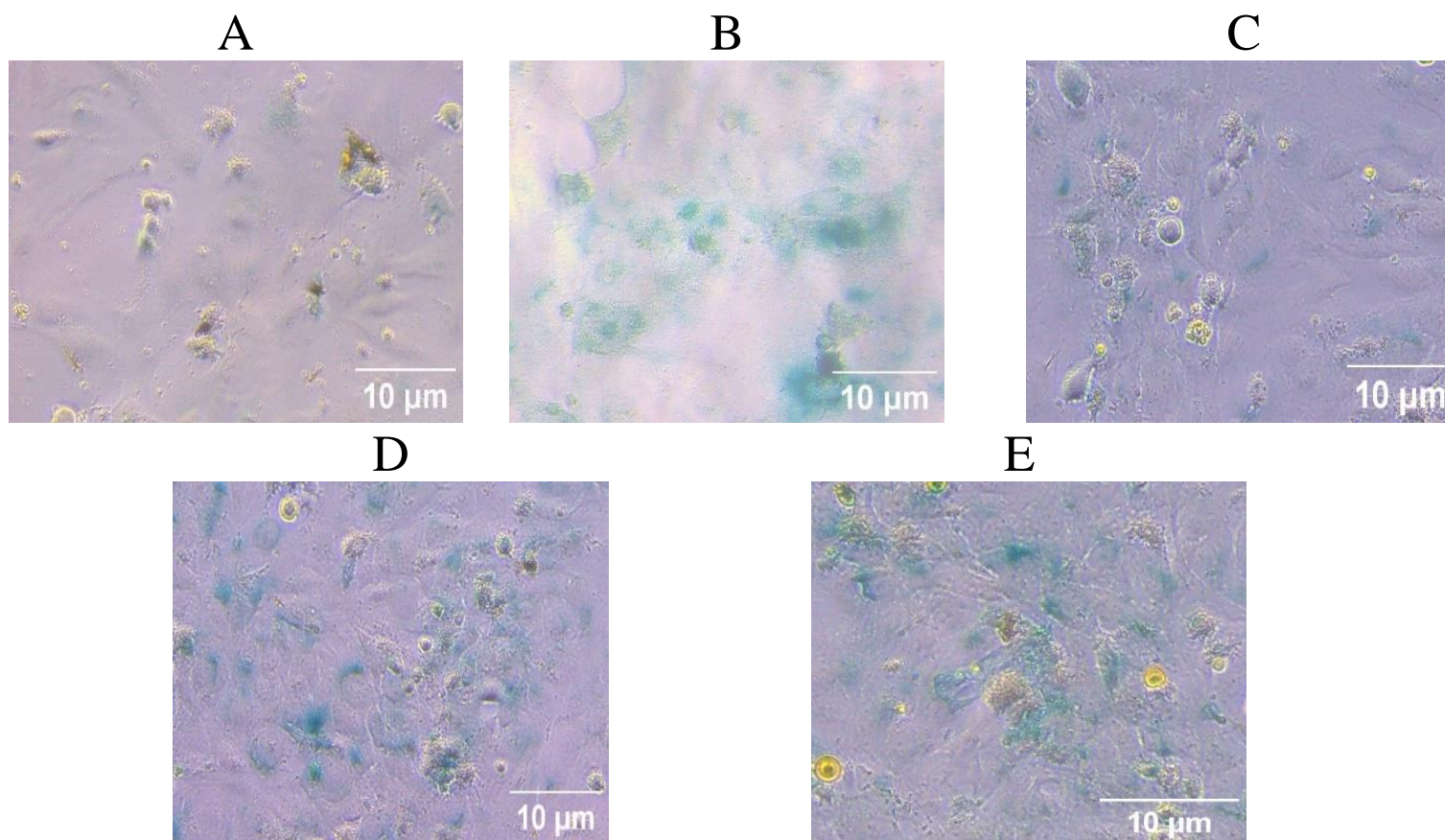

Figure S21: β-galactosidase expression of FHL124 cells treated with $Ti_3C_2T_x$ (**Fig. S21 B**), IL-1β (**Fig. S21 C**), $Ti_3C_2T_x$ and IL-1β (**Fig. S21 D**) and etoposide (**Fig. S21 E**). Scale bar: 10 µm.
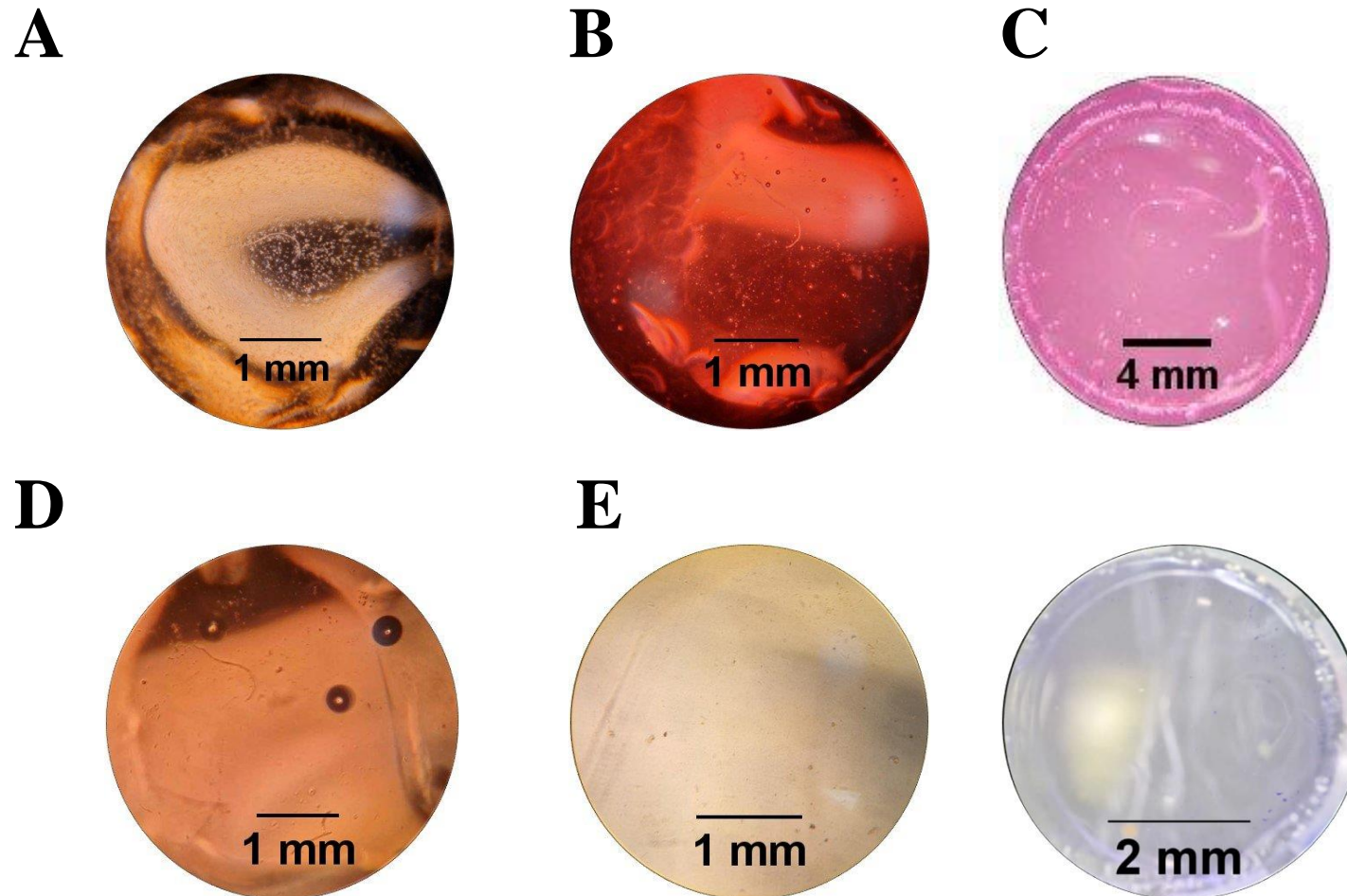
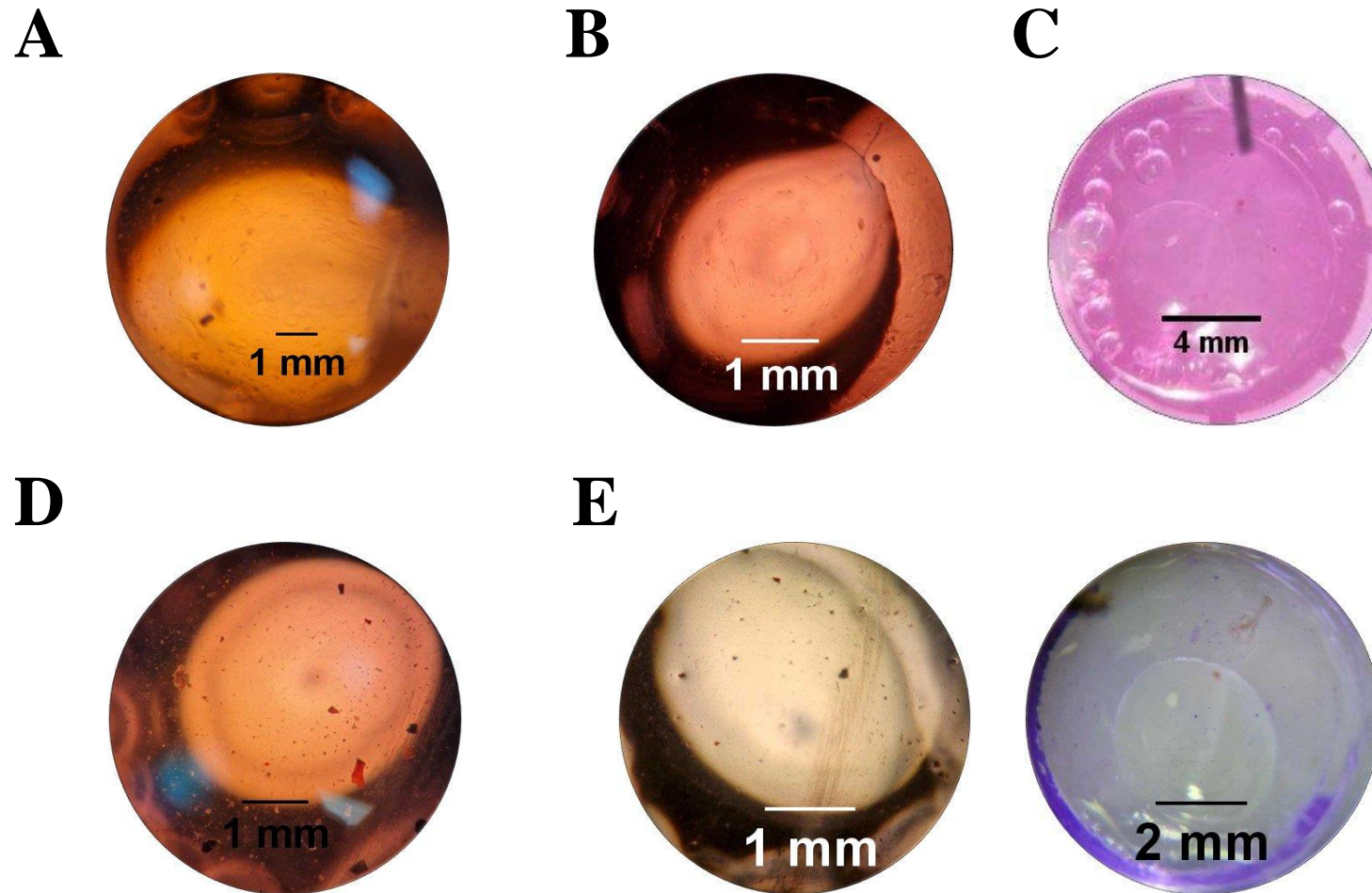6.3.3 Cell migration across the posterior capsule

Figure S22: Light microscope images of a capsule control (n=2). Capsule seeded with cells at 5 x magnification (**Fig. S22 A**), after mock phacoemulsification at 5 x magnification (**Fig. S22 B**) and 2 x magnification (**Fig. S22 C**), after 1-day incubation at 5 x magnification (left) (**Fig. S22 D**) and day 7 at 5 x magnification (left) and 35 x magnification (right) stained with crystal violet (**Fig. S22 E**). (n=2 of 3)

235

Figure S23: Light microscope images of a capsule control (n=3). Capsule seeded with cells at 5 x magnification (**Fig. S23 A**), after mock phacoemulsification at 5 x magnification (**Fig. S23 B**) and 2 x magnification (**Fig. S23 C**), after 1-day incubation at 5 x magnification (left) (**Fig. S23 D**) and day 7 at 5 x magnification (left) and 35 x magnification (right) stained with crystal violet (**Fig. S23 E**). (n=3 of 3)
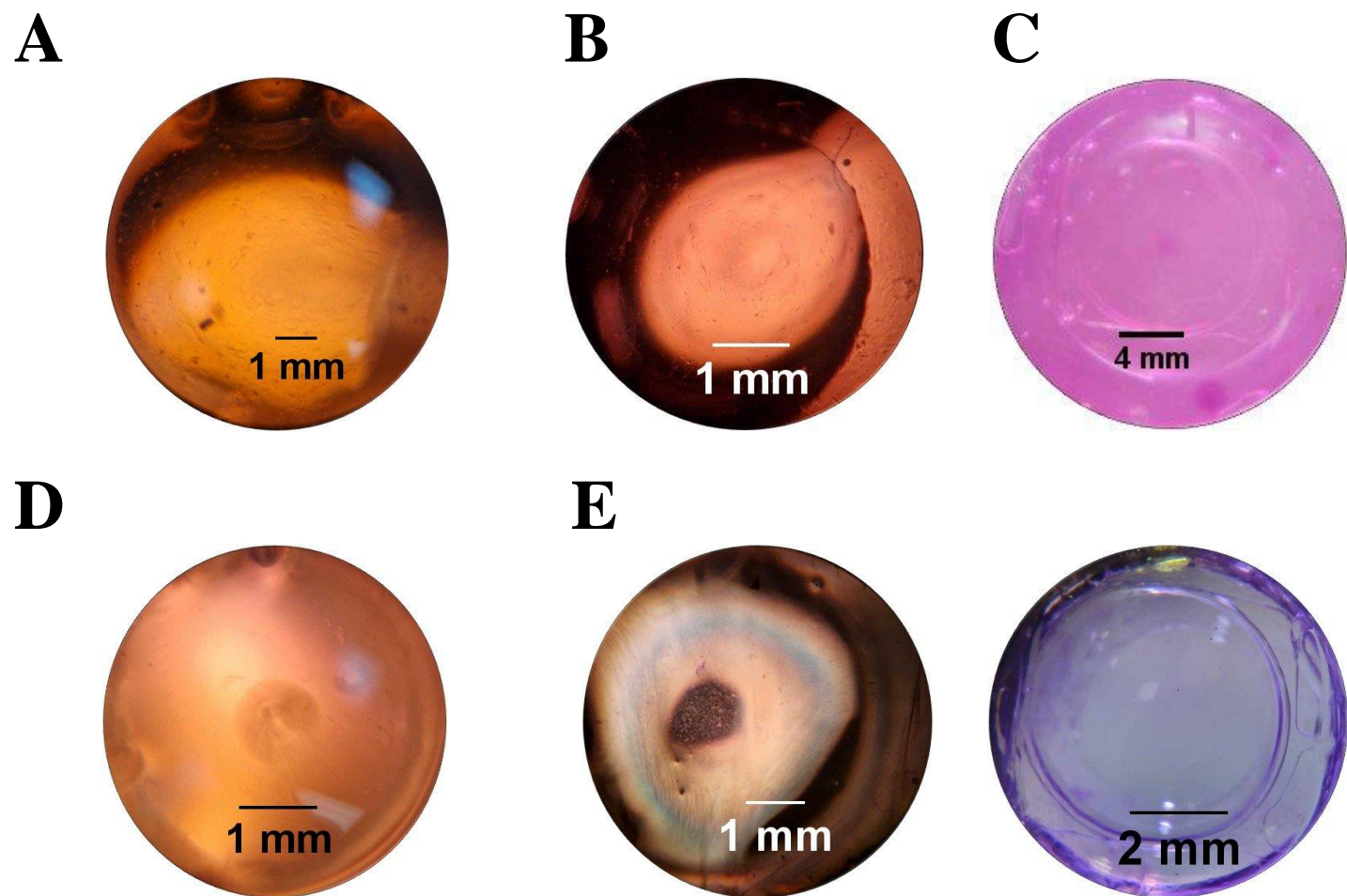
Figure S24: Light microscope images of an implanted hydrophobic IOL (n=2). Capsule seeded with cells at 5 x magnification (**Fig. S24 A**), after mock phacoemulsification at 5 x magnification (**Fig. S24 B**) and 2 x magnification (**Fig. S24 C**), after 1-day incubation at 5 x magnification (left) (**Fig. S24 D**) and day 7 at 5 x magnification (left) and 35 x magnification (right) stained with crystal violet (**Fig. S24 E**). (n=2 of 3)
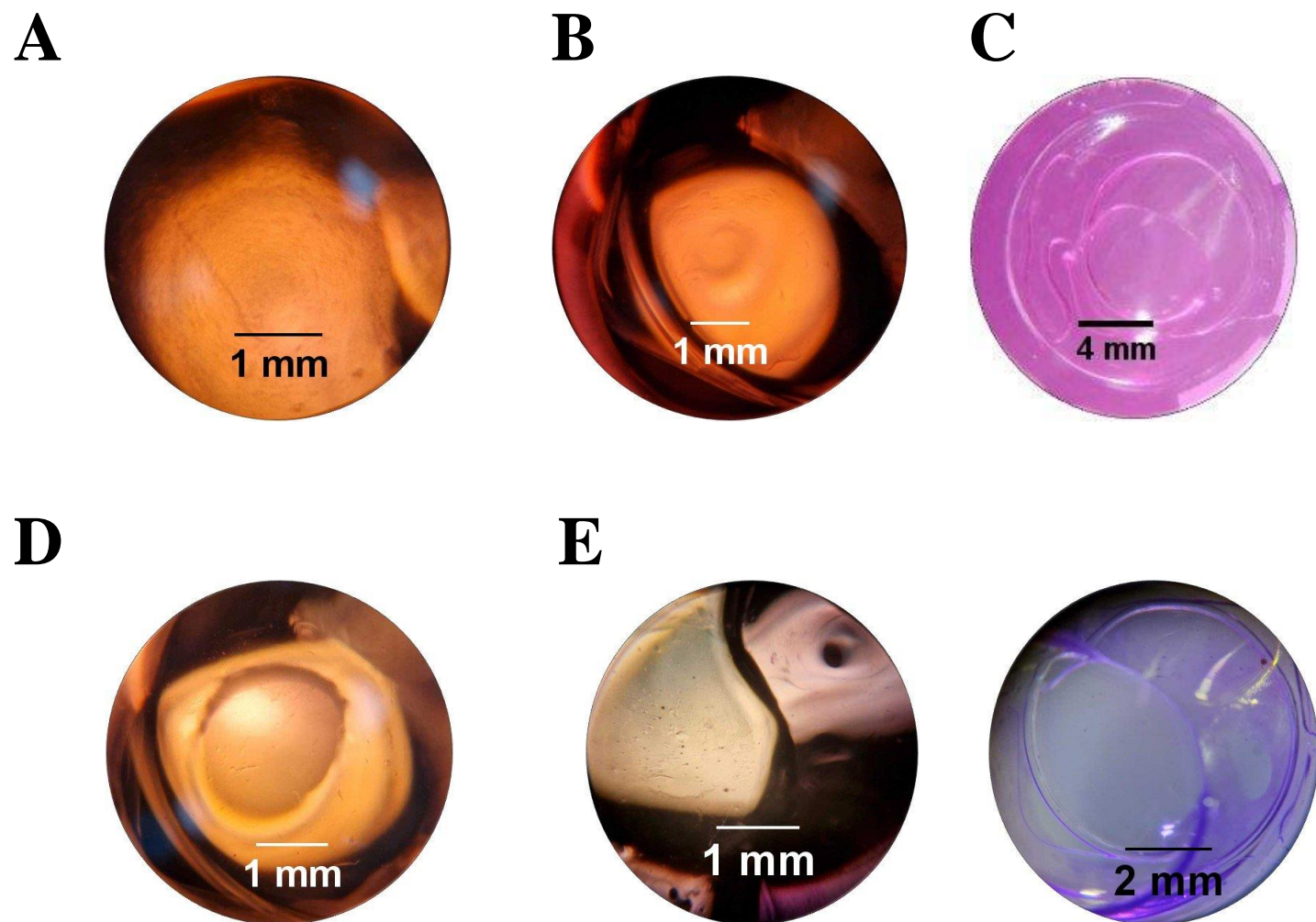
Figure S25: Light microscope images of an implanted hydrophobic IOL (n=3). Capsule seeded with cells at 5 x magnification (**Fig. S25 A**), after mock phacoemulsification at 5 x magnification (**Fig. S25 B**) and 2 x magnification (**Fig. S25 C**), after 1-day incubation at 5 x magnification (left) (**Fig. S25 D**) and day 7 at 5 x magnification (left) and 35 x magnification (right) stained with crystal violet (**Fig. S25 E**). (n=3 of 3)
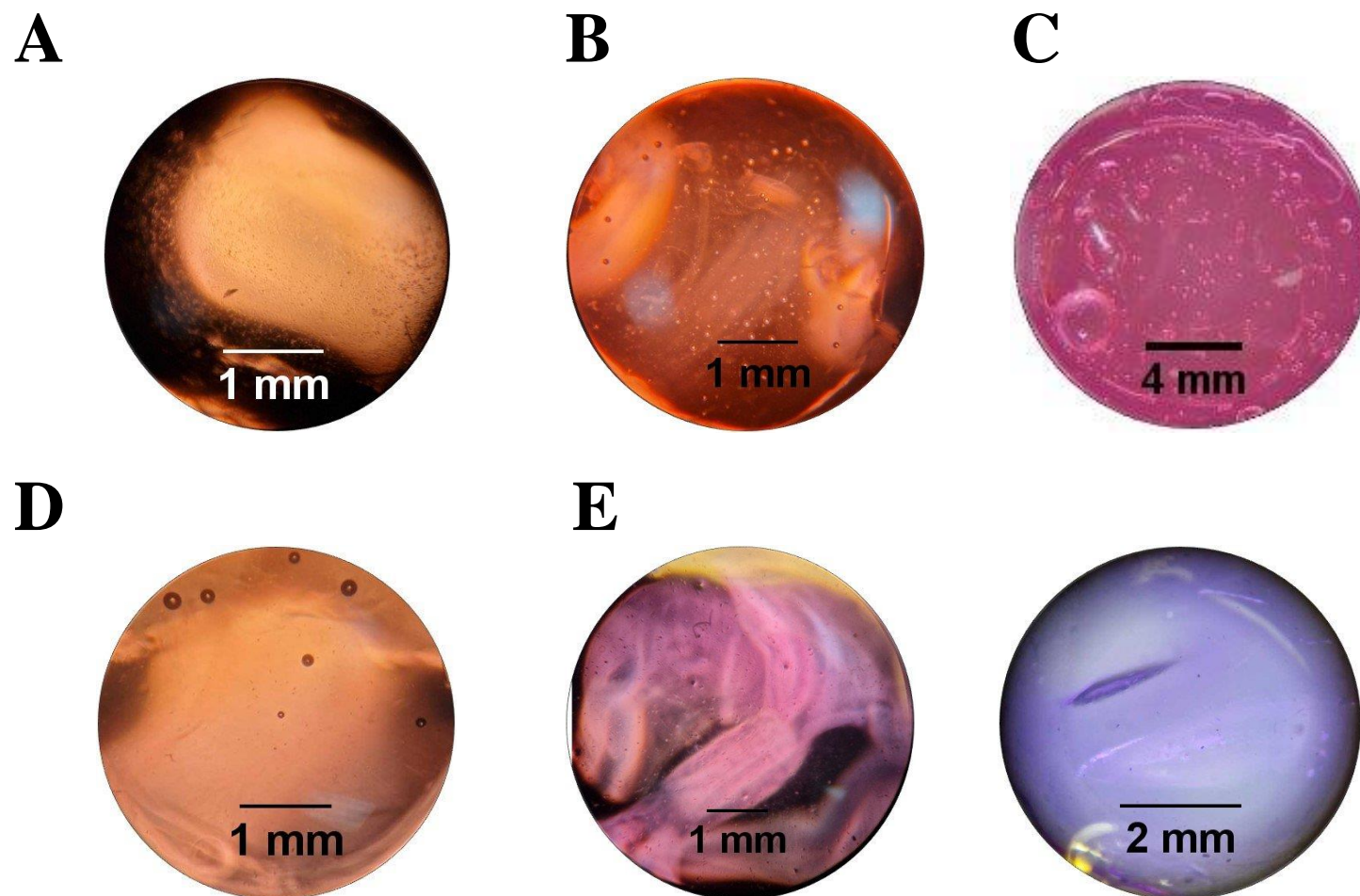
238

Figure S26: Light microscope images of an implanted hydrophilic IOL (n=2). Capsule seeded with cells at 5 x magnification (**Fig. S26 A**), after mock phacoemulsification at 5 x magnification (**Fig. S26 B**) and 2 x magnification (**Fig. S26 C**), after 1-day incubation at 5 x magnification (left) (**Fig. S26 D**) and day 7 at 5 x magnification (left) and 35 x magnification (right) stained with crystal violet (**Fig. S26 E**). (n=2 of 3)
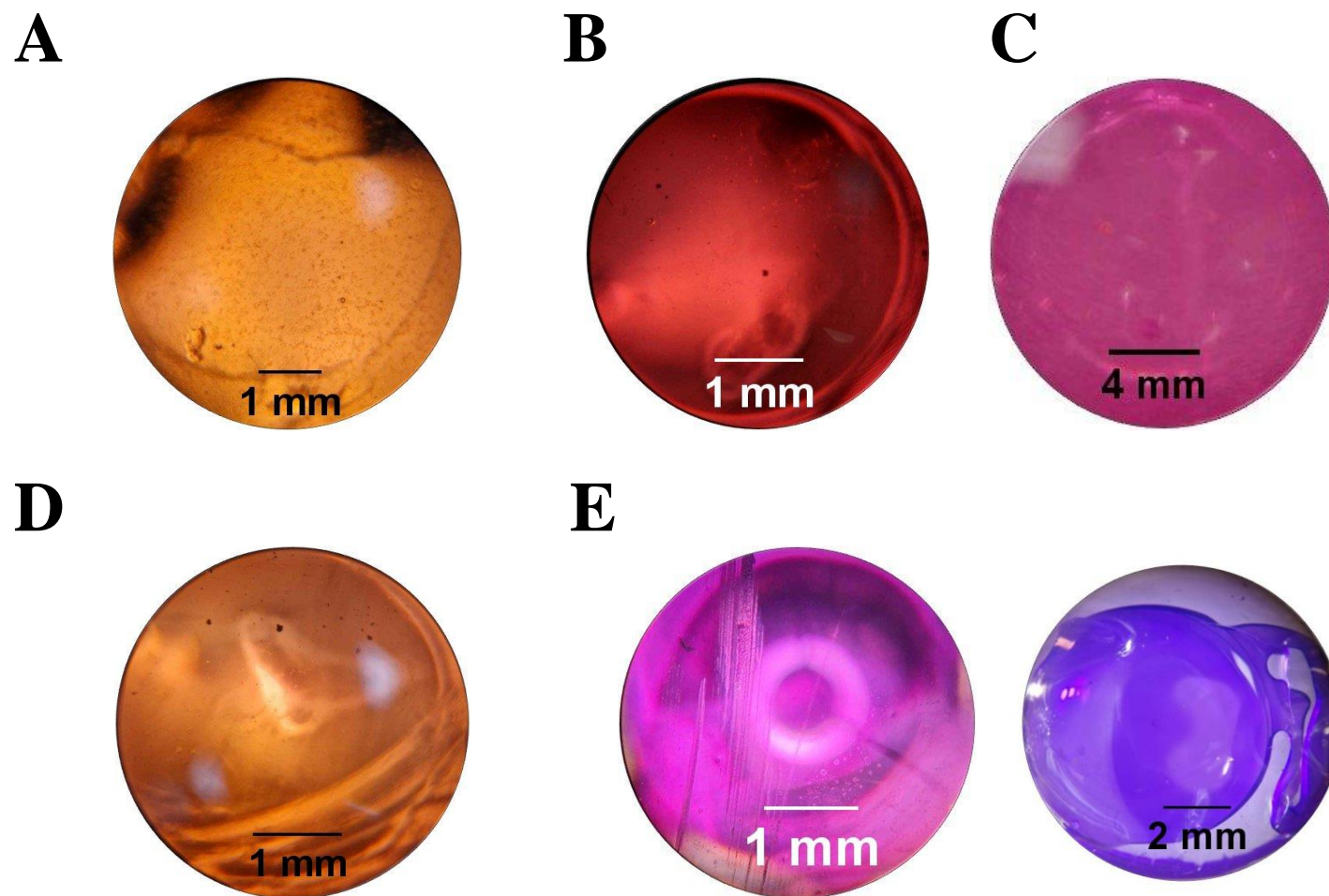
Figure S27: Light microscope images of an implanted hydrophilic IOL (n=3). Capsule seeded with cells at 5 x magnification (**Fig. S27 A**), after mock phacoemulsification at 5 x magnification (**Fig. S27 B**) and 2 x magnification (**Fig. S27 C**), after 1-day incubation at 5 x magnification (left) (**Fig. S27 D**) and day 7 at 5 x magnification (left) and 35 x magnification (right) stained with crystal violet (**Fig. S27 E**). (n=3 of 3)
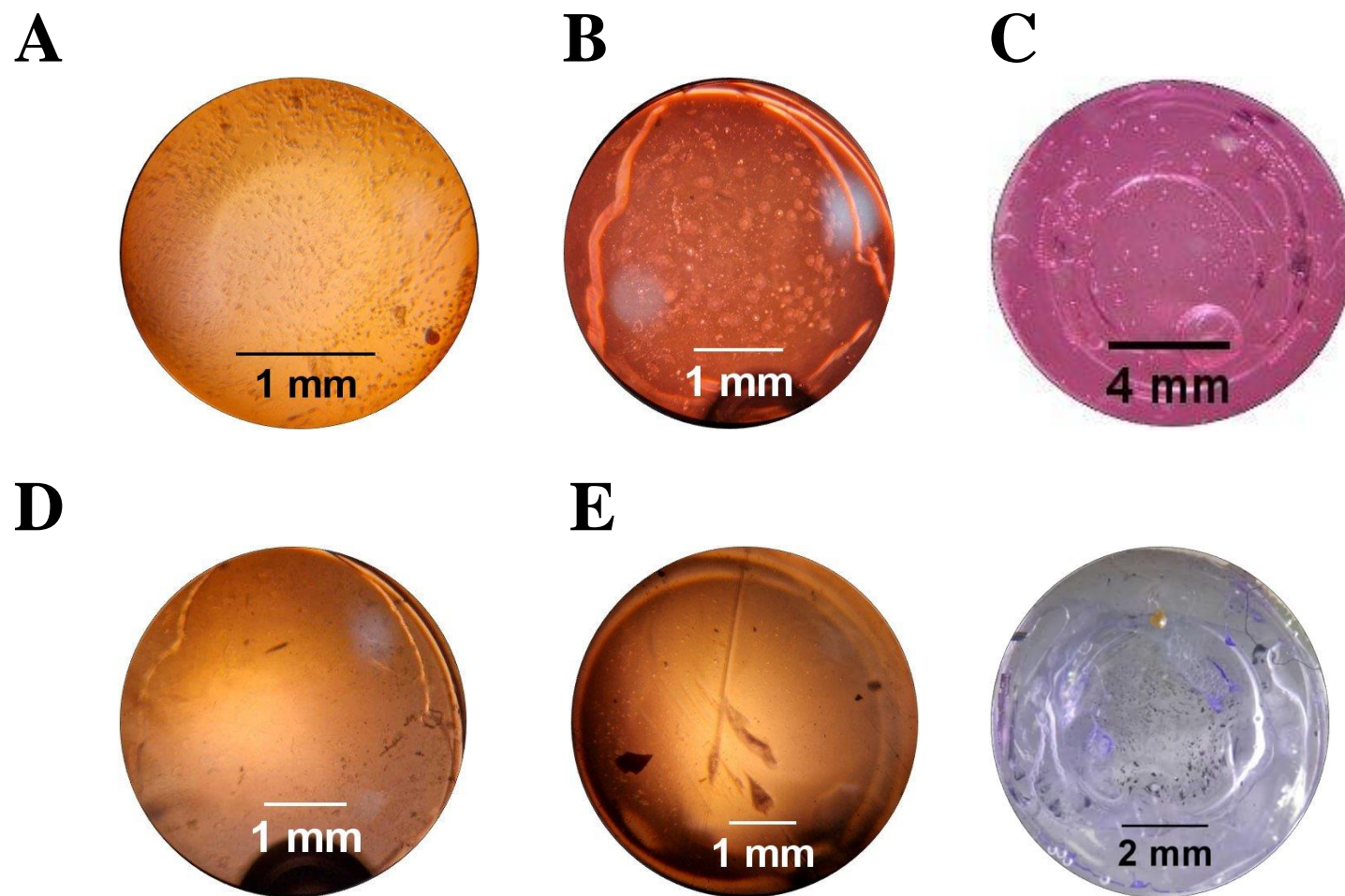
Figure S28: Light microscope images of an implanted $Ti_3C_2T_x$-coated hydrophobic IOL (n=2). Capsule seeded with cells at 5 x magnification (**Fig. S28 A**), after mock phacoemulsification at 5 x magnification (**Fig. S28 B**) and 2 x magnification (**Fig. S28 C**), after 1-day incubation at 5 x magnification (left) (**Fig. S28 D**) and day 7 at 5 x magnification (left) and 35 x magnification (right) stained with crystal violet (**Fig. S28 E**). (n=2 of 3)

Figure S29: Light microscope images of an implanted $Ti_3C_2T_x$-coated hydrophobic IOL (n=3). Capsule seeded with cells at 5 x magnification (**Fig. S29 A**), after mock phacoemulsification at 5 x magnification (**Fig. S29 B**) and 2 x magnification (**Fig. S29 C**), after 1-day incubation at 5 x magnification (left) (**Fig. S28 D**) and day 7 at 5 x magnification (left) and 35 x magnification (right) stained with crystal violet (**Fig. S29 E**). (n=3 of 3)
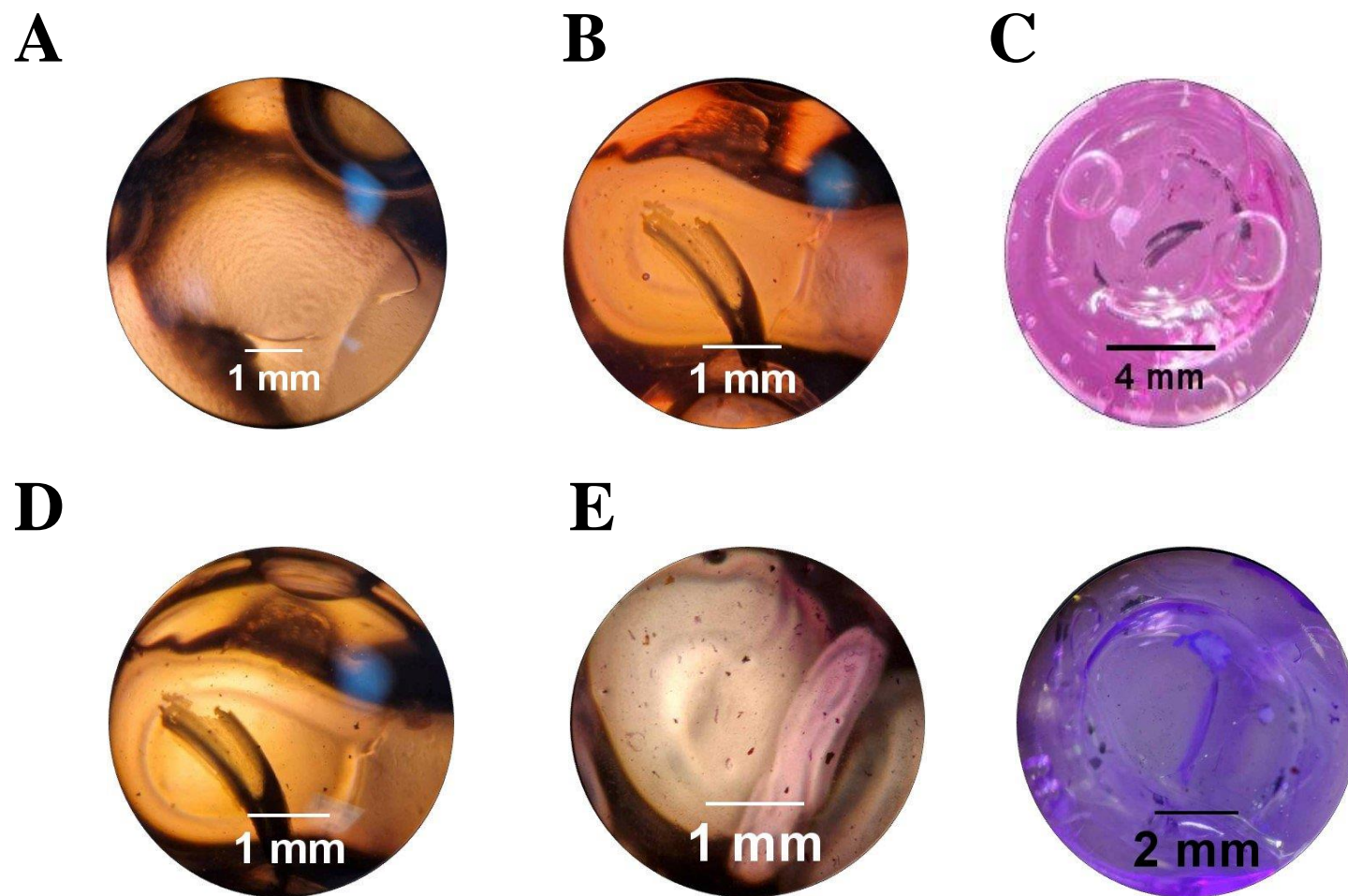
Appendix 2 - Publications and conference abstracts

1. Optoelectronic nanomaterials to reduce the complications associated with cataract surgery. Cooksley, G.; Lacey, J.; Dymond, M.K.; Gogotsi, Y.; Sandeman, S. (*Abstract and poster presentation*) – "MXene 2020: 10 Years Later" Virtual Conference. Drexel University, Philadelphia, PA, USA. 3-7th August 2020

2. Factors Affecting Posterior Capsule Opacification in the Development of Intraocular Lens Materials. Cooksley, G.; Lacey, J.; Dymond, M.K.; Sandeman, S. *Pharmaceutics* **2021**, *13*, 860. https://doi.org/10.3390/pharmaceutics13060860

3. Investigating the impact of $Ti_3C_2T_x$ (MXene) within the capsule bag on the development of posterior capsule opacification. Cooksley, G.; Lacey, J.; Dymond, M.K.; Gogotsi, Y.; Sandeman, S. (*Abstract and poster presentation*) – 31st Conference of the European Society for Biomaterials with 43rd Annual Congress of the Iberian Society of Biomechanics and Biomaterials (SIBB). Porto, Portugal. 5-9th September 2021

4. Investigating the impact of $Ti_3C_2T_x$ (MXene) within the capsule bag on the development of posterior capsule opacification. Cooksley, G.; Lacey, J.; Dymond, M.K.; Gogotsi, Y.; Sandeman, S. (*Abstract and oral presentation*) – 32nd Conference of the European Society for Biomaterials. Bordeaux, France. 4-8th September 2022

5. Positive resolution of the wound-healing response contributing to posterior capsule opacification by $Ti_3C_2T_x$ MXene. Cooksley, G.; Lacey, J.; Dymond, M.K.; Gogotsi, Y.; Sandeman, S. (*Abstract and oral presentation*) – 8th International Conference on the Lens. Kailua-Kona, Hawaii. 4-9th December 2022

6. Positive resolution of the wound-healing response in lens epithelial cells by $Ti_3C_2T_x$ MXene coatings for use in accommodative intraocular lens devices. Cooksley, G.; Dymond, M.K.;

Stewart, N., Bucca, G., Hesketh, A., Lacey, J., Gogotsi, Y. and Sandeman, S. *2D Mater.* **2022**,10, 1, 014003. https://doi.org/10.1088/2053-1583/ac95a7

Mentoring

- Supervision of BY392 final year undergraduate students, University of Brighton, UK. March 2020

- Designed and delivered my own course "Help or hinder: the biocompatibility of biomaterials" in university-style tutorials to KS4 pupils. The Scholar's Programme, The Brilliant Club, Jan - April 2021; Feb-April 2022

- Delivered pre-designed Biology GCSE course in university-style tutorials to KS4 pupils. The Brilliant Tutoring Programme, The Brilliant Club, April-June 2021

- Supervision of CORE Undergraduate Research Placement Opportunity, Centre for Stress and Age-related Diseases, University of Brighton, UK. June-July 2021

- Supervision of BY392 final year undergraduate students, University of Brighton, UK. Oct - May 2021/2

Grants

- Young Investigator's Award (*external*), National Foundation for Eye Research
- Pump Priming Project (*internal*), Centre of Regenerative Medicine and Devices, University of Brighton, UK.
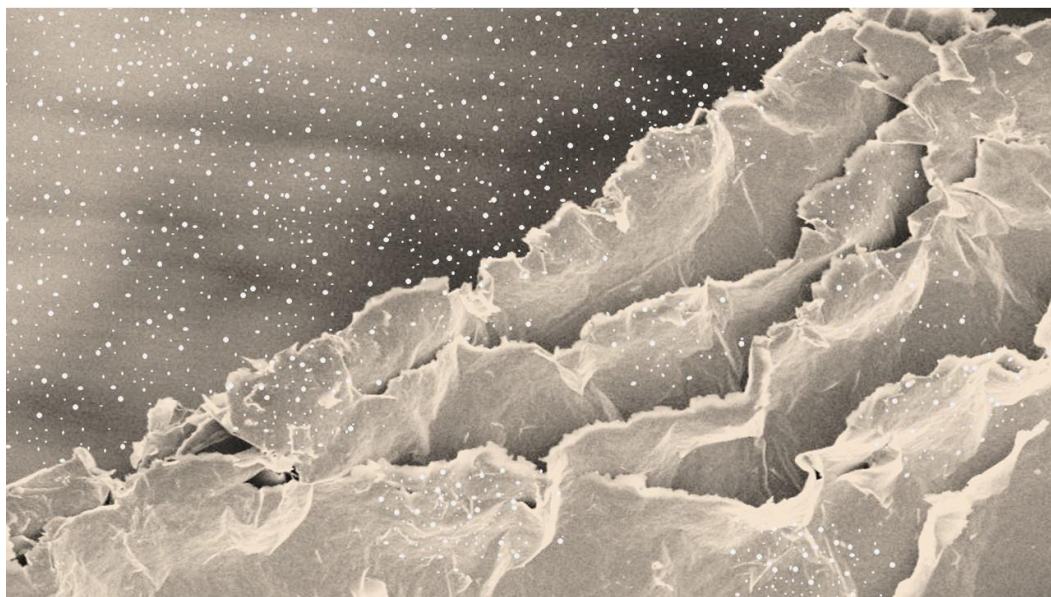
2nd place winner of NanoArtography 2022

This artwork was created by preparing a free-standing film of titanium carbide MXene and tearing the film into smaller fragments to show a cross-section of the multi-layer and delaminated flakes. The non-uniform breaking of the MXene film produced sharp edges which looked like mountain peaks. A snowy mountain scene is depicted to symbolise the outstanding accomplishments and contributions of MXene, to many disciplines since its discovery, much like the pioneering climbers who first climbed Mt. Everest.